الجمهورية الجزائرية الديمقراطية الشعبية
People's Democratic Republic of Algeria
وزارة التعليم العالي و البحث العلمي
Ministry of Higher Education and Scientific Research

Kasdi Merbah University
Ouargla
Faculty of Applied Sciences
Mechanical Engineering
Department

Ref :……

جامعة قاصدي مرباح
ورقلة
كلية العلوم التطبيقية
قسم الهندسة الميكانيكية

المرجع:.....

A thesis submitted to obtain the diploma of:

Doctorate of University in: Mechanical Engineering

Option: Materials Engineering

Theme

Elaboration and characterization of metal oxide thin films doped with different metals: Application to gas detection

Presented by:
Mr. Mohamed Zakaria Merad

Publicly defended on: 23/02/2026
In front of the jury committee composed of:

President	**Dr. Abderrahim beloufi**	**Pr.**	**Univ. Ouargla**
Advisor	**Dr. Lahcene Fellah**	**MCA**	**Univ. Ouargla**
Co-advisor	**Dr. Yazid Helal**	**MCA**	**Univ. Ouargla**
examiner	**Dr. Imane Rezgui**	**Pr.**	**Univ. Ouargla**
Examiner	**Dr. Said Benramache**	**Pr.**	**Univ. Biskra**
examiner	**Dr. Okba Belahssan**	**Pr.**	**Univ. Biskra**

Academic Year: 2024/2025

Acknowledgements

Dear Esteemed Members of the Jury,

As I prepare to present my doctoral thesis, I wish to express my deepest gratitude for the invaluable contributions each of you made long before the defense day. Your expertise, dedication, and encouragement shaped not only my research but also my growth as a scholar.

To Dr. ***Abderrahim Beloufi****, President of the jury: Thank you for your leadership in structuring the evaluation process and for your early feedback, which helped me, refine the thesis's framework with clarity and rigor.*

To Dr. ***Lahcene Fellah****, my advisor: Your steadfast guidance was the cornerstone of this work. From the initial proposal to the final draft, your patience, critical insights, and belief in my potential kept me anchored during moments of doubt. You taught me to pursue excellence without losing sight of curiosity.*

To Dr. ***Yazid Helal****, co-advisor: Your meticulous attention to detail and constructive critiques strengthened the methodological foundations of this research. Your ability to balance rigor with empathy made every discussion a source of motivation and clarity.*

To Dr. ***Imane Rezgui****, Pr.* ***Said Benramache****, and Pr.* ***Okba Belahssan****: I am profoundly grateful for the time you invested in reviewing my work prior to the defense. Your thoughtful questions, suggestions, and engagement with my ideas pushed me to elevate the depth and coherence of my arguments.*

This journey was made meaningful not only by your academic expertise but also by the humanity, you brought to mentorship. Your collective efforts-reading drafts, offering feedback, and challenging my assumptions-were instrumental in shaping a project I am proud to defend.

Thank you for believing in the value of this work and for investing in my development as a researcher.

I carry forward the lessons you have imparted with humility and gratitude.

With deepest respect and appreciation,

Merad Mohamed Zakaria

Dedications

I dedicate this work:

To my mother and sister for their affection and love

To Dr. Fellah Lahcene

To my colleagues

To my friends (Nassira, Djamel, Habiba, Zinou, Saleh, Mahi, Hamid, Ghafour)

To all the Mechanical Engineering teachers and administrative staff

To all those I love from near and far

And to all those who have supported me

Mohamed Zakaria

Table of Contents

Table of contents (1)

Table of contents (2)

Table of contents (3)

Table of contents (4)

Table of contents (5)

List of Figures (1)

List of Figures (2)

List of Figures (3)

List of Figures (4)

List of Figures (5)

List of Tables (1)

List of Tables (2)

List of equations (1)

$NiCl_{2(aq)} + 2H_2O_{(aq)} \xrightarrow{Heat} 2HCl_{(g)} + Ni(OH)_{2(s)}$	Eq.2.1
$NiCl_{2(aq)} + 2H_2O_{(aq)} \xrightarrow{Heat} 2HCl_{(g)} + NiO_{(s)} + H_2O_{(g)}$	Eq.2.2
$Zn(CH_3COO)_{2(liq)} + H_2O_{(liq)} \longrightarrow ZnO_{(s)} + 2CH_3COOH_{(g)}$	Eq.2.4
$Zn(CH_3COOH)_2.2H_2O_{(s)} \rightarrow Zn(CH_3COOH)_{2(s)} \begin{cases} \xrightarrow{Primary} Zn(CH_3COOH)_{2(liq)} \\ \xrightarrow{Secondary} Zn_4O(CH_3COOH)_{6(s)} \rightarrow Zn_4O(CH_3COOH)_{6(liq)} \end{cases} \rightarrow ZnO_{(s)} + CO_{2(g)} + CH_3COCH_{3(g)}$	Eq.2.5
$m = M \times C \times V$	Eq.2.6
$, f = \frac{C_{mother\,(stock)}}{C_{daughter}} = \frac{V_{flask}}{V_{pipette}}$	Eq. 2.7
$f = \frac{C_{mother\,(stock)}}{C_{daughter}} = \frac{0.50\ \text{mole/L}}{0.40\ \text{mole/L}} = 1.25$	Eq. 2.8
$V_{pipette} = \frac{50\ \text{mL}}{1.25} = 40\ \text{mL}$	Eq. 2.9
$2d_{(hkl)} \cdot \sin\theta_{(hkl)} = n\lambda$	Eq. 2.10
$\text{POC}(hkl) = \frac{I(hkl)}{\sum_{all\ peaks} I(hkl)}$	Eq. 2.11
$d_{hkl} = \frac{a_{hkl}}{\sqrt{h^2 + k^2 + l^2}}$	Eq.2.12
$a_{cub} = d_{hkl} \cdot \sqrt{h^2 + k^2 + l^2}$	Eq.2.13
$\frac{1}{d_{hkl}^2} = \frac{4}{3}\left(\frac{h^2 + hk + k^2}{a_{hex}^2}\right) + \frac{l^2}{c_{hex}^2}$	Eq.2.14
$D = \frac{K \cdot \lambda}{\beta_{FWHM} \cdot \cos\theta}$	Eq. 2.15
$\delta = \frac{1}{D^2}$	Eq. 2.16
$\varepsilon = \frac{\beta_{FWHM} . \cos\theta}{4}$	Eq. 2.17

List of equations (2)

$V_{hex} = \frac{\sqrt{3}}{2} a_{hex}^2 \cdot c_{hex}$	Eq. 2.18
$APF = \frac{2\pi \cdot a_{hex}}{3\sqrt{3} \cdot c_{hex}}$	Eq. 2.19
$T = T_0 \cdot e^{-\alpha \cdot th}$	Eq. 2.20
$(\alpha h\nu)^n = A(h\nu - E_g)$	Eq. 2.21
$(\alpha h\nu)^2 = A(h\nu - E_g)$	Eq. 2.22
$\alpha(h\nu) = \alpha_0 exp\left(\frac{h\nu - (E_g - E_u)}{E_u}\right)$	Eq. 2.23
$\ln(\alpha) = \ln(\alpha_0) + \frac{h\nu}{E_u} - \frac{E_g}{E_u} + 1$	Eq. 2.24
$\ln(\alpha) = \left(\frac{1}{E_u}\right) h\nu + \text{constant}$	Eq.2.25
$n^4(E_g - 0.365) = 154$	Eq. 2.26
$n = kE_g^C$	Eq. 2.27
$n^4 E_g = 95$	Eq. 2.28
$n = 4.084 - 0.62.E_g$	Eq. 2.29
$n^2 = 1 + \left(\frac{A}{E_g + B}\right)^2$	Eq. 2.30
$\rho = \frac{1}{\sigma} = \frac{\pi}{\ln 2} \cdot th \cdot \frac{V}{I} = 4.53236 \cdot th \cdot \frac{V}{I}$	Eq. 2.31

List of abbreviations (1)

a,b,c	Cristal cell parameters
AB2O4	Perovskite structure(2)
ABO3	Perovskite structure(1)
AE	Auger Electrons
AFM	Atomic Force Microscope
ALD	Atomic Layer Deposition
APF	Atomic Packing Factor
Ba	barium
BSE	Backscattered Electrons
BTS	Band Theory of Solids
C	Carbone
CB	Conduction Band
CBD	Chemical Bath Deposition
CE	Conduction Electrons
CL	Cathodoluminescence
CRAPC	Centre de Recherche Scientifique et Technique en Analyses Physico-Chimiques
Cu	Copper
CVD	Chemical Vapor Deposition
DCT	Dip-Coating Technique
DFT	Density Functional Theory
Ea	Activation energy
EBIC	Face Centered Cubic phase
EBIC	Electron-Beam-Induced Current
Ec	Conduction band energy level
Ef	Fermi energy level
Eg	Bandgap energy
Eu	Urbach disorder energy
Ev	Valence band energy level
FEGs	Field-Emission Guns
FG	Forbidden Gap
FTIR	Fourier-transform infrared spectroscopy
FWHM	Full Width at Half Maximum,
FZ	Forbidden Zone

List of abbreviations (2)

hcp	Hexagonal Compact
L	Length
LED	Light Emitting Diode
LPE	Liquid Phase Epitaxy
MAH	Microwave-Assisted Hydrothermal
MBE	Molecular Beam Epitaxy
MO	Metal oxide
Mo	Molybdenum
Ni	Nickel
POC	Preferential Orientation Coefficient
Pt	Maximum height of the profile
PVD	Physical Vapor Deposition
PVP	Polyvinyl Pyrrolidone
R3z	Average third highest peak to third lowest valley height
R3zISO	Average third highest peak to third lowest valley height
Ra	Roughness average
Rku	Kurtosis
RMS	RMS
Rp	Maximum roughness peak height
Rpm	Average maximum roughness peak height
Rq	Root mean square roughness
Rt	Maximum height of the roughness
Rtm	Average maximum height of the roughness
Rv	Maximum roughness valley depth
Rvm	Average maximum roughness valley depth
Ry=Rmax	Maximum peak to valley roughness
Rz	Average maximum height of the profile
RzISO	Average maximum height of the roughness
Rzk	Skewness
SE	Secondary Electrons
SEM	Scanning Electron Microscope
Si	Silicium

List of abbreviations (3)

Sn	Tin
SPT	Spray Pyrolysis Technique
TCOs	Transparent Conductor Oxides
TEM	Transmission Electron Microscope
th	film thickness
Ti	Titanium
UV	Ultraviolet
VB	Valence Band
VE	Valence Electrons
W	Tungsten
Wa	Waviness average
Wq	Root mean square waviness
Wq	Root mean square waviness
Wy=Wmax	Waviness maximum height
XRD	X-Ray Diffraction
Zn	Zinc
Δa	Average absolute slope
Δq	Root mean square (RMS) slope
Δwq	Root mean square (RMS) wavelength of the profile
θ	Bragg angle
λ	Radiation wavelength
λa	Average wavelength of the profile
ρ	Electrical resistivity
σ	Electrical conductivity
Sn	Tin

General Introduction

General Introduction

Metal oxide semiconductors represent a cornerstone of modern materials science, offering a unique combination of tunable electronic, optical, and chemical properties essential for advanced technologies[1]. These materials, ranging from simple binary oxides (e.g., ZnO, NiO, SnO_2) to complex ternary structures (e.g., perovskites)[2-4], exhibit wide bandgaps, high thermal stability, and versatile conductivity mechanisms[5]. Their intrinsic properties-such as optical transparency, surface reactivity, and defect-dependent electrical behavior-enable critical applications in gas sensing [6, 7], transparent electronics, catalysis, energy conversion (solar cells, batteries), and optoelectronics (LEDs, displays) [8, 9]. The ability to manipulate these properties through doping, nanostructuring, and defect engineering makes metal oxides indispensable for developing sustainable and efficient devices. For instance, doping strategies can transform insulating oxides into conductive transparent electrodes (e.g., Al-doped ZnO) [10] or enhance catalytic activity for environmental remediation[11]. The ongoing quest for earth-abundant, low-cost alternatives to conventional semiconductors further underscores their significance in next-generation technologies.

Despite their potential, significant challenges hinder the optimization of metal oxide thin films for practical applications. Key among these is the difficulty in achieving stable and efficient p-type conductivity in oxides like NiO, which suffer from intrinsic self-compensation effects and dopant migration under operational stresses [12-17]. Additionally, scalable synthesis methods often compromise film quality, leading to defects, inhomogeneous dopant distribution, or poor crystallinity that degrade performance. The quest for low-cost, high-performance materials also demands exploration of novel dopants-such as barium (Ba)-whose impact on the structural and functional properties of host oxides like NiO and ZnO remains poorly understood. Furthermore, integrating computational design with experimental validation to predict and optimize doping outcomes is still nascent. These gaps are particularly acute for gas-sensing applications, where tailored surface reactivity, stability in harsh environments, and precise control over charge transport are essential yet elusive goals.

To address these challenges, this thesis adopts an experimental approach. Experimentally, cost-effective deposition techniques-especially spray pyrolysis-are leveraged to synthesize undoped and Ba-doped NiO, ZnO, and ZnNiO thin films. The homemade spray pyrolysis system enables precise control over precursor chemistry, substrate temperature, and deposition parameters to ensure film uniformity and stoichiometry. Advanced characterization methods, including X-ray diffraction (XRD), scanning electron microscopy (SEM), UV-Vis spectroscopy, Fourier-transform infrared (FTIR) analysis, and four-point probe electrical measurements, systematically evaluate structural,

morphological, optical, and electrical properties. This integrated strategy facilitates a comprehensive understanding of doping mechanisms, structure-property relationships, and performance trade-offs.

This thesis is structured into five chapters:

Chapter 1 provides a foundational overview of metal oxide semiconductors, detailing the crystallographic, electronic, and optical properties of NiO and ZnO, and reviews low-cost thin-film deposition methods (hydrothermal, sol-gel, spray pyrolysis).

Chapter 2 describes the experimental methodology, including the design of the spray pyrolysis system, substrate preparation, precursor synthesis, and characterization techniques.

Chapter 3 presents the structural, morphological, optical, and electrical analysis of undoped and Ba-doped NiO thin films, elucidating doping-induced modifications.

Chapter 4 extends this analysis to Ba-doped ZnO thin films, examining dopant effects on phase purity, bandgap, and conductivity.

Chapter 5 investigates Ba-doped ZnNiO composite films, focusing on phase evolution, interfacial effects, and multifunctional performance for gas-sensing applications. Together, these chapters advance the rational design of doped metal oxide thin films for efficient, scalable gas detection systems.

Chapter-1
Overview of Metal Oxide Semiconductors

Chapter-1
Overview of Metal Oxide Semiconductors

1.1. Advances in Metal Oxide Semiconductors and Doped MxOy Systems

1.1.1. Introduction

Thin-film materials are a critical area of study for understanding their physical and chemical properties, particularly when describing single or multiple atomic layers of a material with a thickness of less than one micrometer. Thin films are defined as layers of material ranging from a few nanometers to several micrometers in thickness. A key step in many thin-film applications is the controlled synthesis or deposition of materials using specialized deposition techniques. A common example is the mirrors used daily in households, where the reflective surface is created by coating the back of a thin glass plate with a specific metal or alloy. Traditionally, chemical silvering (a chemical process) was the dominant deposition technique for coating applications. Today, cathode sputtering has gained greater prominence compared to silvering in various coating technologies [18, 19].

Although coating technology has a documented history spanning over 5,000 years, its evolution and new applications continue to advance over time. Recent developments in thin-film materials and deposition techniques have enabled significant technological breakthroughs across numerous fields [20]. One indicator of research activity in this area is the annual number of publications on specific materials. Figure 1.1 illustrates the growth in publications on nickel oxide, zinc oxide, barium nickel oxide, and barium-doped zinc oxide from the 1990s to the first half of 2025. These four metal oxides are among the most studied due to their superior properties, with zinc oxide being the most extensively researched in recent years.

Today, thin-film coatings are successfully applied in superconducting technologies (e.g., high-layer magnets, power cable rotors, water purification), magnetic recording media, semiconductor devices, light-emitting diodes (LEDs), optical coatings (anti-reflective layers), hard coatings (cutting tools), energy generation (thin-film solar cells), and energy storage (thin-film batteries). Thus, thin-film coating applications represent a significant portion of the economies of many countries. Consequently, it is essential to review the historical evolution of these concepts, traditional deposition techniques, and their application areas.

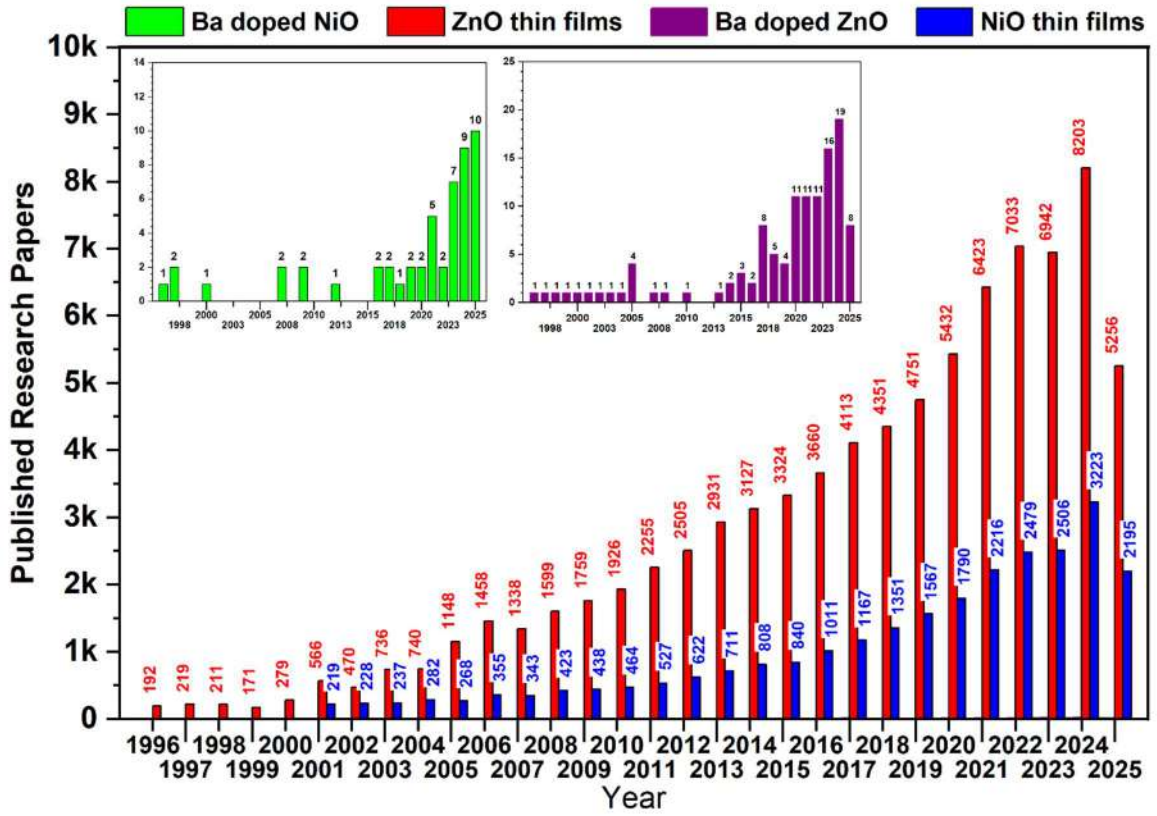

Figure 1.1: Total number of scientific papers on zinc oxide, nickel oxide, barium-doped zinc oxide, and barium-doped nickel oxide (Data collected from *ScienceDirect*).

1.1.2. A Brief History of Thin-Film Coatings

The observation and interpretation of interference patterns in thin films, such as oil films and color spectra, date back to the work of early scientists, including Robert Boyle, Robert Hooke, and Isaac Newton, between 1660 and 1687 [21].

Historical records indicate that W. R. Grove was the first to publish a research article on cathodic deposition and ion etching techniques in 1852 [22-24]. Sputtering deposition, a high-efficiency thin-film coating method, emerged as one of the earliest technologies developed by researchers. By the mid-19th century, significant progress in thin-film preparation began. In 1852, Bunsen and Grove synthesized metallic thin films using chemical reactions and glow discharge sputtering. Later, in 1857, Michael Faraday achieved thin-film deposition via thermal evaporation [25]. By 1876, Adams successfully deposited selenium thin films on platinum substrates, and by 1887, vacuum evaporation techniques were advanced by August Kundt[26]. Studies by Louis Fizeau, Jules Jamin, and Georg Quincke further expanded the understanding of thin-film properties [27].

In 1907, German scientist Karl Baedeker first observed electrical conductivity and optical transparency in the visible spectrum in cadmium oxide (CdO) thin films [28]. The practical use of transparent conducting oxides ($TCOs$) began with the discovery of tin-doped indium oxide (In_2O_3:Sn) by Georg Rupprecht in 1954 [29]. Theoretical foundations were later established by Paul Drude's

work on electron transport in materials. By the 1960s, binary compounds like $SnO_2, In_2O_3, and\ ZnO$ were recognized as exceptional $TCOs$. Over time, thin-film technology evolved rapidly due to its precision and compactness. By 1968, Hogarth pioneered co-evaporation techniques in vacuum environments, marking a milestone in advanced deposition methods [30].

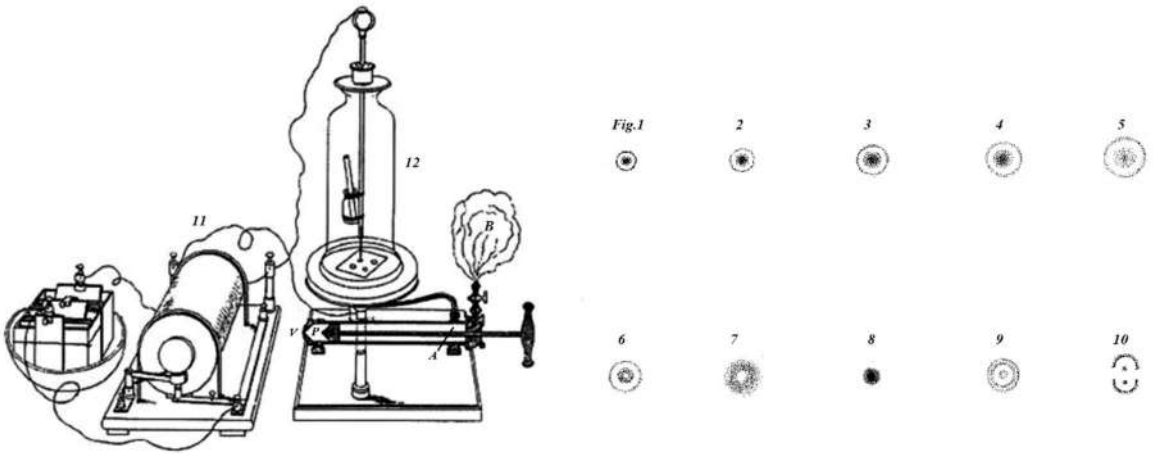

Figure 1.2: Experimental Setup for Sputtering and Film Deposition: Grove's pioneering apparatus demonstrates the process of sputtering a steel target in an 'air vacuum' to deposit oxidized films on a substrate, followed by cleaning with nitrogen discharge. This setup highlights early investigations into the effects of gas composition, electrode polarity, and metal properties on film formation, displaying Grove's insights into oxygen's negative ion behavior and its role in deposition processes [20, 23].

1.1.3. Fundamentals of Metal Oxide Semiconductors

1.1.3.1. Definition and Classification

Metal oxide semiconductors are materials made up of metal cations coordinated to anions of oxygen that can be either crystalline or amorphous and are defined by the fact that the valence band is filled and the conduction band is unfilled, separated by a bandgap representing the semiconducting characteristic [9, 31, 32].

Metal oxide semiconductors are roughly classified as binary oxides-for example, $ZnO, SnO_2\ and\ TiO_2$-possessing a stoichiometry that is relatively simple and often exhibit large bandgaps with good chemical and thermal stability [9, 33]. In addition to binary oxides, there are ternary and quaternary systems such as perovskite oxides and spinels, which contain multiple species of metals, which provides not only additional compositional flexibility, but also additive tuning of additional placement of different metal species into different lattice locations [33-36]. In many cases, the crystalline arrangement defines many of the properties; for example, properties from perovskite oxides with a ABO_3 structure or spinels with a AB_2O_4 structure can be tuned by changing the distribution of the cation species and sometimes the lattice distortions [4, 31]. Generally, binary oxides exhibit n-type conductivity due to the intrinsic donor defect, while more complex stoichiometry makes p-type conduction feasible through careful engineering of incorporation of dopants and defect

compensation [37-39]. The classification of these systems is not only based on the number of elements present but also on their electronic structure and conduction mechanism, which provide a basis for both fundamental research and application-specific design.

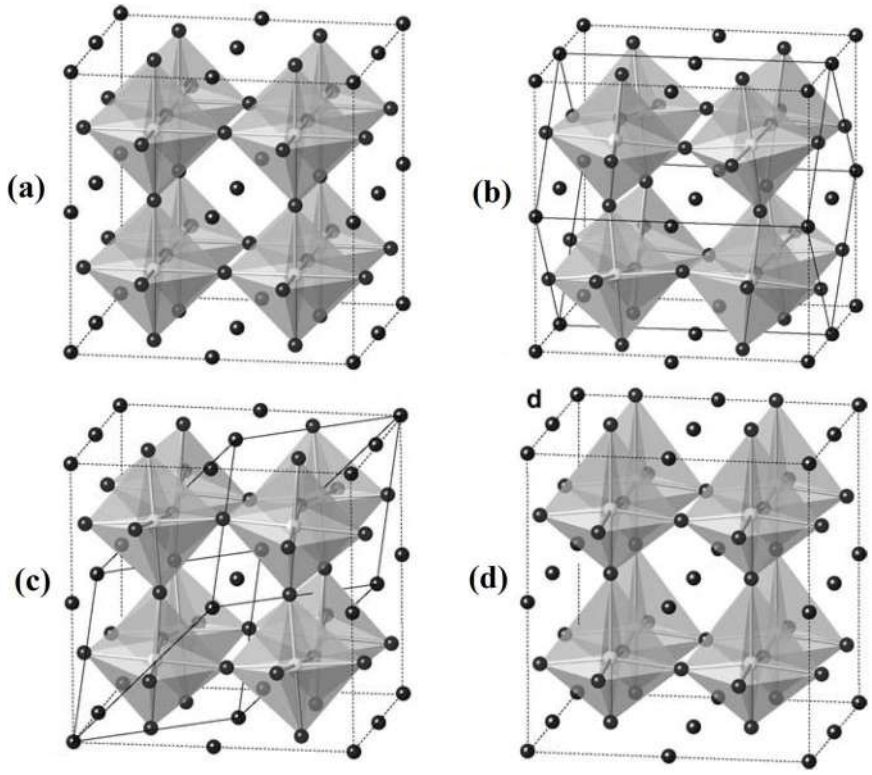

Figure 1.3: Different representations of the perovskite structure, each representing $2 \times 2 \times 2$ pseudocubic cells: (a) $Pm\bar{3}m$ (such as : $SrTiO_3$); (b) $Pbnm$, such as $SrRuO_3$; (c) $R\bar{3}c$ ($La_{0.7}Sr_{0.3}MnO_3$); (d) Ferroelectric $PbTiO_3$ ($P4mm$). Insets (b, c) display the orthorhombic and rhombohedral unit cells, respectively.[40]

1.1.3.2. Electronic Structure and Conduction Mechanisms

The electronic properties of metal oxide semiconductors depend on the band structure of the semiconductors. In metal oxides, the valence band (typically made up of oxygen 2p orbitals) is nearly full and the conduction band (which is derived from metal cation orbitals) is mostly empty, and the emptiness level is determined by the energy difference between the bands (the bandgap) that allows electron excitation (see Figure 1.4 and Figure 1.5) [1, 31, 41]. Typically, the bandgaps of many binary oxides are in the range of 3-4 eV, which gives them intrinsic optical transparency in the visible light absorbing range, while also providing high breakdown voltages and stability for chemically corrosive environments [33]. In most cases, intrinsic defects such as oxygen vacancies or metal interstitials will provide additional energy states close to the conduction band edge that function as shallow donor states; for this reason, n-type conductivity is ubiquitous in metal oxide semiconductors [42]. N-type doping is often common for this reason, as the formation energy of these oxygen vacancies is

comparatively low, while realizable p-type conduction represents a significant challenge because of the localization of the oxygen 2p orbitals at the valence band maximum, which results in high "*hole*" effective masses and (further) compensation associated with donor-type defects [37].

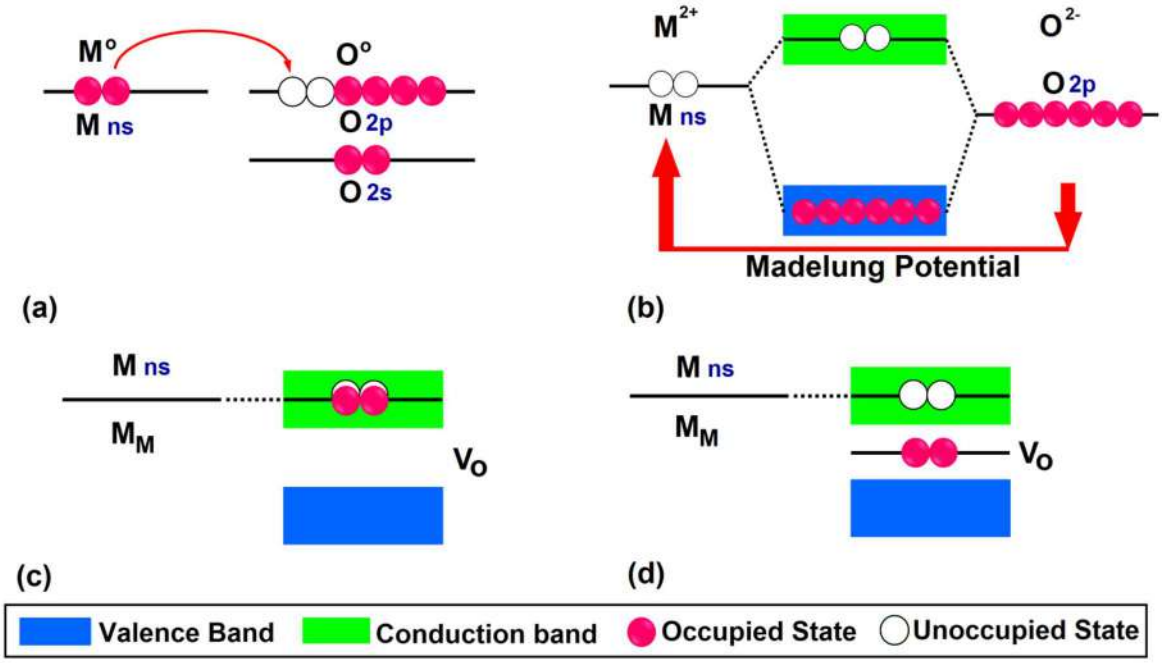

Figure 1.4: Schematic representation of the electronic structures of ionic oxide semiconductors. (a, b) Bandgap formation mechanisms in ionic semiconductors. (c, d) The electronic structures of defects in metal oxides are presented. Solid and hollow spheres are used to represent the occupied and unoccupied states, respectively [1].

Consequently, the conduction of these materials is largely controlled by defect chemistry and any extrinsic dopants that may or may not be intentionally introducing to adjust carrier concentrations and mobility. There is a critical relationship between the intrinsic crystallographic characteristics and extrinsic dopant amounts, and referring to this in the context of n vs. p-type behavior is essential; in order to adjust the overall performance of functional applications [31].

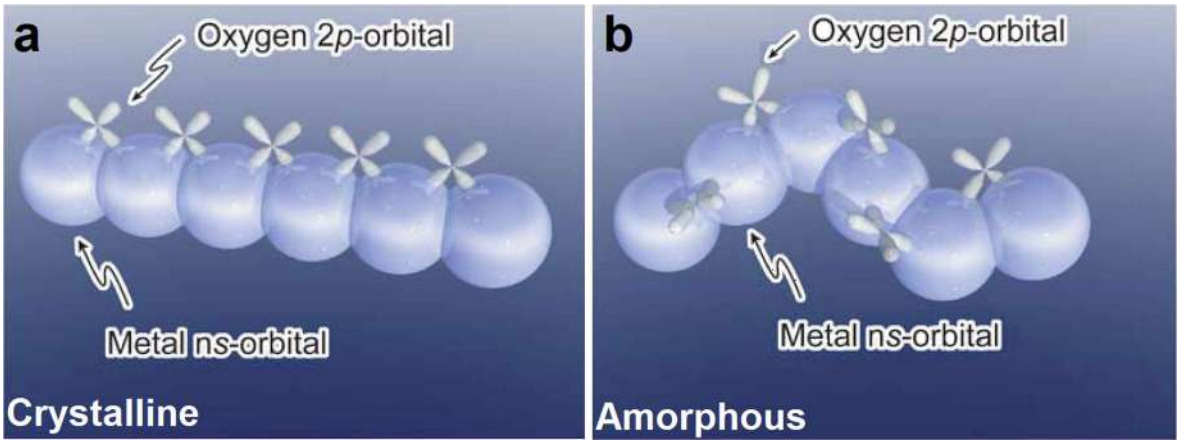

Figure 1.5: Carrier transport in amorphous oxide semiconductors: metal ns orbitals enable efficient pathways in both crystalline and amorphous phases [1, 43].

1.1.3.3. Key Properties for Functional Applications

The multifunctionality of both inorganic and organic metal oxide semiconductors arises from the combination of their electrical, optical, thermal, and chemical properties. For example, high electrical conductivity in metal oxide semiconductors occurs at high enough densities of free carriers (donor defect electrons or acceptor dopant "$holes$") and is typically seen in many classical binary systems such as ZnO as a product of n-type conduction caused largely by shallow donor states provided by an oxygen vacancy [42]. Additionally, another characterization specific to many metal oxide semiconductors is optical transparency; due to the wide bandgap, large E_g (3-4 eV), the absorption of visible light is minimized, making them ideal for both transparent electrode and display applications [31]. In general, along with their conductivity and optical transparent properties, metal oxide semiconductors are generally thermally stable and chemically inert; these properties allow their frequent usage in high temperature and harsh chemical environments, specifically in catalysis and sensor applications [37]. The surface reactivity, which resembles the bulk properties and will be dependent on the configuration and density of defects, including oxygen vacancies or substitutional elements, is key in governing the gas-sensing performance and catalytic activity of these metal oxides since defects can provide reactive or catalytic active sites [33]. Thus, for new discoveries in metal oxide semiconductors, developing distinct configurations of defect densities, which can be achieved by either controlled synthesis, post deposition treatments or doping, must be conducted to maximize performance [31].

1.1.4. State of the Art in Low-Cost Doped Metal Oxide Systems

1.1.4.1. Doping strategies

While recent advances have focused dramatically on the deliberate introduction of dopant atoms into metal oxide lattices to change the microstructure, enhance electrical properties, and customize the optical properties for special end applications. In n-type doping, Al, Ga or F, are typically substituted into ZnO, and substitution at Zn^{2+} sites introduces additional free electrons into the conduction band, grow the increased carrier concentration [37, 44, 45]. Similarly, doping SnO_2 with antimony is nowadays an established method to improve conductivity, while keeping the large bandgap present for optical transparency, and Sb has the additional advantage of providing defect states close to the conduction band minimum, which further assists electron transport [37, 46]. On the other hand, p-type doping presents a much greater challenge for oxide semiconductors, principally because of the difficulty of producing the mobile "$holes$", however, progress has been achieved through dopants like copper in NiO or lithium in CuO, which result in acceptor states which partially overcame the self-compensation, the phenomenon is generally observed in such systems [47, 48]. Advanced methods of doping materials like ZnO, such as co-doping and heterostructuring, may include the creation of

$ZnO:Al/CuO$ composites, in which the engineered heterojunction of an n-type ZnO phase works with a p-type CuO phase for also improved charge separation and higher overall devices efficiency [37]. This doping method is necessary not just to control the conducting type; it can also manipulate and engineer bandgap, and stabilize defects, which can all have drastic effects on device performance and efficiency.

1.1.4.2. Low-cost material systems and earth-abundant oxides

Economic viability and sustainable materials are catalysts in the progress of next generation semiconductor devices. Currently, researchers are working on using common metals like $CuO, Fe_2O_3, and\ WO_3$ as alternatives to more expensive or rare materials [33]. Given the low toxicity, abundance, and cost of production of these materials it is naturally an attractive way to go from the lab to the marketplace. Alternative materials such as $MXenes$ and two-dimensional (2D) MoO_3 (i.e., nanosheets) structural systems are gaining attention because unique structural layering provides excellent surface-to-volume ratios and tunable electronic properties, making them strong candidates in catalytic, energy storage, and flexible electronic applications [49].

The utilization of these economically advantageous and abundant oxide systems and applying advanced doping techniques, there is a unique platform for multifunctional semiconductor design, which can be utilized across a wide scope of applications including gas sensors and energy conversion systems. In addition to the desire for performance also comes the purpose of environmentally feasible and economically viable electronic systems that incorporate high performance.

1.1.4.3. Synthesis techniques enabling scalability

Achieving scalable production of high-quality doped metal oxide thin layers and powders is as critical as the choice of dopants and host materials because synthesis routes directly affect crystalline quality, dopant distribution, and defect concentrations. A variety of solution-based synthesis techniques have emerged as cost-effective and easily scalable methods to produce nanostructured oxide materials; among these, sol-gel deposition technique, hydrothermal elaboration method, and spray pyrolysis are frequently employed because of their simplicity, low processing temperatures, and ability to produce fine control of particle size and morphological characteristics [50].

These techniques benefit from the fact that they typically require inexpensive precursors and energy-efficient processes, enabling the production of large volumes of doped metal oxide powders or thin films that possess a high degree of homogeneity and controlled nanostructuring. However, vapor-phase methods such as chemical vapor deposition technique (noted as CVD) and sputtering are employed when precise control over film thickness, uniformity, and surface quality is necessary, although traditionally these methods involve higher costs and energy inputs; recent developments in

these processes have aimed to reduce the consumption of the energy and costs while maintaining high material quality [50].

Complementing these conventional approaches, modern microwave-assisted synthesis and green chemistry techniques have emerged as powerful alternatives by significantly reducing reaction times, energy consumption, and environmental impact [50]. Such eco-friendly processes ensure that the manufacturing of doped metal oxide systems can be scaled up to industrial levels and adhere to sustainability criteria, thereby enhancing the potential of these materials for future applications.

1.1.5. Challenges and Opportunities

1.1.5.1. Operational stability and environmental stress

One of the principal challenges in the practical deployment of doped metal oxide semiconductors is ensuring their long-term operational stability in environments subject to thermal and humidity fluctuations. These devices are often exposed to severe conditions that can promote dopant migration, change defect distributions, and even induce phase transformations over time [51]. For example, the presence of temperature-induced stress has been shown to accelerate the development of additional oxygen vacancies or to induce the aggregation of dopant clusters. This phenomenon can result in an increase in electrical resistivity and the reduction of the optical transparency for prolonged periods. Addressing these issues involves not only optimizing synthesis conditions and post-deposition thermal treatments but also exploring effective encapsulation and surface passivation strategies that can protect the delicate dopant configurations from adverse environmental exposures.

1.1.5.2. Trade-offs between scalability and performance

The creation of affordable doped metal oxide systems faces an ongoing problem: balancing mass production with the precision needed to keep top-notch electronic and structural performance. Making these materials through solutions like sol–gel or hydrothermal methods offers cheap ways to produce large amounts. However, these approaches often result in materials that are not as crystalline as they should be or have uneven dopant spread. This can slow down how electrons move and make devices work worse [52]. As a result, many scientists are working hard to improve these large-scale techniques. They are trying to make the process better-for example, by heating the materials or changing how much of each ingredient they use. The goal is to create nanostructured films that have clear shapes and spread dopants.

1.1.5.3. Sustainability and eco-friendly processing

Green development has become a key factor in materials studies creating a big chance to come up with eco-friendly ways to make metal oxide semiconductors. Scientists now focus on cutting down

the harm to nature from oxide processing. They aim to use less toxic solvents lower energy use, and find ways to reuse old materials [33]. For example, using microwaves to help make these materials shows great promise. It can lead to quick, energy-saving processes that also make fewer unwanted side products. What's more, eco-friendly methods are now part of both liquid-based and gas-based ways to make these materials. This ensures that the whole life of these semiconductor materials is kinder to the planet and makes more financial sense.

1.1.5.4. Opportunities through computational and experimental integration

A very promising path toward the development of low-cost doped metal oxide systems is the interaction between computational modeling and experimental synthesis and characterization. Sophisticated simulation methods, including density functional theory (DFT), have become essential tools for predicting the influence of particular dopants on the electronic structure and defect formation energies in oxide semiconductors [42]. Such computational results not only minimize the need for trial-and-error methods but also enable the design of heterostructures and co-doped systems with specific properties. High-throughput computational screening is now common practice to search large parameter spaces and thus accelerate the discovery of new inexpensive compositions with optimal performance for applications such as photovoltaics, sensing, and catalysis. The combined strategy of coupling theoretical models with experimental protocols is now starting to produce materials with enhanced charge separation, improved catalytic activity, and increased durability under operating conditions [51].

1.1.6. Detailed Discussion and Future Directions

Recent studies have underlined that the main cause of the observed n-type conduction in binary systems such ZnO is the intrinsic formation of oxygen vacancies during synthesis. Growing films under oxygen-deficient conditions causes oxygen vacancies to form easily and function as shallow donor states providing free electrons [31]. By means of precisely optimal annealing steps or control over the oxygen partial pressure during deposition, researchers have been able to fine-tune the defect density and hence attain enhanced electrical conductivity and optical properties. More complicated oxides such as perovskites and spinels provide a multidimensional approach to bandgap engineering by simultaneous control of cation stoichiometry, defect compensation, and heteroepitaxial strain [33]. These materials show a great variety of phenomena, including improved dielectric responses, based on their mixed-cation frameworks.

When dopant levels and processing conditions are balanced suitably, these materials show a great variety of phenomena including enhanced dielectric responses and improved catalytic activity due to their mixed-cation frameworks. Design strategies in many of these situations entail the integration of

computationally guided predictions with experimental feedback; for example, DFT studies have helped identify which dopant species are most likely to generate the desired shallow acceptor or donor states while minimizing the formation of compensating deep-level traps [42]. Such combined methods highlight the need of exact defect and dopant management since they have produced prototype devices with better photocatalytic efficiency and gas sensing performance.

Low-dimensional oxide structures-such as 2D metal oxides and $MXenes$, which profit from quantum confinement and a high surface to volume ratio, also show great promise for study. With improved charge transport and reactive surface sites especially beneficial in photocatalytic and sensing applications, two-dimensional systems such as exfoliated MoO_3 nanosheets show unique electronic and catalytic properties different from their bulk counterparts [49]. Likewise, $MXenes$-usually produced by selective etching of layered ternary compounds-offer metallic-like conductivity together with adjustable surface chemistries, which makes them ideal candidates for integration into composite devices. Early-stage studies combining these novel low-dimensional materials with conventional metal oxides are already showing promise in obtaining extraordinary performance in next-generation electronic and energy-conversion applications.

Looking ahead, more developments in synthesis methods are probably going to be very important in closing the distance between industrial production and laboratory-scale experiments. By means of ongoing innovation in microwave-assisted synthesis and green chemistry paths, doped metal oxides that not only satisfy strict performance criteria but also follow sustainability and cost-effectiveness targets [50]. While ensuring that dopants remain uniformly distributed within the host lattice over time, the combination of fast, energy-efficient processing techniques with advanced post-synthesis treatments is expected to minimize flaws that adversely affect device operation. Furthermore, better control of grain boundaries and morphological aspects at the nanoscale will boost electrical conductivity and optical transparency, so enabling the realization of high-performance doped metal oxide films for a range of applications.

Despite these positive advancements, there are still several major challenges to be solved. Dopant migration and the growth of defect populations can lead to device deterioration over time, especially when devices are exposed to industrial or outdoor environments [51]. Maintaining long-term operational stability in the face of humidity and heat stress is a chronic issue. One of the main obstacles still facing the p-type doping community is overcoming intrinsic self-compensation. In order to minimize the creation of deep acceptor states that act as charge carrier trap centers, careful interface engineering and innovative co-doping strategies are needed [47]. More advanced synthesis

procedures will be needed to address these problems, as well as the creation of reliable passivation and encapsulation techniques to shield delicate oxide films from environmental deterioration.

From an application standpoint, the integration of these doped metal oxides into real-world devices such as flexible electronics, photovoltaic cells, gas sensors, and transparent displays necessitates further research into interface engineering. Achieving low-resistance contacts, creating stable heterojunctions between dissimilar materials, and optimizing band alignment across interfaces are all active research areas that will determine the success of these advanced semiconductor systems in commercial applications [51]. Recent studies have focused on modifying surface chemistry, optimizing dopant distributions near interfaces, and employing graded doping profiles to facilitate efficient charge injection and extraction. These efforts not only improve device performance but also enhance operational reliability and longevity.

1.2. Overview of the zinc and nickel oxides

1.2.1. Nickel Oxide (NiO) Thin Films

1.2.1.1. Crystallographic and Structural Properties

NiO thin films have been demonstrated to exhibit a cubic, rock salt–type crystal structure characterized by a face-centered cubic (FCC) phase, where nickel cations and oxygen anions occupy octahedral sites in a regular arrangement (as shown in Figure 1.3). This crystallographic arrangement, often confirmed by X-ray diffraction (XRD) studies, results in a polycrystalline film with predominant diffraction peaks typically aligned along the (111) plane, although reflections from other orientations are also observed depending on deposition conditions [53, 54]. Moreover, synthesis methods such as spray pyrolysis have been shown to yield NiO films with nanoscale crystallite sizes that can vary from around 15 to 20 nm as a function of deposition parameters and dopant content, thereby influencing structural parameters including grain boundaries, lattice strain, and dislocation densities [55, 56]. In addition, subtle shifts in lattice parameters and variations in the full width at half maximum (FWHM) of the diffraction peaks indicate that both intrinsic defects and deliberate dopant incorporation can alter the crystalline quality, thereby affecting the overall microstructural properties of the films [57, 58]

1.2.1.2. Electronic and Electrical Properties

Electronically, NiO is well known as a wide band gap semiconductor that typically exhibits p-type conductivity. This behavior is primarily attributed to the presence of intrinsic defects, such as nickel vacancies and oxygen interstitials, which act as acceptor sites by creating "$hole$" carriers within the lattice [53, 56]. Electrical characterization, including four-point probe measurements and Hall effect

experiments, has revealed that undoped NiO thin films generally display very high resistivity; however, this resistivity can be dramatically reduced through processes that enhance the concentration of these intrinsic defects, or via extrinsic doping [59]. In several studies, the deliberate incorporation of dopants such as copper (Cu) has not only modified the carrier concentration-often increasing the density of "*holes*"-but also altered the mobility and resistivity of the films, thus providing an effective route to tailor electronic transport properties for specific device applications [59, 60].

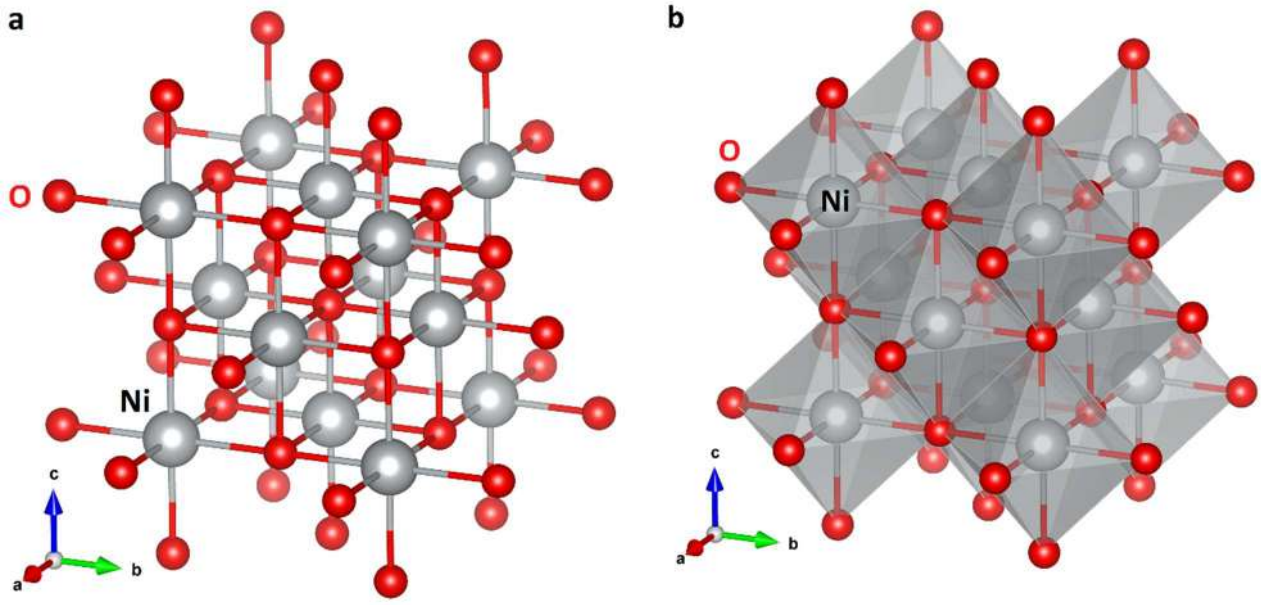

Figure 1.6: Crystal structure of bulk NiO. The coordination of the cations is shown, with Ni^{+2} ions represented by the larger grey spheres and O^{-2} ions by the smaller red spheres. Representations: (a) ball-and-socket and (b) polyhedral representation, of the face-centered cubic structure of NiO, where the Ni^{+2} cations occupy the centers of the octahedral sites.

1.2.1.3. Optical Properties

Optically, pristine NiO thin films are recognized for their semitransparent nature and wide optical band gap, with values that typically range from about 3.2 to 3.6 eV in direct transition scenarios. This wide band gap underpins their high transparency in the visible spectrum while ensuring strong absorption in the ultraviolet (UV) range, making them beneficial for applications that require high optical quality and solar control functionalities [53, 54]. Furthermore, the optical behavior in NiO films is not static; doping (both intrinsic and extrinsic) plays a crucial role in modifying parameters such as the absorption edge, refractive index, and even photoluminescence emission characteristics. Various studies have reported that increased dopant content (for instance, with copper or neodymium) can narrow the band gap and increase the Urbach energy, which is indicative of the disorder and defect-induced tail states within the band gap [57, 58].

1.2.1.4. Doping Types in NiO Thin Films

Doping in NiO thin films can be broadly categorized into two classes: intrinsic doping and extrinsic (substitutional) doping. Intrinsic doping in NiO arises naturally from the non-stoichiometric nature of the films, stemming from native defects such as nickel vacancies and oxygen interstitials. These defects create acceptor states within the NiO lattice that facilitate p-type conduction by generating "$hole$" carriers without the need for intentional impurity addition [53, 56]. In contrast, extrinsic doping involves the deliberate substitution of Ni or O ions with foreign elements to further tailor the material's electrical and optical characteristics. Such extrinsic dopants include transition metals (e.g., copper, cobalt) or rare earth elements (e.g., neodymium, lanthanum), which are introduced into the lattice through methods like spray pyrolysis, sputtering, or sol–gel processes [58, 61].

1.2.1.5. Extrinsic Doping (Substitutional) in NiO

As shown in Figure 1.4, the extrinsic doping in NiO thin films is primarily achieved through substitutional methods, whereby dopant ions replace host ions in the lattice. For instance, copper (Cu) doping has been widely explored; Cu^{+} ions can replace Ni^{2+} ions within the lattice, thereby increasing "$hole$" carrier concentration and reducing the overall electrical resistivity of the films [59, 61]. Similarly, studies on cobalt (Co) doped NiO films indicate that Co substitution affects crystallite size, surface roughness, and alters the optical band gap, typically tuning it in the range of about 2.1 to 2.5 eV; such modulation of the band gap directly stems from the substitutional incorporation of Co ions into the NiO matrix [61]. Other extrinsic dopants, including lanthanum (La) and neodymium (Nd), have also been investigated; these dopants further influence the crystallinity and electronic properties by alleviating lattice strain or by promoting the formation of secondary phases at grain boundaries, thereby enhancing carrier concentration and improving the overall film performance for applications like transparent electrodes and sensor devices [58, 62].

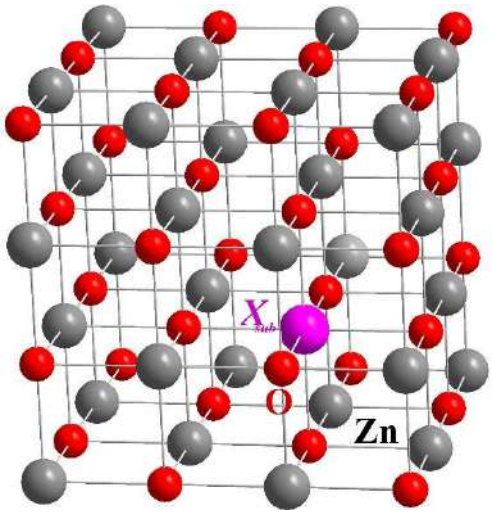

Figure 1.7: Extrinsic (substitutional) doping of NiO by different atoms (such as, Cu, Co, La).

1.2.1.6. Intrinsic Doping in NiO

Intrinsic doping in NiO films originates from the material's inherent non-stoichiometric behavior during film growth. In a stoichiometric ideal scenario, the $Ni:O$ ratio would be 1:1; however, in practical synthesis processes such as spray pyrolysis or magnetron sputtering, deviations occur due to kinetic limitations and post-deposition treatments. These deviations result in nickel vacancies and oxygen excess, which act as native acceptors and lead to intrinsic p-type conductivity in the NiO films [53, 56]. The defect density-quantified by parameters such as dislocation density and microstrain is closely linked to the optical and electrical performance, as a higher concentration of these native defects not only narrows the optical band gap but also enhances ionic mobility and charge-carrier concentration, thereby playing an essential role in the functional tuning of the films [57, 62].

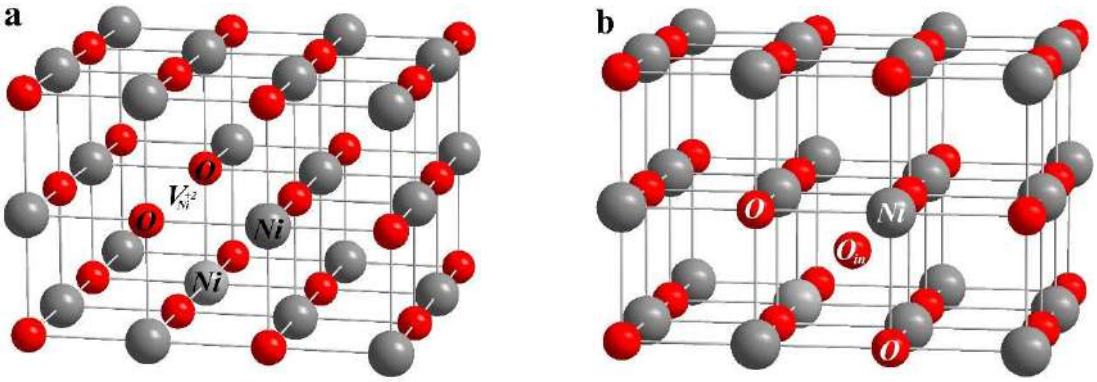

Figure 1.8: Intrinsic p-type conductivity of NiO caused by native point defects such as nickel vacancies (V_{Ni}) and (b) oxygen interstitials (O_{in}).

1.2.2. Zinc Oxide (ZnO) Thin Films

1.2.2.1. Crystallographic and Structural Properties

ZnO thin films are distinguished by their canonical hexagonal wurtzite crystal structure, which exhibits a pronounced preferential orientation along the c-axis, corresponding to the (002) plane. This well-defined crystallographic arrangement is crucial for many applications and is routinely confirmed by XRD studies that reveal sharp and intense diffraction peaks, signifying high crystallinity and phase purity [63, 64]. In many instances, the deposition techniques used, such as chemical sol–gel dip-coating, sputtering, or spray pyrolysis, yield surface morphologies that include nanospheres, nanorods, or textured films with low surface roughness, which are further characterized by scanning electron microscopy (SEM) and atomic force microscopy (AFM) [64, 65]. The choice of precursor and the resulting deposition conditions (e.g., substrate temperature and ambient pressure) have a significant influence on the crystallite size, texture coefficient, and overall microstructure of ZnO films, thereby providing additional handles for property tuning [65, 66].

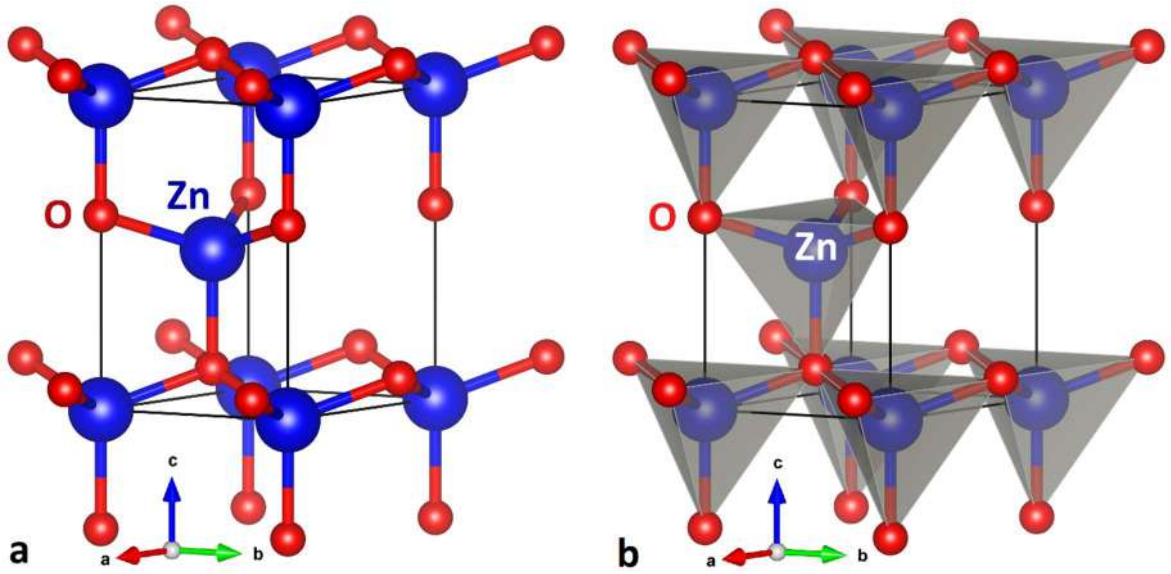

Figure 1.9: Crystal structure of bulk ZnO. The coordination of the cations is shown, with Zn^{+2} ions represented by the larger blue spheres and O^{-2} ions by the smaller red spheres. Representations: (a) ball-and-socket and (b) polyhedral representation, of the face-centered cubic structure of ZnO, where the Zn^{+2} cations occupy the centers of the tetrahedral sites.

1.2.2.2. Electronic and Electrical Properties

ZnO thin films are generally characterized by their intrinsic n-type conductivity (as shown in Figure 1.6), which predominantly arises from native point defects such as oxygen vacancies (V_O) and zinc interstitials (Zn_{in}). Although early studies postulated oxygen vacancies as the driving force behind free carrier generation, it is now widely accepted that additional factors-including unintentional hydrogen incorporation-also contribute to the high carrier concentrations observed [66, 67].

The electrical conductivity in ZnO films is highly sensitive to the deposition method, and post-annealing treatments have been shown to further enhance mobility and reduce the resistivity of the films by improving crystallinity and reducing defect-induced scattering mechanisms [66]. Additionally, co-doping techniques that combine various extrinsic elements can lead to substantial improvements in carrier concentration and mobility, making ZnO films promising as transparent conducting oxides (TCOs) in a range of optoelectronic devices [68].

1.2.2.3. Optical Properties

ZnO thin films exhibit a wide direct band gap, typically in the range of 3.2 to 3.4 eV, which imparts a high level of transparency in the visible region along with strong absorption in the UV region [64, 65].

The optical properties are further influenced by factors such as film thickness, grain size, and defect density, as these parameters affect both the absorption coefficient and the refractive index of the films [64, 66]. Moreover, the phenomenon known as the Burstein–Moss shift is frequently observed in doped

ZnO films, where increased carrier concentration pushes the absorption edge to higher energies, resulting in an apparent widening of the band gap [68]. With high optical transmittance values often exceeding 80–90% in the visible range, ZnO thin films are well suited for applications requiring minimal optical loss, such as in solar cells, displays, and white-light-emitting diodes (LEDs) [69].

1.2.2.4. Doping Types in ZnO Thin Films

Doping in ZnO thin films, similar to the case of NiO, is classified into two principal categories: intrinsic and extrinsic doping. Intrinsic doping originates from native defects such as oxygen vacancies, zinc interstitials, or even unintentional incorporation of hydrogen during growth, which all contribute to the native n-type conductivity of ZnO [66, 67].

Extrinsic doping, on the other hand, involves the deliberate incorporation of substitutional impurities-often elements from group III such as aluminum (Al), gallium (Ga), or indium (In), or even elements from group IV-to further enhance conductivity by increasing free carrier density, as these dopant ions readily substitute for the Zn^{2+} ions in the lattice [65, 68].

1.2.2.5. Extrinsic Doping (Substitutional) in ZnO

Substitutional extrinsic doping in ZnO thin films is a well-established method to tailor the electrical and optical properties for specific applications. In many cases, dopants such as Al, Ga, In, and Sn are incorporated during the film deposition process by substituting for the Zn atoms in the wurtzite lattice, thereby introducing additional free electrons into the conduction band and significantly enhancing electrical conductivity [66, 68]. These dopants typically have ionic radii that are comparable to that of Zn^{2+}, allowing them to be substitutionally incorporated with minimal lattice distortion while still influencing the carrier concentration and mobility [66]. Furthermore, some studies have demonstrated that co-doping strategies, in which two or more dopant species are introduced simultaneously, can optimize the charge carrier density while preserving or even enhancing the optical transmittance-a critical attribute for transparent conductor applications [66, 67].

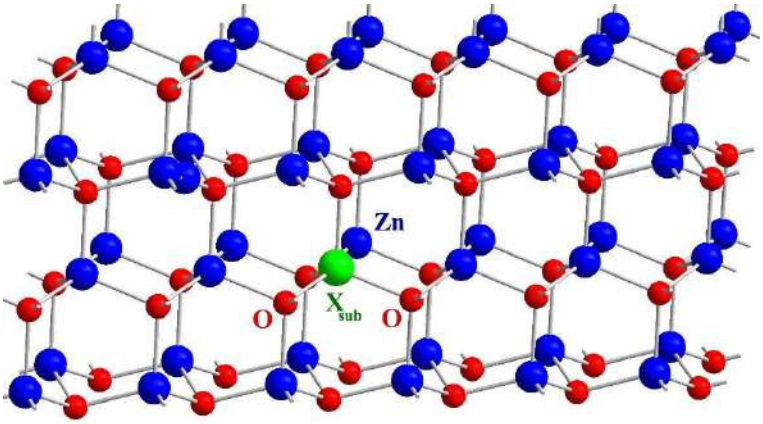

Figure 1.10: Extrinsic (substitutional) doping of ZnO by different atoms (such as, Al, Ga, In).

1.2.2.6. Intrinsic Doping in ZnO

As shown in Figure 1.11, the intrinsic doping in ZnO is governed by unavoidable point defects introduced during the thin-film synthesis process. Predominantly, oxygen vacancies (V_O) and zinc interstitials (Zn_i) serve as shallow donors that contribute to the natural n-type conductivity of ZnO, with their formation being highly dependent on the growth conditions such as substrate temperature, oxygen partial pressure, and the specific deposition technique employed [65, 67, 70]. These native defects can be manipulated to some extent by optimizing the deposition parameters, but regardless, they form the underlying basis for the inherent electronic performance of undoped ZnO thin films [63, 66].

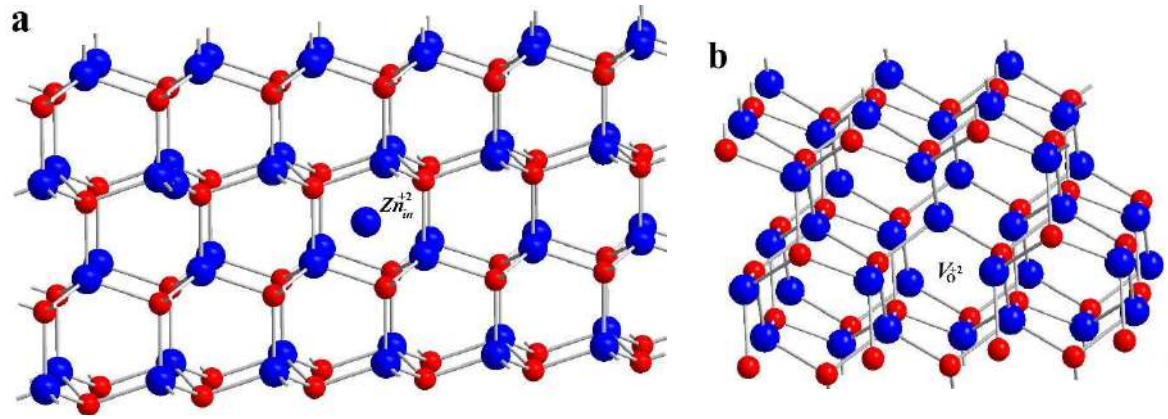

Figure 1.11: Intrinsic n-type conductivity of ZnO caused by native point defects such as zinc interstitials (Zn_{in}) and (b) oxygen vacancies (V_O).

1.2.3. Discussion and Comparative Insights

The contrasting and complementary characteristics of NiO and ZnO thin films make them both attractive for distinct yet sometimes overlapping technological applications. In NiO, the cubic rock salt structure and p-type conductivity-primarily arising from intrinsic defects-stand in marked contrast to $ZnO's$ hexagonal wurtzite structure and its naturally n-type behavior due to intrinsic donor defects. In both materials, however, extrinsic doping via substitutional incorporation of appropriate dopant atoms plays a pivotal role in further steering the electrical conductivity, optical band gap, and carrier mobilities to desired levels.

For NiO thin films, extrinsic doping strategies such as the introduction of Cu, Co, La, or Nd can tailor the material's properties by either enhancing the p-type conductivity or, in some cases, modulating the optical band gap to better match device requirements. The use of Cu doping, for instance, has been shown to reduce the energy difference between the conduction band and the Fermi level, leading to improved charge transfer properties and electrochromic performance. On the other hand, intrinsic doping in NiO-dictated by deviations from ideal stoichiometry through nickel vacancies and oxygen

interstitials-remains critical for its inherent p-type behavior even in the absence of intentional impurity addition [53, 59].

Similarly, in ZnO thin films, extrinsic doping using group III elements such as Al, Ga, and In has proven to be an effective route to enhance the n-type conductivity without substantially compromising the material's optical transparency. The substitution of Zn atoms with these dopants provides additional free electrons, thereby bolstering conduction while ensuring that the wide band gap-typically around 3.3 eV-remains sufficiently large to guarantee high visible light transmittance [65, 68]. Conversely, intrinsic doping through the formation of native defects such as oxygen vacancies continues to be a dominant factor in establishing the electrical properties of ZnO, and meticulous control over the deposition environment is essential to effectively manage the balance between intrinsic and extrinsic contributions [66, 67].

The choice of deposition technique ranging from spray pyrolysis and sol–gel methods for NiO to magnetron sputtering and chemical vapor deposition for ZnO-also plays a significant role in determining the microstructural features and, thus, the ultimate performance of the films. For example, spray pyrolysis-a relatively cost-effective and scalable method-has been used effectively for both NiO and ZnO to produce films with controlled crystallinity and surface morphology, which in turn directly affects the optical transmission and electrical conductivity [54, 65]. Furthermore, post-deposition treatments such as annealing have been shown to reduce defect densities and improve crystalline order, thereby enhancing carrier mobility in both classes of films [58, 66].

1.2.4. Application-Relevant Considerations

The tunability of these materials through doping strategies has critical implications for their use in devices. NiO thin films, with their adjustable optical band gap and improved p-type conductivity upon extrinsic doping, are promising candidates for window layers in solar cells, electrochromic devices, and gas sensors (see diagram in Figure 1.12). The ability to engineer these films via both extrinsic dopants like Cu or Co and intrinsic modification through controlled stoichiometry allows for optimized performance in energy saving and display technologies [61, 62].

Conversely, the robust n-type conductivity and high transparency observed in ZnO thin films make them suitable for TCO applications, such as in flat panel displays, touch screens, and photovoltaic devices. Extrinsic doping using group III elements further enhances their utility, ensuring that the films not only provide excellent optical quality but also carry sufficient electrical conduction to serve as effective electrode materials [66, 68].

Moreover, the interplay between intrinsic defects and intentional doping provides a versatile platform for tailoring the films' responses under various operating conditions. For instance, the formation of intermediate defect states through intrinsic doping in NiO can be leveraged to modify its

photoluminescence behavior, while in ZnO, controlling the concentration of oxygen vacancies is key to achieving desired electronic conduction profiles [53, 67].

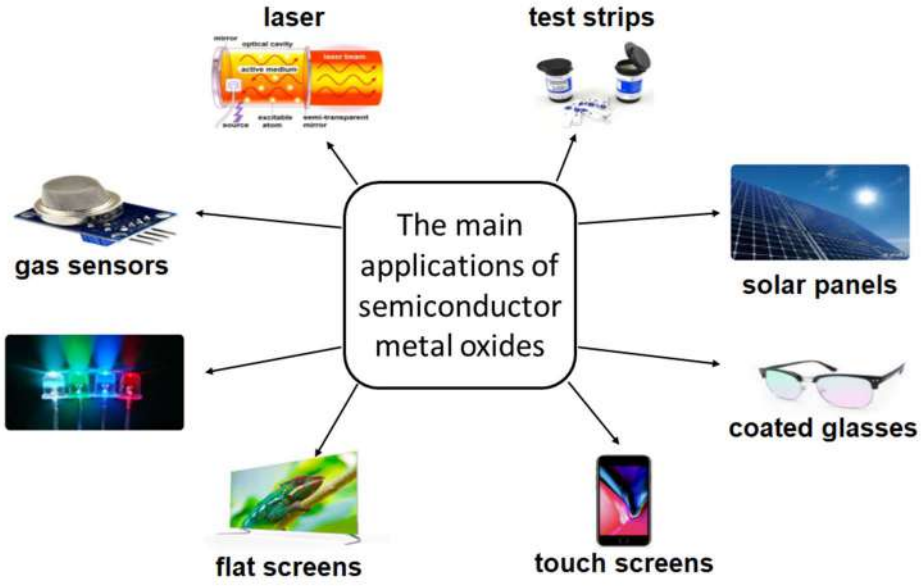

Figure1.12: Some applications of metal oxide semiconductors in industry and everyday life.

1.3. Low-cost thin film deposition methods

Thin-film materials have been a focal point of research for decades because they are incredibly versatile and useful-imagine everything from tiny nanoscale electronics to those energy-efficient coatings on your windows! These materials can be engineered for a huge variety of uses, which is why scientists and engineers keep finding new ways to make them.

When it comes to creating thin films, there are two main categories of techniques: physical and chemical methods. Think of it like building something with either "hands-on" tools or "chemistry-based" reactions.

Physical methods involve moving material from a source to a substrate without changing its chemical makeup. Techniques here include physical vapor deposition (PVD) -like laser ablation [71], molecular beam epitaxy (MBE)[72], or magnetron sputtering [73, 74]-where atoms or molecules are vaporized or ionized and then settle onto a surface to form the film.

On the flip side, chemical methods rely on reactions to grow the material. These split into two camps: *gas-phase* and *liquid-phase* approaches (as shown in Figure 1.14). For gas-phase, think chemical vapor deposition (CVD) or atomic layer deposition (ALD) [75], where gases react to deposit the film. Liquid-phase methods are like mixing ingredients in a solution first. Examples include spray pyrolysis [76, 77], sol-gel processing [12], electrodeposition[78], chemical bath deposition (CBD) [79], liquid phase epitaxy (LPE) [80], and coating techniques like spin-coating [81] or dip-coating technique (DCT) [82].

The cool thing is, these methods let researchers tailor thin films to specific needs. Whether you are making a high-speed transistor or a flexible solar cell, you can tweak the process to control things like thickness, structure, or even the exact mix of materials. That is why these techniques are so vital-they bridge the gap between lab experiments and real-world applications, even on large scales like coating entire buildings.

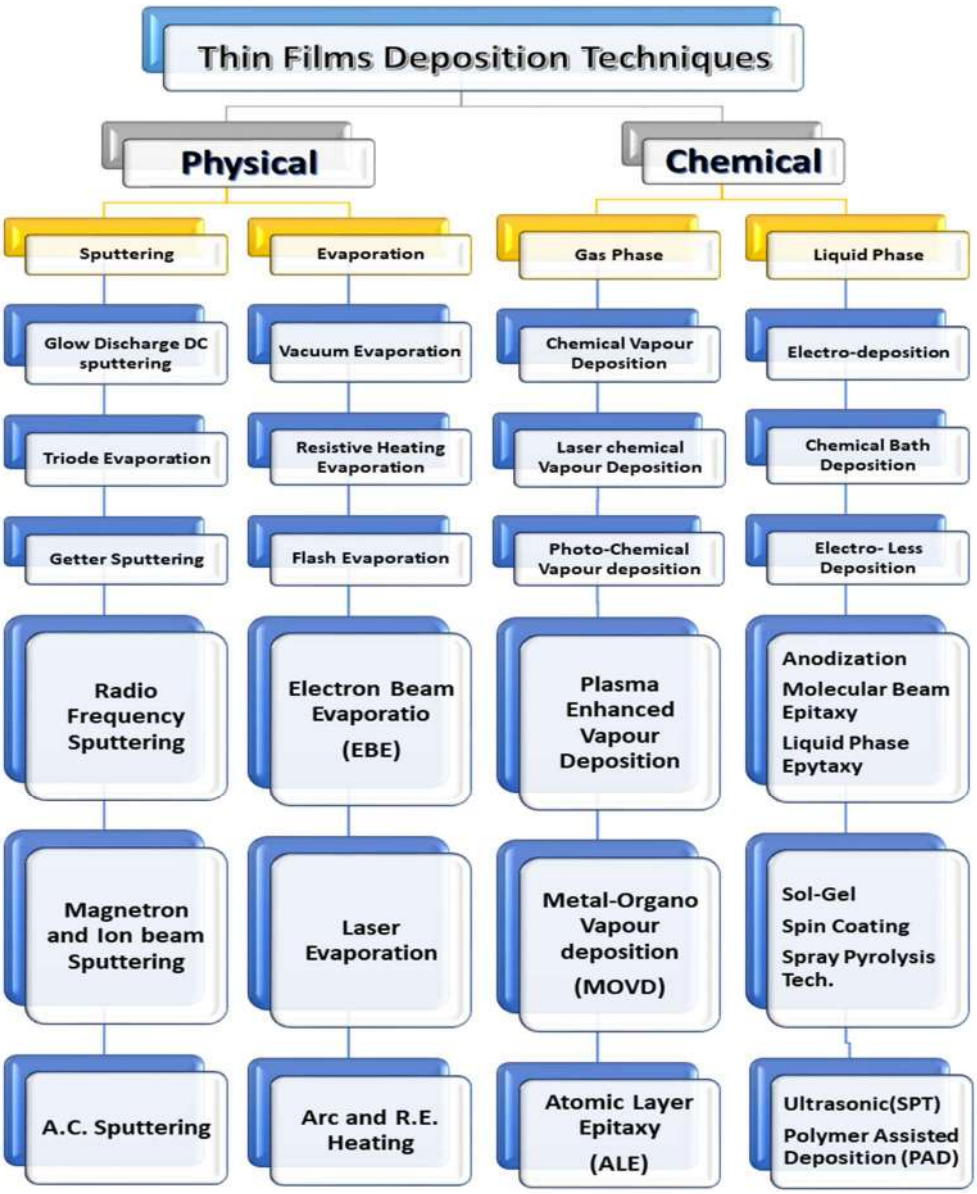

Figure 1.13: Diagram of the most common thin-film deposition processes.

1.3.1. Hydrothermal elaboration method

1.3.1.1. Definition

Hydrothermal deposition is a method used to grow materials under high-pressure, at moderate temperature (typically 100-250°C) water or eco-solvents based environments. It's widely applied in materials science for creating crystals, thin films, and nanostructures. The process mimics natural mineral formation but accelerates it in controlled lab settings[83].

Hydrothermal deposition is a fundamental technique of modern materials science, enabling the synthesis of advanced materials at moderate temperatures (typically 100-250°C) and self-generating pressures (10-50 bar) using aqueous or solvent-based environments[84].

In contrast to high-energy processes such as chemical vapor deposition, this process exploits water's own properties under sub-critical conditions, such as its reduced dielectric constant, which enhances the solubility of organic precursors, since the strong dissociation of ions (H_3O^+/OH^-) acts as a catalyst in reactions without the need for aggressive chemicals (such as acids and bases)[85-87]. This technique was originally developed for mineral crystallization. However, it is now being applied to nanomaterials, energetic materials and functional coatings.

Figure 1.14: Synthesis of nanostructured metal oxide.

1.3.1.2. Historical development

The origins of the technique date back to 1845, when German geologist and metallurgist Karl Emil von Schafhäutl (1803-1890) synthesized microscopic quartz crystals in a homemade pressure cooker [88]. The works of von Schafhäutl was followed around 1848 by his compatriot Robert Bunsen [89], who grew carbonate crystallites using ammonium chloride solvents in sealed glass tubes. By 1851, Henri de Sénarmont had achieved systematic crystallization (e.g. corundum: Al_2O_3) [90]. In the 1940s, just after the Second World War, the development of electronics led to an increase in quartz production by laboratories, including the American "Bell" laboratory.

The latter part of the 20th century witnessed two significant paradigm shifts: Initially, the advent of nanoscience redirected scholarly attention from macroscopic crystals to nanostructured materials.

Subsequently, the principles of green chemistry underscored the ecological advantages of hydrothermal deposition in contrast to solvent-intensive methodologies. Contemporary advancements in the 2020s are aimed at process intensification-microwave-assisted techniques now reduce reaction durations from several days to mere hours, concurrently enhancing the quality of the resulting crystals.

1.3.1.3. Main principles of hydrothermal deposition:

1.3.1.3.A. Process Mechanics:

The process of hydrothermal deposition is contingent upon temperature-driven solubility gradients. A typical apparatus is considered here. An autoclave is used to separate a hot "nutrient zone" (precursor dissolution) from a cooler "growth zone" (deposition). Convection currents facilitate the transportation of dissolved species, thereby inducing supersaturation and subsequent crystallization on substrates that have been seeded with material. Three mechanisms have been identified as governing this phenomenon:

The first method is the temperature-difference method. The predominant approach involves the exploitation of thermal gradients [91, 92].

The second technique is the metastable-phase technique. It is imperative to exploit solubility differences between the precursor and product phases [91, 93].

The third technique is reduction. The process entails the utilization of chemical reductants, such as ethylenediamine, for the deposition of oxides[91, 94].

Table 1.1: Main process variables and their impact

Variable	Impact on the deposit	Range
Temperature	▪ Controls supersaturation. ▪ Higher temperature means faster reaction kinetics.	99-301°C
Reaction time	▪ Provides control over crystal size and morphology	few minutes to many days
pH	▪ Modifies precursor solubility. ▪ Alters particle stability	
Precursor ration	▪ Effects of stoichiometry and phase purity	Specific to the model

1.3.1.3.B. Solvent Specific Behaviors

Water under hydrothermal conditions exhibits distinct behavior compared to ambient water. The magnitude of water polarization peaks increases near 200°C, which promotes ion dissociation and accelerates the reactions such as metal oxide formation. At the same time, the lower dielectric

constant (~30 at 250°C vs. 80 at 25°C) enhances the solubility of organic precursors, thus enabling the synthesis of single-pot hybrid materials. These characteristics are the foundation of the advantages of hydrothermal deposition, as it allows for high crystallinity without the need for post-annealing, which is essential for temperature-sensitive substrates.

1.3.1.4. Recent Innovations in Methodology

1.3.1.4. (a). Microwave-Assisted Hydrothermal (MAH)

The microwave-assisted hydrothermal (MAH) methodology amalgamates microwave irradiation, typically operating at a frequency of 2.45 GHz, with conventional reactor systems. Microwaves enhance chemical reaction processes through the following mechanisms:

- Dipolar polarization: the rotational motion of water molecules and solvents.
- Ionic conduction: the translocation of ions (charged entities) across a membrane or within a solution, culminating in the generation of an electrical current.

A study conducted in 2021 revealed that the synthesis of $BaTiO_3$ nanoparticles utilizing the Microwave-Assisted Hydrothermal (MAH) technique necessitates a mere 30 minutes, in stark contrast to the 24 hours required by traditional methodologies. The microwave-assisted hydrothermal (MAH) technique yields nanoparticles characterized by enhanced size uniformity. Furthermore, energy reductions of up to 60% can be realized by substituting conventional convective heating approaches with direct molecular excitation methods.

1.3.1.4. (b). Sustainable Pathways

Recent research has placed a strong emphasis on the valorization of waste:

Precursors derived from biomass: The process of cellulose hydrolysates forming carbon quantum dots is of particular interest.

The process of water recycling is of particular significance in contemporary industrial contexts, where the efficient management of water resources is paramount to maintaining operational efficiency and environmental sustainability. Closed-loop systems have been demonstrated to minimize liquid waste. For instance, the hydrothermal treatment of sewage sludge at 220°C results in the production of phosphorus-rich hydrochar, with an 84% recovery of phosphorus, which can be utilized as a fertilizer. Notably, this process retains carbon as a fuel source. Such "circular" adaptations are consistent with green materials standards.

1.3.1.5. Characterization of Deposits

Post-synthesis analysis must address three material questions:

- **Phase purity**: XRD identifies crystallographic phases (e.g., distinguishing $NiFe_2O_4$ from Fe_2O_3 mixtures).

- **Morphology**: SEM/TEM reveal nucleation modes-*self-assembly* in silicon-doped hydroxyapatite nanorods versus *Ostwald ripening* in undoped samples.
- **Surface chemistry**: Zeta potential measurements correlate surface charge (e.g., IEP shifts in Ni-poor ferrites) with colloidal stability.

Table 1.2: The properties of widely encountered hydrothermal deposits

Material	Main Application	Hydrothermal Advantage
ZnO nanorods	Nanofluids for heat transfer	Aspect ratio control using a polyvinyl pyrrolidone (PVP) surfactant [95]
Si-doped hydroxyapatite	Bone implants	Adjusting the stoichiometry at low temperatures
$NaTaO_3/Ir$	Catalysts for water separation	One-step heteroatom doping
$Fe_3O_4@C$ composites	Lithium-ion anodes	Core-shell structure by solvothermal carbonization

1.3.1.6. Recent Advances and perspectives

Researchers now combine hydrothermal deposition with other techniques, like microwave heating, to speed up reactions. Studies in Advanced Materials highlight its role in creating "smart" materials that respond to stimuli, such as temperature-sensitive polymers.

1.3.1.6. (a). Presence of persistent barriers or obstacles:

The initial stage of the process studied is known as "particle aggregation". The growth process of high surface energy nanomaterials (e.g. $NiFe_2O_4$) involves aggregation, which requires the use of enrobing agents. However, these agents are likely to contaminate surfaces during the process, thus introducing impurities.

Secondly, in situ monitoring capability is limited. The opacity of the reactor prevents real-time observation of nucleation and growth events.

Thirdly, scalability considerations and pressure trade-offs must be taken into account. Large-volume autoclaves have difficulty maintaining temperatures in excess of 200°C.

1.3.1.6.(b). Emerging Frontiers

• Hybrid reactors: The integration of sonication or electrochemical controls facilitates multi-step deposition [96, 97].

• Machine learning: In 2020s, models were developed to predict ZnO nanorod aspect ratios from precursor ratios, and these models were subsequently entered into testing [98, 99].

• Advanced substrates: In the context of nuclear reactors, $FeCrAl$ alloy claddings have been found to host corrosion-resistant ferrite deposits via a process known as hydrothermal sealing.

The trajectory is clear: next-generation hydrothermal deposition will prioritize *precision over pragmatism*, leveraging computational tools and operando analytics to transcend empirical optimizations.

1.3.2. Sol-gel deposition technique

The sol-gel deposition technique is a chemical process used to synthesize inorganic materials through colloidal suspensions (sol) and gelation. It involves hydrolysis and condensation reactions of metal alkoxides or salts, forming a networked structure. This method enables precise control over material composition, porosity, and morphology, making it ideal for thin films, nanoparticles, and hybrid composites[100, 101].

Key advantages include low-temperature processing, molecular-level homogeneity, and compatibility with complex substrates. Applications span energy storage (e.g., batteries, solar cells), catalysis, and biomedical devices (e.g., bioactive coatings). Recent advancements focus on optimizing sol-gel parameters for scalable production and integrating smart functionalities, such as stimuli-responsive behaviors.

Challenges include shrinkage during drying and limited mechanical strength in bulk forms. However, innovations in templating agents and hybrid organic-inorganic systems have mitigated these issues. The technique's adaptability aligns with trends in sustainable materials and nanotechnology, as highlighted in interdisciplinary research.

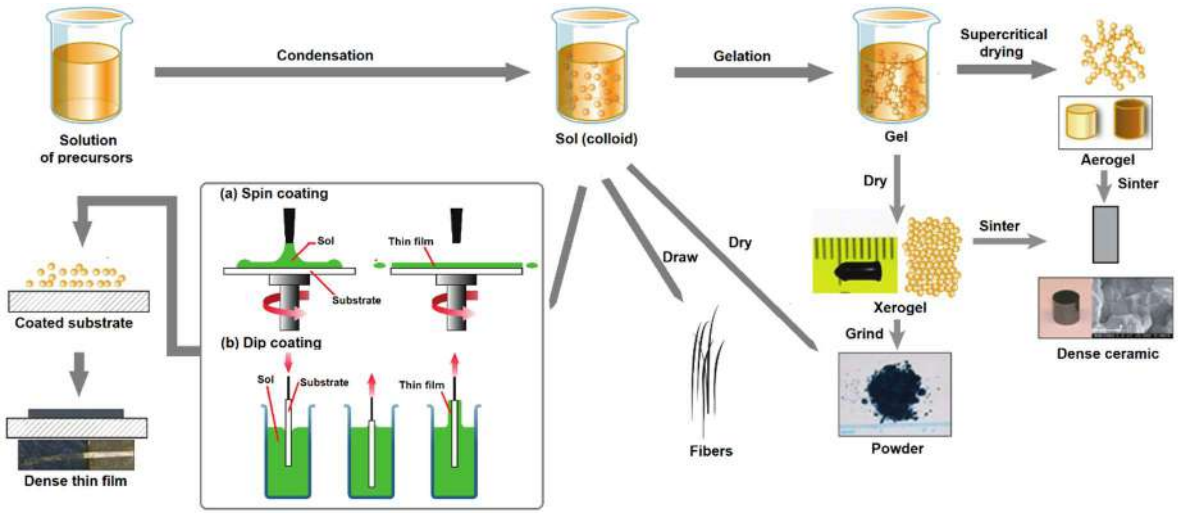

Figure 1.15: A variety of products that can be prepared using the sol-gel process.

1.3.3.Spray pyrolysis technique

Spray pyrolysis technique (SPT) is a workhorse technique in materials science for depositing thin films and synthesizing powders. It's cheap, versatile, and doesn't need vacuum systems. We can see it everywhere in labs studying solar cells, sensors, and coatings. This technique is important in materials science because it is simple, can be used on a wide scale, and can produce complex compositions (Figure 1.2).

Early uses focused on oxide coatings for sensors and batteries. Over time, advancements expanded its application to photovoltaics, catalysis, and biomedical devices.

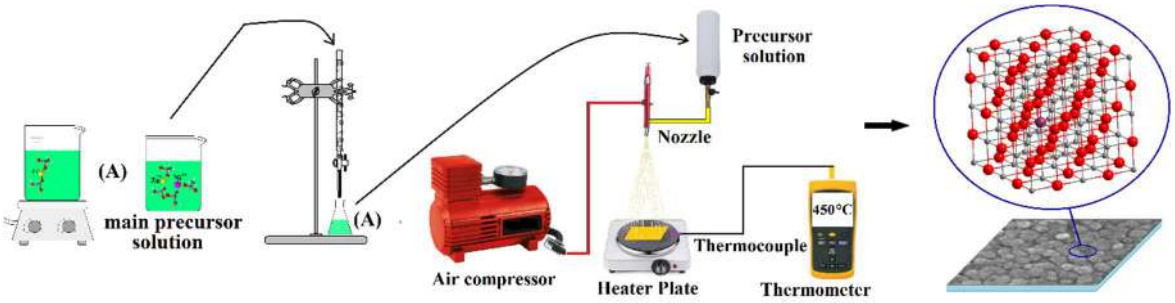

Figure 1.16: Schematic sketch of chemical spray pyrolysis process.

1.3.3.1.Fundamental idea and its operational mechanism

The principle of spray pyrolysis is to transform a liquid precursor into a solid material through thermal decomposition. A solution of the precursor is sprayed onto a heated glass or metal substrate. The solution is produced by dissolving metal salts (solute) in water, alcohol, or a mixture (water and alcohol), known as solvents. When the droplets touch the hot surface of the substrate, the solvent evaporates and chemical reactions form a solid film or powder. Each droplet behaves like a microscopic chemical reactor. This makes it possible to control reactions on a micrometric scale.

The process occurs in four steps:

1) **Atomization**: Liquid precursor (metal salts, polymers) is atomized into droplets.
2) **Transport**: Droplets are carried by gas (air, nitrogen) to a heated surface.
3) **Evaporation**: Solvent evaporates, leaving solid particles or films.
4) **Pyrolysis**: Thermal decomposition of the precursor ensures material crystallization to form the final material.

Droplet size matters a lot. Pneumatic nozzles give a broad size range, while ultrasonic ones make smaller, more uniform droplets. If the droplets are too big, you get uneven films; too small, and they might vaporize before hitting the substrate.

Spray pyrolysis is not new. It started in 1966 when Chamberlin and Skarman used it to make cadmium sulfide films for solar cells. Back then, it was all about simplicity: a spray gun, a heater, and open air. No vacuum chambers or fancy targets.

By the 1970s-80s, people were depositing oxides like TiO_2 and ZnO for transparent coatings. The 1990s saw a boom-researcher figured out how to mix precursors for complex materials (think ITO for displays) and even layered structures.

1.3.3.2. Main Spray Systems

- **Pneumatic**: in this system, gas pressure breaks the liquid into droplets, accelerating them by entrainment. The system is simple, but messy, and droplet size varies.
- **Ultrasonic**: Uses high-frequency sound waves. Gives finer, more even droplets. Better for quality films.

Table 1.3: Comparing spray generation methods

Method	Droplet Size	Uniformity	Best For
Pneumatic	10–100 µm	Low	Thick films, coatings
Ultrasonic	1–20 µm	High	Nanoparticles, optoelectronics

1.3.3.3. Control parameters for the spray pyrolysis technique

- **Temperature**: reactions will be incomplete if the working temperature is too low; on the other hand, if it is too high, the films will crack or delaminate from the substrate.
- **Solution composition**: the choice and quality of the precursor influence the purity of the deposited material.
- **Gas flow and pressure**: these factors control droplet arrival speed and travel time to the substrate, as well as droplet size.
- **Distance between source and target**: this determines how much solvent evaporates into the air, and how much useful material is lost along the way.

1.3.3.4. Potential Application of the spray pyrolysis

The flexibility of the “Spray Pyrolysis” is remarkable. The following types of deposits are possible:

- **Oxides**: ZnO, NiO for sensors, TiO_2 for antireflection coatings.
- **Chalcogenides**: Like CMTS (Cu_2MgSnS_4) for solar cells.
- **High-k dielectrics**: Hafnia or zirconia for transistors.
- **Luminescent powders**: Europium-doped yttria for LEDs.

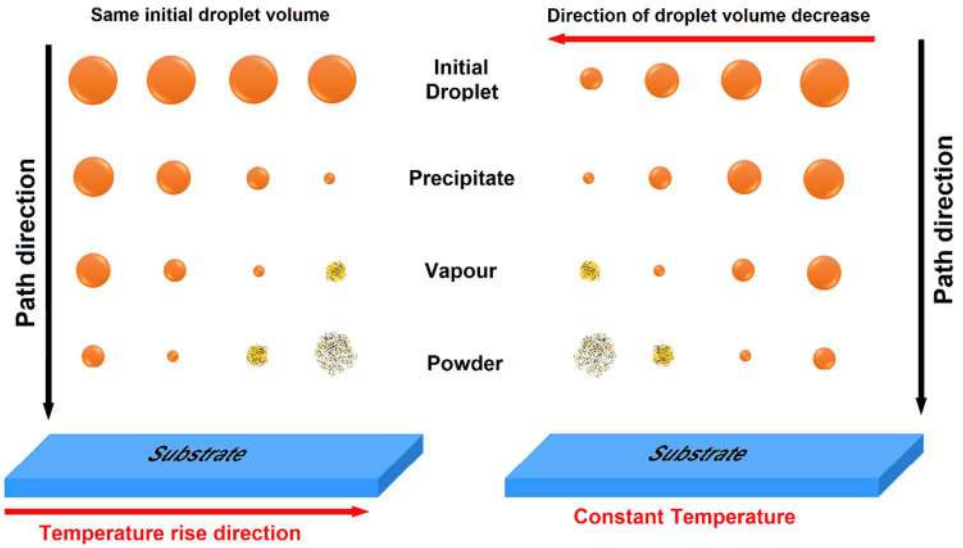

Figure 1.17: Diagram illustrating the evolution of aerosol droplets as they approach the hot substrate (target) in two situations. (a) Same initial droplet volume and increasing substrate temperature, (b) decreasing initial droplet volume and constant substrate temperature.

1.3.3.5. Most particularly important applications.

- **Solar cells**: SP-made CdS layers are dirt-cheap and effective. CMTS films hit ~1.47 eV bandgaps, ideal for photovoltaics.
- **Transparent electrodes**: ITO and ZnO: Al films from spray pyrolysis (SP) conduct well and let light through.
- **Sensors**: SnO_2 films detect gases because spray pyrolysis (SP) gives them porous, reactive surfaces.
- **Biomedical**: Silver-doped fights bacteria. Spray pyrolysis (SP)'s control over nanostructure helps here.

Table 1.4: Application examples with main properties.

Material	Application	Main Property	Performance
CMTS (Cu_2MgSnS_4)	Photovoltaic	$E_g \approx 1.47eV$	Efficiency~0.78/100
SnO_2: F	TE	$\rho \approx 10^{-6}\Omega.m$	Transparency~80/100
Y_2O_3: Eu^{3+}	LC	Red emission	High brightness

Chapter-2 Thin Film Fabrication and Analysis: Deposition Methods and Characterization Techniques

Chapter-2
Thin Film Fabrication and Analysis: Deposition Methods and Characterization Techniques

2.1. Introduction

This chapter outlines the methodologies for synthesizing precursor solutions and depositing thin films of zinc oxide (ZnO), nickel oxide (NiO), barium-doped zinc oxide ($Ba:ZnO$) and barium-doped nickel oxide ($Ba:NiO$) onto transparent glass substrates. The precursor solutions zinc acetate, nickel chloride, barium chloride, and their controlled mixtures are prepared using standardized protocols to ensure stoichiometric accuracy and solution stability. The deposition setup employs a solution-based technique, optimized to achieve uniform film formation. Following deposition, the structural, morphological, optical, and electrical properties of the films are analyzed using complementary techniques: X-ray diffraction (XRD) for crystallinity, scanning electron microscopy (SEM) for surface morphology, UV-visible spectrometry for optical bandgap estimation, Fourier-transform infrared spectroscopy (FTIR) for chemical bonding analysis, and four-point probe measurements for electrical resistivity. These methods collectively enable a comprehensive evaluation of film quality and doping effects, critical for advancing functional oxide-based thin-film applications

2.2. Description of the Homemade Spray Pyrolysis Technique (SPT) System

Figure 2.1 presents a schematic representation of the chemical spray pyrolysis system. The homemade spray pyrolysis technique (SPT) system, utilized for the deposition of the thin films, is illustrated in Figure 2.1. This system enables the synthesis of thin films through a series of well-defined processing steps, which are critical for achieving high quality and uniform layers. The three primary steps involved in the spray pyrolysis deposition process are as follows:

a. Atomization of the precursor solution: The precursor solution, containing the desired metal salts, is transformed into fine droplets using a compressed air-assisted atomizer. This step ensures the generation of a uniform aerosol mist, which is essential for the deposition of homogeneous thin films.

b. Aerosol transport of the droplets: The atomized droplets are transported by a carrier gas (typically compressed air) toward the heated substrate. The efficiency of this step depends on the stability of the aerosol flow and the distance between the atomizer and the substrate.

c. Evaporation and decomposition of the droplets: Upon reaching the heated substrate, the solvent in the droplets evaporates, and the precursor salts undergo thermal decomposition. This results in the formation of a solid film on the substrate surface, initiating the growth of the thin film.

The homemade SPT system consists of several key components, each playing a vital role in the deposition process:

1. ***Precursor solution container***: A transparent glass bottle with a capacity of 50 mL is used to hold the precursor solution. The solution is fed by gravity into a low-flow atomizer, ensuring a consistent and controlled supply of the precursor during the deposition process.
2. ***Substrate heater and holder***: The substrate is placed on a custom-made brass plate, which is heated by an electrical resistance element. The temperature of the substrate is precisely regulated using a digital temperature controller connected to a thermocouple. This setup allows for a temperature range of 20°C to 500°C, which is critical for controlling the thermal decomposition and crystallization of the thin films.
3. ***Atomizer and flow solution controller***: The atomizer is responsible for transforming the precursor solution into a fine spray of droplets. The flow rate of the precursor solution and the size of the droplets are controlled by adjusting the compressed air pressure and the solution flow rate. This component is essential for achieving uniform film deposition.

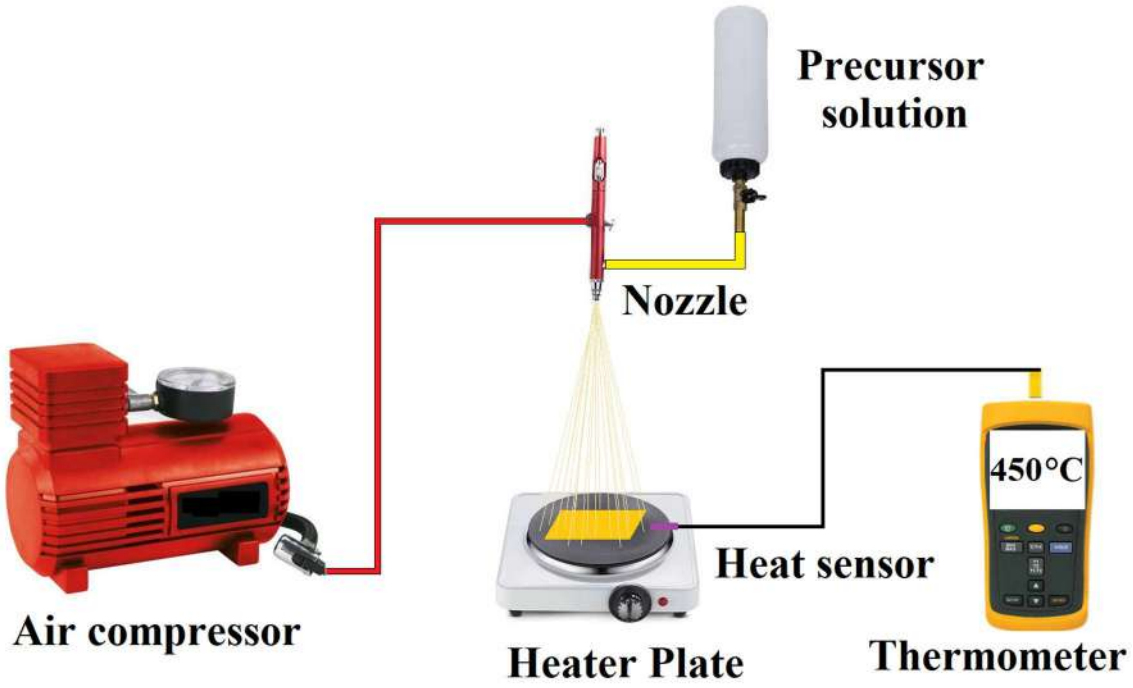

Figure 2.1: Schematic sketch of chemical spray pyrolysis system.

4. ***Atomizer holder***: The atomizer is mounted on an adjustable holder, allowing for precise control of the distance between the atomizer and the substrate. This parameter is crucial for optimizing the deposition efficiency and the uniformity of the thin films.
5. ***Air compressor***: The system is equipped with a reservoir-type electrical air compressor, which supplies compressed air to the atomizer. The compressor consists of a rotary pump that draws atmospheric air and stores it in a high-capacity air tank. A pressure gauge and a bypass control valve are attached to the tank, enabling precise regulation of the output pressure. The compressed air is delivered to the atomizer through a rigid, non-expandable tube, ensuring a stable and consistent flow during the deposition process.

This homemade SPT system offers a cost-effective and flexible approach for the deposition of the thin films, allowing for precise control over key deposition parameters such as substrate temperature, precursor flow rate, and atomizer-substrate distance. These features make it an ideal tool for investigating the influence of processing conditions on the structural, optical, and electrical properties of the synthesized films.

Figure 2.2: The homemade spray pyrolysis technique (SPT) system.

2.3. Experimental procedure

2.3.1. Selecting the deposition substrate

The layers of zinc oxide and nickel oxide that are the subject of this investigation are deposited onto conventional microscope glass substrates. The selection of glass as the substrate for deposition is attributable to its advantageous thermal expansion characteristics and its ability to alleviate stresses at the interface between the layer and the substrate. Additionally, economic factors played a significant role in the material selection, considering its transparency, which is

highly conducive for the optical characterization of films within the visible spectrum. To facilitate an optical examination of the thin films comprised of zinc oxide and nickel oxide, glass substrates were employed with the aim of achieving a pristine deposition of the aforementioned thin films, the optical properties of which are particularly sensitive to the techniques of surface preparation.

2.3.2. Preparation of substrates

The glass substrates used in this study are TICARE -cat-no-7102 optical microscope slides, with dimensions of 75×25×1mm^3 (as showed in Figure 2.3). These substrates were selected due to their availability, cost-effectiveness, and suitability for studying the optical properties of thin films. Additionally, the thermal expansion coefficient of the glass closely matches that of zinc oxide (ZnO) and nickel oxide (NiO), minimizing thermal stress at the film-substrate interface during deposition and cooling. This compatibility is crucial for reducing defects such as cracking or delamination, which can arise from mismatched thermal expansion coefficients.

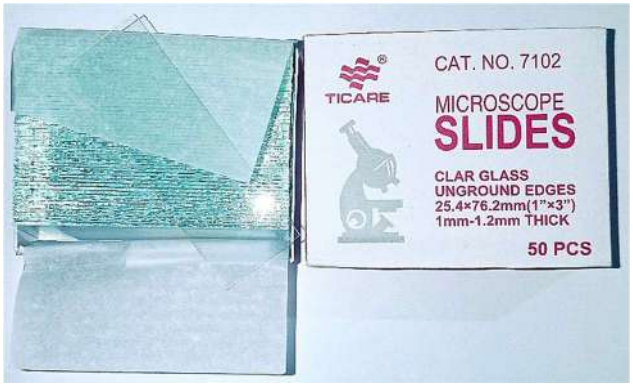

Figure 2.3: Glass substrates used are TICARE -cat-no-7102 optical microscope slides.

To ensure high-quality film deposition, the substrates must be meticulously cleaned to remove contaminants such as grease, dust, and organic residues. Contamination can adversely affect film adhesion, uniformity, and overall quality. In this work, the substrates were cleaned using a systematic procedure involving an ultrasonic bath and a series of chemical treatments. The cleaning process was carried out as follows:

1. **Initial rinsing**: The substrates were first washed with tap water to remove loose particles, followed by rinsing with distilled water to eliminate any dissolved impurities.
2. **Chemical cleaning**: Each substrate was sequentially immersed in hydrochloric acid (HCl) and acetone (C_3H_6O) solutions. The HCl treatment removes inorganic contaminants, while acetone effectively dissolves organic residues. After each immersion, the substrates were thoroughly rinsed with distilled water to remove any residual chemicals.

3. **Drying**: The cleaned substrates were dried using a hairdryer and lint-free paper towels to prevent water spots or streaks that could interfere with film deposition.

This rigorous cleaning procedure ensures that the substrates are free from contaminants and possess a surface suitable for strong adhesion of the thin films. Once cleaned, the substrates are ready for use in the deposition process. Proper substrate preparation is a critical step in thin film fabrication, as it directly influences the structural, optical, and morphological properties of the deposited films.

2.3.3. Steps and Parameters of the Thin Films Deposition

In the chemical spray deposition technique, the structural, compositional, and functional properties of the deposited films are highly influenced by a variety of process variables, commonly referred to as deposition parameters. These parameters include the substrate temperature, precursor solution flow rate, carrier gas (air) flow rate, deposition time, substrate material quality, size of the atomized droplets, distance between the atomizer and the substrate, and the concentration of the precursor solution. Each of these variables plays a critical role in determining the morphology, crystallinity, thickness, and overall quality of the resulting thin films.

The deposition of the thin films via the spray pyrolysis technique (SPT) is carried out after the preparation of the substrates and precursor solutions. The procedure is outlined in the following steps:

1. Loading the precursor solution: A measured quantity of the prepared precursor solution is transferred into the dedicated glass bottle connected to the atomizer. This ensures a consistent supply of the solution during the deposition process.
2. Adjusting the atomizer-substrate distance: The distance between the atomizer and the substrate holder is carefully set by adjusting the position of the atomizer holder. This parameter is critical for controlling the droplet size and distribution on the substrate surface.
3. Regulating the air pressure: The air pressure is fine-tuned using the control valve on the compressor, with the pressure gauge providing real-time feedback. Proper air pressure ensures the generation of a uniform aerosol mist and stable droplet transport.
4. Controlling the solution flow rate: The flow rate of the precursor solution is adjusted using the control button on the sprayer. This step is essential for maintaining a consistent deposition rate and achieving uniform film thickness.

5. Positioning the substrate: The cleaned glass substrate is placed on a ceramic plate, which serves as the substrate holder on the electric heater. The heater is equipped with a temperature regulator to maintain precise control over the substrate temperature.
6. Heating the substrate: The substrate is heated to the desired deposition temperature, typically around 450°C. This temperature is chosen to facilitate the thermal decomposition of the precursor and the formation of a crystalline metal oxide thin film.
7. Initiating the deposition process: Once the substrate reaches the target temperature, the precursor solution is sprayed onto the hot surface. To compensate for the temperature drop caused by the spraying process, the deposition is carried out intermittently. This allows the electric heater to restore the substrate temperature, ensuring consistent film growth.
8. Pyrolysis reaction: upon interaction with the thermally elevated substrate, the droplets of the precursor solution engage in a pyrolysis reaction. The solvent, specifically water, undergoes evaporation, resulting in the decomposition of the metal salt. This chemical transformation yields the requisite metal oxide.
9. ***Reaction of decomposition of nickel(II) chloride hexahydrate***:

In the course of the spray pyrolysis of $NiCl_2 \cdot 6H_2O$, the reaction mechanism is indicative of a thermal decomposition of nickel chloride resulting in the formation of nickel oxide, facilitated by the presence of water and atmospheric oxygen. The resultant films may exhibit either an amorphous $Ni(OH)_2$ configuration or a crystalline NiO morphology, as delineated by the subsequent reactions [14, 16]:

$$NiCl_{2(aq)} + 2H_2O_{(aq)} \xrightarrow{Heat} 2HCl_{(g)} + Ni(OH)_{2(s)} \quad \text{Eq.2.1}$$

$$NiCl_{2(aq)} + 2H_2O_{(aq)} \xrightarrow{Heat} 2HCl_{(g)} + NiO_{(s)} + H_2O_{(g)} \quad \text{Eq.2.2}$$

If nickel hydroxide is present in the films, it cannot be detected by X-ray diffraction due to its anticipated amorphous nature [102]. Nevertheless, research by Kamal et al. [102] has indicated that the formation of $Ni(OH)_2$ is more likely to occur at lower substrate temperatures (below 420°C) than at the temperature employed in the present study (450°C). According to Kamal et al. [102], during the reaction of the precursor in contact with the hot substrate, two intermediate reactions can occur.

1-Removal of water of hydration at temperatures below 200°C.

2-Removal of water due to decomposition of nickel hydroxide at temperatures above 250°C.

$$Ni(OH)_{2(s)} \xrightarrow{Heat} NiO_{(s)} + H_2O_{(g)} \quad \text{Eq.2.3}$$

10. ***Reaction of decomposition of zinc acetate dihydrate***:

The vapor produced around the droplet prevents direct contact between the liquid phase and the substrate surface when aerosol droplets pass over the thermally heated substrate surface (140–590°C) under appropriately specified experimental conditions. This phenomenon is seen when the temperature reaches a certain point, known as the Leidenfrost temperature [103, 104]. The droplets can undergo thermal breakdown and produce a highly adherent zinc oxide layer because the vaporization process allows for a continuous replenishment of the vapor phase [103, 104]. ZnO is produced via the heat breakdown of a volatile molecule, such as zinc acetate dihydrate, which follows this chemical process [105-107]:

$$Zn(CH_3COO)_{2(liq)} + H_2O_{(liq)} \longrightarrow ZnO_{(s)} + 2CH_3COOH_{(g)} \qquad \text{Eq.2.4}$$

According to Tiburcio-Silver et al.[108], the growth kinetics of ZnO films produced by the pyrosol process differ from those reported for layers produced by pneumatic spraying, using the same source compound and obtained on the same type of substrate. The aforementioned researchers further contend that, in contrast to the assertions of other authors, the thermal decomposition of zinc acetate dihydrate yielding ZnO occurs according to the following reaction scheme [108, 109]:

$$Zn(CH_3COOH)_2.2H_2O_{(s)} \rightarrow Zn(CH_3COOH)_{2(s)} \begin{cases} \xrightarrow{\text{Primary}} Zn(CH_3COOH)_{2(liq)} \\ \xrightarrow{\text{Secondary}} Zn_4O(CH_3COOH)_{6(s)} \rightarrow Zn_4O(CH_3COOH)_{6(liq)} \end{cases} \rightarrow ZnO_{(s)} + CO_{2(g)} + CH_3COCH_{3(g)} \qquad \text{Eq.2.5}$$

11. Cooling the substrate: After the deposition process is complete, the heating is turned off, and the substrate is allowed to cool gradually to room temperature on the substrate holder. This slow cooling process prevents thermal shock, which could otherwise lead to cracking or breaking of the glass substrate.

Table 2.1: The optimum values range of some the thin film deposition parameters

Parameters	**values**
Air pressure	1-2 bar
Temperature of the substrate	450 (±5) °C
Flow of the precursor solution	2.0-5 mL/min
Distance between the atomizer nozzle and the substrate surface	15-25 cm
Concentration of the precursor solution	0.05-0.40 mole/L
Deposition time	4-15 min
Volume of the precursor solution	5-25 ml

In this study, the deposition of the thin films was carried out by carefully controlling and optimizing these parameters. The specific values used for each parameter, such as substrate temperature, solution concentration, and deposition time, are summarized in Table 2.1. By maintaining these parameters at their optimum values, we ensured the reproducibility and consistency of the deposition process, enabling a detailed investigation of the relationship between deposition conditions and the resulting film properties. This approach not only facilitates the synthesis of high-quality oxides thin films but also provides valuable insights into the optimization of the spray pyrolysis technique for other metal oxide systems.

2.4. Experimental conditions and solution preparation

2.4.1. Preparation method of the pure NiO precursor solutions

The preparation of the precursor solution is a critical step in the synthesis of nickel oxide (NiO) thin films using the spray pyrolysis technique (SPT). To achieve a specific molar concentration, a precisely measured quantity of nickel (II) chloride hexahydrate ($NiCl_2 \cdot 6H_2O$) (see Figure 2.4) was dissolved in a known volume of doubly distilled water (H_2O). The mass of $NiCl_2 \cdot 6H_2O$ was accurately determined using a high-precision electronic scale to ensure consistency and reproducibility in the solution concentration (see Figure 2.5).

To enhance the solubility of the nickel salt and prevent the formation of unwanted hydroxides or oxides during the dissolution process, a few drops of hydrochloric acid (HCl) were added to the solution. The acidic environment stabilizes the nickel ions in the solution, ensuring a homogeneous mixture. The solution was then heated to 60°C and continuously stirred using a magnetic stirrer for one to two hours. This step promotes complete dissolution of the nickel salt and facilitates the formation of a clear, transparent, and homogeneous green solution, indicative of the presence of nickel ions in the aqueous phase.

The resulting precursor solution is now ready for use in the SPT deposition process. The quality and stability of the precursor solution are crucial for achieving uniform and high-quality NiO thin films, as any inconsistencies in the solution can lead to defects or variations in the film properties. This method of precursor preparation ensures a reliable and reproducible starting point for the deposition of NiO thin films with controlled stoichiometry and morphology.

Figure 2.4: Nickel (II) chloride hexahydrate [$NiCl_2.6\ H_2O$].

Figure 2.5: Electronic scale and magnetic stirrer utilized in the present study.

2.4.2. Calculation of the Mass of Nickel (II) Chloride Hexahydrate

The mass of nickel (II) chloride hexahydrate ($NiCl_2 \cdot 6H_2O$) required for the preparation of the precursor solution can be calculated using the following expression:

$$m = M \times C \times V \qquad \text{Eq.2.6}$$

, where:

m is the mass of $NiCl_2 \cdot 6H_2O$ in grams (g),

M is the molar mass of $NiCl_2 \cdot 6H_2O$ in grams per mole (g/mole),

C is the desired molar concentration of the solution in moles per liter (mole/L),

V is the volume of doubly distilled water in liters (L).

This equation ensures precise control over the concentration of the precursor solution, which is essential for achieving consistent and reproducible results in the deposition of NiO thin films. The molar mass of $NiCl_2 \cdot 6H_2O$ is calculated by summing the atomic masses of its constituent elements, taking into account the six water molecules in the hydrated form. Accurate

measurement of the mass using a high-precision electronic scale is critical to avoid deviations in the solution concentration, which could affect the properties of the deposited films.

Additionally, Table 2.2 summarizes some key physicochemical properties of nickel (II) chloride hexahydrate, such as its molecular weight, solubility, and thermal stability. These properties are important for understanding the behavior of the precursor during the dissolution process and its subsequent decomposition during the spray pyrolysis deposition. For instance, the high solubility of $NiCl_2 \cdot 6H_2O$ in water ensures the formation of a homogeneous solution, while its thermal decomposition characteristics influence the formation of NiO thin films on the heated substrate.

Table 2.2: Summary of the physicochemical properties of nickel (II) chloride hexahydrate.

Property	Value
Physical state	solid
Cristal color	green
Chemical formula	$NiCl_2 \cdot 6H_2O$
Molecular weight	237.69 g/mole
Melting point	140 °C
Density	1.92 g/cm^3
Water solubility	2540 g/L at 20°C
Purity	98%

2.4.3. Preparation method of the pure ZnO precursor solutions

The preparation of the precursor solution constitutes a critical step in the synthesis of zinc oxide (ZnO) thin films using the spray pyrolysis technique (SPT). In order to achieve a specific molar concentration, a precisely measured quantity of zinc (II) acetate dihydrate $Zn(CH_3COO)_2 \cdot 2H_2O$, see Figure 2.6) was dissolved in a known volume of doubly distilled water (H_2O). The mass of $Zn(CH_3COO)_2 \cdot 2H_2O$ was meticulously determined using a high-precision electronic scale to ensure consistency and reproducibility in the solution concentration. The preparation protocol is delineated in the following paragraph.

2.4.3.1. Experimental Procedure for Preparing Zinc Acetate Mother Solution

To prepare a 0.50 M zinc acetate dihydrate solution (250 mL), first calculate the required mass: 0.50 mole/L × 0.250 L × 219.50 g/mole = 27.438 g. Combine 83 mL ethanol and 167 mL distilled water in a beaker to create the solvent mixture. Add 27.438 g zinc acetate dihydrate to the solvent. Place a magnetic stir bar in the beaker and position it on a shaker plate. Mix at medium speed, following this temperature sequence: 25°C for 20 minutes, then 40°C for 20

minutes. After this, add 4–5 drops of concentrated hydrochloric acid (HCl). Increase the temperature to 50°C and mix for 30 minutes. Significant evaporation will occur, producing visible steam. Reduce the temperature to 40°C and continue mixing for 15 minutes. The solution will clarify and reduce in volume by 25–30%. Turn off the heat and allow the solution to cool to room temperature while maintaining medium-speed stirring for 30 minutes.

The prepared precursor solution is now ready for use in the solution-based deposition process. Consistency and stability of the solution are critical, as even minor variations can lead to defects or uneven properties in the final zinc oxide (ZnO) thin films. This preparation method ensures a consistent foundation for producing high-quality ZnO films with precise composition and structure.

Additionally, Table 2.3 summarizes some key physicochemical properties of zinc (II) acetate dihydrate, such as its molecular weight, solubility, and thermal stability. These properties are important for understanding the behavior of the precursor during the dissolution process and its subsequent decomposition during the spray pyrolysis deposition. For instance, the high solubility of $Zn(CH_3COO)_2 \cdot 2H_2O$ in water ensures the formation of a homogeneous solution, while its thermal decomposition characteristics influence the formation of ZnO thin films on the heated substrate.

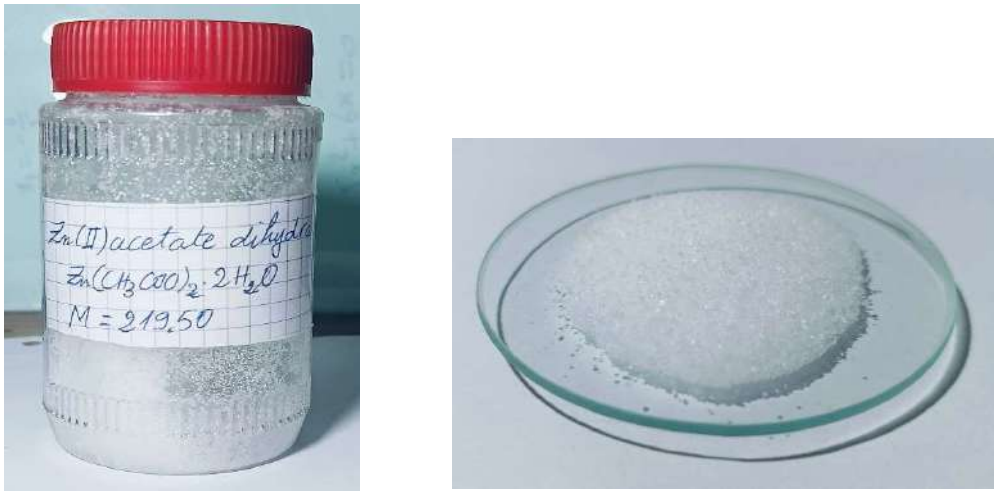

Figure 2.6: Zinc (II) acetate dihydrate [$Zn(CH_3COO)_2 \cdot 2H_2O$].

Table 2.3: Summary of the physicochemical properties of zinc (II) acetate dihydrate.

Property	**Value**
Physical state	solid
Cristal color	white
Chemical formula	$Zn(CH_3COO)_2 \cdot 2H_2O$
Molecular weight	219.50 g/mole

Melting point	237 °C
Density	1.735 g/cm^3
Water solubility	430 g/L at 20°C
Purity	> 99%

2.4.3.2. Experimental Procedure for Preparing a Dilute Zinc Acetate Solution

To prepare 50 mL of a 0.40 M zinc acetate solution from a 0.50 M stock solution, follow these steps:

1. Select a 50 mL volumetric flask and a 40 mL volumetric pipette.
2. Calculated using the dilution factor:

$$f = \frac{C_{mother\,(stock)}}{C_{daughter}} = \frac{V_{flask}}{V_{pipette}} \quad \text{Eq. 2.7}$$

$$f = \frac{C_{mother\,(stock)}}{C_{daughter}} = \frac{0.50\ \text{mole/L}}{0.40\ \text{mole/L}} = 1.25 \quad \text{Eq. 2.8}$$

$$V_{pipette} = \frac{50\ \text{mL}}{1.25} = 40\ \text{mL} \quad \text{Eq. 2.9}$$

3. Use the pipette to transfer 40 mL of the stock solution into the flask.
4. Add distilled water to the flask until the bottom of the meniscus reaches the calibration mark.
5. Seal the flask and invert it repeatedly to ensure thorough mixing. This method ensures precise dilution while maintaining solution homogeneity.

Subsequently, the identical procedure was repeated to generate the remaining diluted daughter solutions. The following table (Table 2.4) offers a concise summary of the parameters of the solutions that were prepared.

Table 2.4: Summary of the parameters of the diluted solutions prepared.

Diluted solution number		1	2	3	4	5	6	7	8
Vol. prepared	mL	50	50	50	50	50	50	50	50
Vol. of stock solution used	mL	5	10	15	20	25	30	35	40
Concentration after dilution	mole/L	0.05	0.10	0.15	0.20	0.25	0.30	0.35	0.40

2.4.4. Preparation of undoped and Ba^{2+}-doped (Zn^{2+}, Ni^{2+}) solutions.

In order to prepare Zinc Nickel oxide thin films in equal quantities (50% Zn and 50% Ni), two precursor mother solutions of the same molar concentration ($C_m = 0.50 mole/L$) were

prepared. The mother solutions are Zinc acetate $(Zn^{+2}, 2CH_3COO^-)_{(aq)}$ and Nickel chloride $(Ni^{+2}, 2Cl^-)_{(aq)}$, respectively. The salts utilized were zinc acetate dihydrate $[Zn(CH_3COO)_2.2H_2O]_{(s)}$ and nickel chloride hexahydrate $(NiCl_2.6H_2O)_{(s)}$.

Subsequently, two equal volumes of the precursor solutions were taken, and they were diluted to obtain solutions of the same molar concentration ($0.15\ mole/L$). Finally, the two solutions of equal volume and concentration were mixed to obtain a mixture containing equivalent amounts of $Zn^{2+}\ and\ Ni^{2+}$ ions.

For the doping of this final mixed solution, a barium chloride solution $(Ba^{2+}, 2Cl^-)_{(aq)}$ containing the dopant Ba^{2+} ions from the barium chloride dihydrate $(BaCl_2.2H_2O)_{(s)}$ was prepared, according to the parameters shown in Table 2.5.

Table 2.5: Parameters and quantities used for the doping solution.

		$BaCl_2 \cdot 6H_2O$
Molar Mass	$M(g/mole)$	244.26
Concentration	$C_m\ (mole/L)$	0.15
Volume	$V_m\ (mL)$	100
Dissolved mass	$m\ (g)$	3.664

As illustrated in Table 2.6, a summary of some of the physical and chemical properties of barium chloride dihydrate (See Figure 2.7) is provided.

Table 2.6: Summary of the physicochemical properties of Barium (II) chloride dihydrate.

Property	**Value**
Physical state	solid
Cristal color	white
Chemical formula	$BaCl_2 \cdot 6H_2O$
Molecular weight	244.26 g/mole
Density	3.0979 g/cm^3
Melting point	962°C
Solubility in water	35.8 g/100mL at 20°C
Purity	> 98%

Figure 2.7: Barium chloride dihydrate.

2.5. Thin Film Characterization and Analysis Techniques

2.5.1. Structural Characterization Techniques

2.5.1.1. X-ray Diffraction (XRD)

X-ray diffraction (XRD) is a fundamental analytical technique employed to characterize crystal structures, identify constituent phases in chemical compounds, and assess the degree of crystallinity. By comparing diffraction patterns with extensive databases—such as the Inorganic Crystal Structure Database (ICSD), which catalogs over 1,535 compounds, the International Centre for Diffraction Data (ICDD, formerly JCPDS) with more than 1,004,568 reference patterns, and the Crystallography Open Database (COD) containing 459,555 entries—XRD enables the detection of crystalline phases within a material. Additionally, it determines key structural parameters, including lattice constants, atomic positions in the crystal lattice, and crystal size/orientation. The method also facilitates the analysis of material properties like strain levels and internal stress. XRD is applicable to crystalline materials, whether fully or partially ordered, that exhibit a periodic atomic arrangement.

2.5.1.2. X-ray Diffraction Principle

X-rays, a form of electromagnetic radiation, exhibit wavelengths ranging from 0.01 to 10 Å, with the subset of 0.01–10 Å commonly utilized for material analysis. X-ray diffraction (XRD) arises from the coherent scattering of X-rays as they interact with ordered atomic structures. This diffraction phenomenon stems from the interference of waves scattered by individual

atoms within a material, and its characteristics depend on the crystal structure's type and properties.

When a monochromatic X-ray beam is directed at a sample (as illustrated in Figure 2.8), it interacts with the electron clouds of the atoms. In crystalline materials, this interaction triggers diffraction. Constructive interference occurs when scattered X-ray waves align in phase, amplifying their intensity and producing distinct diffraction peaks. Conversely, destructive interference cancels out waves when phases clash. This selective reinforcement of waves follows the Bragg condition, mathematically defined by the equation[110]:

$$2d_{(hkl)} \cdot \sin\theta_{(hkl)} = n\lambda \qquad \text{Eq. 2.10}$$

,where, n is an integer, λ is the X-ray wavelength, d_{hk} is the interplanar spacing in the crystal lattice, and θ_{hkl} is the incident beam angle relative to the crystal planes.

The Bragg condition depends on the spacing between atomic planes in the crystal lattice. As a result, each set of atomic planes (hkl), spaced at a distance d_{hkl}, acts as a source of diffracted X-rays at the incident angle θ_{hkl} (see Figure 2.8).

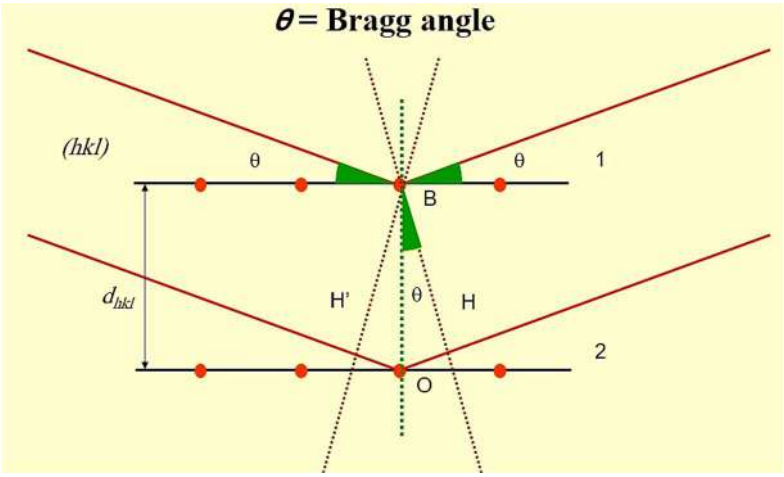

Figure 2.8: For diffraction to occur, the Bragg condition must be satisfied.

2.5.1.3. Data Collection and Instrumentation

Data were collected using a Philips X'Pert MPD diffractometer configured in a θ–2θ angular scan mode (single-axis goniometer) (See Figure 2.9-a). The scan parameters included a step size of 0.017° and a dwell time of 5 seconds per step. The system features a 256-channel linear detector array and employs a copper X-ray tube (Cu-Kα radiation) with a characteristic wavelength of λ = 1.54056 Å. A schematic of the experimental setup is illustrated in Figure 2.9-b.

For zinc oxide (ZnO), nickel oxide (NiO), and zinc nickel oxide (ZnNiO) thin film samples, X-ray diffraction analysis was conducted using the Bragg-Brentano goniometer geometry to

generate the diffractograms, which plots the intensity of diffracted X-rays as a function of the scattering angle (2θ). This configuration ensures precise measurement of crystalline phase information and structural properties.

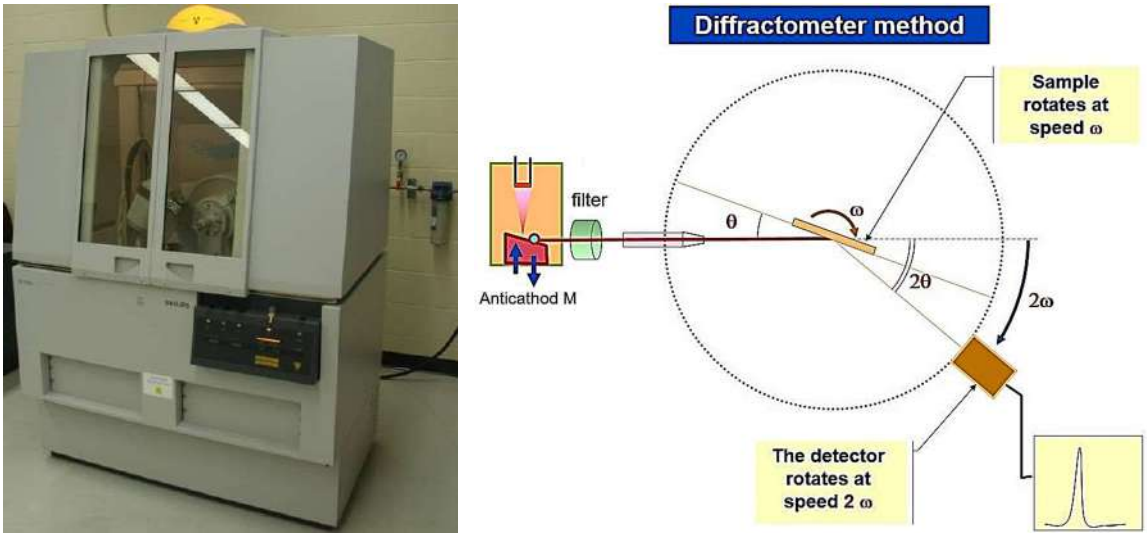

(a) (b)

Figure 2.9: The Bragg-Brentano configuration of the goniometer.

2.5.1.4. Experimental conditions

X-ray diffraction patterns were obtained using a Philips X'Pert MPD powder diffractometer configured in the Bragg-Brentano geometry. Experimental parameters included:

- An X-ray source generated by a copper anode X-ray tube operated at 40 kV and 30 mA.
- Monochromatized Kα radiation with a wavelength of λ (α) = 1.54056 Å, filtered through a curved graphite crystal monochromator.
- Careful alignment of the sample holder with the goniometer's rotational axis to ensure optimal data quality.
- Data collection over an angular range of (10°–100°) 2θ, with a step size of 0.017°. Crystallographic phases and lattice parameters were analyzed using ICSD and PDF-2 reference databases, integrated with HighScore Plus software (v.3.0.5) for phase identification and refinement

2.5.1.5. Structural characterization

A. Miller indices of crystallographic planes.

The X-ray diffraction (XRD) pattern of a stoichiometric zinc oxide (ZnO) and nickel oxide (NiO) powder, as shown in Figure 2.10, were modeled using data from ICDD cards no. 00-036-1451 and 00-047-1049, respectively. These reference cards and those corresponding diffraction profiles served as a benchmark for validating measurements and computational analyses

conducted in this study. The experimental XRD spectra of ZnO and NiO samples were systematically evaluated to correlate observed diffraction peaks with those predicted by the reference patterns, aiding in phase identification and structural characterization.

Comparing the selected reference pattern with experimental data from the investigated samples enables identification of the Miller indices for the first five diffraction peaks.

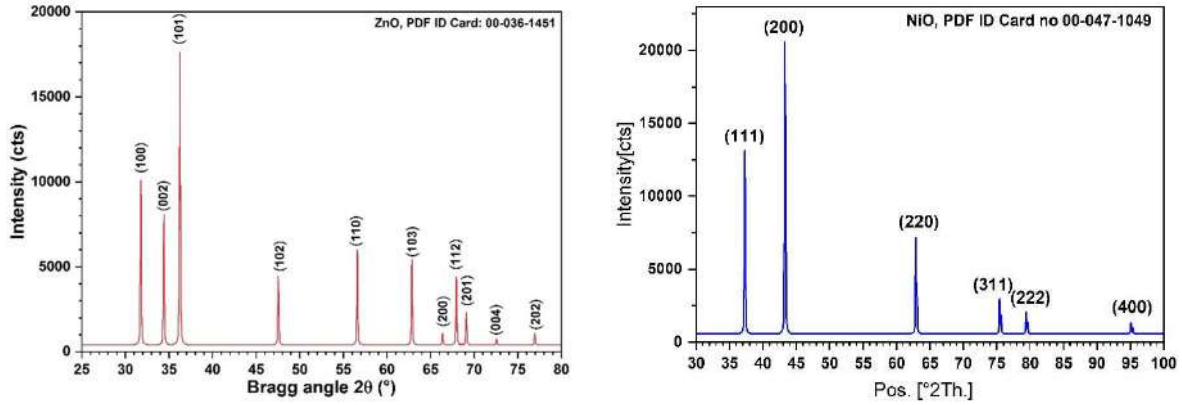

Figure 2.10: X-ray diffractograms of zinc oxide and nickel oxide modeled by the reference cards (PDF: 00-036-1451) and (PDF: 00-047-1049), respectively.

B. Preferential Orientation Coefficient (POC)

The comprehension of preferential orientation is of paramount importance, as it elucidates the directional configuration and growth dynamics of the grains that constitute the thin film, which subsequently informs its structural evolution. This understanding empowers researchers to modulate the growth pathway and technique by preemptively customizing the attributes of the substrate. The degree of preferential orientation within the synthesized thin film can be quantified utilizing the formula delineated below:

$$\mathrm{POC}(hkl) = \frac{I(hkl)}{\sum_{all\ peaks} I(hkl)} \qquad \text{Eq. 2.11}$$

, where $I(hkl)$ is the measured intensity of the peak.

The so-called Muller-Nowoczin-Schmitt relation [111]describes the dominant or preferential orientation of the crystal plane (hkl) in polycrystalline thin film. In the event that the crystal plane (hkl) is the sole prevailing orientation and consequently exhibits complete dominance, its formation factor is equivalent to unity, i.e., [POC (hkl) = 1].

C. Measuring the inter-reticular distance (interplanar spacing)

It is well established that each diffraction angle (θ) corresponds to a specific lattice plane (hkl), defined as a set of parallel atomic planes that coherently reflect X-rays at that angle. The interplanar spacing (d) between consecutive planes within a reflection family plays a central

role in this relationship. The Bragg equation (Equation 2.10) mathematically links the diffraction angle, interplanar spacing, and the wavelength of the reflected radiation.

Additionally, for any crystal lattice, the Miller indices (hkl) are intrinsically tied to the interplanar distance and the lattice constants of the material.

Nickel oxide, which crystallizes in a face-centered cubic structure, has an interplanar spacing determined by the following relationship [112]:

$$d_{hkl} = \frac{a_{hkl}}{\sqrt{h^2 + k^2 + l^2}} \quad \text{Eq.2.12}$$

The lattice constant (a_{cub}) for cubic structure was calculated using the following equation [113]:

$$a_{cub} = d_{hkl} \cdot \sqrt{h^2 + k^2 + l^2} \quad \text{Eq.2.13}$$

Zinc oxide, which crystallizes in a hexagonal close-packed (hcp) structure, exhibits interplanar spacing governed by the following relationship [112, 114]:

$$\frac{1}{d_{hkl}^2} = \frac{4}{3}\left(\frac{h^2 + hk + k^2}{a_{hex}^2}\right) + \frac{l^2}{c_{hex}^2} \quad \text{Eq.2.14}$$

In addition, the lattice parameters ($a_{hex} and\ c_{hex}$) for the hexagonal structure of zinc oxide were calculated using the previous expression ((eq.2.14)[114].

D. Grain Size Measurement (Coherent diffraction domain)

A key parameter derived from X-ray diffraction (XRD) analysis is the average grain size of deposited thin films. The Debye-Scherrer equation is utilized to estimate this parameter, where β denotes the width of the diffraction peak at half its maximum intensity (Full Width at Half Maximum, FWHM) or its integrated breadth (Integral Width) (see Figure 2.11) [114-117].

$$D = \frac{K \cdot \lambda}{\beta_{FWHM} \cdot \cos\theta} \quad \text{Eq. 2.15}$$

Where K=0.98 which corresponds to spherical shape of grains, λ is the X-ray wavelength of Cu-Kα, θ is the diffraction angle (in radians) and β_{FWHM} is the full width at half maximum of the peak.

E. Other microstructural parameters

The values of dislocation densities (δ) are calculated using the relation [114, 118-120]:

$$\delta = \frac{1}{D^2} \quad \text{Eq. 2.16}$$

Where D is the grain size.

The lattice strain (ε) is calculated using the relation [120, 121]:

$$\varepsilon = \frac{\beta_{FWHM} \cdot \cos\theta}{4} \qquad \text{Eq. 2.17}$$

Where the lattice parameter of the strained films was obtained from the XRD data.

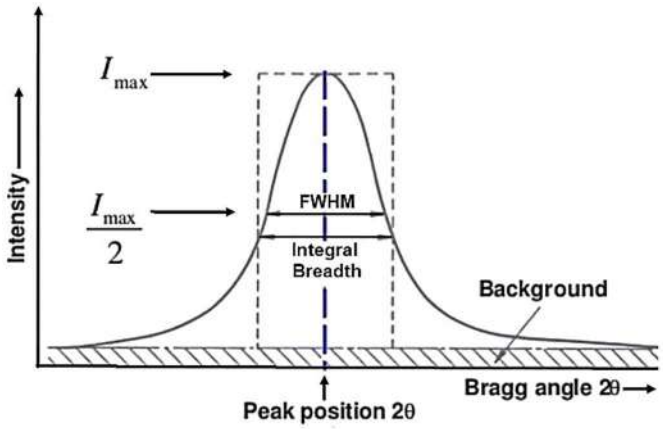

Figure 2.11: The diffraction peak at half its maximum intensity (Full Width at Half Maximum, FWHM) or its integral width (Integral Width).

Also, the volume of the hexagonal unit cell "V" of ZnO phase was calculated using[114]:

$$V_{hex} = \frac{\sqrt{3}}{2} a_{hex}^2 \cdot c_{hex} \qquad \text{Eq. 2.18}$$

The atomic packing factor (APF) is the fraction of the volume of a unit cell that is occupied by atoms or ions and it is calculated using the relation [122] :

$$APF = \frac{2\pi \cdot a_{hex}}{3\sqrt{3} \cdot c_{hex}} \qquad \text{Eq. 2.19}$$

2.5.2. Morphological characterization of thin films

Scanning electron microscopy (SEM) emerged around the same time as transmission electron microscopy (TEM), but commercial SEMs took longer to develop. German physicist Max Knoll and Ernst Ruska pioneered early SEM concepts, but the first working SEM was built by Manfred von Ardenne in 1938 [123]. Vladimir Zworykin and colleagues then created an SEM with a 50-nm resolution probe in 1942 [124]. A Cambridge University team led by Professor Charles Oatley [125] advanced the technology, leading to the first commercial SEM (the Cambridge Stereoscan) in 1965. By the 1960s, researchers like Pease [126] improved resolution to 10 nm using a 5-nm beam. Biologists quickly adopted SEMs to study tissues and cells, and by the 1970s, resolution reached 5–6 nm. Innovations like energy-dispersive X-ray

spectroscopy (EDS) for chemical analysis and freeze-fracture techniques expanded SEM's capabilities [127].

The 1980s brought major leaps: field-emission guns (FEGs) from Hitachi and JEOL allowed ultra-high resolution ($< 1\,nm$) and lower-voltage imaging, which materials scientists embraced. In 1986, Cambridge Instruments introduced the first digital SEM, enabling image storage, artifact reduction, and user-friendly software. This made SEM accessible to most scientists via Windows-based systems. Biologists then used FEG SEMs to study cells and tissues at high magnification under low voltages-previously achievable only with TEM [128]. By the 1990s, probe precision and sensitivity improved, letting researchers detect lighter elements (low atomic numbers) more effectively[129].

2.5.2.1. Scanning electron microscopy (SEM)

As illustrated in Figure 2.12, the electron microscopes (SEMs) use a focused electron beam to scan a sample's surface pixel by pixel. As the beam interacts with the sample, it emits particles like secondary electrons, backscattered electrons, and X-rays. Detectors capture these signals, which scientists analyze to study surface features, composition, and structure.

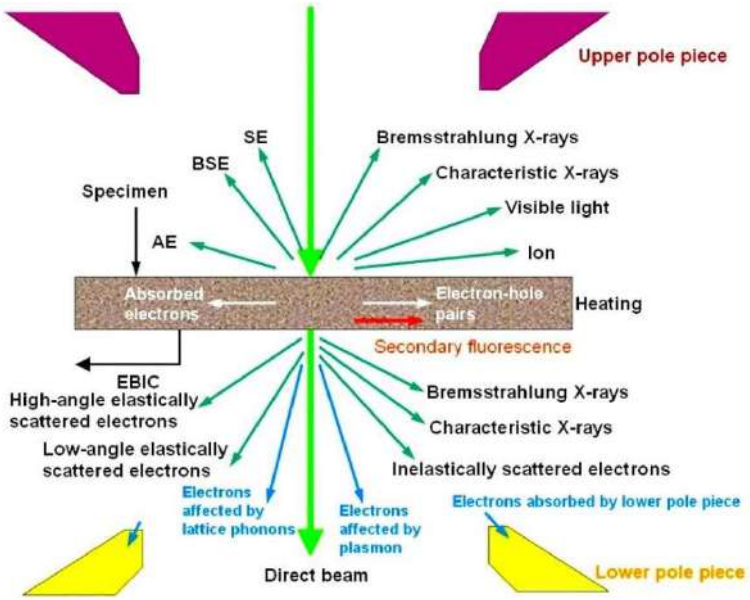

Figure 2.12: Key Products of Electron-Matter Interactions: BSE (Backscattered Electrons), SE (Secondary Electrons), CL (Cathodoluminescence), AE (Auger Electrons), and EBIC (Electron-Beam-Induced Current)[130].

2.5.2.2. Operating principle of the scanning electron microscope (SEM)

In the electron gun, a heated V-shaped tungsten filament emits electrons. A 15 kV voltage between the anode and a metal cylinder (Wehnelt) repels electrons from the filament tip toward

the sample at the anode's base. Electromagnetic lenses and stigmators in the microscope column focus these electrons into a narrow beam aimed at the sample on the specimen stage[129].

Deflector coils near the sample move the beam in two perpendicular directions, scanning the surface in a grid pattern. One coil shifts the beam horizontally, while the other moves it vertically. When the primary electron beam hits the sample, it releases secondary electrons, backscattered electrons, X-rays, Auger electrons, and transmitted electrons.

Secondary electrons come from the top nanometer of the sample's surface, and are collected by a detector with a nearby positively charged grid. Negatively charged secondary electrons are drawn to the grid, pass through it, and hit a scintillator, which converts them into light. This light enters a photomultiplier, amplifying the signal into an electrical pulse used to form an image [129].

The electrical signal from the photomultiplier synchronizes with the beam's scan motion to display the image on a cathode-ray screen, where each sample point corresponds to a bright or dark pixel.

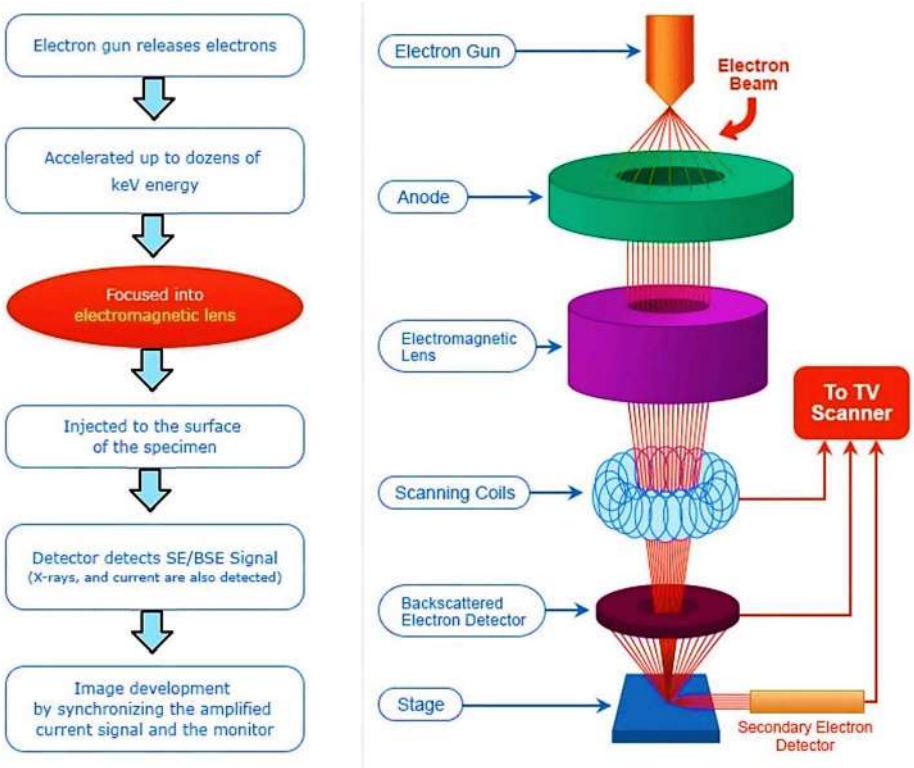

Figure 2.13: Schematic Diagram of Scanning Electron Microscope [131].

The microscope and sample must be in a vacuum, as air molecules would slow electrons and disrupt the beam.

Electron microscopes produce grayscale images; colors are added later using software. X-rays emitted during the scan reveal an element's identity, as their energy depends on the atom's type.

By mapping X-ray signals, scientists create chemical maps of the sample, though with lower resolution (≈3 μm) than surface images[129, 131].

2.5.2.3. Description of the scanning electron microscope (SEM) used

In this study, we analyzed the surface features, microstructure, and quality of thin films using a Quanta 650 FEG field-emission scanning electron microscope (FE-SEM). High-resolution imaging helped us measure grain size, surface roughness, and film uniformity, which we linked to the films' structural and optical properties to assess their quality.

The Quanta 650 FEG operates in high vacuum, low vacuum, and environmental (ESEM) modes, enabling analysis of conductive, non-conductive, and moist samples. Equipped with detectors for secondary electrons, backscattered electrons, and transmitted electrons, it provides detailed imaging and nanoscale analysis. It also includes energy-dispersive X-ray spectroscopy (EDS) for elemental mapping.

This instrument is widely used in materials science and semiconductor research due to its versatility and high-resolution capabilities.

2.5.2.4. Investigation of Surface Topography and Microstructure in Thin Films Using Advanced Imaging Techniques

Scanning electron microscopy (SEM) was central to analyzing the structural and morphological properties of thin films deposited on conventional microscope glass substrates. SEM imaging at magnifications of 20,000×, 50,000×, 100,000×, and 200,000× revealed detailed surface topography, grain structures, and film uniformity. Initial qualitative assessments involved visual inspection of the images to identify surface features, defects, and potential irregularities. For quantitative analysis, Gwyddion 64-bit was used to measure surface roughness, quantify particle dimensions, and conduct statistical analysis of film properties. These data were further refined using OriginPro-2022 , which generated statistical distributions—such as roughness histograms and particle size plots—to validate trends and ensure rigorous interpretation. Together, these methods provided critical insights into the structural quality of the thin films, directly linking their morphology to optical clarity and mechanical durability. This dual approach of visual and computational analysis enabled a comprehensive evaluation of how film composition and substrate interactions influence performance in practical applications.

2.5.3. Optical characterization

Optical methods are widely used to characterize material properties. Compared to electrical methods, they are non-destructive and avoid the challenging process of creating ohmic contacts. Two main categories of optical methods exist:

- Response-based methods: These examine how materials react to light stimuli, such as photoluminescence and cathodoluminescence.
- Property-analysis methods: These measure optical characteristics like transmittance, reflectance, and ellipsometry. These techniques can determine parameters such as the refractive index, material thickness, and band gap [132-134].

2.5.3.1. UV-visible spectroscopy

Spectroscopic techniques using light-matter interactions in the UV-Visible-NIR range (300–2500 nm) have been widely studied, though this region provides limited structural information about compounds compared to advanced methods like NMR or XRD. While UV-Visible spectroscopy (200–800 nm) focuses on electronic transitions (e.g., π→π*, n→π*) and is less dominant for structural analysis, it remains critical for quantitative applications such as concentration measurements via the Beer-Lambert law (as shown in Figure 2.14). The inclusion of wavelengths up to 2500 nm (near-infrared, or NIR) broadens the range but requires clarification, as UV-Visible and NIR are distinct scientifically. Despite its structural limitations, UV-Visible spectroscopy is indispensable for purity assessments, electronic transition studies, and routine quantitative analysis [135-137].

$$T = T_0 \cdot e^{-\alpha \cdot th} \qquad \text{Eq. 2.20}$$

Where α : is the absorption factor and th is the layer thickness.

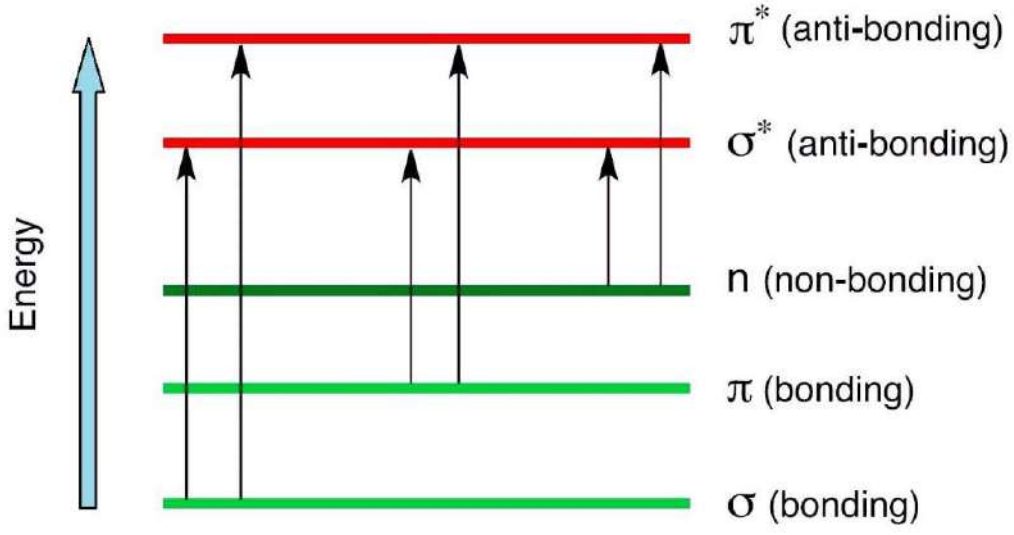

Figure 2.14: Excited-State Electronic Transitions Driven by Visible and UV Light Absorption

We used a Shimadzu UV-1800 double-beam UV-Vis spectrophotometer to measure the optical transmittance spectra of deposited thin films from 200–900 nm (Figure 2.16). This analysis determined key optical properties, including the absorption edge, optical bandgap, and

transparency of the films. Transmittance spectra were analyzed to assess how precursor concentration and the degree of doping influenced the optical behavior of undoped and barium-doped ZnO, NiO, and ZnNiO thin films—critical for optoelectronic device applications.

The spectrum shows how transmittance changes with wavelength. Transmittance (%) is calculated as the ratio of transmitted light intensity to incident light intensity.

These curves enabled film thickness calculations. Key optical properties analyzed include the absorption edge, absorption coefficient, absorbance, and valence bandwidth [133].

Sample transmittance is measured by subtracting reference glass transmittance from sample transmittance. The reference beam passes through a bare glass slide, while the measurement beam passes through the film-on-substrate [138]. (as shown in Figure 2.15)

The calculation and analysis of optical quantities was conducted using SpectraGryph V.1.2 software.

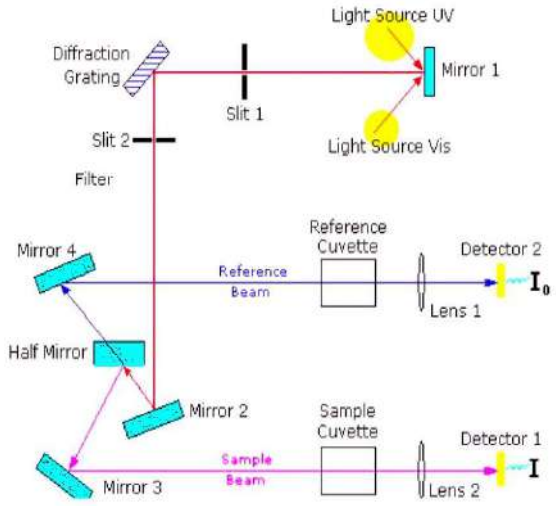

Figure 2.15 : Schematic representation of the UV-VIS-NIR spectrophotometer

Figure 2.16: PC-controlled UV-visible spectrophotometer.

2.5.3.2. Optical parameter measurements

A. Determining the Band Gap Value

The band gap is the minimum energy needed for photons to be absorbed by a semiconductor. Fundamental absorption occurs when electrons jump from the valence to conduction band, creating an abrupt absorption threshold that reveals the band gap.

Using semiconductor absorption theory and assuming parabolic bands, Bardeen's equation links the absorption coefficient to photon energy ($h\nu$), enabling optical band gap calculations for many semiconductors, as shown by the following equation:

$$(\alpha h\nu)^n = A\left(h\nu - E_g\right) \qquad \text{Eq. 2.21}$$

In the given equation, E_g denotes the optical gap energy, A is a constant, and n is equal to $2\ or\ 1/2$, depending on whether the gap transition is direct or indirect.

In the case of a direct gap, such as that observed in ZnO, NiO and ZnNiO (the oxides under consideration here), α is expressed as a function of E_g, according to the following equation:

$$(\alpha h\nu)^2 = A\left(h\nu - E_g\right) \qquad \text{Eq. 2.22}$$

To determine the band gap (E_g), plot $(\alpha h\nu)^2$ versus photon energy ($E = h\nu, in\ eV$). Extrapolate the linear region of $(\alpha h\nu)^2$ to where it intersects the x-axis ($\alpha^2 = 0$). This yields E_g, as shown in Figure 2.17.

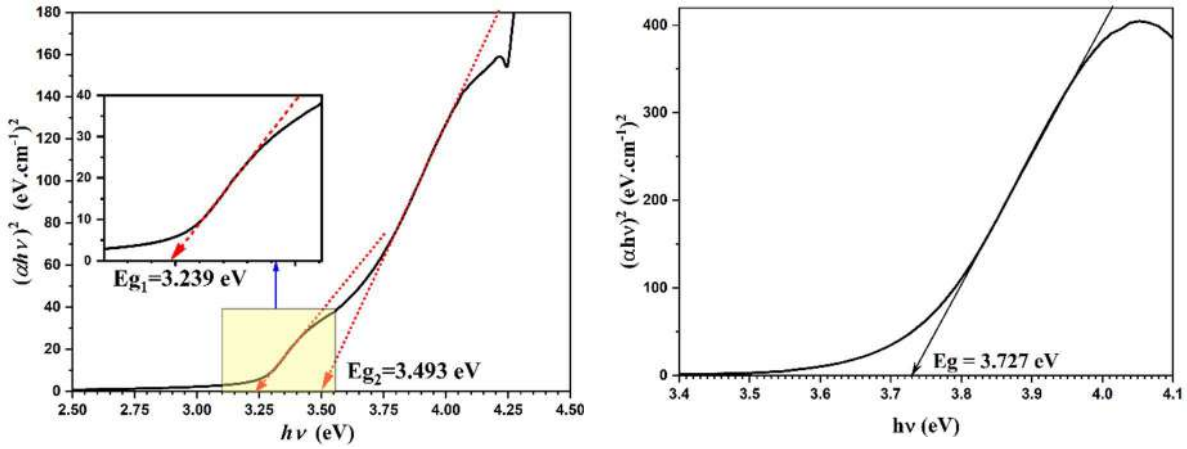

(a) (b)

Figure 2.17: Determination of the energy gap E_g by linear extrapolation from the variation of $(\alpha h\nu)^2$ as a function of hν spectrum energy for a) Ba-doped ZnNiO and b) Ba-dopedNiO thin films.

The method begins by calculating the absorption coefficient (α, in cm^{-1}). For direct-transition semiconductors, plot $(\alpha h\nu)^2 versus\ h\nu$. The linear portion of this curve, when extrapolated to $\alpha^2 = 0$, gives E_g.

B. Urbach disorder energy Calculation

The spray pyrolysis technique (SPT) is a process used for depositing films through pyrolytic reactions. When atoms reach the substrate, they can bond at their point of contact. This often leads to atoms in the film lattice being positioned non-ideal, causing variations in the width of Ba-O bonds. As a result, the band edges defined by E_v and E_c in the crystal lattice may stretch. Localized band-tail states have been detected at the edges of the band gap, particularly in the valence (BV) and conduction (BC) bands. These states exist for energies between $E_c and\ E_v$, and they are considered extended states (Figure 2.18). The width of these tails, known as the Urbach energy, reflects the level of disorder present.

The absorption coefficient (α) can be calculated using the Urbach Tail Equation:

$$\alpha(h\nu) = \alpha_0 exp\left(\frac{h\nu - (E_g - E_u)}{E_u}\right) \quad \text{Eq. 2.23}$$

Where α_0 is a constant, E_g is the bandgap energy, and E_u is the Urbach energy.

We linearize the previous equation by taking the natural logarithm of each side, and we obtain:

$$\ln(\alpha) = \ln(\alpha_0) + \frac{h\nu}{E_u} - \frac{E_g}{E_u} + 1 \quad \text{Eq. 2.24}$$

Rearranged as:

$$\ln(\alpha) = \left(\frac{1}{E_u}\right) h\nu + \text{constant} \quad \text{Eq.2.25}$$

The slope of this line is $\frac{1}{E_u}$, so $E_u = \frac{1}{slope}$.

The plot of the curve and the extension of the straight line are shown in Figure 2.19.

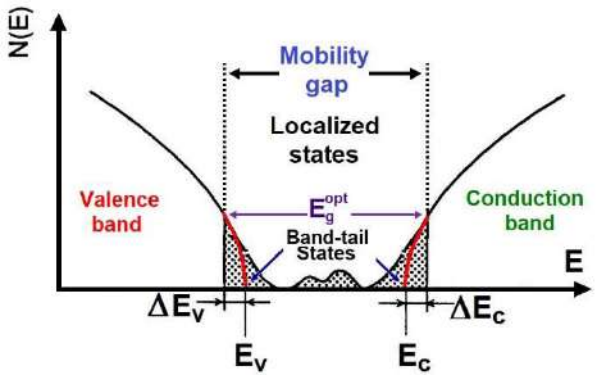

Figure 2.18: Fundamental representation of the density of states in disordered semiconductors, emphasizing the role of localized states and band tails.

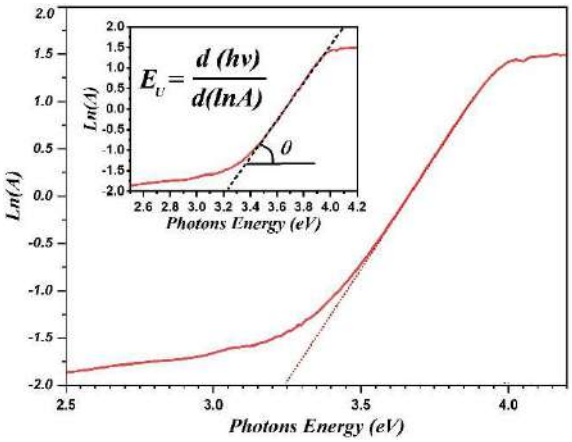

Figure 2.19: Determination of the Urbach disorder energy from the variation of $ln(\alpha)$ as a function of $h\nu$.

C. Refractive Index Calculation

The refractive index n of thin films deposited on transparent microscope glass slides is calculated using the following models: Reddy-Nazeer [136, 139, 140] (Eq. 2.26), Kumar-Singh [140-142] (Eq. 2.27), Moss [140, 142] (Eq. 2.28), Ravindra [3, 140] (Eq. 2.29), and the Herve-Vandamme model [140, 143, 144] (Eq.2.30).

$$n^4(E_g - 0.365) = 154 \quad \text{Eq. 2.26}$$

$$n = kE_g^C \quad \text{Eq. 2.27}$$

Where $k = 3.3668$ *and* $C = -0.32234$

$$n^4 E_g = 95 \quad \text{Eq. 2.28}$$

$$n = 4.084 - 0.62.E_g \quad \text{Eq. 2.29}$$

$$n^2 = 1 + \left(\frac{A}{E_g + B} \right)^2 \quad \text{Eq. 2.30}$$

Where $A \approx 13.6\ eV$ *and* $B \approx 3.47\ eV$

2.5.4. Characterization by Fourier transform infrared spectroscopy (FTIR)

For infrared analysis, we used an Agilent FTIR spectrometer at CRAPC laboratories (Ouargla). This device employs Fourier Transform technology and includes an integrated touchscreen PC with the MicoLab-Touch interface. The interface simplifies measurements, data analysis, and report generation to just three touches.

The MicoLab-Touch software is user-friendly, guiding operators step-by-step through experiments. It can also connect to an external PC for advanced control, offering flexibility for different workflows (as shown in Figure 2.20).

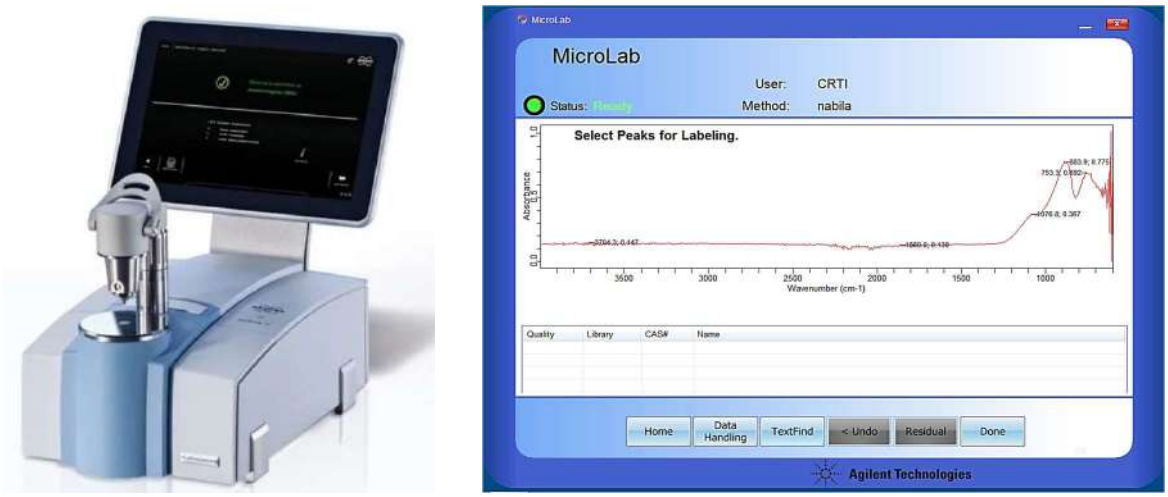

Figure 2.20: FTIR spectrometer and MicoLab-Touch user interface.

2.5.5. Measurement of electrical resistivity: The 4-probe method

The four-point probe technique (which is distinct from the Van der Pauw technique) quantitatively assesses the resistivity of thin film materials. In order to implement this method, one must position four probes at a significant distance from the peripheries of the sample and ensure their alignment in a linear configuration[145, 146].

A current source transmits a predetermined current between probes 1 and 4. Concurrently, a voltmeter quantifies the voltage differential between probes 2 and 3. The resistance exhibited between probes 2 and 3 is derived by dividing the measured voltage by the applied current.

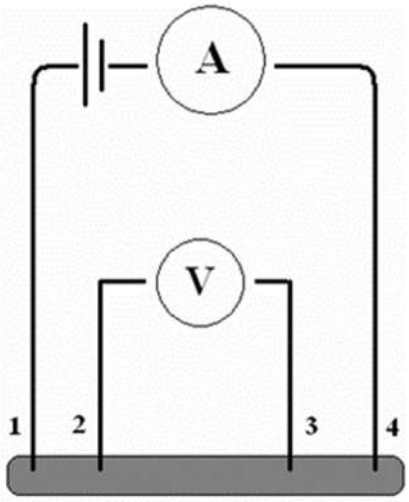

Figure 2.21: The four-probe method.

As demonstrated in Figure 2.21, the application of current (I) between outer probes (1 and 4) can be utilized to calculate the resistivity (ρ) and conductivity (σ) of the film through the measurement of voltage (V) between inner probes (2 and 3). This calculation is performed using the following equation [147-149]:

$$\rho = \frac{1}{\sigma} = \frac{\pi}{\ln 2} \cdot th \cdot \frac{V}{I} = 4.53236 \cdot th \cdot \frac{V}{I} \qquad \text{Eq. 2.31}$$

Where (th) is the film thickness.

In the present work, the electrical properties of the films were measured using a coplanar configuration with four gold electrodes deposited on the film surface. A Keithley 2400 low-voltage source meter was employed to measure the current-voltage (I-V) characteristics and determine the electrical conductivity of the films.

Chapter-3 Discussion and interpretation of results for Ba-doped NiO thin films

Chapter-3
Discussion and interpretation of results for Ba-doped NiO thin films

3.1. Introduction

Nickel oxide (NiO) is a versatile transition metal oxide. It serves critical roles in optoelectronics, catalysis, and energy storage. These applications rely on the material's unique optical, electrical, and magnetic properties. Consequently, fabricating high-quality NiO thin films is essential for advanced technology. Chemical deposition offers significant scalability and cost-effectiveness.

This chapter utilizes the spray pyrolysis technique (SPT) to deposit NiO films. SPT is a widely adopted chemical method for preparing metal oxides. The process involves atomizing a precursor solution into fine droplets. These droplets are sprayed onto a heated substrate. Upon contact, thermal decomposition occurs immediately. Hydrolysis and pyrolysis reactions then form a continuous solid film. Researchers favor SPT for its simplicity and efficiency.

Controlling deposition parameters is vital for film quality. Variables such as substrate temperature, precursor concentration, and spray rate dictate outcomes. Adjusting these factors allows precise control over thickness and morphology. For example, substrate temperature directly influences crystallinity and grain size. Similarly, precursor composition affects the optical bandgap and transparency. Optimizing these parameters ensures specific performance standards.

Here, we detail the elaboration of NiO thin films on glass substrates. The discussion includes underlying chemical reactions and specific deposition mechanisms. We also examine the characterization techniques used to evaluate the films. X-ray diffraction (XRD) analyzes the crystallographic structure. Scanning electron microscopy (SEM) reveals surface morphology. UV-Vis spectroscopy measures optical behavior. Together, these methods provide a comprehensive understanding of the material. This analysis supports the development of efficient NiO-based devices.

3.2. Characterization of undoped of NiO thin films

3.2.1. Structural properties

Figure 3.1 shows the XRD diffractograms of NiO thin films deposited on a glass substrate at 450°C. X-ray diffraction was used to study the crystal structure of the films as a function of

the molar concentration of the precursor solutions (0.05 to 0.35 mole/L). The most intense diffraction peaks, indexed to the (111), (200), and (220) planes, appear at Bragg angles 2θ in the ranges of 36.57°–37.18°, 42.64°–42.95°, and 61.13°–62.09°, respectively. Weaker secondary peaks, corresponding to the (311) and (222) planes, are also observed at 2θ angles of 73.85°–74.71° and 77.55°–81.40°. The analysis reveals that the NiO films exhibit a polycrystalline nature with a face-centered cubic (FCC) structure, specifically the $Fm\bar{3}m$ space group (number 225). This identification is consistent with the ICDD standard reference pattern 00-047-1049.

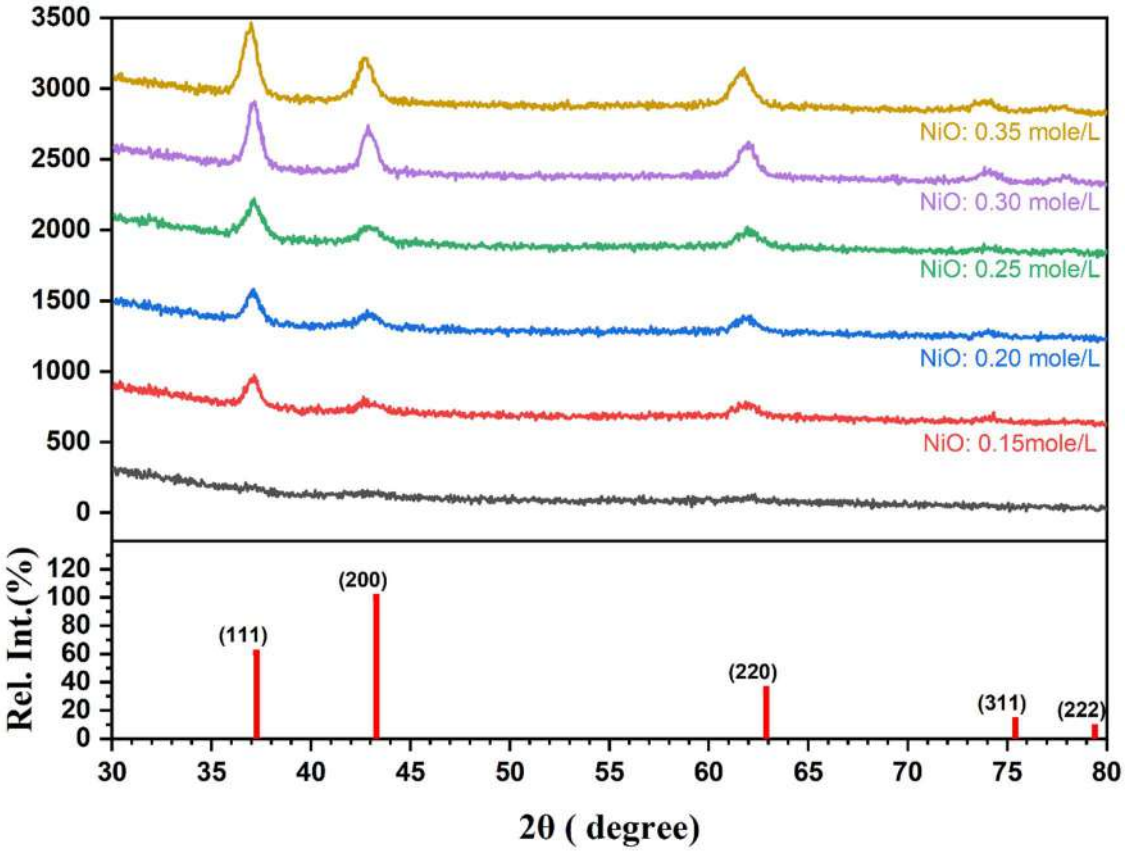

Figure 3.1: XRD diffractograms of NiO thin films deposited on glass substrate at different precursor molarities.

The intensity of the diffraction peaks varies with the molar concentration of the precursor, reaching a maximum at a concentration of 0.10 mole/L, indicating improved crystallinity at this concentration [150]. The crystallite size was estimated using the Debye-Scherrer formula, while other structural parameters, such as lattice constants, mean strain, dislocation density, and crystallite size, were calculated using appropriate equations and are summarized in **Table 3.1.** The obtained lattice parameter values are slightly larger than that of standard NiO (a_o = 4.177 Å), suggesting the presence of internal strain, crystal defects, or impurities in the films. These

observations are consistent with results reported in the literature [55, 151]. The mean strain, which is compressive in nature, is represented by its absolute value in Figure 3.6 for clearer interpretation. These analyses highlight the influence of deposition conditions on the structural properties of the NiO films.

Figure 3.2 presents an XRD diffractogram of NiO nanoparticles synthesized at a precursor concentration of 0.35 mole/L, accompanied by an inset zoomed-in view of the peak positions. The primary XRD spectrum plots the relative intensity of diffracted X-rays against the diffraction angle 2θ, covering a range of approximately 30° to 80°. Distinct peaks are observed, indicating the presence of crystalline phases in the NiO sample. These peaks are characteristic of a well-defined crystal structure. Above the peaks, schematic structural models of the NiO crystal.

The inset provides a detailed, zoomed-in view of the peak positions, represented as a stick diagram. This format simplifies the identification of peak locations and their corresponding Miller indices: (111), (200), (220), (311), and (222).

The distinct peaks in the XRD diffractogram confirm the crystalline nature of the NiO nanoparticles. The Miller indices (111), (200), (220), (311), and (222) are consistent with a face-centered cubic (FCC) structure, matching the known Bunsenite phase of NiO (JCPDS No. 00-047-1049). The 2θ values of the peaks can be used to calculate the lattice parameters of the NiO crystal, providing information about the unit cell dimensions. Slight deviations from standard values may indicate internal strain or defects [55, 151].

The width of the peaks is inversely related to the crystallite size, as described by the Scherrer equation. The relatively sharp peaks in this pattern suggest that the NiO nanoparticles are well crystallized, with minimal size-related broadening. The relative intensities of the peaks can reveal information about the preferred orientation of the crystallites. Deviations from the standard powder diffraction pattern may indicate texturing or anisotropic growth during synthesis. The inset structural models are instrumental in correlating the observed diffraction peaks with specific atomic planes in the NiO lattice. This visualization aids in understanding how the crystal structure contributes to the diffraction pattern.

The **table 3.1** provides a detailed analysis of the relationship between precursor molarity and crystallographic parameters, including Bragg angle, full width at half maximum (FWHM), interplanar spacing (d_{hkl}), lattice constant (a_{hkl}), crystallite size (D_{hkl}), dislocation density (δ), and microstrain (ε). As the precursor molarity increases from 0.10 to 0.35 mole/L, the Bragg

angle for the (111) plane shifts slightly from 36.572° to 37.182°, indicating subtle changes in the crystallographic orientation. This shift may be attributed to variations in lattice strain or defects introduced during the synthesis process. The full width at half maximum (FWHM) values, which reflect the broadening of diffraction peaks, generally increase with higher molarity, suggesting a reduction in crystallite size or an increase in microstrain within the crystal lattice. This observation is consistent with the Debye-Scherrer equation, which establishes a correlation between peak broadening and reduced crystallite size, as well as elevated defect densities [110].

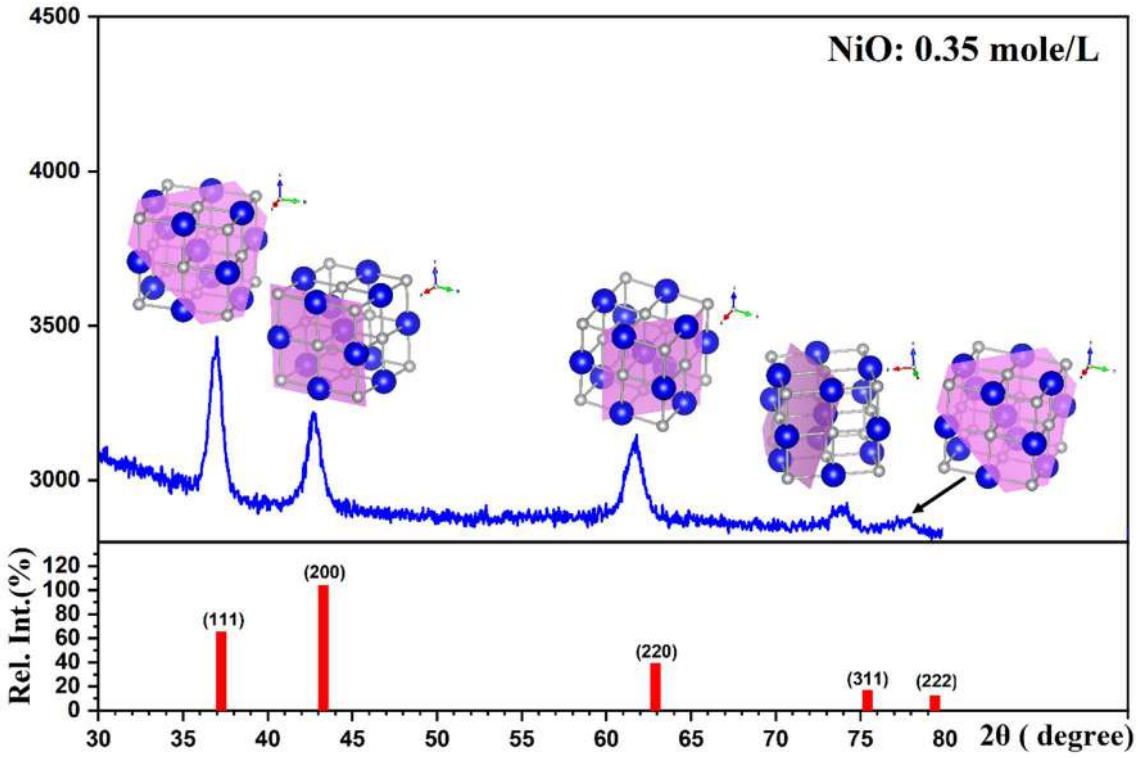

Figure 3.2: XRD diffractogram of an undoped NiO thin film deposited on a glass substrate for a precursor molarity of 0.35 mole/L.

Furthermore, a slight decrease in the interplanar spacing (d_{hkl}) from 2.4550 Å to 2.4162 Å is observed with increasing molarity, suggesting potential modifications in the lattice parameters. These variations may be attributed to internal strain, defects, or impurities, as evidenced by the calculated lattice constants (a_{hkl}), which range from 4.1850 Å to 4.2523 Å. These values are slightly larger than the standard lattice parameter for NiO ($a_0 = 4.177$ Å, JCPDS No. 00-047-1049), further confirming the presence of lattice distortions. Furthermore, a substantial decrease in crystallite size (D_{hkl}) from 72.01 nm to 13.01 nm has been observed as the molarity increases, accompanied by a concomitant rise in dislocation density (δ) and microstrain (ε). These observations indicate that elevated precursor concentrations favor the formation of smaller crystallites with higher defect densities. Consequently, the mechanical,

optical, and electronic properties of the material may be influenced by these changes in crystallite size and defect density.

The observed increase in microstrain (ε) and dislocation density (δ) with higher molarity emphasizes the role of precursor concentration in controlling the structural properties of NiO thin films. For instance, Al-Hada NM et al., Toma FTZ et al. and Wang et al. [152-154] demonstrated that higher precursor concentrations can enhance defect densities, significantly impacting the electronic and optical characteristics of nanomaterials. In a similar manner, Selim MM et al. and Kim et al. [155, 156] found that variations in precursor molarity during the synthesis of metal oxides lead to changes in particle size distribution and surface area, which are critical for catalytic applications. Additionally, Zhang Z. et al., and Zhang B. and Zhang Y. [157, 158] reported a strong correlation between increased defect density and mechanical weakening in crystalline materials, emphasizing the importance of optimizing synthesis conditions to achieve desired functional properties. Furthermore, Pecharsky and Zavalij, and Yoshio W.E.M. and Kozo Shinoda [159, 160] discussed how peak broadening in XRD patterns can be attributed to both crystallite size reduction and lattice strain, providing a theoretical foundation for interpreting the observed trends in full width at half maximum (FWHM) and microstrain.

In summary, the data underscores the critical influence of precursor molarity on the structural and functional properties of NiO thin films. By regulating the precursor concentration, researchers can precisely manipulate crystallite size, defect density, and lattice strain, thereby enabling the design of materials with customized properties for applications in catalysis, sensors, and energy storage. These findings are consistent with established principles in materials science and are supported by recent studies exploring the effects of synthesis parameters on material performance.

Table 3.1: Structural parameters of undoped NiO thin films at different precursor molarities.

Precursor molarity	Bragg Angle	FWHM	d_{hkl}	a_{hkl}	D_{hkl}	$\delta \times 10^{15}$	ε
[mole/L]	[2θ°]	[2θ°]	[Å]	[Å]	[nm]	[line/m^2]	[%]
0.10	36.572	0.1162	2.4550	4.2523	72.01	0.192	0.0276
0.15	37.134	0.5747	2.4192	4.1902	14.58	4.702	0.1362
0.20	37.034	0.4581	2.42545	4.2011	18.29	2.990	0.1086
0.25	37.100	0.5749	2.4215	4.1939	14.58	4.710	0.1363
0.30	37.182	0.6441	2.4162	4.1850	13.01	5.906	0.1526
0.35	36.990	0.6117	2.4283	4.2059	13.70	5.332	0.1450

As illustrated in Figure 3.3, the impact of precursor molarity on the structural properties of undoped NiO thin films reveals a multifaceted interplay between synthesis conditions and material properties. As the precursor molarity increases, the initial observation is a decrease in the lattice parameter (a_{hkl}), which suggests a potential contraction of the lattice due to increased incorporation of oxygen vacancies or stress induced by the growth process. The deviation between the measured values of the lattice constant for the prepared NiO films and the mean value indicates the presence of deformation in the films. The source of this deformation is related to the film grain size, which is contingent on the film deposition conditions [161]. However, at higher precursor molarities, beyond 0.2 mole/L, (a_{hkl}) exhibits an upward trend, suggesting potential relaxation of the lattice or a shift in the growth mechanism.

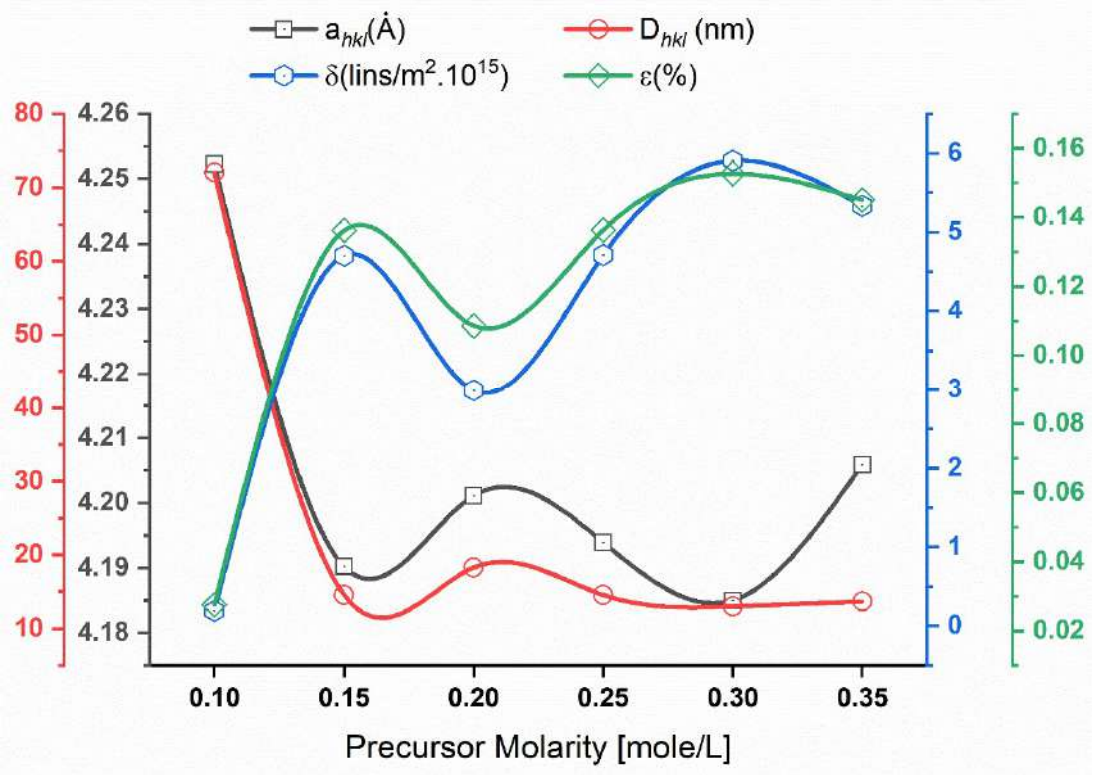

Figure 3.3: Variation in crystallite size, mean strain, lattice parameter, and dislocation density of undoped NiO thin films as a function of precursor molarity.

The crystallite size (D_{hkl}) displays an initial sharp decrease, followed by a subsequent gradual increase, suggesting that higher precursor concentrations may initially impede crystal growth but subsequently promote it, potentially due to enhanced surface diffusion or reduced nucleation density. The dislocation density (δ) mirrors this trend, indicating that the defect concentration is inversely related to crystallite size. Conversely, the mean strain (ε) displays an initial increase followed by a decrease, signifying that the films experience increasing stress

with higher precursor molarity up to a certain point, after which stress relaxation mechanisms become dominant. This behavior could be attributed to variations in the film growth rate, stoichiometry, and defect formation, which are all influenced by precursor concentration.

It can also be seen that the film with the best structural properties has the lowest average strain value, which has an effect on the degree of crystallization[162].

This phenomenon is analogous to observations made in other metal oxide thin films, where precursor concentration exerts a substantial influence on the microstructure and defect chemistry [163-167]. The observed variations in these parameters are crucial for tailoring the properties of NiO thin films for specific applications, as they directly influence the material's electronic, optical, and catalytic behavior.

3.2.2. Morphological properties of undoped NiO thin films

The scanning electron microscopy (SEM) image (presented in Figure 3.4) depicting the surface of an undoped nickel oxide (NiO) thin film reveals a network of nanoscale cracks, presumably resulting from tensile stresses encountered during fabrication processes, such as drying or annealing [168-170]. These cracks, discernible at a magnification of 200,000×, exist within the nanoscale dimensions and may significantly influence the film's physical characteristics, including its electrical conductivity and mechanical stability. The microstructural analysis of the film indicates a non-homogeneous distribution, with the cracks potentially attributed to discrepancies in thermal expansion between the film and its supporting substrate [171-174]. Such non-uniformity may adversely affect the operational efficacy of the film in practical applications, such as gas sensing and catalysis, where factors like surface area and structural integrity are paramount [175-177]. While the presence of cracks might augment the surface area, it simultaneously poses a risk to the film's stability and its long-term operational reliability.

In the context of thin films, cracks generally affect surface roughness, thus modifying optical and electrical characteristics, which could render the material less favorable for applications necessitating high integrity, such as sensors or photovoltaic cells [178-181]. The extent to which cracks influence the film is contingent upon their dimensions, distribution, and the degree to which they disrupt the film's continuity [182-185]. Effective management of deposition and subsequent processing techniques is essential for minimizing these defects and ensuring the optimal performance of the film [153, 186-188].

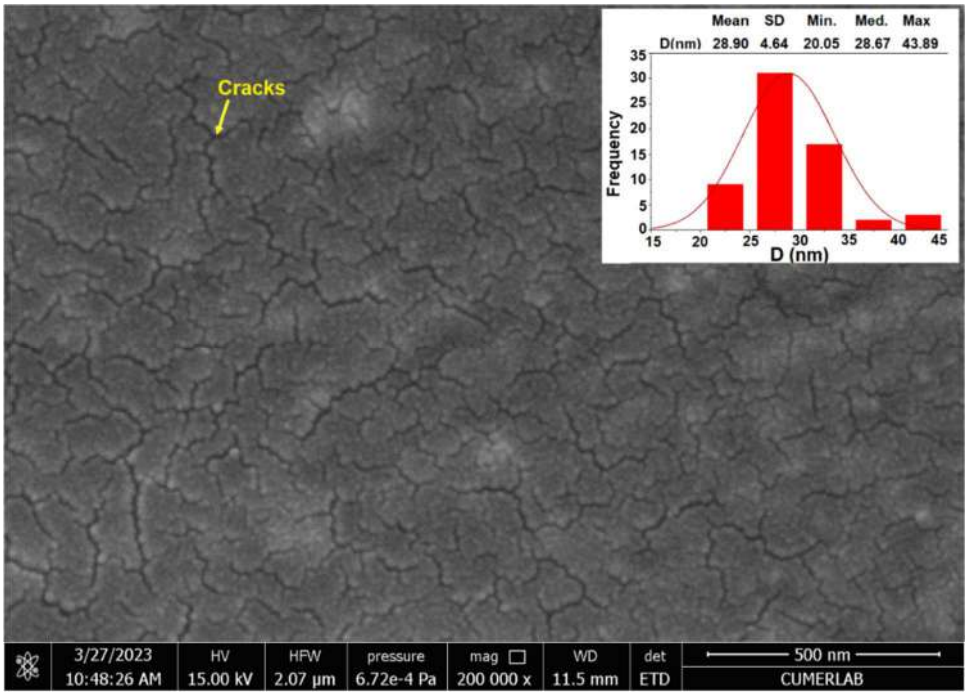

Figure 3.4. SEM image of undoped NiO thin films prepared using the spray pyrolysis technique at 450°C.

The inset in (Figure 3.4.) shows the grain size distribution of an undoped NiO thin film, displayed as a histogram with a Gaussian fit. The mean grain size is 28.9 nm (SD = 4.64 nm), with a range of 20.05–43.89 nm. The median (28.67 nm) closely matches the mean, indicating minimal skew despite slight asymmetry. The distribution peaks near 30 nm, aligning with the mean, but has a longer tail toward larger grains. This suggests most grains cluster around the mean, with fewer larger grains. The narrow standard deviation implies moderate uniformity, beneficial for consistent material properties[189, 190]. However, the tail indicates some larger grains, which may introduce defects affecting electrical and optical performance [191-194]. Grain size influences catalytic and gas-sensing properties, with smaller grains enhancing surface area [195-197]. The distribution's shape likely results from deposition conditions like temperature and annealing [198-200]. Controlled synthesis methods, such as sputtering, may explain the uniform grain growth [201], optimizing performance for applications like sensors and photovoltaics ([202-206].

Figure 3.5 shows the scanning electron microscopy (SEM) image of an undoped nickel oxide (NiO) thin film. The surface displays a granular morphology. Irregular, raised features appear uniformly across the scanned region. This texture suggests a polycrystalline structure. These findings match previous studies on NiO films synthesized via chemical bath deposition [15, 207]. Height variations reach approximately 53.96 nm. This indicates substantial surface roughness. Nucleation and growth dynamics during deposition likely influence this roughness [8]. Grain

size and uniformity critically determine the film's functional properties. Therefore, quantitative particle size distribution analysis provides deeper microstructural insights [208].

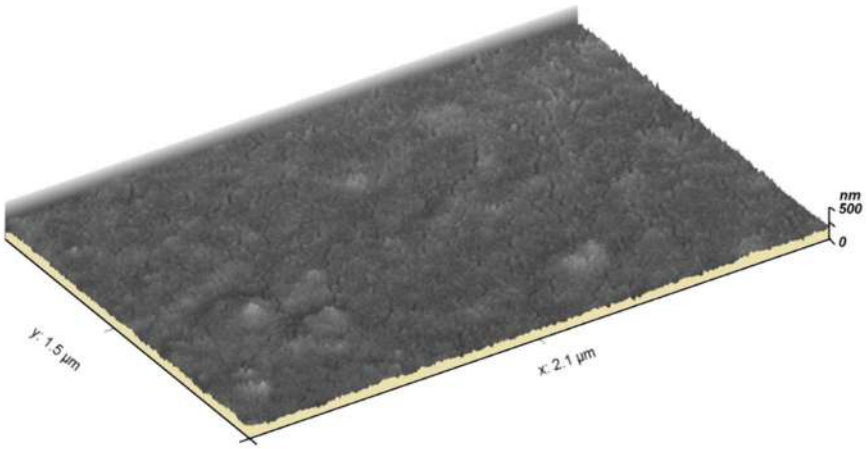

Figure 3.5: Three-dimensional scanning electron microscopy image of the topographical representation of undoped NiO thin film prepared using SPT at 450°C.

The surface roughness of NiO films has been shown to directly affect their catalytic and electrochemical performance, as increased surface area enhances active sites for reactions-a key factor in applications such as supercapacitors [209-211]. The deposition technique (e.g., magnetron sputtering, chemical vapor deposition) exerts a substantial influence on the morphology of the resultant films. For instance, sputtered NiO films frequently exhibit controlled grain growth, a phenomenon attributable to the adjustable plasma parameters [74].

The output of the surface roughness analysis curves is shown in Figure 3.10. The SEM analysis of the undoped NiO thin film reveals a surface characterized by a moderate roughness, as indicated by the roughness average (Ra) of 23.26 nm and a root mean square roughness (Rq) of 29.86 nm. These values suggest a textured surface, which can significantly influence the film's physical and chemical properties. The relatively low maximum height of the roughness (Rt = 0.226 µm) and maximum peak to valley roughness (Ry = 0.224 µm) alongside a low skewness (Rsk = -0.143) indicates a somewhat symmetrical distribution of peaks and valleys, though slightly skewed towards valleys. The kurtosis (Rku = 3.55) suggests a leptokurtic distribution, indicating the presence of sharp peaks and valleys. The spatial parameters, such as the mean spacing of profile irregularities (Sm = 10.31 nm) and average wavelength ($\lambda_a = 10.30nm$), provide insights into the lateral dimensions of the surface features. The hybrid parameters, including the average absolute slope ($\Delta a = 14.20\mu m^{-1}$) and RMS slope ($\Delta q = 18.48\mu m^{-1}$), quantify the steepness of the surface irregularities. Such roughness characteristics are crucial in determining the film's performance in various applications, including catalysis,

sensing, and electronic devices. Surface roughness significantly influences contact area, adhesion, and reactivity, which are essential considerations in these fields. For instance, increased roughness can enhance the surface area available for catalytic reactions or improve the sensitivity of gas sensors [202, 212, 213].

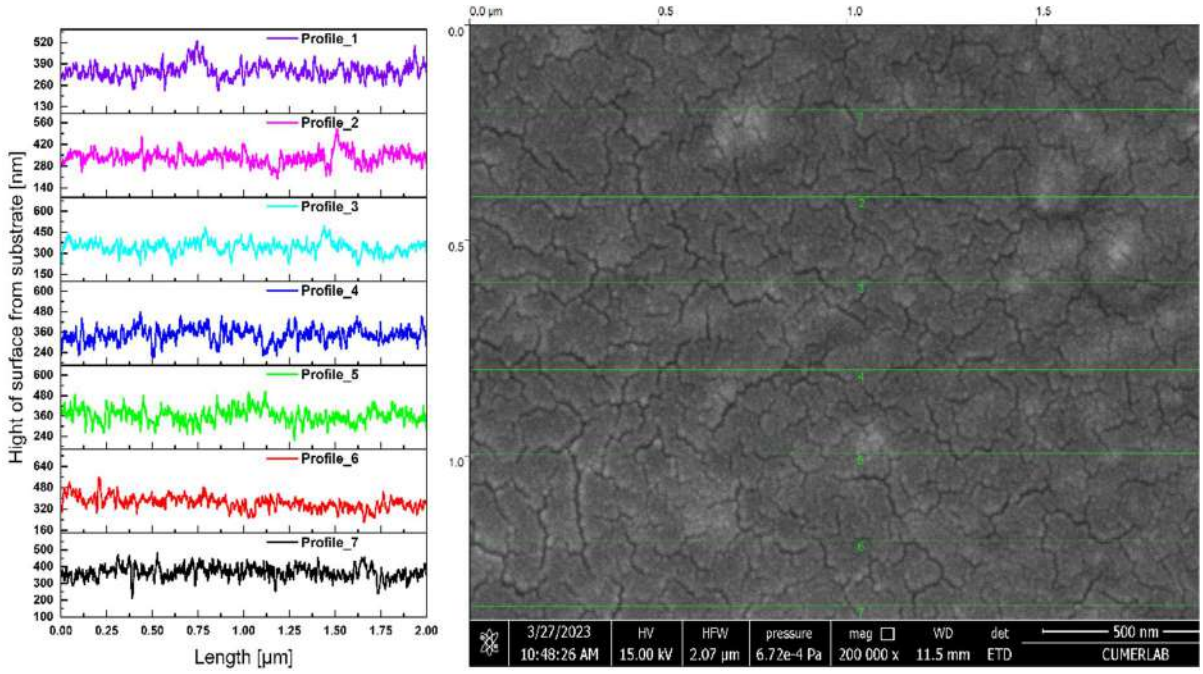

Figure 3.6: Profile curves measured along the lines shown on the SEM image of undoped NiO thin films prepared by the spray pyrolysis technique at 450°C.

3.2.3. Optical properties of undoped NiO thin films

As illustrated in Figure 3.7, the transmission spectra of undoped NiO thin films deposited at 450°C on microscope glass substrates are presented.

The transmission spectra of undoped NiO thin films for various precursor molarities exhibit clear variations in optical behavior as a function of concentration. Specifically, as the precursor molarity increases from 0.05 mole/L to 0.40 mole/L, there is a general decrease in transmission across the measured wavelength range of 300 to 950 nm. This observation indicates that increasing the precursor concentration results in the formation of thicker or more optically absorbing films, thereby limiting light transmission. Conversely, at lower precursor concentrations, such as 0.05 mole/L, the transmission is higher, suggesting a relatively thinner or more transparent film. The spectra manifest a pronounced increase in transmission within the UV region (approximately 350 nanometers), which becomes more accentuated as the molarity rises, thereby suggesting that the film's band gap may be influenced by the precursor concentration [214-217]. This phenomenon is consistent with the established relationship between increased molarity and enhanced film thickness or crystallinity, both of which have

been demonstrated to influence optical properties such as transparency and light absorption [218, 219]. The decrease in transmission at longer wavelengths (above 600 nm) for higher molarities indicates increased light scattering or absorption, possibly due to increased film density or defect formation [220-222]. These observations are of critical importance for tailoring NiO thin films for specific applications, such as transparent conductive oxides or optical coatings, where controlled optical properties are essential [223-227].

Figure 3.8 presents Tauc's plots of $(\alpha hv)^2$ versus the photon energy hv for undoped NiO thin films with varying precursor molarities, ranging from 0.05 mole/L to 0.40 mole/L. The plots exhibit a discernible linear region in the high-energy domain, from which the optical band gap (E_g) of the films can be ascertained. As the precursor molarity increases, the onset of absorption shifts slightly, indicating a change in the electronic structure of the films. The calculated optical bandgaps from these plots demonstrate that films with higher precursor concentrations generally exhibit lower band gaps compared to those with lower molarity. This observation suggests that increasing the precursor concentration could result in films with enhanced crystallinity or thickness, which in turn may affect the electronic structure and the degree of disorder[218]. This, in the case of the optical transitions, could be affected by the increase in precursor concentration [55, 220, 228, 229].

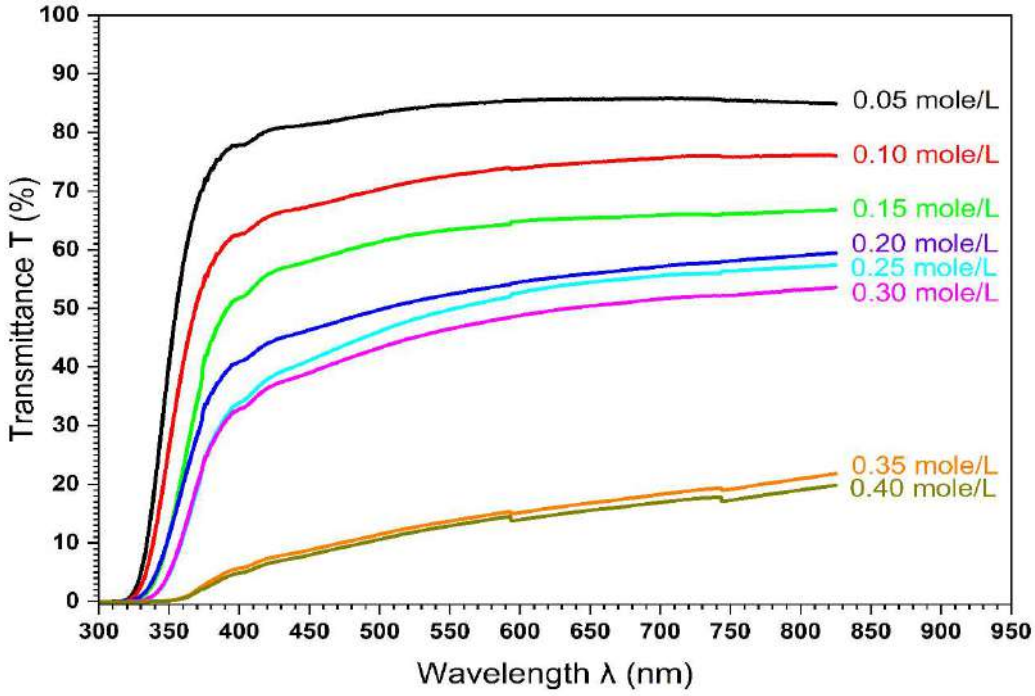

Figure 3.7: Transmission spectra of undoped NiO thin film samples for different precursor molarities.

The presence of a well-defined linear region at higher energies indicates that the films retain a direct bandgap, which is characteristic of semiconducting materials like NiO [230-232]. The

changes in band gap values are important for tailoring the films for various applications, such as gas sensing and catalysis, where optical properties play a critical role in performance [233-235]. The molarity-dependent behavior further underscores the importance of controlling the deposition parameters to optimize the material's properties for specific device applications. The band gap and Urbach disorder energy values were given in Table 3.4.

Table 3.2: Optical energy bandgap and Urbach energy of undoped NiO thin film samples for varying precursor molarities.

Molality mole/L	Optical energy bandgap Eg [eV]	Urbach energy disorder Eu [meV]
0.05	3.799	184.649
0.10	3.784	220.622
0.15	3.742	262.977
0.20	3.738	289.546
0.25	3.682	302.703
0.30	3.672	306.084
0.35	3.585	408.073
0.40	3.452	415.540

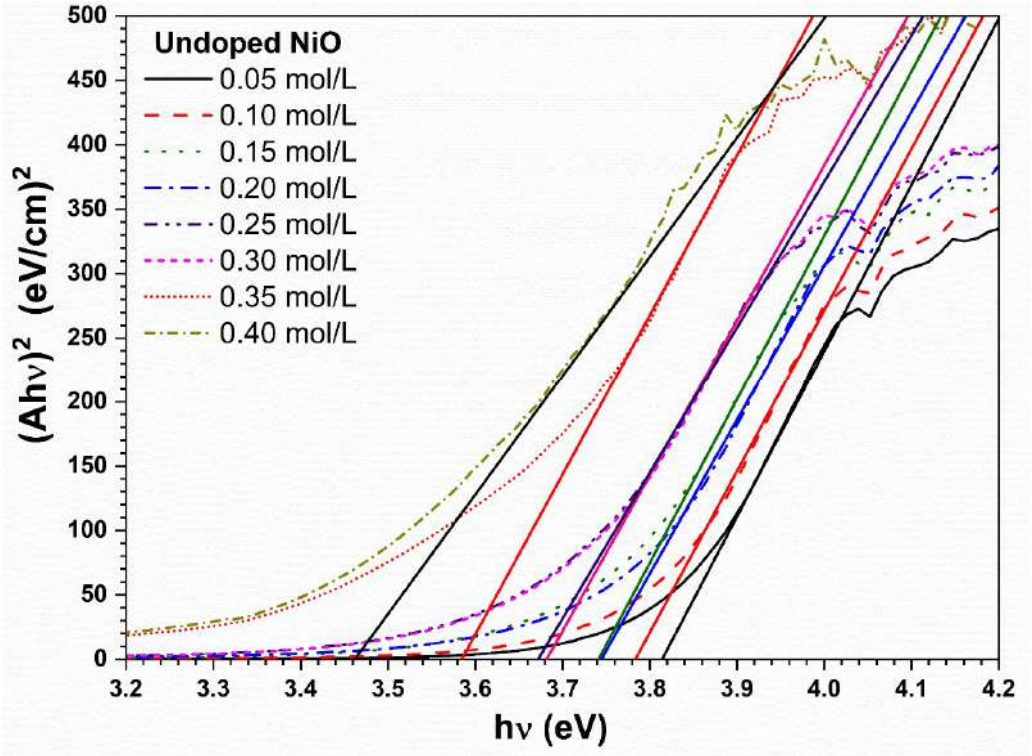

Figure 3.8: Plot of $(\alpha h\nu)^2$ versus incident photon energy $(h\nu)$ of undoped NiO thin films at different precursor molarities.

Figure 3.9 shows the variation of optical bandgap energy (E_g) and Urbach energy (E_u) in undoped NiO thin films as a function of precursor concentration (0.05–0.40 mole/L). As

concentration increases, E_g decreases systematically from ~3.85 eV to ~3.40 eV, indicating bandgap narrowing. This trend suggests increased electronic disorder, likely due to defect states introduced at higher precursor concentrations [236-238]. Concurrently, E_u measure of structural disorder rises with concentration, reinforcing the correlation between defect density and optical properties [53, 204, 220].

The reduction in E_g aligns with the Urbach tail broadening, as higher E_u values reflect greater lattice distortions and localized states within the bandgap [239, 240]. This behavior is characteristic of solution-processed oxides, where precursor chemistry influences crystallinity and defect formation [241]. The data imply that excessive precursor concentrations (>0.40 mole/L) may degrade film quality by amplifying disorder, as evidenced by the steep E_g and E_u trends.

These findings highlight the trade-off between optical tunability and structural integrity in NiO films. For optoelectronic applications, intermediate concentrations (~0.20–0.30 mole/L) might balance bandgap engineering with minimal disorder-induced losses [13, 242].

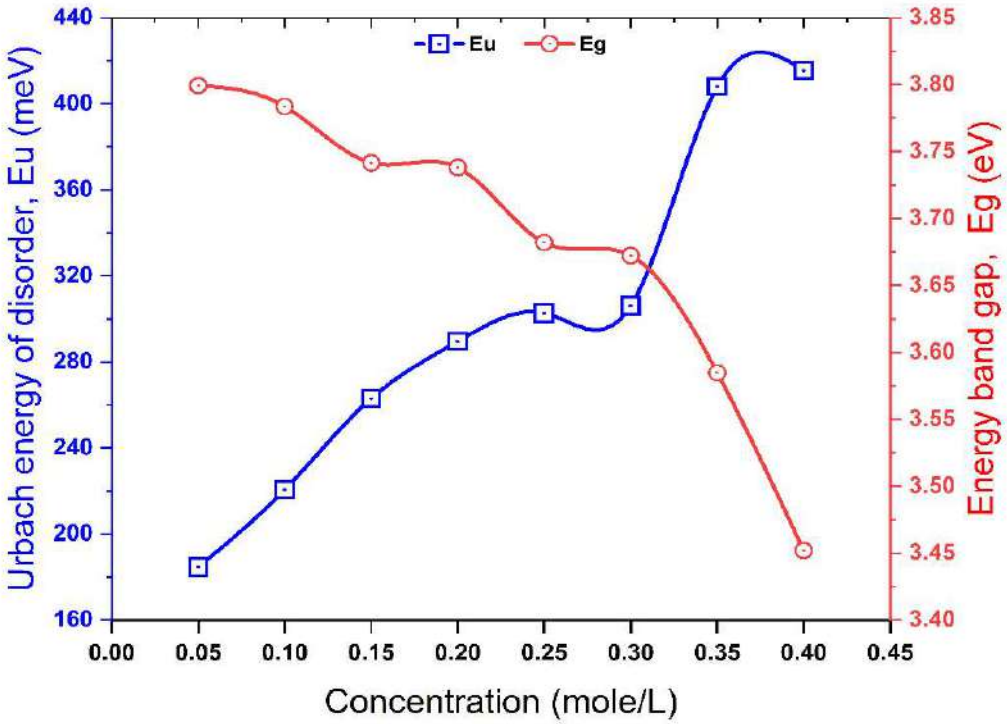

Figure 3.9: The variation of Urbach energy and band gap energy of undoped NiO thin films as a function of precursor molarity.

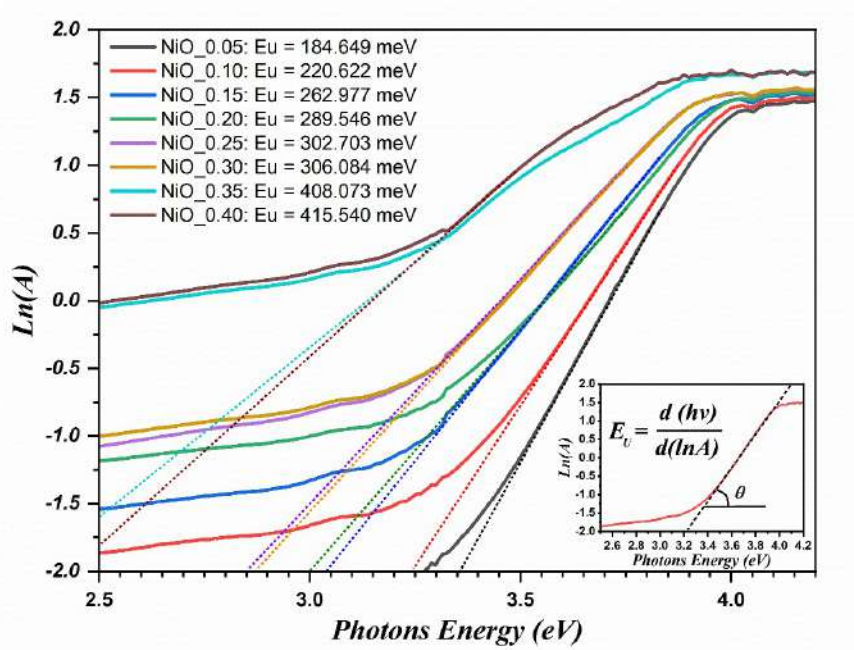

Figure 3.10: Plot of $Ln(A)$ versus incident photon energy $(h\nu)$ of undoped NiO thin films at different precursor molarities.

Figure 3.11 illustrates the evolution of the refractive index (n) and Urbach energy (E_u) in undoped NiO thin films as a function of precursor concentration (0.05–0.40 mole/L). As the precursor concentration increases, the refractive index (n) experiences a monotonic rise from approximately 2.14 to 2.24, indicating an enhancement in optical density due to improved film compactness or increased polarizability at higher precursor loadings [243, 244]. Concurrently, E_u experiences a proportional increase from ~160 meV to ~440 meV, indicating an enhancement in structural disorder and defect-induced band-tail states [239].

Key Observations:

- **Refractive Index Trend:** The rise in n suggests denser packing or reduced porosity at higher concentrations, consistent with solution-processed films where precursor availability promotes complete condensation reactions [241].
- **Urbach Energy Correlation:** The increase in E_u mirrors the rise in n, implying that defect formation (e.g., nickel vacancies or interstitial oxygen) accompanies densification. This observation aligns with the Urbach rule, which states that disorder broadens the absorption edge [13, 239, 240, 245].
- **Competing Effects:** While higher concentrations have been shown to improve optical density, which is beneficial for photonic devices, the associated disorder (high E_u) may degrade charge transport, necessitating a trade-off [11, 246].

Interpretation:

The data suggest that precursor concentration tunes both optical and structural properties. Specifically, precursor concentrations ranging from approximately 0.20 to 0.25 mole/L appear to optimize the balance between a moderate n (~2.18) and acceptable disorder (E_u~280 meV). The strong E_u-concentration dependence underscores the necessity for post-deposition annealing or doping to mitigate defects in films grown at high concentrations.

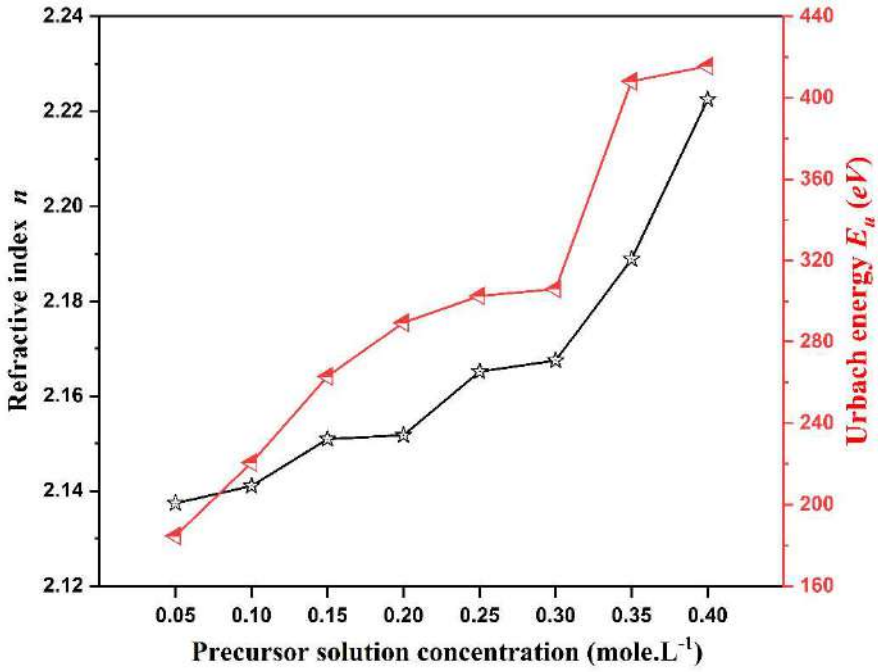

*

Figure 3.11: The variation of Urbach energy and refractive index (n) of undoped NiO thin films as a function of precursor molarity.

The optical bandgap (E_g) of undoped NiO thin films decreases systematically from 3.799 eV to 3.452 eV as the precursor molality increases from 0.05 to 0.40 mole/L, indicating a reduction in the insulating character due to defect-induced bandgap narrowing [236-238]. The experimental refractive index (n_{exp}) increases correspondingly from 2.4527 to 2.5510, suggesting a rise in optical density with higher molality. Theoretical models predict this trend but exhibit varying degrees of agreement with experimental data. The Reddy-Nazeer [139] and Kumar-Singh [141] relations overestimate n across all concentrations, while the Moss model [142] and Ravindra [3] formulas yield closer but still imperfect matches. Notably, the Herve-Vandamme model [144]provides the best alignment with n_{exp} particularly at higher molalities (e.g., 2.2046 vs. 2.5510 at 0.40 mole/L), likely due to its incorporation of both bandgap and electronic polarizability effects. The discrepancies among models highlight the limitations of purely empirical approaches in capturing defect-mediated optical responses. These results underscore the need for refined theoretical frameworks that account for structural disorder in solution-processed NiO films [140, 247-249].

Table 3.3: The optical bandgap and refractive index of undoped NiO thin films have been computed for various precursor molarities through different analytical approaches.

Molality	Optical energy bandgap	Refractive index (n)					
			Reddy-Nazeer[139]	Kumar-Singh[141]	Moss[142]	Ravindra[3]	Herve-Vandamme[144]
mole/L	Eg(eV)	Exp.	Eq. (2.21)	Eq. (2.22)	Eq. (2.23)	Eq. (2.24)	Eq. (2.25)
0.05	3.7992	2.4527	2.5878	2.1896	2.2362	1.7285	2.1214
0.10	3.7837	2.4569	2.5907	2.1925	2.2385	1.7381	2.1249
0.15	3.7415	2.4686	2.5987	2.2004	2.2448	1.7643	2.1346
0.20	3.7381	2.4695	2.5994	2.2010	2.2453	1.7664	2.1354
0.25	3.6820	2.4851	2.6103	2.2118	2.2538	1.8012	2.1485
0.30	3.6722	2.4878	2.6122	2.2137	2.2553	1.8072	2.1508
0.35	3.5847	2.5126	2.6298	2.2310	2.2689	1.8615	2.1717
0.40	3.4519	2.5510	2.6577	2.2583	2.2904	1.9438	2.2046

3.2.4. Electrical properties of undoped NiO thin films

The optical bandgap (E_g) of undoped NiO thin films decreases from 3.799 eV to 3.452 eV as molality increases from 0.05 to 0.40 mole/L, consistent with defect-induced bandgap narrowing in wide-bandgap semiconductors (~3.6–4.0 eV) [250, 251]. This reduction suggests the introduction of mid-gap states due to structural disorder or lattice distortions [252-255]. Electrical conductivity (σ) peaks at 0.10 mole/L ($0.07438\ (\Omega \cdot cm)^{-1}$) before declining at higher concentrations. The initial rise in σ likely results from increased charge carriers due to defects, while the subsequent drop indicates excessive disorder or carrier scattering [247, 248]. The lowest σ ($0.00396\ (\Omega \cdot cm)^{-1}$) at 0.35 mole/L, despite a smaller E_g, implies defect-dominated carrier trapping. These trends demonstrate the trade-off between bandgap tuning and charge transport, necessitating optimized synthesis conditions. Improved crystallinity reduces defect scattering, enhancing carrier mobility [256].

Table 3.4: Optical and electrical parameters of undoped NiO thin film at varying precursor molarity concentrations.

Molality $mole/L$	Optical energy bandgap $E_g\ [eV]$	Conductivity $\sigma[(\Omega.cm)^{-1}]$
0.05	3.799	0.04015
0.10	3.784	0.07438
0.15	3.742	0.04654
0.20	3.738	0.06225
0.25	3.682	0.00825
0.30	3.672	0.01413
0.35	3.585	0.00396
0.40	3.452	0.00465

3.3. The impact of Ba doping on the physical properties of NiO thin films

3.3.1. Structural properties of Ba-doped NiO thin films

Figure 3.17 presents the X-ray diffraction patterns of undoped and Ba-doped (0-8 at.%) NiO thin films deposited on a microscope slides as substrates, recorded in the 2θ range of 30-85°. All films exhibit polycrystalline structure with a face-centered cubic (FCC) phase (ICDD card No. 04-047-1049), showing preferential orientation along the (111) plane. Four characteristic diffraction peaks were identified at 37.09° (111), 42.86° (200), 61.13° (220), and 74.08° (311). The diffraction intensity systematically decreases with increasing Ba concentration, contrary to the observations by Boulila et al.[257]. This discrepancy may stem from differences in synthesis conditions or measurement parameters.

The observed peak broadening and intensity reduction are attributed to lattice strain induced by Ba incorporation. The significant ionic radius mismatch between $Ba^{2+}(0.135\,nm)$ and $Ni^{2+}(0.069\,nm)$, with a radius ratio $r(Ba^{2+})/r(Ni^{2+}) = 1.942$, causes: ① Crystal lattice distortion, ② Formation of point defects (vacancies), and ③ Dislocation generation.

Microstructural analysis was performed using Gaussian fitting of the (111) and (200) peaks to determine: ① Full width at half maximum (FWHM), ② Crystallite size (via Scherrer equation), and ③ Lattice strain.

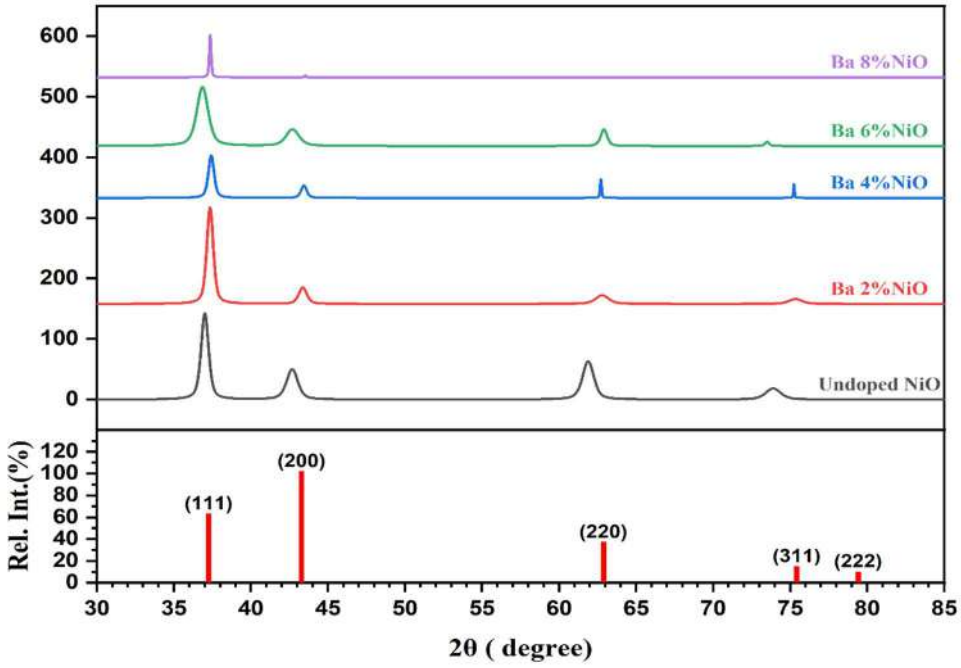

Figure 3.12: X-ray diffraction diffractograms of undoped NiO and Ba doped NiO thin films prepared at 450 °C, with different concentration of barium.

Figure 3.13 illustrates the relationship between the crystallite size (D) and the diffraction angle (2θ) of Ba-doped NiO thin films, specifically for the (111) crystallographic plane, as a function of barium doping percentage. Initially, with increasing Ba doping, a noticeable shift in the 2θ peak towards lower angles is observed, indicating an expansion of the lattice parameter. This expansion is likely due to the incorporation of larger Ba^{2+} ions into the NiO lattice, replacing smaller Ni^{2+} ions, consistent with Vegard's law for substitutional solid solutions [258].

Simultaneously, the crystallite size (D) increases, peaking at around 4% Ba doping, suggesting that moderate doping promotes grain growth. However, beyond 4% Ba, both 2θ and D show a decreasing trend. The reduction in 2θ implies a contraction of the lattice, possibly due to strain relaxation or the formation of defects, while the decrease in crystallite size suggests inhibition of grain growth at higher doping levels. This observation could be attributed to the formation of secondary phases or increased defect density, which hinders the diffusion of atoms necessary for crystallite growth[110]. The complex interplay between lattice strain, defect formation, and grain growth kinetics, as influenced by Ba doping, ultimately determines the structural characteristics of the NiO thin films.

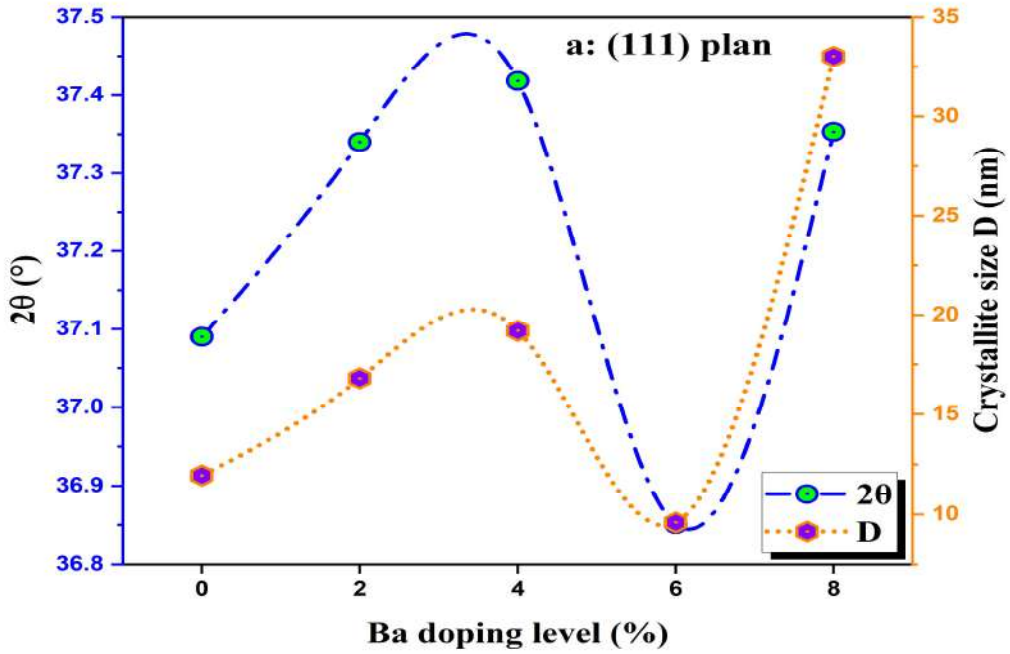

Figure 3.13: Correlation between the crystallite size and the diffraction angle of Ba-doped NiO thin films, for the (111) plane, at varying barium percentages.

Figure 3.14 depicts the relationship between the crystallite size (D) and the diffraction angle (2θ) of Ba-doped NiO thin films for the (200) crystallographic plane, as a function of barium doping concentration. Similar to the (111) plane, an initial increase in 2θ with increasing Ba doping is observed, suggesting a lattice expansion due to the substitution of Ni^{2+} ions by larger Ba^{2+} ions. This trend aligns with the principles of solid solution formation [258]. The crystallite size (D) concurrently increases, peaking at approximately 4% Ba doping, indicating that moderate doping promotes grain growth. However, beyond this critical doping level, a decrease in both 2θ and D is noted. The reduction in 2θ may signify a relaxation of strain or the introduction of defects, leading to lattice contraction. The decrease in crystallite size suggests

that higher Ba concentrations impede grain growth, possibly due to the formation of secondary phases or an elevated defect density that limits atomic diffusion [110]. The observed trends in the (200) plane closely mirror those seen in the (111) plane, suggesting a consistent structural response to Ba doping across different crystallographic orientations. This implies that the underlying mechanisms governing lattice parameter changes and crystallite growth are not significantly influenced by the specific plane under consideration, highlighting the bulk nature of the doping effects.

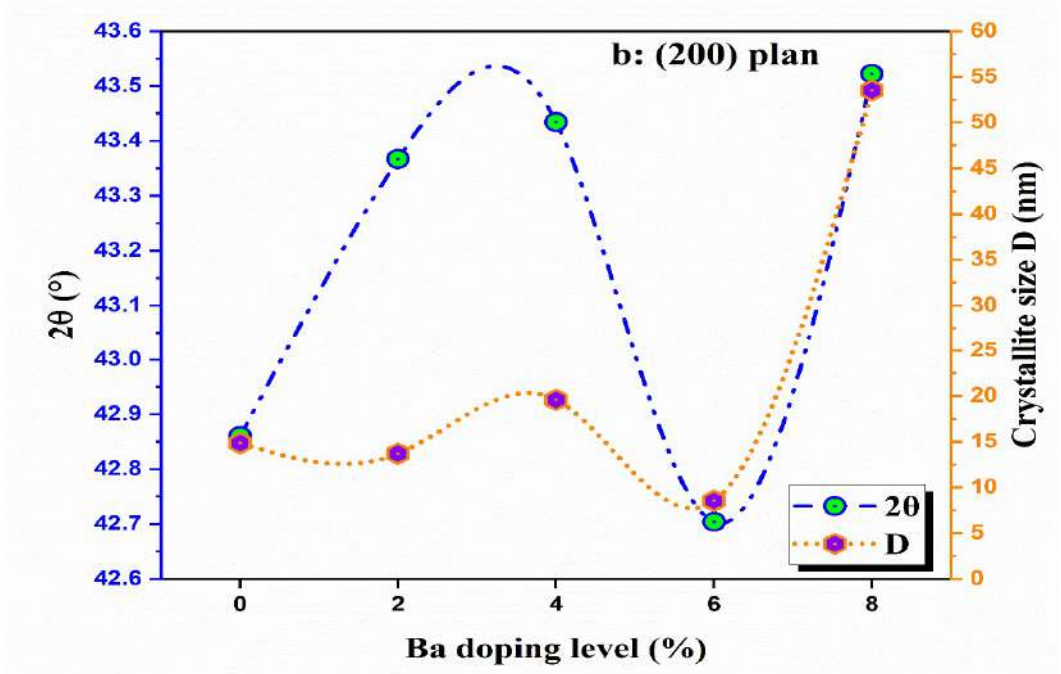

Figure 3.14: Correlation between the crystallite size and the diffraction angle of Ba-doped NiO thin films, for the (200) plane, at varying barium percentages.

Tables 3.5 and 3.6 summarize the results of the microstructural property analysis of undoped and barium-doped NiO thin films.

Indeed, the XRD analysis of undoped and Ba-doped NiO thin films reveals significant structural modifications induced by Ba incorporation. For the (111) and (200) diffraction peaks, the undoped NiO exhibits lattice parameters (a) of ~0.419 nm and ~0.422 nm, respectively, consistent with the cubic structure of NiO (JCPDS No. 47-1049). Upon Ba doping, the lattice parameter initially decreases (e.g., to 0.416 nm for 2 at.% Ba in the (111) plane), suggesting substitutional incorporation of smaller Ba^{2+} ions (1.42 Å) into Ni^{2+} (0.69 Å) sites, inducing compressive strain[259-261]. However, at 6 at.% Ba, an anomalous increase in lattice parameter (0.422 nm for (111)) occurs, possibly due to interstitial doping or secondary phase formation [262-265].

The crystallite size (D), calculated using the Scherrer equation, varies non-monotonically with doping. For (111), D increases from 11.95 nm (undoped) to 33.02 nm (8 at.% Ba), indicating enhanced crystallinity at higher doping levels. Conversely, 6 at.% Ba shows a minimum D (~9.59 nm), likely due to strain-induced fragmentation [266]. The dislocation density (δ) and microstrain (ε) follow inverse trends with D, peaking at 6 at.% Ba (δ ~10.9×10^{3} nm^{-2}, ε ~0.63%), confirming defect proliferation at intermediate doping. The (200) plane exhibits similar trends but with larger D and lower ε, suggesting anisotropic strain relaxation. These results align with Vegard's law deviations at high doping, where lattice distortion dominates [110, 258].

Table 3.5: Structural parameters of Ba doped NiO thin films as function of Ba doping percentage of (111) and (200) diffraction peaks (part 1).

Samples	(111) diffraction peak.				(200) diffraction peak.			
	2θ (°)	β(FWHM) (rad)	d (nm)	a (nm)	2θ (°)	β(FWHM) (rad)	d (nm)	a (nm)
Undoped NiO	37.090	0.01224	0.24220	0.41949	42.860	0.01003	0.21083	0.42166
NiO: Ba 2 at.%	37.340	0.00871	0.24063	0.41678	43.367	0.01089	0.20848	0.41697
NiO: Ba 4 at.%	37.418	0.00762	0.24015	0.41595	43.434	0.00762	0.20818	0.41635
NiO: Ba 6 at.%	36.851	0.01525	0.24371	0.42212	42.704	0.01743	0.21157	0.42313
NiO: Ba 8 at.%	37.353	0.00443	0.24055	0.41665	43.522	0.00279	0.20778	0.41555

Table 3.6: Structural parameters of Ba doped NiO thin films as function of Ba doping percentage of (111) and (200) diffraction peaks (part 2).

Samples	(111) diffraction peak.				(200) diffraction peak.			
	2θ (°)	D (nm)	$\delta \times 10^{-3}$ (m^{-2})	ε (%)	2θ (°)	D (nm)	$\delta \times 10^{-3}$ (m^{-2})	ε (%)
Undoped NiO	37.090	11.95	7.00	0.506	42.860	14.85	4.54	0.407
NiO: Ba 2 at.%	37.340	16.80	3.54	0.360	43.367	13.70	5.33	0.442
NiO: Ba 4 at.%	37.418	19.20	2.71	0.315	43.434	19.58	2.61	0.309
NiO: Ba 6 at.%	36.851	9.59	10.90	0.631	42.704	8.54	13.7	0.708
NiO: Ba 8 at.%	37.353	33.02	0.917	0.183	43.522	53.53	0.349	0.113

3.3.2. Morphological properties of Ba-doped NiO thin films

Figures 3.15 (a-d) illustrate the morphological characteristics of as-deposited NiO thin films subjected to varying levels of Ba doping. The scanning electron microscopy (SEM) images delineate distinct nanostructures and indicate a notable similarity in morphology among the as-deposited NiO nanoparticles. These nanoparticles demonstrate consistent geometrical forms, encompassing both spherical and elliptical configurations. In a majority of instances, the phenomenon of nanoparticle agglomeration was noted. The dimensions and morphology of

nanoparticles are recognized to be affected by a multitude of factors including the type of solvent utilized [267], the temperature and characteristics of the substrate [268, 269], the concentration of the precursor solution [270], as well as the deposition methodology [271]. Prior investigations have established that these parameters are vital in the regulation of crystal nucleation and orientation [272]. The nanoparticle dimensions derived from the SEM imagery were found to be congruent with those obtained through X-ray diffraction (XRD) and SEM analysis. Additional insights regarding the sample dimensions and morphology were acquired through SEM examination. A histogram representing particle size was generated for each sample and incorporated into the SEM imagery. Table 5 provides a comprehensive overview of the statistical findings derived from these images. The results exhibit a commendable alignment with the particle size estimations acquired from XRD analysis employing the Debye-Scherrer formula (equation 1).

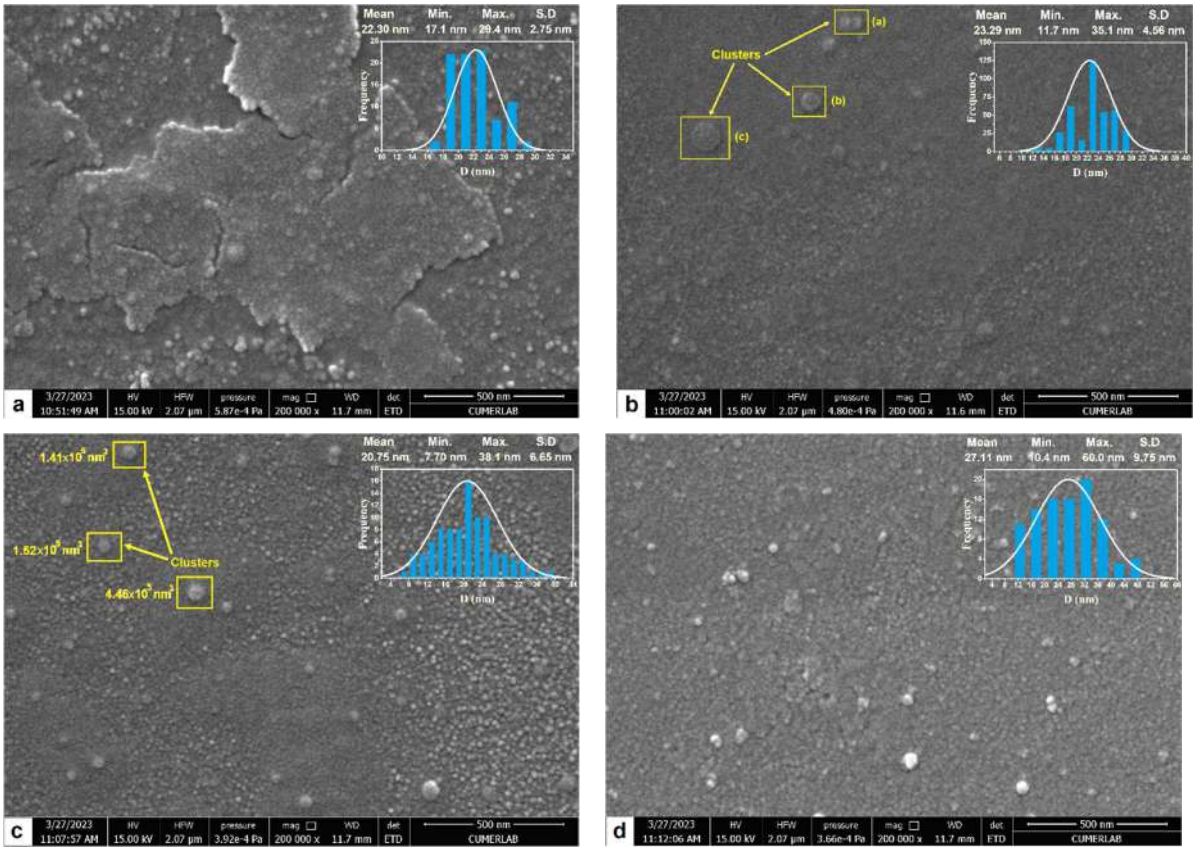

Figure 3.15: Various morphologies of SEM images of as-deposited NiO thin films: (a) Ba 2 at. % NiO, (b) Ba 4 at. % NiO, (c) Ba 6 at. % NiO and (d) Ba 8 at. % NiO.

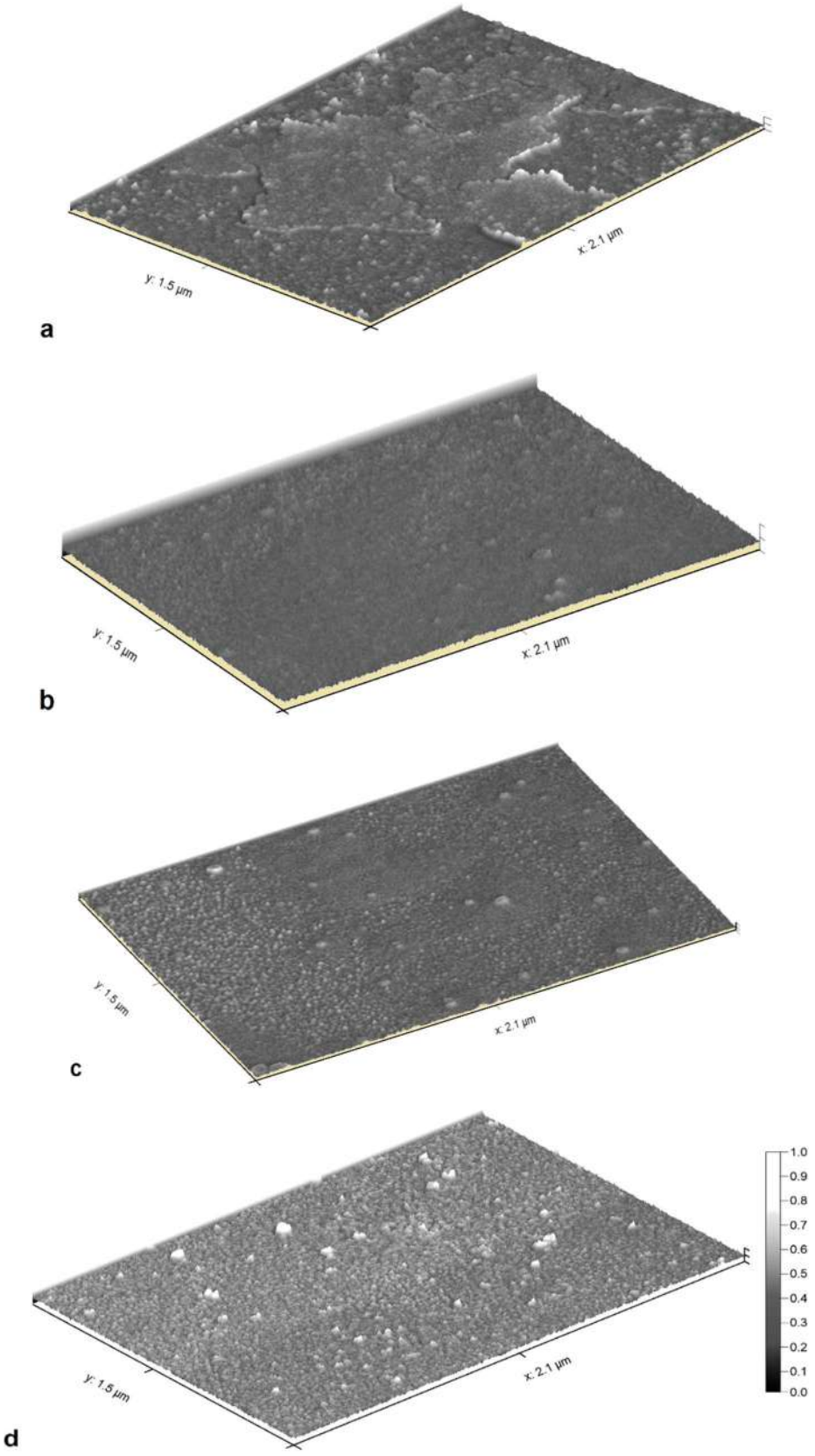

Figure 3.16: Three-dimensional scanning electron microscopy image of the topographical representation of Ba-doped NiO thin films prepared using SPT at 450°C.

Table 3.7: The grain size, roughness, and thickness parameters of undoped and doped NiO nanostructured films.

Samples	D: Particle size				Ra	t
	Mean (nm)	Min. (nm)	Max. (nm)	SD (nm)	(nm)	(nm)
Undoped NiO	12.50	7.30	19.60	2.78	23.57	560.3
Ba2%NiO	22.30	17.10	29.40	2.75	27.89	213.2
Ba4%NiO	23.29	11.70	35.10	4.56	30.35	240.5
Ba6%NiO	20.75	7.70	38.10	6.65	36.46	375.6
Ba8%NiO	27.11	10.40	60.00	9.75	39.06	236.5

3.3.3. Surface state analysis of deposited Ba-doped NiO thin films

This section analyzes the surface state of Ba-doped NiO thin films. Figure 3.17(a) displays profile curves from the SEM image. The films contain 2 at.% Ba doping. They were prepared via spray pyrolysis at 450°C. This analysis reveals key morphological traits. These traits help explain the film's interfacial properties.

Amplitude parameters show a moderately rough surface. The average roughness (Ra) is 27.89 nm. The root mean square roughness (Rq) is 37.24 nm. These values suggest uniform nanoscale features. Skewness (Rsk) is low at 0.068. This indicates a balanced distribution of peaks and valleys. Kurtosis (Rku) is high at 4.95. This implies a sharp, peaked texture. Such textures are typical for polycrystalline films with controlled growth [273, 274].

Spatial parameters reflect a regular nanostructured morphology. The mean spacing (Sm) is 10.80 nm. The average wavelength (λa) is 11.56 nm. Homogeneous nucleation likely caused this during deposition [275, 276]. The maximum profile height (Pt) is 0.49 µm. Waviness metrics are minimal. This suggests few large-scale defects. This quality aligns with sol-gel or sputtered thin films [178, 206, 277, 278].

Surface roughness influences charge transport and interfacial reactions [2, 279-281]. These results match the film's functional performance. Spacing and wavelength data support strain-minimized growth. This aligns with XRD crystallite size data (D ≈ 16.8 nm for (111) peaks, Table 3.8). Morphological control is vital for gas sensors or photovoltaics. In these applications, the surface-to-volume ratio governs efficiency [282, 283].

Figure 3.17(b) displays profile curves derived from the SEM image. These curves represent Ba 4%-doped NiO thin films prepared using spray pyrolysis at 450°C. Surface roughness analysis reveals specific morphological traits. The root mean square roughness (Rq) is 0.038 nm, and the roughness average (Ra) is 0.030 nm. These values indicate a smooth surface at the nanoscale. Positive skewness (Rsk = 0.242) suggests a surface dominated by peaks. The

kurtosis value (Rku = 2.98) is close to 3. This indicates a Gaussian height distribution [273, 274, 284].

Spatial parameters show a mean spacing of irregularities (Sm) of 6.95 nm. The average wavelength (λa) is 7.37 nm. This structure is more closely packed than the 2 at.% Ba sample. Increased Ba incorporation likely affects nucleation dynamics. This results in reduced feature spacing [8]. Hybrid parameters show steeper surface gradients. The RMS slope (Δq) is 32.87 μm^{-1}. This is nearly double the 2 at.% sample value. Greater local curvature may enhance surface reactivity [2, 280].

The maximum profile height (Pt) is 0.288 µm. Waviness parameters (Wa) are 0.019 nm. These values indicate minimal large-scale undulations. This suggests well-controlled deposition. Overall, 4 at.% Ba doping creates a more uniform peak distribution. It also produces finer nanoscale features and sharper local curvatures. These changes likely influence electronic and catalytic properties. Surface roughness affects charge transport and active site availability [285, 286]. Results correlate with XRD data showing increased crystallite size. Ba incorporation may promote ordered surface growth. This maintains nanoscale texture beneficial for gas sensing [287].

Figure 3.17(c) shows profile curves for 6% Ba-doped NiO films prepared at 450°C. The surface morphology represents an intermediate state between the 2% and 4% samples. Roughness values increase compared to lower doping levels. The root mean square roughness (Rq) is 0.047 nm, and the average roughness (Ra) is 0.036 nm. Positive skewness (Rsk = 0.175) indicates a peak-dominated surface. This resembles the 4% sample but is less pronounced. Kurtosis (Rku = 3.42) suggests a height distribution slightly sharper than Gaussian [273, 274, 284]. Spatial parameters also show intermediate spacing. The mean spacing of irregularities (Sm) is 10.36 nm. This trend suggests competing effects during film growth [8]. The maximum profile height (Pt) reaches 0.512 µm. This indicates taller features than those at lower doping levels. Strain effects likely drive these changes. At 6%, lattice distortion may begin overriding grain-refining effects [2, 178, 279-281]. This correlates with XRD data showing reduced crystallite size (Table 3.9). The 6% level appears to be a structural transition point.

Figure 3.17(d) presents data for 8% Ba-doped films. The morphology transforms dramatically at this concentration. Roughness increases by approximately three orders of magnitude. Ra reaches 39.06 nm, and Rq measures 48.96 nm. This suggests a fundamental change in growth mechanics [273, 274, 284]. The maximum profile height (Pt) is 370.35 nm. Spatial parameters show tighter feature spacing. Sm is 7.29 nm. Skewness (Rsk = 46.97) is exceptionally high. However, kurtosis (Rku = 3.14) remains near Gaussian. Hybrid parameters

indicate sharp surface gradients ($\Delta q = 39.52\ \mu m^{-1}$). This could enhance surface area for catalysis [2, 178, 279-281].

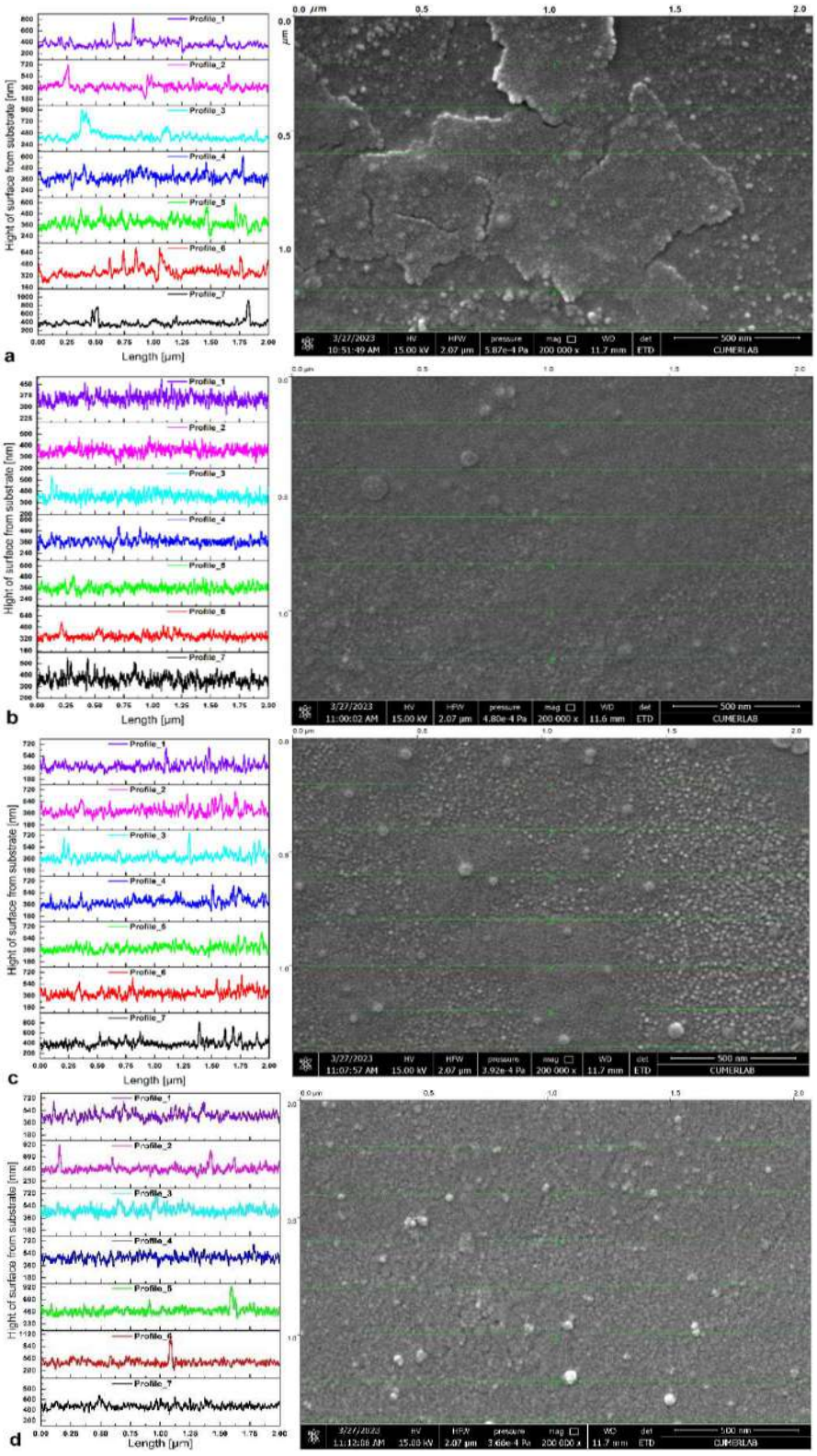

Figure 3.17: Profile curves measured along the lines shown on the SEM image of Ba-doped NiO thin films prepared by the spray pyrolysis technique at 450°C.

This shift likely results from critical strain accumulation. Surface buckling may occur [285, 286]. Secondary phases could also alter growth kinetics. XRD data shows increased crystallite size here (Table 3.9). Long-range order improves, but nanoscale disorder increases. This roughening may improve gas sensing. However, it could compromise electrical continuity [287].

3.3.4. Optical properties of Ba-doped NiO thin films

Figure 3.18 displays transmittance spectra for undoped and barium-doped nickel oxide (NiO) thin films. The data span wavelengths from 320 nm to 840 nm, covering UV, visible, and near-infrared regions. Five samples are compared: undoped NiO, and NiO doped with 2%, 4%, 6%, and 8% Ba. Undoped NiO shows the highest optical transmittance. Transmittance decreases steadily as Ba concentration increases. The undoped film exhibits a sharp absorption edge near 350–400 nm, marking the bandgap transition. Beyond this edge, transmittance reaches 65–70% in the visible and NIR ranges. Ba-doped films follow a similar spectral shape but with lower overall transmittance. A slight redshift of the absorption edge occurs with higher Ba content. This shift suggests bandgap narrowing due to doping. Reduced transmittance likely stems from increased light scattering, morphological changes, or new phase formation induced by Ba incorporation. These results demonstrate that Ba doping effectively tunes the optical properties of NiO thin films. Such control could benefit applications in optical filtering, light absorption, or photocatalysis, where bandgap engineering is essential.

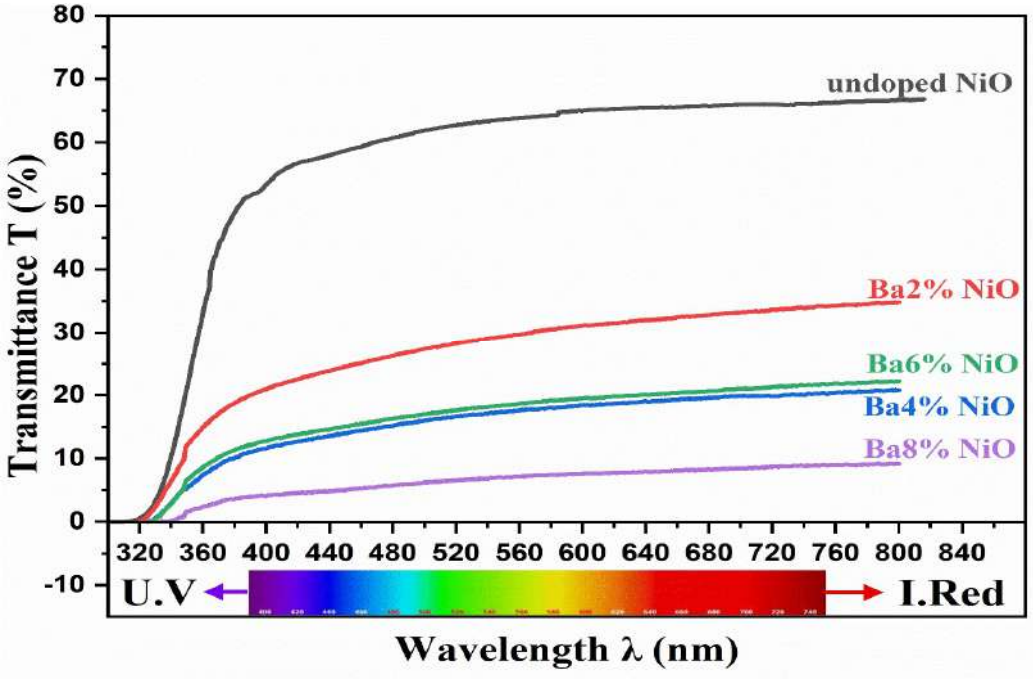

Figure 3.18: Transmission spectra of undoped and Ba-doped NiO thin film samples for different precursor molarities.

Figure 3.19 displays Tauc plots [288] for five different nickel oxide (NiO) thin films, illustrating the relationship between the squared absorption coefficient multiplied by photon energy $(\alpha h\nu)^2$ and the incident photon energy $(h\nu)$. Each plot features a linear fit applied to the absorption edge region, with the extrapolated line intersecting the $(h\nu)$ axis to determine the optical bandgap energy (E_g) of the corresponding film. This approach follows the Tauc method [288], a widely established technique for characterizing the bandgap of semiconductor materials. The linear dependence of $(\alpha h\nu)^2$ on $(h\nu)$ confirms a direct bandgap transition, consistent with the known electronic structure of NiO. The bandgap values, explicitly indicated on each plot, are derived from the x-intercepts of these extrapolations, under the fundamental assumption that near the band edge, optical absorption follows the direct transition model.

The optical and structural properties of undoped and Ba-doped NiO thin films exhibit notable variations with doping concentration, as summarized in Table 3.8. The undoped NiO film possesses a bandgap energy (Eg) of 3.742 eV, which is consistent with the range (3.6–4.0 eV) reported by Chen et al. [289] for pure NiO thin films, confirming the intrinsic wide-bandgap nature of NiO. In contrast, Schuler et al. [290] reported an Eg of 3.5 eV for 1 at.% barium-doped NiO thin films, suggesting that even minimal doping can induce measurable bandgap reductions. In the present study, a progressive decrease in Eg is observed with higher Ba concentrations, declining from 3.727 eV (2 at.% Ba) to 3.450 eV (6 at.% Ba), followed by a slight increase to 3.495 eV (8 at.% Ba). This non-monotonic trend indicates that low Ba doping ($\leq$ 2 at.%) has a modest effect on Eg, aligning with Anandan et al. [267], who reported 3.74–3.89 eV for 2 at.% Ba-doped NiO. However, at higher doping levels (4–8 at.%), the bandgap narrowing becomes more pronounced, approaching the range (3.52–3.60 eV) calculated by Boulila et al. [257] for Ba-doped NiO. This reduction may arise from several factors: (i) the introduction of defect states within the bandgap due to Ba substitution, as discussed by Schuler et al. [290]; (ii) structural modifications, such as lattice strain or increased disorder; and (iii) the Burstein-Moss effect, where high doping concentrations may shift the absorption edge.

Additionally, the morphological analysis reveals a clear correlation between Ba doping and surface roughness (Ra), which increases from 23.26 nm (undoped) to 39.06 nm (8 at.% Ba). This enhanced roughness, likely due to grain growth and structural distortions induced by Ba incorporation, could contribute to light scattering effects, further influencing the optical absorption characteristics. The observed thickness variations (e.g., 375.6 nm for 6 at.% Ba vs. 213.2 nm for 2 at.% Ba) may also modulate the optical response, as thicker films often exhibit different defect densities and interfacial effects. Collectively, these findings highlight the

tunability of NiO's optoelectronic properties through Ba doping, with implications for applications in transparent electronics and photocatalysis.

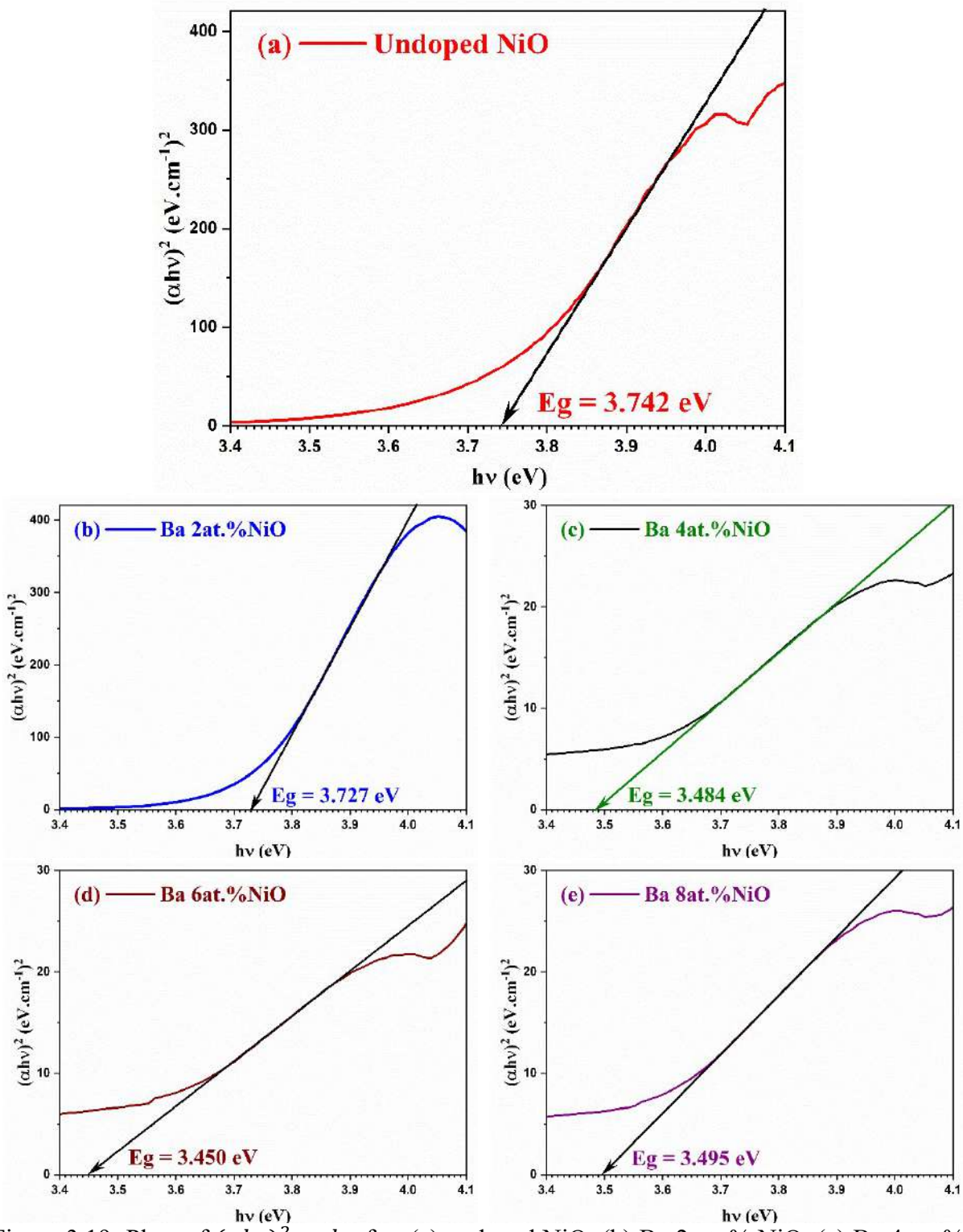

Figure 3.19: Plots of $(\alpha h\nu)^2$ vs $h\nu$ for: (a) undoped NiO, (b) Ba 2 at. % NiO, (c) Ba 4 at. % NiO, (d) Ba 6 at. % NiO, (e) Ba 8 at. % NiO doped thin films.

Table 3.8: Summary of morphological, structural, and optical parameters of undoped and doped NiO nanostructured films.

Samples	t: thickness [nm]	Ra: roughness [nm]	$D_{(111)}$ [nm]	$D_{(200)}$ [nm]	E_g [eV]	E_u [meV]
Undoped NiO	360.3	23.26	11.95	14.85	3.742	262.977
Ba 2 at.% NiO	213.2	27.89	16.80	13.70	3.727	356.642
Ba 4 at.% NiO	240.5	30.35	19.20	19.58	3.484	334.164
Ba 6 at.% NiO	375.6	36.46	9.59	8.54	3.450	327.337
Ba 8 at.% NiO	236.5	39.06	33.02	53.53	3.495	303.144

Figure 3.20 displays ln(A) plots against photon energy (hv). These data represent barium-doped nickel oxide (Ba:NiO) thin films. Doping levels range from 2 to 8 at.% Ba. We fitted the linear regions within the sub-bandgap range. This determined the Urbach energy (E_u). This value quantifies structural disorder. We calculate E_u as the inverse slope of the linear fits. It corresponds to the width of the exponential absorption tail. This parameter highlights structural imperfections. Examples include lattice distortions and defect states from Ba doping. The analysis follows the Urbach rule for disordered semiconductors. Varying the concentration allows us to study Ba incorporation effects. We can observe how doping changes the structural quality of NiO films.

Table 3.11 presents the Urbach energy (E_u) values. These numbers reveal significant changes in structural disorder. The undoped NiO film shows the lowest disorder. Its E_u value is 262.977 meV. This aligns with the ordered structure of pure NiO [289]. Doping with 2 at.% Ba increases E_u sharply to 356.642 meV. This indicates a substantial introduction of defects. Lattice distortions also occur. Chen et al. [289] noted that dopants typically disrupt the NiO lattice. However, higher doping concentrations (4-8 at.% Ba) show a gradual decrease. E_u drops from 334.164 meV to 303.144 meV. This suggests defect states may saturate or reorganize. Boulila et al. [257] reported similar non-monotonic behavior. Maximum disorder appeared at intermediate doping levels. The initial increase likely stems from ionic size mismatch. Ba^{2+} ions (~1.35 Å) replace smaller Ni^{2+} ions (~0.69 Å). This creates significant local strain [290]. The subsequent decrease might indicate ordered defect complexes. Secondary phase formation is another possibility [267]. These E_u variations correlate with our optical bandgap analysis. Increased disorder typically narrows the bandgap through tail states [257]. Tracking E_u evolution provides insights into defect engineering. These insights aid optoelectronic applications.

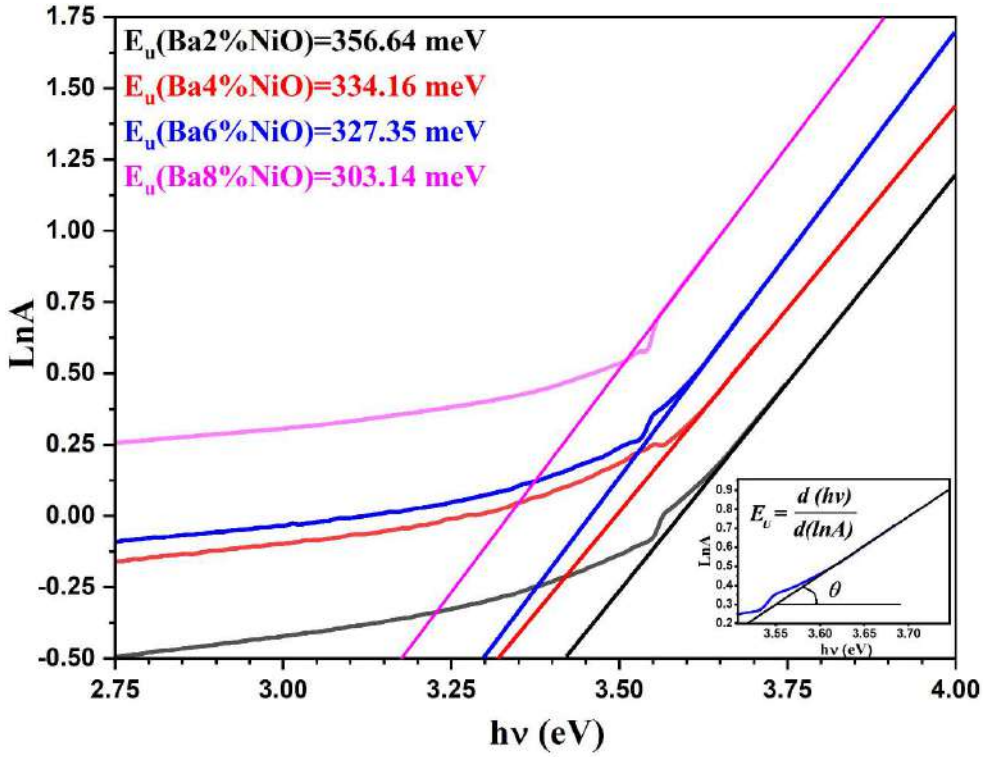

Figure 3.20: Plot of $Ln(A)$ versus incident photon energy ($h\nu$) of Ba-doped NiO thin films at different precursor molarities.

Figure 3.21 demonstrates the intricate relationship between barium doping concentration, structural disorder, and optical properties in NiO thin films through systematic analysis of Urbach energy (E_u) and bandgap energy (E_g) evolution. At low doping concentrations (0-2 at.% Ba), the significant decrease in E_u indicates improved structural order, likely arising from defect passivation or strain relaxation mechanisms, while the corresponding reduction in E_g confirms effective bandgap tuning. This initial regime suggests that controlled Ba incorporation can simultaneously enhance crystallinity and modify electronic structure advantageously. However, at higher doping levels (2-8 at.% Ba), the emergence of non-monotonic E_u fluctuations reveals competing structural effects - including new defect formation, lattice strain accumulation, and potential secondary phase nucleation - that complicate the disorder landscape. Notably, while these structural complexities develop, E_g maintains a consistent decreasing trend, demonstrating the robustness of bandgap engineering through doping despite increasing disorder. The observed inverse $E_g - E_u$ correlation fundamentally connects structural modifications to electronic property changes: initial disorder reduction facilitates bandgap narrowing, while subsequent defect interactions at higher concentrations introduce more complex structure-property relationships. These findings highlight the dual nature of Ba doping in NiO, where optimal low-concentration doping improves both structural and optical

characteristics, but higher doping requires careful optimization to balance bandgap control against disorder-induced effects for device applications.

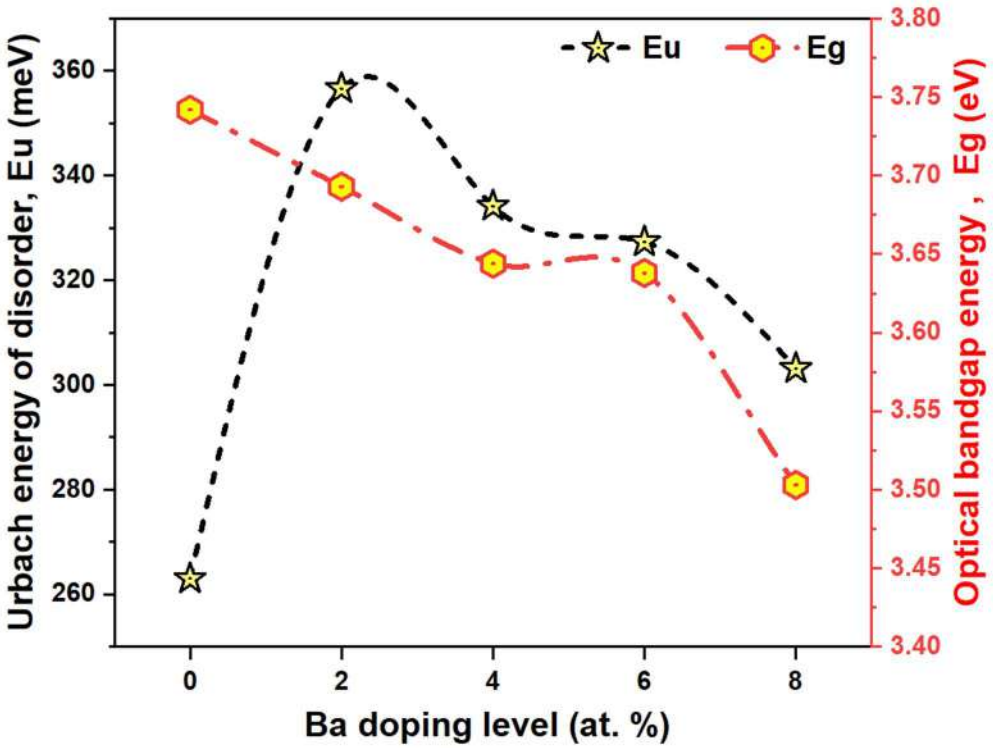

Figure 3.21: Evolution of the optical bandgap energy and Urbach energy as a function of the atomic concentration of the precursor solution for undoped and Ba-doped NiO thin films.

3.4. Fourier Transform Infrared spectroscopy (FTIR) analysis

Fourier Transform Infrared spectroscopic analysis was performed on ZnxNi1xO thin films prepared onto glass substrate under optimized processing parameters. The FTIR spectra were procured in the transmission mode for all prepared samples and are shown in Fig. 3.22.

The strong IR absorption bands observed in all the samples around 566.9 cm^{-1} could be assigned to the characteristic bending vibration modes of the Ni-O bonds in the octahedral ligand field in NiO oxides[291, 292].

However, the intensity of these vibrational modes is found to get slightly increased continuously with an increase in the precursor concentration in NiO.

The absorption band observed around 435cm^{-1} corresponds to the metal-oxygen vibrational mode of the Ni-O-Ni bonds of NiO compounds, the intensity of which was found to be maximum for the NiO sample (0.40 mole/L).

The appearance of additional modes observed around 1100 cm^{-1} can be assigned to the C-H bonds vibrations of the organic residuals, the intensity of which was found to be very low for all concentrations.

Additionally, in Figure 3.22, a gradual shift of these localized Ni-O-NiO vibrational bonds to a higher wavenumber, i.e. 435 to 439.6 cm^{-1}, can be observed with an increase in the concentration of the precursor solution. The shift of these localized bands to higher wavenumber in response to increasing concentration can be attributed to the deformation of the NiO crystal lattice structure. Indeed, the increase in the concentration accompanied by a high temperature (450°C) of calcination promotes the coalescence of the grains in the thin layers of NiO deposited. During coalescence, the grain boundaries move and deform, and the grains rotate and their volume changes. The inference drawn from the FTIR studies of the prepared samples is in accordance with the XRD results.

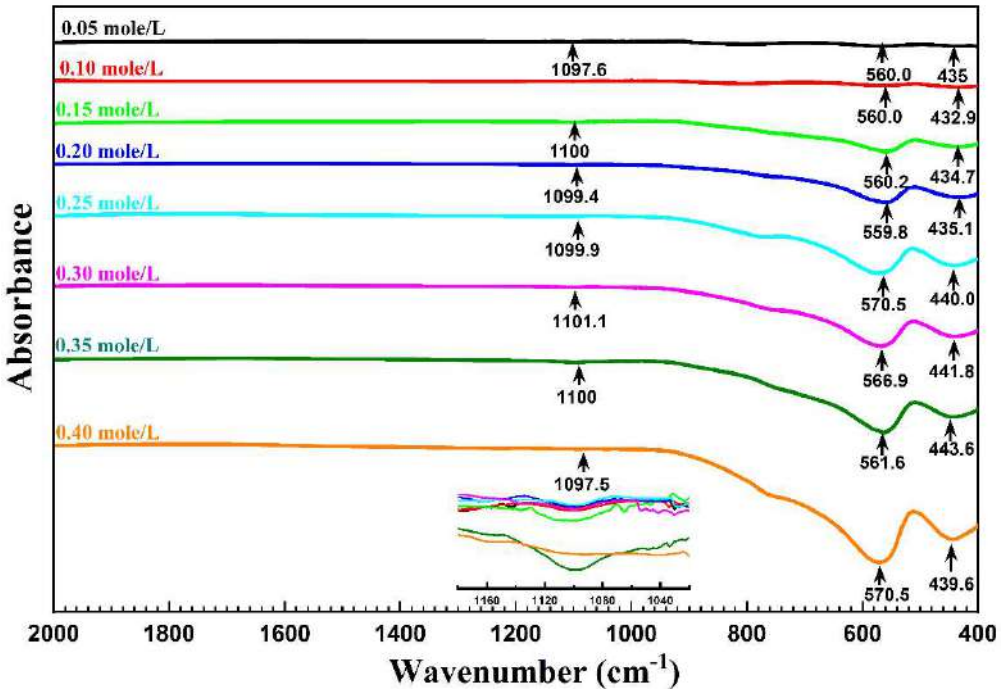

Figure 3.22: FTIR spectra of NiO thin films with varying precursor concentrations.

3.5. Electrical properties of Ba-doped NiO thin films

Electrical conductivity measurements reveal a non-monotonic trend with barium doping in NiO thin films. The undoped sample shows a conductivity of 0.04654 $\Omega^{-1}cm^{-1}$. This value reflects NiO's intrinsic p-type semiconductor behavior. At 2 at.% Ba doping, conductivity decreases to 0.04195 $\Omega^{-1}cm^{-1}$. Low-concentration dopants likely introduce scattering centers. These centers impede charge carrier movement. The downward trend continues at higher doping levels. Conductivity drops to 0.03354 $\Omega^{-1}cm^{-1}$ at 4 at.% Ba. It falls further to 0.02027 $\Omega^{-1}cm^{-1}$ at 6 at.% Ba. Increased doping enhances carrier scattering effects. Possible causes include defect complex formation, increased grain boundary scattering, and lattice distortion. The ionic size mismatch between Ba^{2+} (1.35 Å) and Ni^{2+} (0.69 Å) drives this lattice strain [293, 294].

Interestingly, at 8 at.% Ba, conductivity shows a slight recovery to 0.02414 $\Omega^{-1}cm^{-1}$. This non-linear behavior suggests competing physical mechanisms. Dopant-induced carrier generation and defect-mediated scattering likely act in opposition. Understanding this delicate balance helps researchers optimize NiO thin film performance for practical electronic and optoelectronic applications.

3.6. Conclusion

This chapter investigated undoped and barium-doped nickel oxide (NiO) thin films. We used the spray pyrolysis technique. We examined how precursor concentration and doping levels affect film properties. Undoped films showed a polycrystalline face-centered cubic structure. Optimal crystallinity occurred at 0.10 mole/L precursor concentration. Higher concentrations reduced crystallite size and increased defects. Morphologically, films displayed granular surfaces with nanoscale cracks. Optical transmittance decreased as molarity increased. Electrical conductivity also dropped at higher molarities. A balance was found between 0.20 and 0.25 mole/L.

Barium doping significantly changed film characteristics. We tested levels from 0 to 8 at.%. Crystallite size peaked at 4 at.% Ba. However, lattice distortion increased at higher levels. Dislocation density peaked at 6 at.% Ba. Surface roughness was optimal between 4 and 6 at.% Ba. This range suits catalytic and gas-sensing applications. Optical studies showed bandgap narrowing and reduced transmittance with more barium. Disorder generally decreased but fluctuated at high doping.

In conclusion, precise control over synthesis parameters is essential. Lower barium concentrations improved crystallinity. The 4 to 6 at.% range offered the best balance for device applications. Careful optimization manages the trade-off between bandgap control and structural disorder.

Chapter-4 Discussion and interpretation of results for Ba-doped ZnO thin films

Chapter-4
Discussion and interpretation of results for Ba-doped ZnO thin films

4.1 Introduction

Zinc oxide (ZnO) is one of the most investigated tunable optoelectronic material, due to the tunable optical and electrical properties of these films. The properties can all be increased even further by doping with a barium (Ba) type element but systematic studies of the influence of Ba concentration on structure and functionality are lacking. This chapter investigates: Undoped and Ba-Doped ZnO Layers (0–8 at.% deposited at 450°C; The Doping Effect on their Performance Investigated.

Crystallinity and morphology are measured by X-ray diffraction (XRD) of the material, the structure analyzed in UV-visible spectroscopy and crystal bandgap shifts optical bandgap study scanning electron microscopy (SEM). Electrical resistance measurements will demonstrate variations in conductivity due to doping levels. The deposition temperature is selected as 450°C achieved stability and crystallinity of the films.

This work bridges structural changes to functional properties and specifies the different behavior of ZnO that is incorporated with Ba.

4.2 Analysis and interpretation of results for undoped ZnO thin films

4.2.1. Structural properties of undoped ZnO thin films

Figure 4.1 depicts the X-ray diffraction (XRD) patterns of undoped ZnO thin films deposited on glass substrates, which has been heated to 450°C. It can be see that the patterns display the reflection planes (100), (002), (101), (102), (103), and (004) that correspond to following Bragg angles 31.63°, 34.36°, 36.16°, 47.42°, 62.52°, and 72.31°, respectively. These observations are compatible with the structure of hexagonal wurtzite of ZnO as indicated in the JCPDS card no 36-1451.

We remark that the peaks, which correspond to the (002) reflection planes located at 34.36° have the most important intensity. The preferential direction of growth is along the c-axis of the hexagonal wurtzite structure. It have been reported that c-axis orientation minimizes the surface energy and stabilizes the crystalline structure during the process of film deposition.

The absence of additional peaks confirms the phase purity of the films, with no detectable secondary phases such as $Zn(OH)_2$ or $cubic\ ZnO$, which aligns with the expected hexagonal wurtzite structure [268].

Calculated lattice parameters from the diffraction data reveal slight deviations from standard values: the average "a" and "b" parameters ($a_{ave} = b_{ave} = 3.26909$ Å) and the "c" parameter ($c_{ave} = 5.29784$ Å) are marginally larger than the reference values ($a_{std} = b_{std} = 3.2498$ Å; $c_{std} = 5.2066$ Å).

On the other hand, the expansion of the crystalline structure suggests the presence of strain and stress. These micromechanical phenomena are induced the temperature variation between the thin film and the substrate during the deposition process at 450°C.

Finally, we have noted that the variations in precursor molarity may affect the dynamics of the nucleation phenomenon. It appears that the higher molarities enhance the crystallite growth by increasing precursor abundance [110, 150, 151, 295].

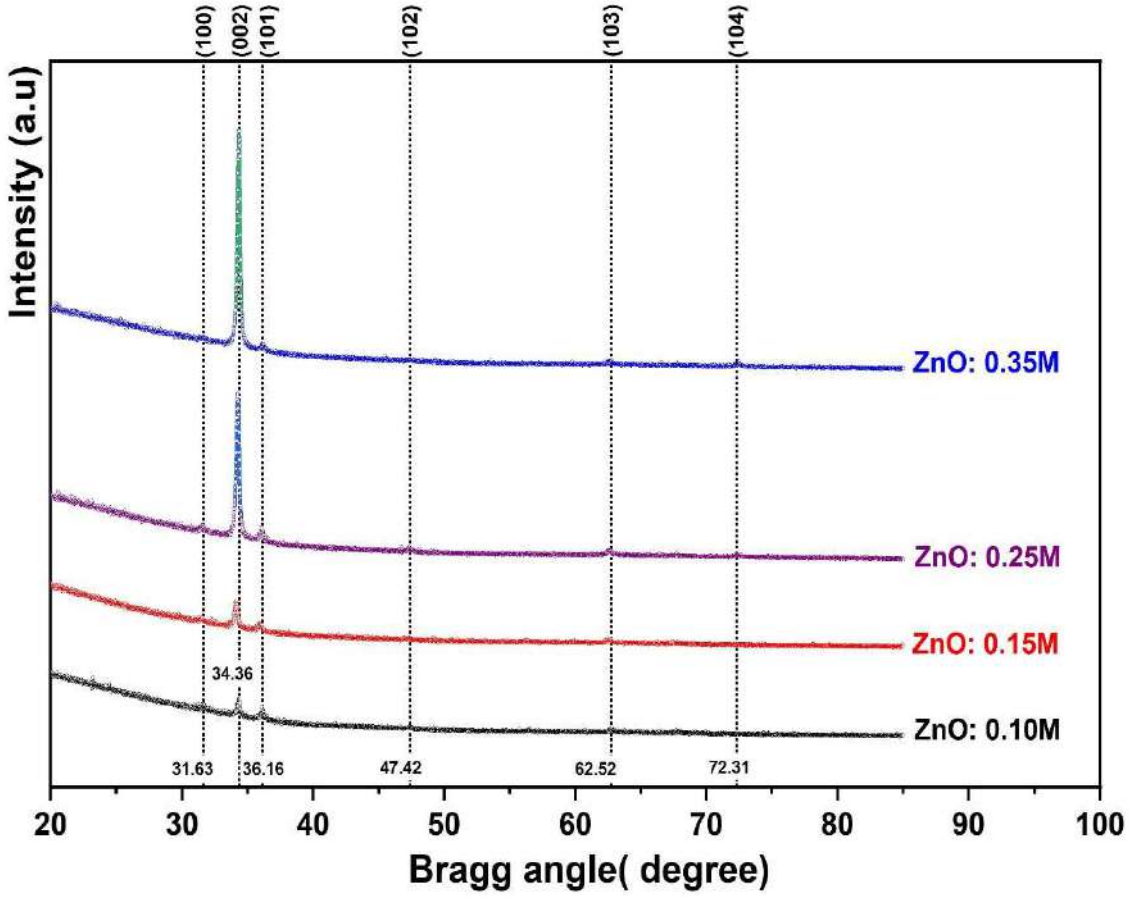

Figure 4.1: XRD diffractograms of undoped ZnO thin films deposited on glass substrate at 450°C with various precursor molarities.

Table 4.1 summarizes the lattice parameters of undoped ZnO thin films synthesized at varying precursor molarities. Looking at Table 4.1, the data reveals how precursor molarity affects the crystal structure of undoped ZnO thin films. All samples adopt the hexagonal wurtzite structure (JCPDS no 36-1451), but their lattice constants (a and c) vary slightly depending on synthesis conditions.

We have noticed that the parameter "a" and "b" varie from 3.27513 to 3.24863 Å, and from 3.27513 to 3.24863 Å for the molarities in the range of 0.10 to 0.35 mole/L, respectively. These computed values are different from bulk ZnO standards ($a_{std} = b_{std} = 3.2498$ Å, $c_{std} = 5.2066$ Å) (as presented in JCPDS card no 36-1456).

Table 4.1: Lattice parameters of undoped ZnO thin films synthesized at varying precursor molarities, derived from X-ray diffraction (XRD) analysis.

Precursor molarity	ZnO (hexagonal)				
	Cell parameters			Cell volume	Atomic Packing Factor
	a_{hex} (Å)	c_{hex}(Å)	c/a	V_{hex}(Å^3)	APF
0.10	3.27513	5.28807	1.61462	49.12300	0.74891
0.15	3.24406	5.32131	1.64032	48.49835	0.73717
0.25	3.30854	5.29780	1.60125	50.22257	0.75516
0.35	3.24863	5.28419	1.62661	48.29582	0.74340

Figure 4.2 shows the systematic variations in $\Delta(2\theta)$ values for undoped ZnO thin films corresponding to precursor molarities ranging from 0.10M to 0.35M. The peak corresponding to the (002) refection plane manifests the most significant negative $\Delta(2\theta)$ values (−0.4 to −0.2), signifying that the tensile strain along the c-axis, can be attributed to thermal expansion discrepancies during deposition at 450°C. In contrast, the peaks corresponding to the (100) and (101) reflection planes exhibit a positive $\Delta(2\theta)$ values (up to +0.8), which indicates the presence of compressive strain within the a-b plane [55, 151].

We are in the presence of an anisotropic deformation, which is a consequence of the hexagonal structure of the wurtzite lattice. Indeed, we know that, in this structure, the c-axis, known as "polar direction," is more sensitive to growth-induced stresses than other directions.

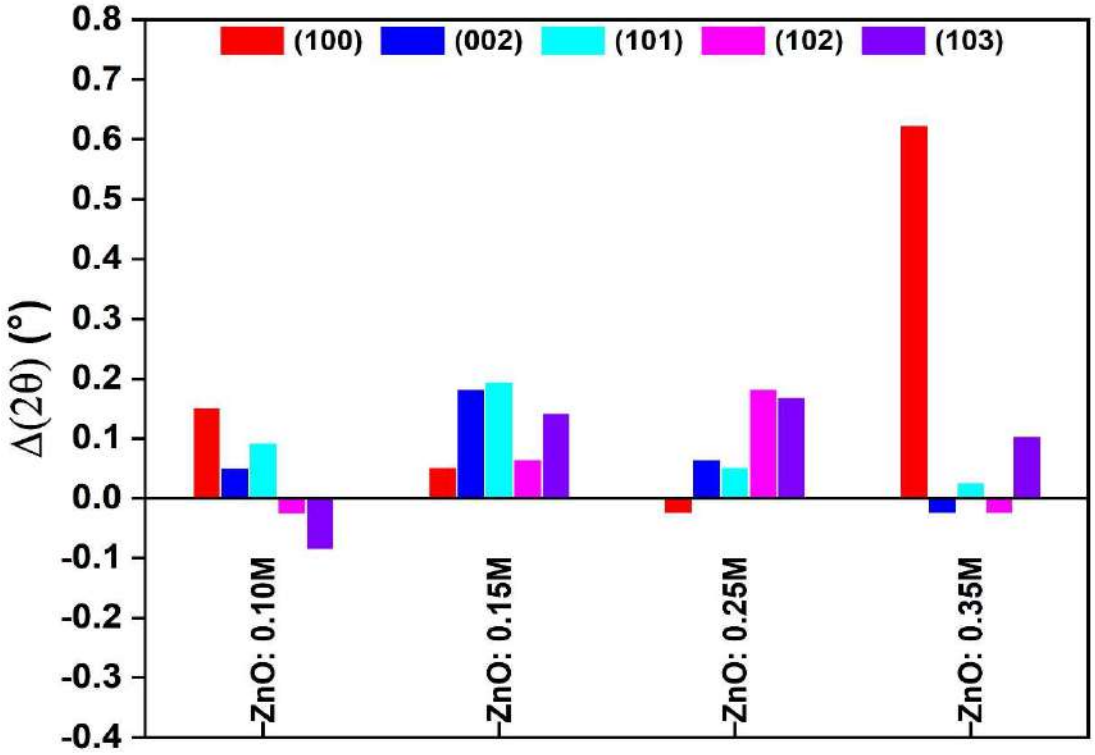

Figure 4.2: Variation of $\Delta(2\theta)$ values as a function of molar concentration of precursor solutions.

Figure 4.2 shows the various peak intensities computed from the experimental X ray diffraction diffractograms of undoped ZnO thin films. We have noticed the increase of the peak intensities with the precursor molarities. As observed in the previous paragraphs, the peak corresponding to the (002) reflection plane is the most intense and it exhibits the highest coefficient of texture (TC) values that increases from 0.297 to 0.706, for the molarities, 0.10 mole/L to 0.35 mole/L, respectively (as shown in Figure 4.4).

These observations reflect the improved crystallite alignment caused by greater ability of individual zinc (Zn) atoms, which are adsorbed on the surface to move and diffuse across the interface during the formation and the growth of the thin film.

On the other hand, the lower molarities (e.g., 0.10 mole/L) exhibit weaker peaks, with intensities less than $10^3 counts$, this phenomenon suggests that the formation of smaller crystallites or incomplete grain growth is impeded by the precursor quantity.

Finally, the higher molarities can drive to a thicker, more ordered films by optimizing the rates of nucleation and minimizing the induced strain.

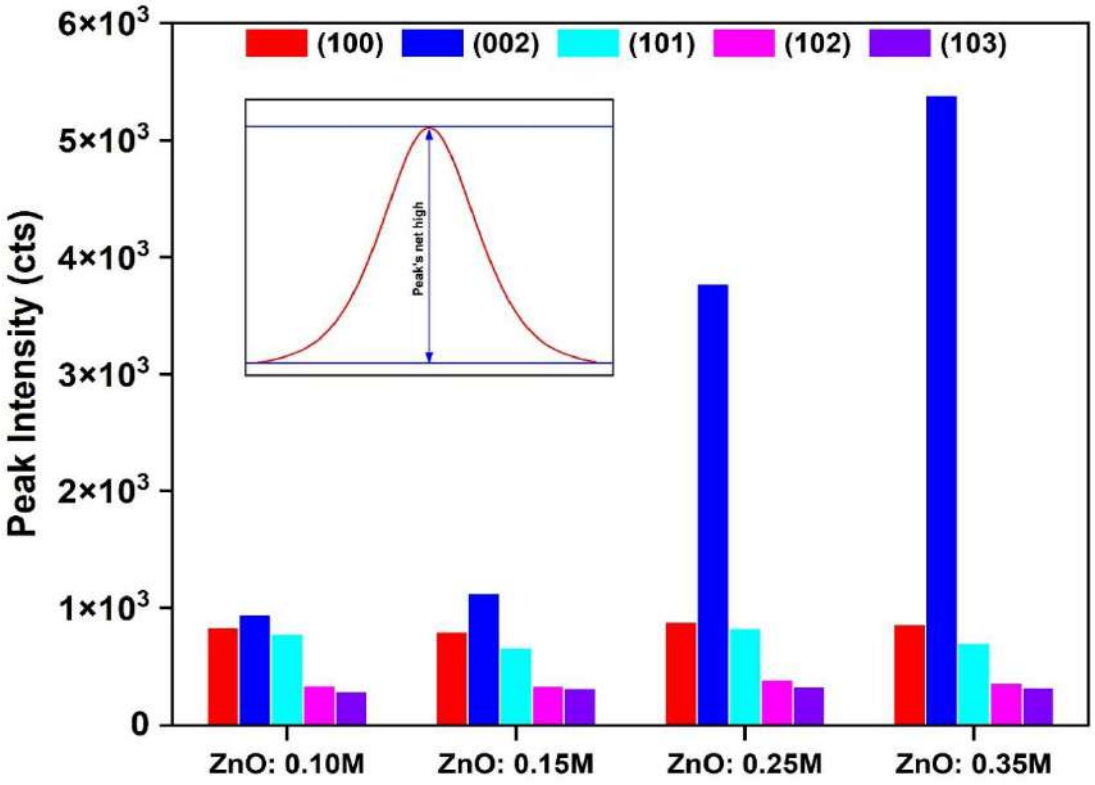

Figure 4.3: X-ray diffraction (XRD) peak intensity dependence on the molar concentration of precursor solutions.

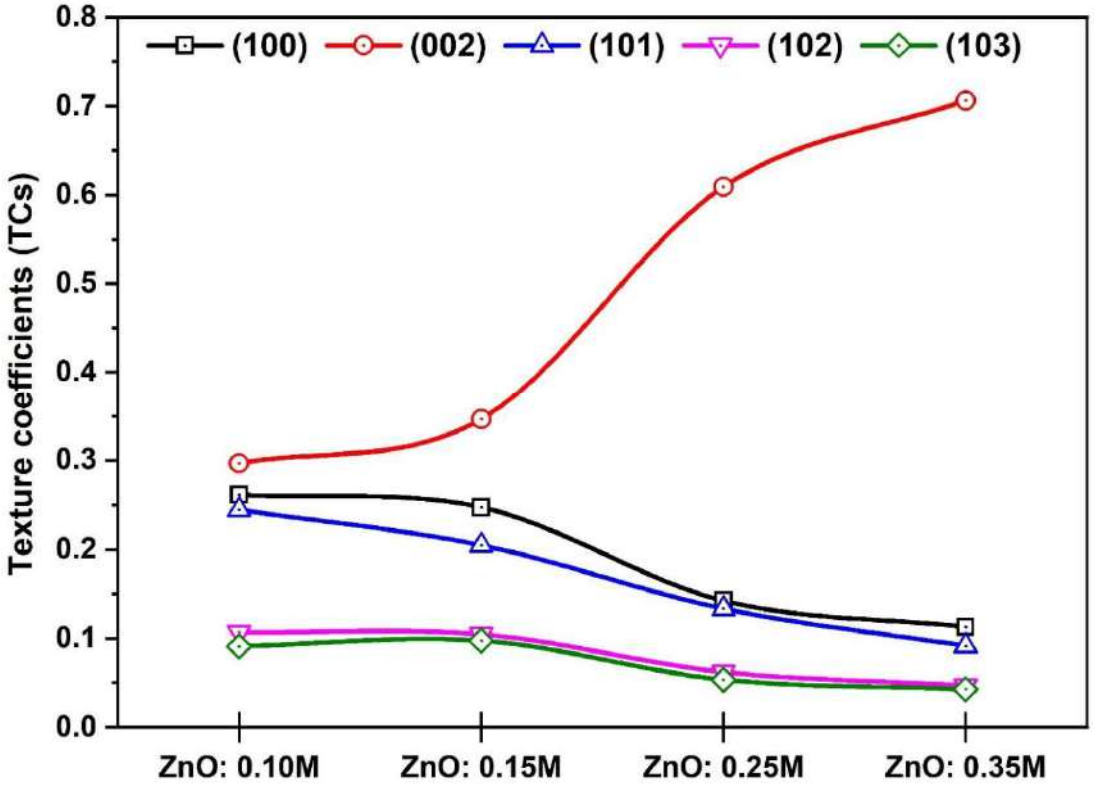

Figure 4.4: Texture coefficients (TCs) for selected crystallographic planes in undoped ZnO thin films as a function of the precursor solution molar concentration.

Table 4.2 presents the microstructural features of undoped ZnO thin films synthesized at varying precursor molarities that have been computed using the (002) reflection plane. We can see that when the molarity increases from 0.10 to 0.35 mole/L, then the crystallite size or the coherent diffraction domain (D_{hkl}) rises from 31.4 nm to 56.4 nm; this indicates an improved crystallinity caused by enhanced precursor quantity and the rates of nucleation [159, 160].

The previous phenomenon supports this trend and aligns with the observed decrease in $\beta(FWHM)$ from 0.01499 to 0.00834 radians, knowing that the sharper diffraction peaks correlate with larger, more ordered microstructures.

On the other hand, the dislocation density (δ), which is a measure of structural defects, decreases significantly from 1.0142×10^{15} to $0.3144 \times 10^{15} lines/m^2$, further confirming reduced lattice imperfections at higher molarities, caused by the heating of the substrate [152-154].

The values of the strain (ε) vary with the molarities. Indeed, for the molarities 0.10 and 0.15 mole/L, the films show a tensile strain (+0.358% and +0.291%), while for a molarity of 0.25 M, it shows a compressive strain (–0.249%), and 0.35 mole/L returns to mild tension (+0.199%).

These fluctuations suggest competing influences of thermal stress (from deposition at 450°C) and a lattice relaxation induced by the precursor quantity. We can suppose that the denser atomic packing (highest $D_{hkl} of$ 45.3 nm) drives a compressive strain for the (0.25 mole/L) thin films. To conclude, the Bragg angle values in the range of (34.1072°–34.3542°) remain close to the bulk ZnO peak corresponding to the (002) reflection plane (34.422°).

Table 4.2: Structural parameters of undoped ZnO thin films synthesized at varying precursor molarities, derived from X-ray diffraction (XRD) analysis of the (002) reflection.

Precursor molarity	Bragg Angle	β	D_{hkl}	$\delta \times 10^{15}$	ε
[mole/L]	[degree]	[rad]	[nm]	[line/m^2]	[%]
0.10	34.3282	0.014989	31.4	1.0142	0.358
0.15	34.1072	0.012175	38.9	0.6608	0.291
0.25	34.2632	0.010409	45.3	0.4873	-0.249
0.35	34.3542	0.008339	56.4	0.3144	0.199

Figure 4.5 shows that crystallite size (D_{hkl}) in undoped ZnO thin films increases from 31.4 nm (0.10 mole/L) to 56.4 nm (0.35 mole/L) with rising precursor molarity. This indicates an

enhanced grain growth at higher concentrations. On the other hand, the dislocation density (δ) decreases from 10^{15} *to* $10^{14} lines/m^2$, which reflects a diminution of the defects as crystallites coalesce into larger coherent diffraction domains [162]. On the other one, the mean strain (ε) decreases from 0.358% to less than 0.10%, which suggests relaxed lattice distortions caused by the improved the zinc (Zn) and oxygen(O) atoms mobility and reduced thermal mismatch at 450°C. As discussed in figures 4.2–4.4, the higher molarities (e.g., 0.35 mole/L) drive thermodynamically stable growth, which favors larger and low-defect crystallites with dominant (002) orientation [163, 166].

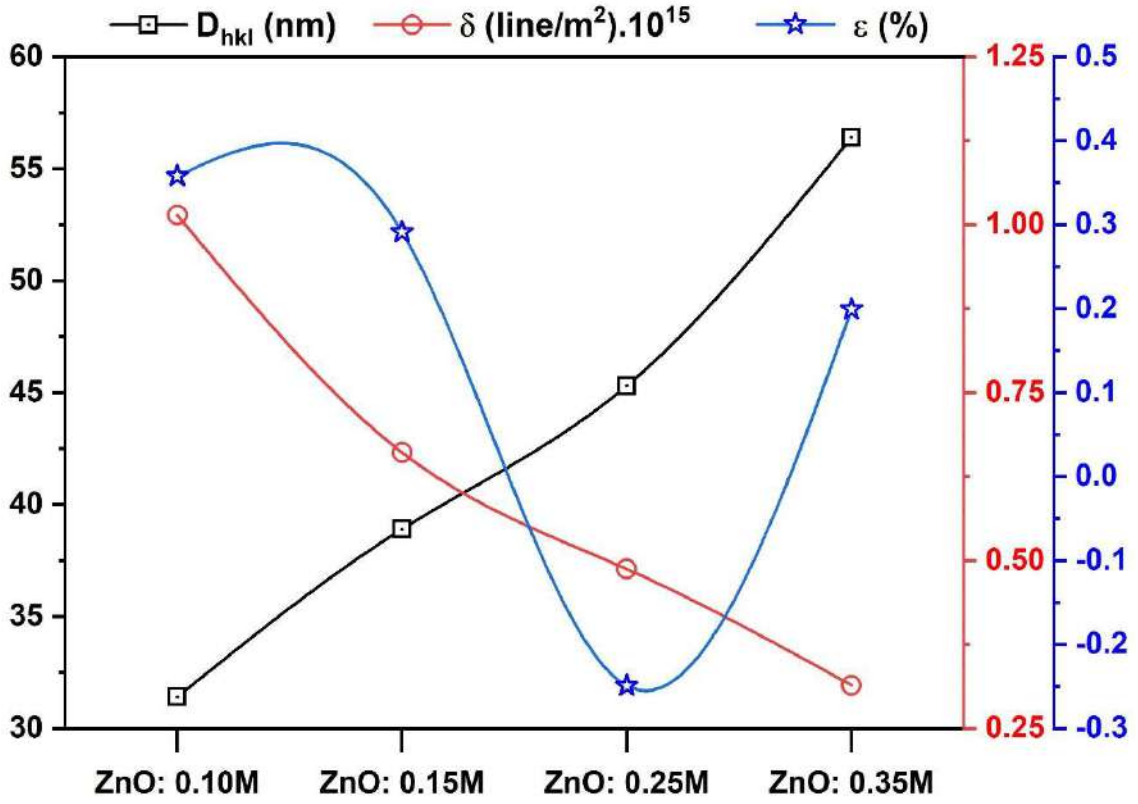

Figure 4.5: Variation in crystallite size, mean strain, and dislocation density of undoped ZnO thin films as a function of precursor molarity.

4.2.2. Scanning electron microscopy (SEM) characterization

Figure 4.6 shows the scanning electron microscopy (SEM) image of undoped ZnO thin film deposited at 450°C. This SEM image reveals a microstructure with fine grains dominated by equiaxed grains, which mean radius in rang of 50 to 70 nm (Table 4.3). A log-normal grain size distribution (histogram and frequency curve) in the inset shows a mean of 60.81 nm, median ~50 nm, standard deviation of 23.64 nm, and outliers >100 nm (red bars), aligning with the observed heterogeneity. The majority of grains align with the statistical mean, exhibiting uniform size and well-defined boundaries, suggesting controlled nucleation during processing.

In addition, we have noticed dispersed elongated grains (average diameter >100 nm, ~3.3σ from the mean) close to the image periphery. These grains correlate with the histogram's skew and are caused by the variations of localized growth or by the unstable cooling rates.

On the other hand, we believe that the micro-hardness of thin films is increased by the presence of smaller grains (average diameter <50 nm) through so-called Hall-Petch strengthening,

Conversely, the larger grains (average diameter >100 nm) can act as sites of crack initiation, reducing ductility [8, 153].

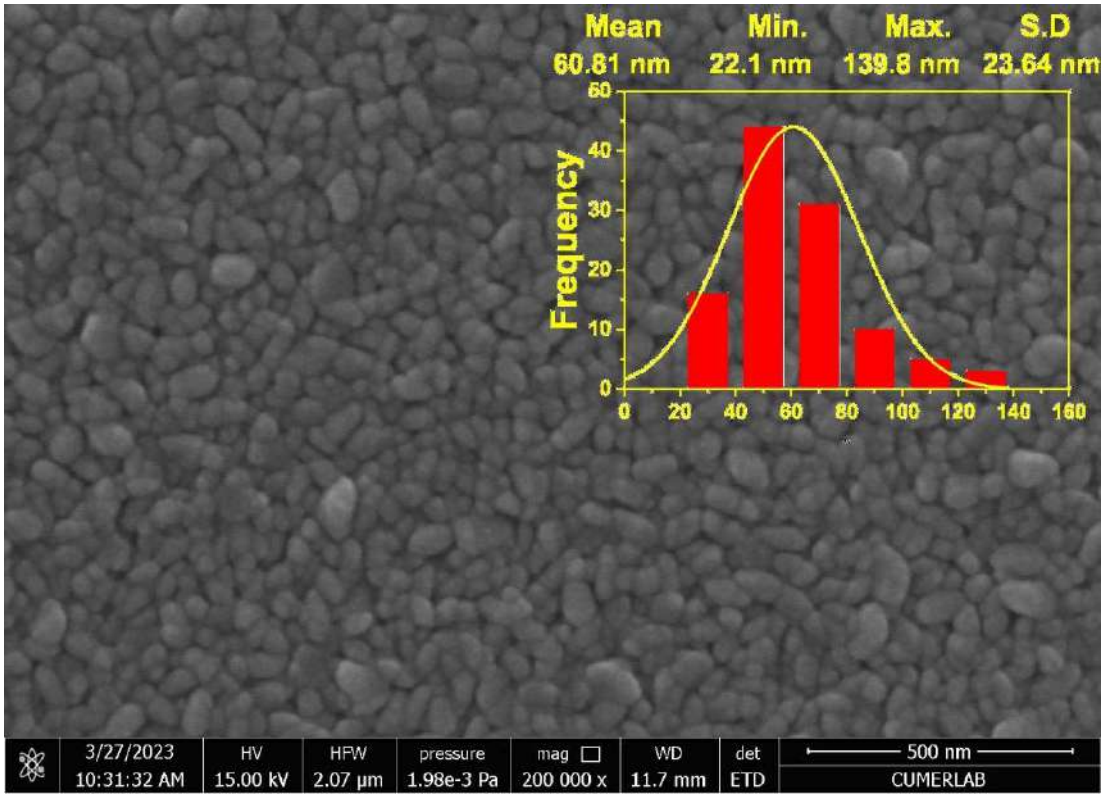

Figure 4.6: SEM image of undoped ZnO thin films prepared using the spray pyrolysis technique at 450°C.

Table 4.3: Grain size, roughness, and thickness parameters of undoped ZnO nanostructured films.

Samples	D: Particle size				Ra	t
	Mean (nm)	Min. (nm)	Max. (nm)	SD (nm)	(nm)	(nm)
Undoped ZnO	60.81	22.10	139.8	23.64	27.00	261

Analysis of 3D-SEM image of undoped ZnO thin films on glass substrate

Figure 4.7 shows the 3D-scanning electron microscopy image of the topographical representation of *undoped ZnO* thin film prepared using SPT at 450°C. This image reveals a

thin film heterogeneous surface with a granular microstructure; this surface has a certain roughness. We have noticed that the surface morphology shows a irregular shaped grains with varying heights.

In addition, we noticed that the grain boundaries are not well defined, which suggests a coalescence phenomenon during the deposition process, and the surface roughness is intense. Also, the thin film presents size and shape heterogeneity, featuring larger clusters (>0.5 µm) interspersed with finer grains (<0.2 µm). Also, the thin film presents the heterogeneity of the shape and grain size, with larger clusters ($cluster\ size\ >\ 0.5\ \mu m$) interspersed with finer grains ($average\ grain\ size\ <\ 0.2\ \mu m$). Finally, the quantitative analysis using Gwyddion software shows roughness parameters: average roughness ($Ra\sim 27nm$), root mean square roughness ($R_q\ \approx\ 36\ nm$), and peak-to-valley height ($R_z\ \approx\ 204\ nm$), which reflects important variability in the thin films' topography. These parameter values suggest an incomplete nucleation process or (and) a high deposition process kinetics of the thin films that leads to agglomeration and possible Ostwald ripening [8].

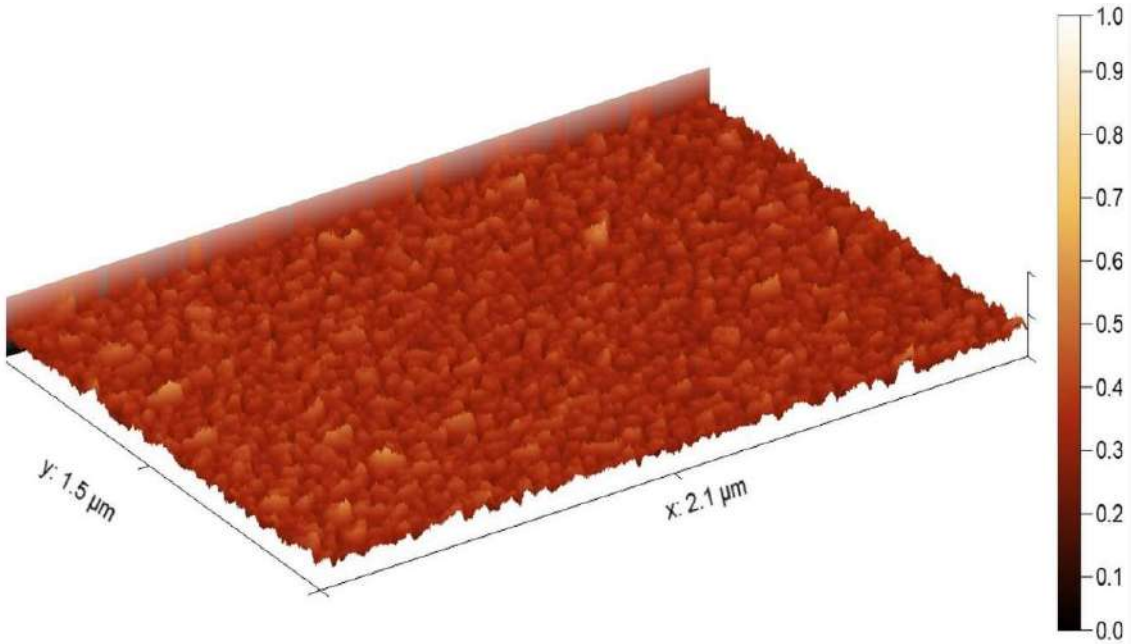

Figure 4.7: Three-dimensional scanning electron microscopy image of the topographical representation of undoped ZnO thin film prepared using SPT at 450°C.

Figure 4.8: Profile curves measured along the lines shown on the SEM image of *undoped ZnO* thin films prepared by the spray pyrolysis technique at 450°C. It is known that the physics, electric, chemical, and optical performances of thin films are affected by their microstructure. Indeed, the surface roughness may increase the electrical resistance of contact, but it could favor

the charge percolation through interconnected grains. On the other hand, the larger grains play the role of stress concentrators, reducing fracture toughness, but the finer grains enhance the microhardness because a mechanical process called Hall-Petch strengthening. The optical behavior of the thin films can be altered by the films' roughness. Indeed, incident light can be scattered, and its transmittance degraded by the films' roughness, in optoelectronic devices.

Functionally, the irregular surface may compromise the interfacial adhesion between the deposited thin films and the glass substrate, which increases the risk of delamination under thermal micro-stresses and provides reactive sites that accelerate corrosion.

Finally, we can summarize some computed parameters of the thin film's surface morphology. The moderate irregularity of the surface is indicated by the roughness average value of $R_a = 27.00\,nm$, and its non-uniform height distribution is given by the root mean square roughness $(R_q = 35.59\,nm)$. This type of distribution is caused by the presence of valleys or localized peaks.

In our calculation, we have found that the maximum height between a peak and a valley is $R_t = 272.76\,nm$, which indicates an important topographical variation with valleys ($R_v = 181.37\,nm$) The maximum peak-to-valley height $(R_t)of\ 272.76\,nm$ highlights significant topographical variation, with peaks ($R_p = 91.39\,nm$) dominated by valleys ($R_v = 181.37\,nm$). We noted that the negative skewness $(R_{sk})of\ -779.49\,nm$ confirms this asymmetry, which shows a thin film surface dominated by deeper valleys.[8, 202, 208, 212].

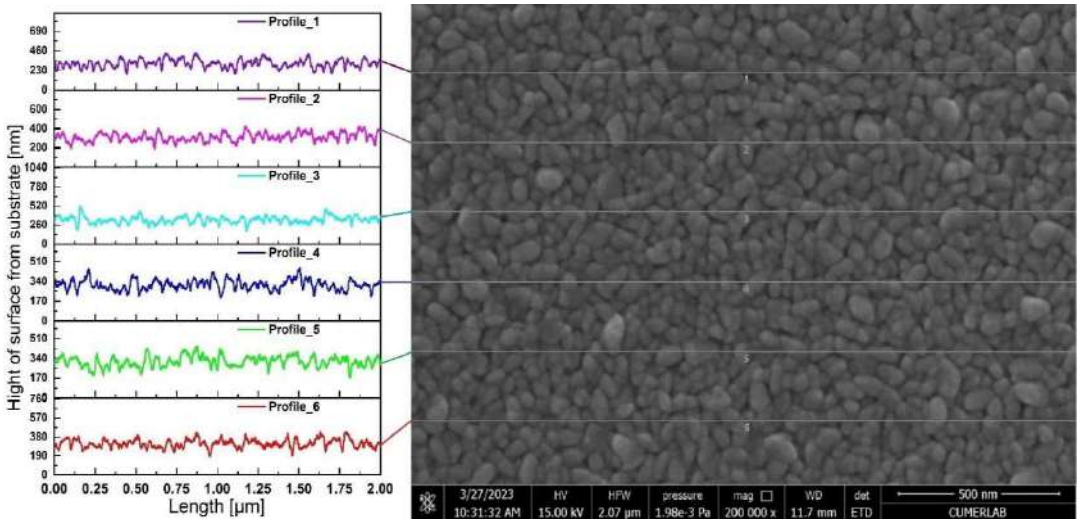

Figure 4.8: Profile curves measured along the lines shown on the SEM image of undoped ZnO thin films prepared by the spray pyrolysis technique at 450°C.

For the analysis of the thin film surface by using wave function models, we have found that the waviness parameters ($W_a = 18.75\,nm, W_q = 23.73\,nm$) are smaller than the roughness parameter values, which indicates that at a finer scale, the roughness property dominates the large-scale undulations. We have found a maximum waviness height equal to ($W_y = 110.06\,nm$).

In addition, we have found that the utilization of spatial parameters enhances and completes our description. Indeed, the computed values of the mean spacing (S_m) of $29.27\,nm$ and the average wavelength (λ_a) of $25.80\,nm$ reveal the presence of regularly spaced surface features (grains, valleys, peaks). The slope variation of the surface or its gradient can be evaluated by the hybrid parameters; indeed, the average absolute slope ($\Delta_a = 7.97\ \mu m^{-1}$) and the root mean square (RMS) slope ($\Delta_q = 10.03\ \mu m^{-1}$) indicate a low gradient of surface variation or, in other words, suggest moderate slope variations [8, 202, 208, 212] .

4.2.3. Optical properties of undoped ZnO thin films

4.2.3. a. Study of the transmission of undoped zinc oxide thin films.

Figure 4.9 shows the transmission spectra of ZnO thin film deposited on microscope glass substrates at 450°C in as-deposited state (no annealing). For this figure, different molarities (0.05-0.40 mole/L) of precursor can extract how these constitute the transmission at UV-vis wavelengths for undoped zinc oxide (ZnO) thin films measured by UV-vis spectroscopy On this figure all the films appear highly transparent in visible range (400-800 nm). Due to fundamental band gap absorption, a distinct transmittance drop is present in the UV region for zinc oxide ZnO [296]. Figure 4.9 shows that a film with 0.05 mole/L there is a fairly sharp increase in transmittance in the 390-420 nm range compared with hexagonal ZnO excitonic absorption [297, 298]. As can be seen in the inset, the absorption edge shifts slightly to blue as the molarity increases from 0.05 to 0.20 mole/L indicating an increase optical band gap possibly depending on anisotropic crystallite size or strain [299]. However, molarities (greater than 0.20 mole/L) are followed by the red shift suggesting a reduced band gap. In summary, these results emphasize the necessity of precursor concentration to manipulate the optical features of ZnO films suitable for applications such as transparent conductors or solar cells [300].

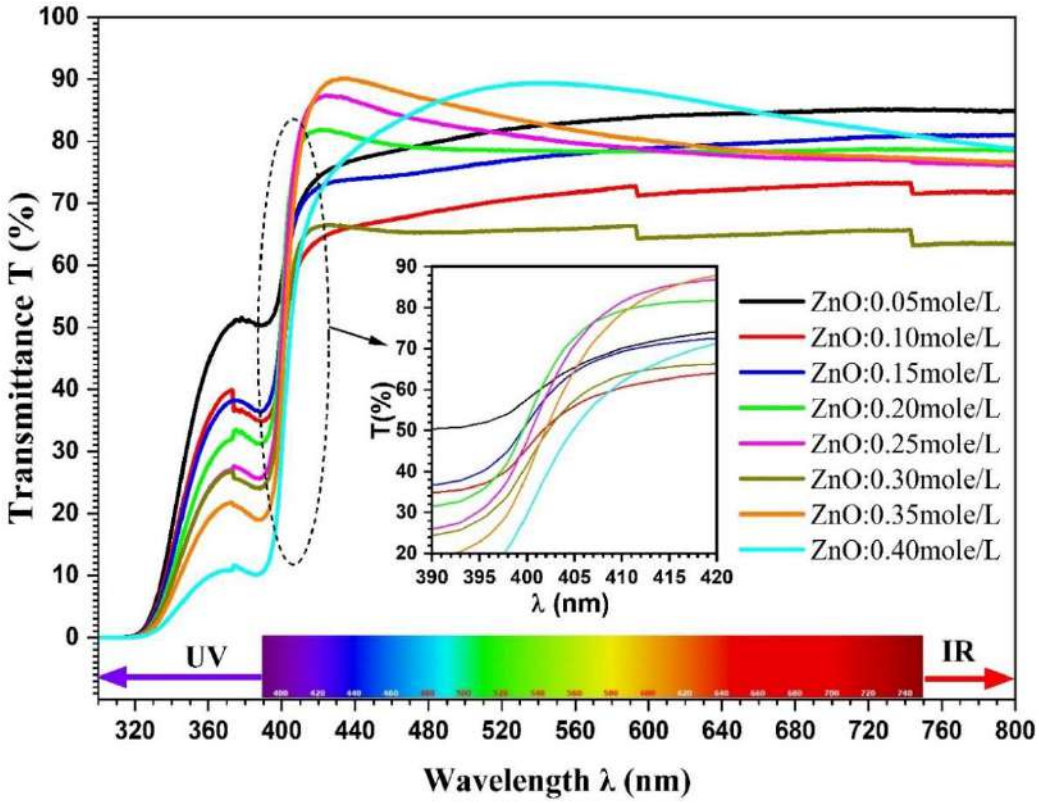

Figure 4.9: Transmission spectra of undoped ZnO thin film samples for different precursor molarities.

Tauc plots of $(\alpha h\nu)^2 vs. h\nu$ for undoped ZnO film prepared by precursor solutions containing 0.05–0.4 M for each will appear on Figure 4.10. Linear portions of the derived and extrapolated (from each linear portion) two sets for band-gap values, E_{g1} and E_{g2}, that move very little with the molarity of precursor. Eg₁ decreases from 3.814 eV at 0.05 M to 3.761 eV at 0.40 M. E_{g2} is between 3.805 and with no strict linear trend. E_{g1} narrows slightly at higher concentrations, which is likely believed to be only due to film thickness, larger crystallites and higher concentration leading to increased defect density that broaden the Burstein–Moss structure and broadens the absorption edge [301]. Thin film gaps correspondingly increased (all measured gaps > bulk ZnO at room temperature ~ 3.37 eV [302] due to these effects. In ZnO spray deposited, the optical band gap was also shown to be successfully tuned via precursor concentration in Ref where it is reported precursor molarity eventually formed thick and much more crystalline films and led to a slight band gap red shift [303]. Table 4.4 datasets the band gap and Urbach disorder energy.

Table 4.4: Optical bandgap and Urbach disorder energies of undoped ZnO thin film for varying precursor molarities.

Molality	Optical energy bandgap		Urbach energy disorder
mole/L	E_{g1} [eV]	E_{g2} [eV]	E_u [meV]
0.05	3.814	3.898	172.76
0.10	3.809	3.850	109.43
0.15	3.804	3.824	82.80
0.20	3.784	3.839	50.68
0.25	3.775	3.857	50.93
0.30	3.790	3.833	77.30
0.35	3.765	3.805	52.22
0.40	3.761	3.820	61.63

Plot of an optical bandgap energy vs molar precursor concentration ranging from 0.05 to 0.40 mole/L; the two bandgap energies, E_{g1} (blue) and E_{g2} (red) shown in Figure 4.11. E_{g1} and E_{g2} drop immensely from 0.05 mole/L having 3.814 and 3.898 eV respectively to (more or less) 3.804 and 3.824 eV at 0.15 mole/L respectively as well. E_{g2} then increases to an initial maximum of 3.857 eV at 0.25 mole/L whereas E_{g1} drops to a concentration of the same ~0.15 mole/L. Beyond 0.25 mole/L, both curves tend a local minimum near 0.35 mole/L ($E_{g1} = 3.765\ eV$), $E_{g2} = 3.805\ eV$) and then recover a bit at 0.40 mole/L.

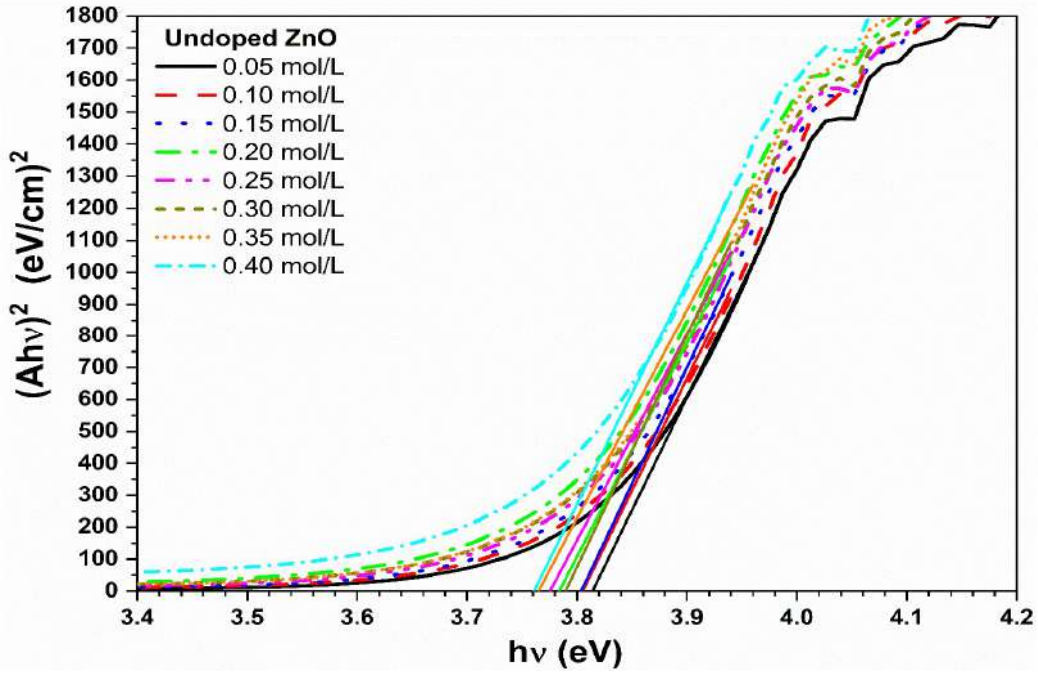

Figure 4.10: Plot of $(\alpha h\nu)^2$ versus incident photon energy $(h\nu)$ of undoped ZnO thin films at different precursor molarities.

These non-monotonic effects are due to the interaction of microstructure and carrier filling: deposition parameters lead to changes in grain size, defect density [236-238], and film thickness which in turn tune optical transitions via band-gap renormalization and the Burstein–Moss shift [142, 302, 304], both in a complementary way.

Per the paragraph above, The Tauc plot of ZnO thin film analysis shows two direct bandgaps (as in table 4.1) attributed to structural or electronic heterogeneities [305]. The dual bandgaps are seminal to the electronic-optical properties of the material, as they dictate absorbance, emission and charge-carrier dynamics [164]; where the structural/ electronic defects (e.g., oxygen vacancies or zinc interstitials) introduce localized electronic states allowing optically multiple transitions they cause tightly confined bandgap (here described by 3.814 eV), which associate with defect-rich places and a broad defect-induced other state [306]. Nanocrystalline domains may further fractionize the bandgap by causing quantum confinement, a size-dependent phenomenon exhibited in nanowires and nanostructured materials [307].

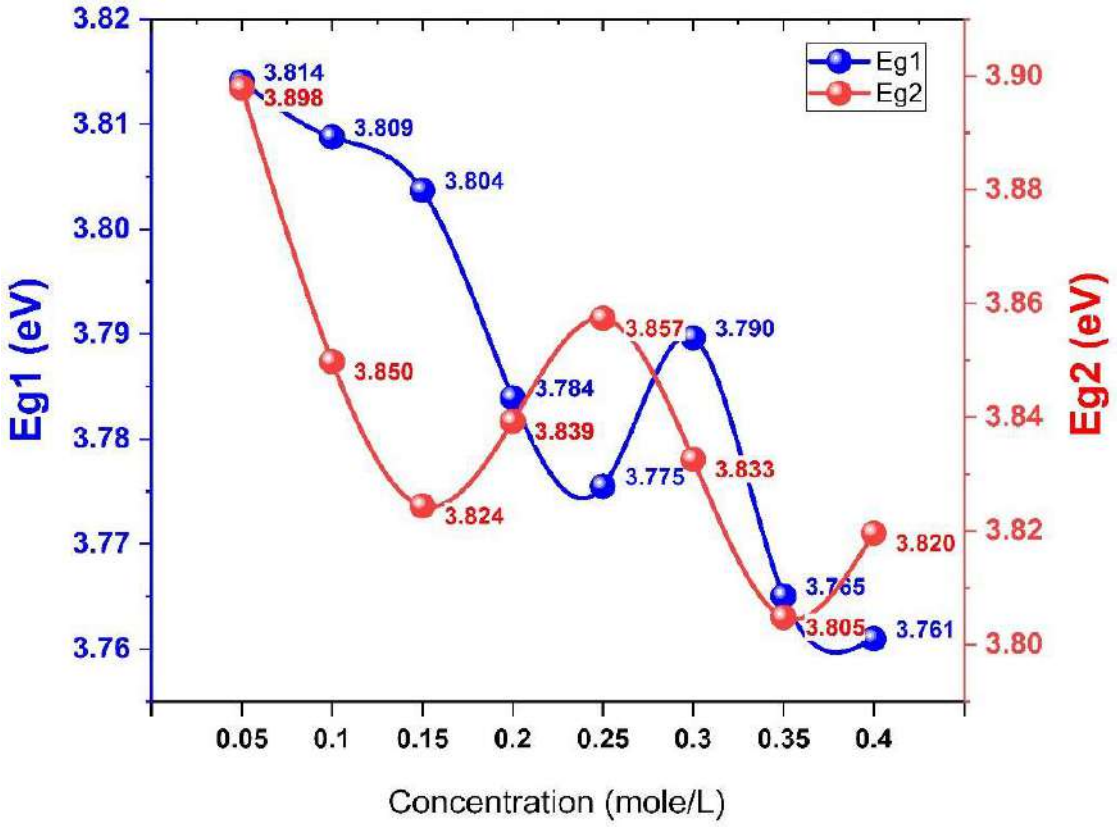

Figure 4.11: The variation of Urbach energy and band gap energy of undoped ZnO thin films as a function of precursor molarity.

This is supplemented by dopants/impurities getting other intermediate energy states and inducing optical transitions [308]. Cellular size characterization in a disordered systems using

the Tauc method to almost directly measure bandgaps from $(\alpha h\nu)^2$ vs. photon energy $(h\nu)$ but with restrictions through the assumptions of parabolic bands and small Coulomb interaction [309]. Dual bandgaps indicate departure from idealized behavior necessitating sophisticated models to further resolve the phase or defect specific contributions [310]. This investigation demonstrates opportunities to manipulate the optical properties of ZnO for these two future applications where bandgap tuning [311], e.g. by adjusting synthesis parameters such as annealing or doping levels. To ensure the best performance in photonics and energy devices, complementary techniques like XRD or photoluminescence spectroscopy are necessary in order to corroborate these transitions [306].

Figure 4.12 (a-h) provides plots of natural log of absorbance $(ln(A))$ v/s transmitted photon energy $(h\nu)$ for ZnO thin films free of dopant that were prepared by the thermal evaporation of precursor sources soles differing precursor molarities. These plots are used to obtain Urbach's disorder energy (E_u). The lower energy end of absorption edge is accompanied by a linear portion that represents Urbach's tail [312, 313], originating from exponential band tails due to static disorder, thermal fluctuations and the defects in materials [313]. Fig. 4.12-a-: When $ln(A)$ is plotted against $h\nu$, the urbach energy is directly determined by the slope of the linear region and E_u depends on Urbach energy that is inversely proportional to the slope [312]. As evident from the figures 4.12 (a-h), the Urbach energy (E_u) is dependent on the precursors doping used for fabrication of different molarities of ZnO thin films Urbach energy variation with precursor molarity. The E_u values for various molarities are given as: 172.76 meV (a); 109.43 meV (b); 82.88 meV (c); 50.68 meV (d); 58.93 mev (e); 77.30 mev (g); 52.22 mev (h) each subfigure .. Lower Urbach energy has been observed to indicate lower disorder in the optical absorption edge resulting in a better crystalline quality of the thin film [312]. The changes in E_u with precursor molarity suggest strong correlation between the synthesis conditions, structural disorder and defect density in ZnO thin films, which are indeed optical properties affecting parameters.

Figure 4.13 shows the optical bandgap E_{g1}, Urbach disorder energy (E_u) and refractive index (n) in undoped ZnO thin films as function of molarity of precursor (0.05–0.40 mole/L). Optical bandgap: 0.05eV (0.05 mole/L) − 3.814 to 0.40eV (0-Mole/L), staring slightly rising at 3.790 V (0.30eL). This observed bandgap reduction in ZnO thin films has been reported to result from increased defect density or structural disorder at levels well-characterized by the precursor concentration. Here Urbach energy (E_u), a structural disorder metric also declines (from 172.76

meV at 0.00 mole/L down to 50.68 meV) until 0.20 mole/L suggesting better crystalline quality up to this point. Simultaneously, E_u increases modestly beyond 0.20 mole/L indicating an increase in disorder (likely stemming from excess precursor-induced lattice strain or secondary phase growth)

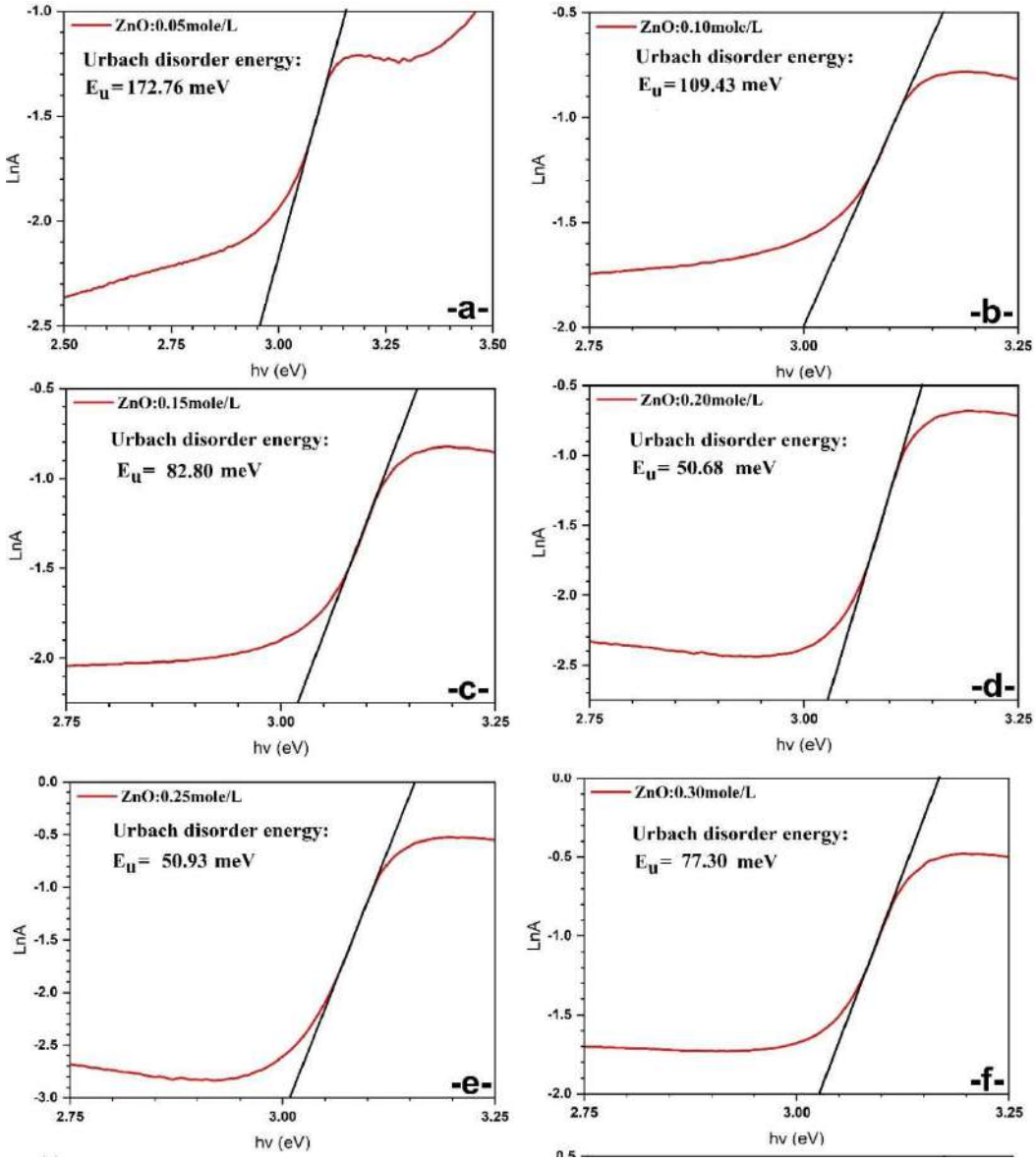

Figure 4.12 (a-f): Plot of $Ln(A)$ versus incident photon energy (hv) of undoped ZnO thin films at different precursor molarities.

The refractive index (n) increases with monotonically from 2.4486 (0.05 mole/L) as in a tighter film arrangement or larger grain size at higher concentrations.. The anomalous rise in E_{g1} and E_u at 0.30 mole/L most notably arises from compositional fluctuations or non-densification of the film during synthesis, due to local composition fluctuations. This suggests the fine balance of precursor availability vs structural order and optical performance in ZnO thin films.

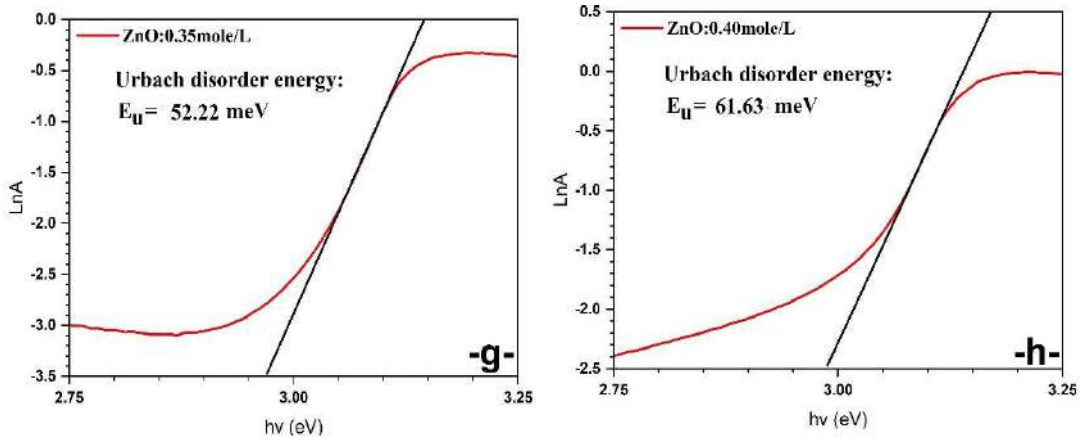

Figure 4.12 (g-h): Plot of $Ln(A)$ versus incident photon energy $(h\nu)$ of undoped ZnO thin films at different precursor molarities.

It has been reported that the changes in the amount of precursor have an important influence on the structure and optical properties of semiconductor thin films, included ZnO thin films. For instance, when you increase the precursor amount, it drives to a lower optical bandgap in materials such as Mg-doped ZnO and CuS due to defects or strain in the structure [314, 315]. Sometimes, higher concentrations result in less transparency (around 57–88%) because thicker or denser films scatter light more [55]. Also, as you raise the precursor levels, the size of the crystallites tends to shrink, which can narrow the bandgap because of quantum effects[316]. However, if the precursor amount gets too high, it can actually hurt the crystalline quality, like we see with GaN films, where too much precursor slows down deposition rates and adds defects [317].

Table 4.5: First optical bandgap and refractive index of undoped ZnO thin films have been computed for various precursor molarities through different analytical methods.

Molality	Optical energy bandgap	Refractive index (n)					
			Reddy-Nazeer [139]	Kumar-Singh[141]	Moss[142]	Ravindra [3]	Herve-Vandamme [144]
mole/L	E_{g1}(eV)	Exp.	Eq. (2.21)	Eq. (2.22)	Eq. (2.23)	Eq. (2.24)	Eq. (2.25)
0.05	3.814	2.4486	2.5850	2.1868	2.2340	1.7193	2.1180
0.10	3.809	2.4501	2.5860	2.1878	2.2348	1.7226	2.1192
0.15	3.804	2.4515	2.5869	2.1887	2.2355	1.7257	2.1204
0.20	3.784	2.4569	2.5906	2.1924	2.2384	1.7380	2.1249
0.25	3.775	2.4592	2.5922	2.1940	2.2397	1.7432	2.1268
0.30	3.790	2.4553	2.5896	2.1913	2.2376	1.7344	2.1236
0.35	3.765	2.4621	2.5942	2.1960	2.2412	1.7497	2.1292
0.40	3.761	2.4632	2.5950	2.1967	2.2418	1.7522	2.1301

In addition, the type of precursor you use can change properties like the refractive index and resistivity. For example, in NiO films, using nickel nitrate gives values that match what is usually reported [244]. These trends show how the amount of precursor interacts with structural issues and the optical performance in semiconductors.

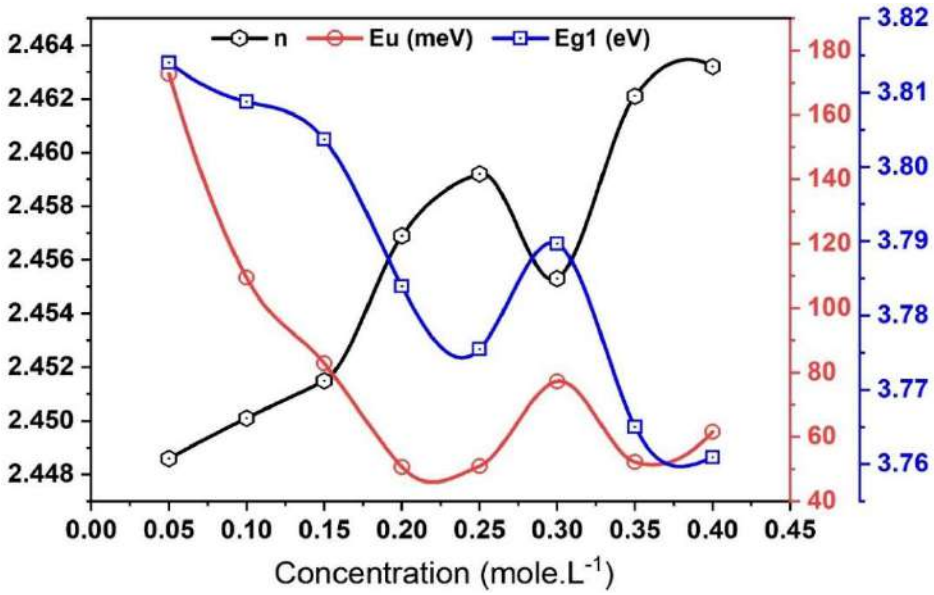

Figure 4.13: Variation of First optical bandgap, Urbach disorder energies, and refractive index (n) of undoped ZnO thin films as a function of precursor molarity.

Table 4.5 provides an overview of the computations performed concerning the optical parameters of undoped zinc oxide (ZnO) thin films. The values calculated include the first optical bandgap energy, Urbach disorder energy, and refractive index. It is noted that the first optical bandgap (E_{g1} value) of undoped ZnO thin films drops gradually from 3.814 eV to 3.761 eV as precursor molality increases from 0.05 to 0.40 mole/L. This is a result of an increase in defect character that leads to bandgap narrowing [236-238]. It is reported that n_{exp}so increases from 2.4486 to 2.4632, which implies higher optical density with, increased molality. Most theoretical models supporting this claim differ in varying degrees with reported experimental results. The Kumar-Singh model [141], Moss [142], Ravindra [3],and Herve-Vandame [144] models consistently underestimate n at all concentrations. Even though the Reddy-Nazeer model [139] was shown to overestimate refractive index values, the claim suggesting it was in closest, alignment with n_{ex} at higher molarities can be made due to their considerations of bandgap and electronic polarization effects, which seem to apply at such concentrations. The discrepancies among the models highlight the shortcomings of purely empirical approaches trying to explain the defect-induced optical [140, 247-249].

4.3 Analysis and interpretation of results for Ba-doped ZnO thin films

4.3.1. Structural properties of Ba-doped ZnO thin films

Figure 4.14 depicts the X-ray diffraction (XRD) patterns of Ba doped ZnO thin films with different concentration of barium, deposited on glass substrates, which has been heated to 450°C. It can be see that the patterns display the reflection planes (100), (002), (101), (102), and (103) that correspond to following average Bragg angles 31.563°, 34.287°, 36.011°, 47.424°, and 62.690°, respectively. These observations are compatible with the structure of hexagonal wurtzite of ZnO as indicated in the JCPDS card no 36-1451.

We remark that the peaks, which correspond to the (002) reflection planes located at ~34.287° have the most important intensity. The preferential direction of growth is along the c-axis of the hexagonal wurtzite structure. It have been reported that c-axis orientation minimizes the surface energy and stabilizes the crystalline structure during the process of film deposition. The absence of additional peaks confirms the phase purity of the ZnO thin films, with no detectable secondary phases such as $Zn(OH)_2$, $cubic\ ZnO$, or pure barium or barium oxides , which aligns with the expected hexagonal wurtzite structure. We can assume that barium atoms may have diffused into $ZnO's$ hexagonal structure by substitution or into vacant sites [268]. As shown in Table 4.6, the calculated lattice parameters from the diffraction data reveal slight deviations from standard values: the average "a" and "b" parameters ($a_{ave} = b_{ave} = 3.26832$ Å) and the "c" parameter ($c_{ave} = 5.22654$ Å) are marginally larger than the reference values ($a_{std} = b_{std} = 3.2498$ Å; $c_{std} = 5.2066$ Å).

Table 4.6: Lattice parameters of ZnO: x % Ba thin films (x = 0, 2, 4, 6 and 8).

	ZnO (hexagonal)				
Samples	a_{hex} (Å)	c_{hex}(Å)	c/a	V_{hex}(Å^3)	APF
Undoped ZnO	3.24406	5.32131	1.64032	48.4984	0.73717
Ba-2% ZnO	3.28222	5.24882	1.59917	48.9698	0.75614
Ba-4% ZnO	3.26268	5.21592	1.59866	48.0851	0.75638
Ba-6% ZnO	3.26702	5.22836	1.60034	48.3281	0.75559
Ba-8% ZnO	3.26135	5.21306	1.59844	48.0196	0.75649
Average value	**3.26832**	**5.22654**	**1.59915**	**48.3506**	**0.75615**

Finally, we have noted that the variations in precursor molarity may affect the dynamics of the nucleation phenomenon. It appears that the higher molarities enhance the crystallite growth by increasing precursor abundance [110, 150, 151, 295].

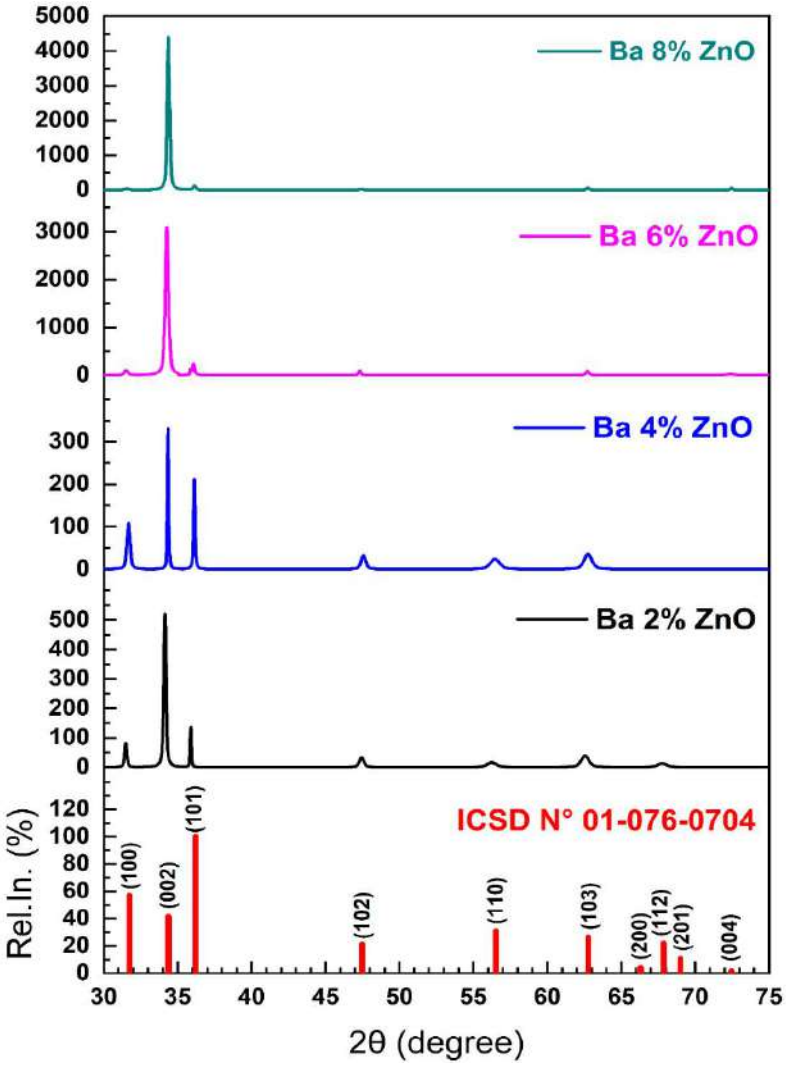

Figure 4.14: X-ray diffraction diffractograms of Ba doped ZnO thin films prepared at 450 °C, with different concentration of barium.

Figure 4.15 shows the dependence of the detected Bragg angle on the Ba doping percentage. By analyzing the deviation $\Delta(2\theta)$ values in Ba-doped ZnO thin films, we have noticed a distinct trend linked to doping concentration and crystallographic orientation. At 2% Ba doping, most diffraction peaks [(100), (002), (101), (103)] exhibit positive $\Delta(2\theta)$ deviations in the range of (0.099 to 0.2802°), which suggest a lattice expansion relative to the reference ZnO structure (JCPDS 36-1456). This expansion is probably caused by the substitution of smaller Zn^{2+} ions (ions radius = 0.74Å) with larger Ba^{2+} ions (ions radius = 0.1.35Å), which induces a tensile micro-strain in the crystalline structure. On the other hand, at 4%Ba doping, we have noticed

that the peak corresponding to the (102) reflection plane presents a negative deviation ($\Delta(2\theta) = -0.0221$), which indicates the presence of induced compressive micro-strain or localized lattice contraction. These internal micro-deformations are caused by the formation of defects or the clustering phenomenon occurred at higher dopant concentrations. On the other one, we have remarked that the peak corresponding to the (101) reflection planes, exhibits the largest Bragg angle deviation, which indicates an enhanced sensitivity to the incorporation of Ba^{2+} ions along this crystalline orientation [258].

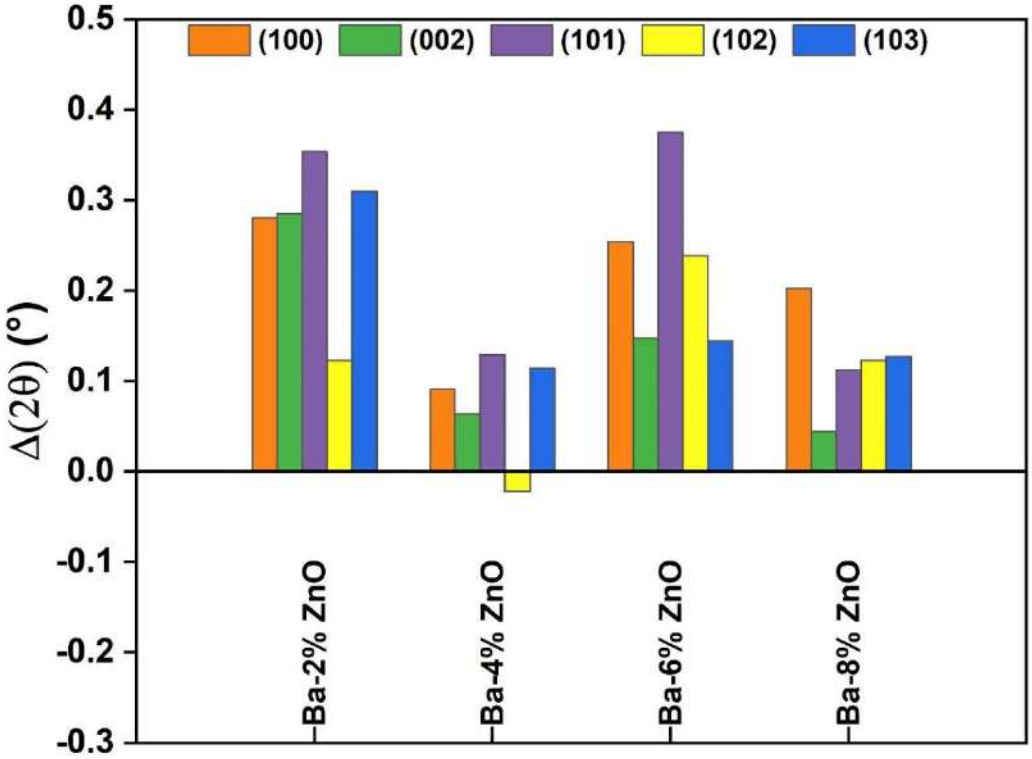

Figure 4.15: Variation of $\Delta(2\theta)$ values as a function of Ba doping atomic percentage.

Figure 4.16 shows the variation of the texture coefficient (TC) of selected reflection planes as function of Ba doping percentage, for $Ba - doped\ ZnO$ thin films synthetized at 450°C.

Indeed, the texture coefficient (TC) analysis of $Ba - doped\ ZnO$ thin films shows trends across crystallographic planes. We have noticed for the (002) plane, the texture coefficient (TC) peak is 3.2149 for $Ba - 2\%\ ZnO$, which indicates a strong preferential growth. However, the texture coefficient (TC) increases to 0.4659 at 4% Ba, which suggests a decrease in the texturation trend in this orientation, caused by the micro-deformation in the lattice or by a competing growth mechanism. We have noticed, however, that at 8% Ba, the texture coefficient (TC) rises again to 0.9477, to approach the dominant orientation, which implies the recovery of the crystalline microstructure or the relaxation of stress.

In addition, the other reflection planes, such as (100) and (101), show a decrease in the texture coefficients (TCs) with increased doping. The texture coefficient of (100) decreases from 0.5032 (2% Ba) to 0.0077 (8% Ba), while the texture coefficient of (101) decreases from 0.8416 to 0.0249.

This reduction indicates a shift toward (002) orientation at a higher level of doping. Finally, the (102) and (103) reflection planes also present minimal texture coefficients ($TCs < 0.05\ at\ 8\%\ Ba$), which emphasizes again an homogenization of texture.

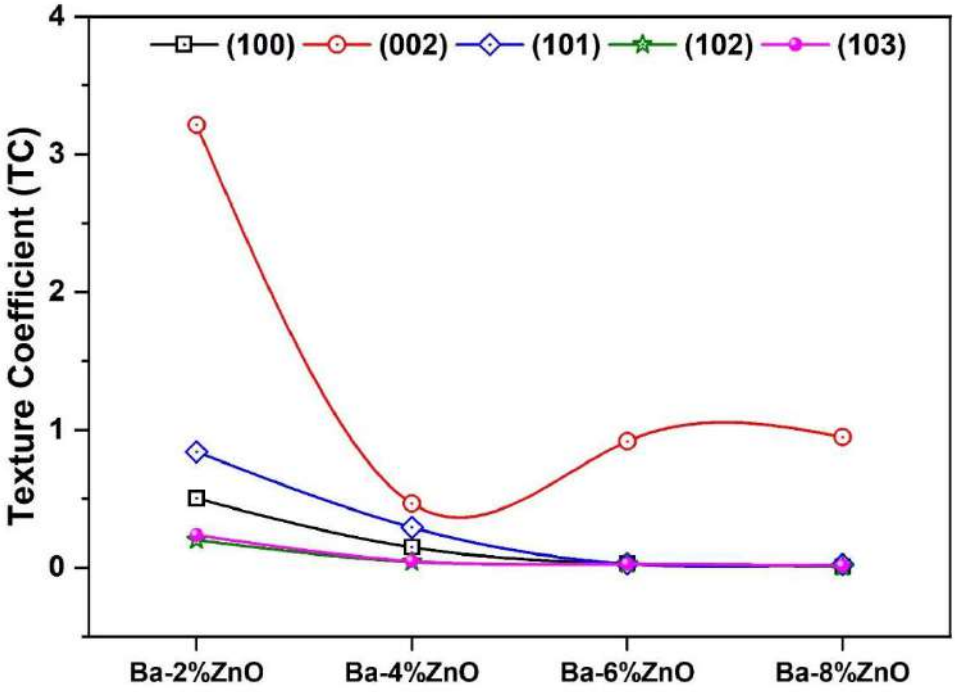

Figure 4.16: Texture coefficients (TCs) for selected crystallographic planes in Ba-doped ZnO thin films as a function of barium content (at.%).

Table 4.7 shows that the crystallite size contrary proportional to mean strain, this may be attributed to the increment of the defects and empty spaces in the crystalline structure as crystallite size decreases. The deviation in the values of the lattice constant of the as-prepared $Ba-doped\ ZnO$ thin films from the bulk ZnO standards value indicates the presence of induced micro-strain in the thin films during the deposition process. The origin of internal micro-strain is related to the grain size of the film, which depends upon to deposition condition of the films [161].

This hypothesis is corroborated by the correlation between the alterations in mean micro-strain and the dislocation density, as evidenced by the changes in barium doping percentage, as illustrated in Figure 4.17. It has been observed that the thin film with the optimal structural

properties shows the lowest mean micro-strain value, which, in consequence, affects the rate and degree of the crystallization pheomenon [162].

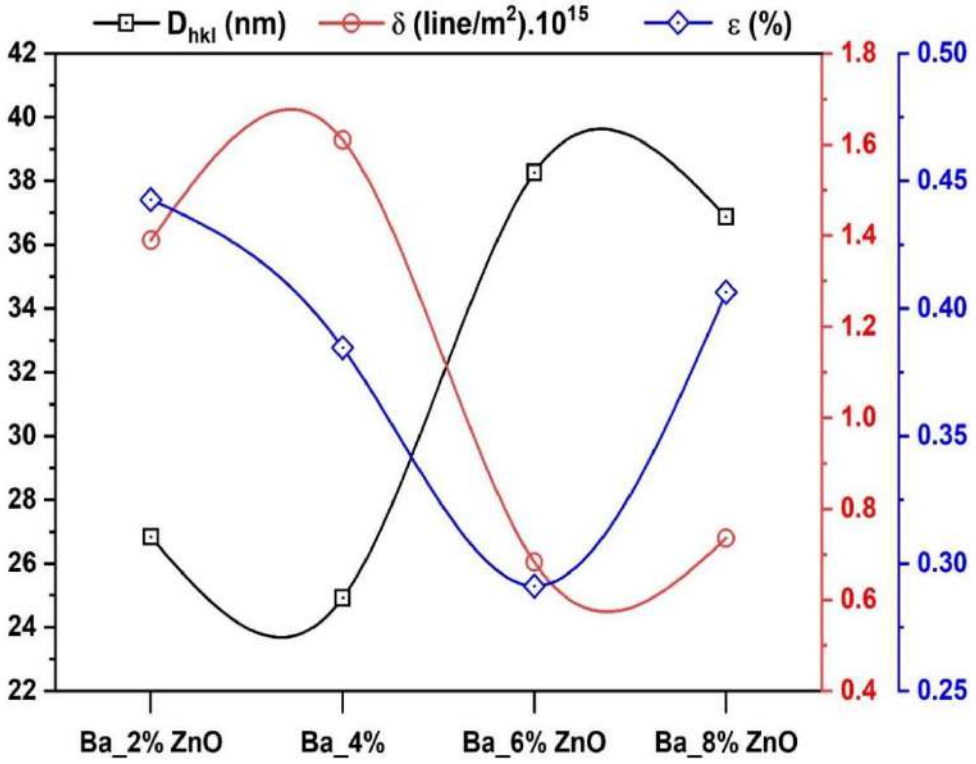

Figure 4.17: Variation in crystallite size, mean strain, and dislocation density of Ba doped ZnO thin films as a function of different Ba percentage.

Table 4.7: Microstructural parameters of ZnO: x % Ba thin films (x = 0, 2, 4, 6 and 8).

	ZnO (hexagonal)				
	Lattice parameters		Crystallite Size	Micro Strain	Dislocation density
Samples	a_{hex} (Å)	c_{hex}(Å)	D_{hkl}(nm)	ε (%)	$\delta \times 10^{15}(m^{-2})$
Undoped ZnO	3.24406	5.32131	38.9	0.2910	0.6608
Ba-2% ZnO	3.28222	5.24882	26.83	0.4427	1.3896
Ba-4% ZnO	3.26268	5.21592	24.92	0.3846	1.6100
Ba-6% ZnO	3.26702	5.22836	38.26	0.2912	0.6831
Ba-8% ZnO	3.26135	5.21306	36.87	0.4063	0.7355

4.3.1. Scanning electron microscopy (SEM) characterization

4.3.1. a- Morphological properties of Ba-doped ZnO thin films

Figures 4.18(a) through 4.18(d) illustrate the morphological features of Ba-doped ZnO thin films. All samples were deposited at 450°C on transparent glass substrates.

Figure 4.18(a) displays the SEM micrograph of a 2% Ba-doped film. The surface shows a granular microstructure dominated by equiaxed grains. Grain sizes range from approximately 50 to 70 nm. The inset histogram confirms a lognormal distribution. The mean grain size is 61.7 nm, with a median of 57.9 nm. Most grains cluster near 58 nm, suggesting uniform nucleation. However, some larger grains reach 120 nm. These likely represent growth anomalies. Grain boundaries are clear, and no porosity is visible. This indicates a relatively pure microstructure. Figure 4.18(b) shows another 2% Ba-doped film at 200,000× magnification. The grains are predominantly equiaxed. However, elongated grains appear in the lower left quadrant. The mean grain size is 64.33 nm, with a median of ~50 nm. The standard deviation is high at 36.23 nm. This suggests heterogeneous grain growth. Non-uniform cooling or incomplete recrystallization may cause this variation. While smaller grains enhance hardness via Hall-Petch strengthening, outliers larger than 100 nm may act as stress concentrators.

In contrast, Figure 4.18(c) reveals a fine-grained microstructure. The mean grain size drops to approximately 23 nm. The range spans 14.3 to 43.5 nm, with a standard deviation of 6.3 nm. The histogram shows a right-skewed distribution with a peak near 23 nm. Most grains are uniform and equiaxed. Clean boundaries indicate high purity and nonexistent porosity. The moderate standard deviation suggests some heterogeneity, possibly from uneven cooling. These fine grains should significantly boost hardness.

Table 4.8: The grain size, roughness, and thickness parameters of undoped and doped ZnO nanostructured films.

Samples	D: Particle size				Ra	t
	Mean (nm)	Min. (nm)	Max. (nm)	SD (nm)	(nm)	(nm)
Undoped ZnO	60.81	22.10	139.8	23.64	27.00	261
Ba2% ZnO	61.85	34.42	120.02	19.87	35.08	242
Ba4% ZnO	64.33	24.50	174.8	36.23	58.10	275
Ba6% ZnO	23.14	14.30	43.50	6.28	34.29	356
Ba8% ZnO	21.96	13.5	33.20	4.18	39.19	320

Finally, Figure 4.18(d) presents a similar fine-grained structure at 200,000× magnification. Most grains are equiaxed and uniformly distributed. Some darker regions hint at defects or secondary phases. Grain boundaries appear slightly diffuse, but significant porosity is absent. The mean grain size is 21.96 nm, with a median of ~22 nm. The standard deviation is low at 4.18 nm. The range is 13.5 to 33.2 nm. Approximately 85% of grains fall between 15 and 25 nm. This low deviation indicates tight process

control during synthesis. The consistent fine grain size supports enhanced hardness, while the negligible number of large grains reduces the risk of crack initiation.

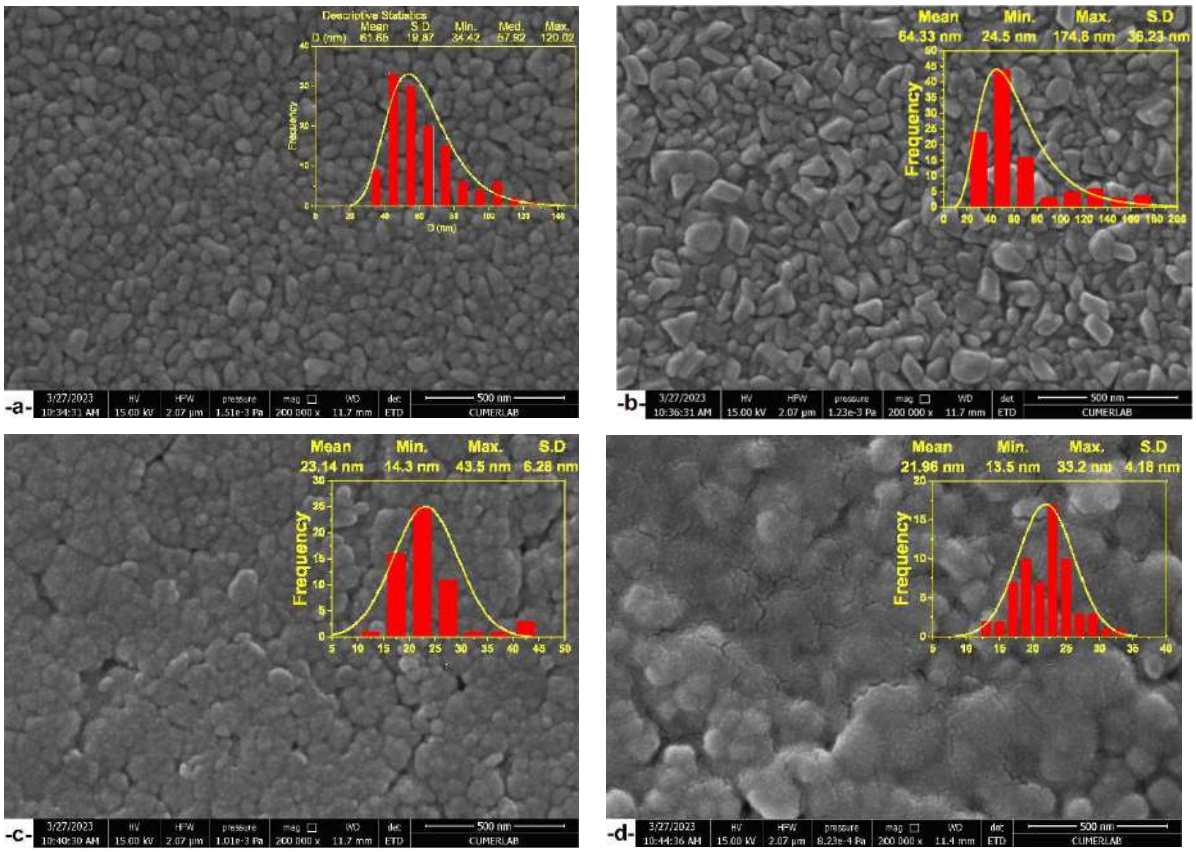

Figure 4.18: Various morphologies of SEM images of as-deposited ZnO thin films: (a) Ba 2 at. % ZnO, (b) Ba 4 at. % ZnO, (c) Ba 6 at. % ZnO and (d) Ba 8 at. % ZnO.

4.3.1. b- Analysis of 3D-SEM image of Ba-doped ZnO thin films

❖ **Analysis of 3D-SEM Image of Ba 2%-Doped ZnO Thin Film**

Figure 4.19-a- (a-) is $Ba\ 2\% - doped\ ZnO$ thin film deposited on glass showed a granular structure (see Figure 5.3), (b-) was observed by 3D-SEM, characterized by as-fabricated low and the rough heterogeneous surface. The morphology has some irregularly shaped grains of uneven heights as seen in due to color variations (dark red corresponds to high regions, lighter colors correspond lower regions). Coalescence during deposition can be inferred from ill-defined grain boundaries, and large clusters larger than 0.5 µm are measured interspersed with smaller grains (<0.2 µm in size) Quantitative analysis using Gwyddion software shows high values for average roughness ($R_a = 35.08\ nm$) root mean square roughness ($R_q = 43.54\ nm$) and the maximum peak-to-valley height ($R_t = 262.57nm$). General skewness ($R_{sk} = -225.93\ nm$) and high kurtosis ($R_{ku} = 2954.25\ nm$) imply challenging surface features,

such as sharp valleys and spiky peaks. Non-uniform grain distribution is indicated by spatial metrics (e.g., S_m= grain mean separation on average 35.67 nm for irregularities).

❖ **Analysis of 3D-SEM Image of Ba 4%-Doped ZnO Thin Film**

Figure (4.19-b-) shows a 3D-SEM image of Ba 4%-doped ZnO thin film grown on glass, as deposited in 2D-cone packaging. It is a shiny surface showing clear grain roughness of anisotropic grain morphologies in diverse dimensions. The grain boundaries are unclear, probably due to coalescence/agglomeration during deposition. Heterogeneity seen in size of grain, larger grains (>>) alongside with small (0.5 μm) clusters as well. Quantitative Gwyddion data shows super extreme roughness (Ra = 58.08 nm), roughness RMS (h)=77.27 nm and peak -to-valley trough depth of maximum peak ($R_t = 488.04\ nm$) The skewness is manifested as positive ($R_{sk} = 393.11\ nm$) and strongly kurtotic ($R_{ku} = 3816.11\ nm$) sharp spiky surface. Non-uniform grain distribution: The spatial metrics (e.g., mean distance between defects $S_m = 36.07\ nm$) emphasize this by showing heterogeneity from which hybrid parameters (e.g., RMS slope, $\Delta_q = 12.6552\ \mu m^{-1}$) provide transition topographical irregularities.

❖ **Analysis of 3D-SEM Image of Ba 6%-Doped ZnO Thin Film**

A Ba 6% doped ZnO thin film on glass, imaged by SEM in 3D (Figure 4.19-c.) shows to be granular on glass. The roughness of the surface has very irregular shaped grains of unequal heights. Deposition leads to coalescence, grain boundaries are diffuse. Heterogeneity in the sizes of the grains is observed: large clusters (>0.5μm) and submicrometer-sized grains (< 0.2 μm). Quantitative analysis of the roughness via Gwyddion shows a substantial amount: average roughness ($R_a = 34.29nm$), $R_q = 45.19\ nm$ root mean square roughness and maximum peak-to-valley height $R_t = 383.00\ nm$. The negative skewness ($R_{sk} = -246.69\ nm$) implies more valleys than peaks and very high kurtosis ($R_{ku} = 4272.75\ nm$) suggests teardrop shaped features combined with low geometrical slope. Non-uniform grain distribution (such as spatial metrics eth: mean spacing of irregularities, $S_m = 23.20\ nm$) and hybrid parameters (for e.g., RMS slope $\Delta_q = 10.48\ \mu m^{-1}$) will demonstrate that the surface has a large range in topographical variations.

❖ **Analysis of 3D-SEM Image of Ba 8%-Doped ZnO Thin Film**

Figure (4.19-d): 3D-SEM image of a granular Ba 8%-doped ZnO thin film on glass. Irregular grains of brightness variation (dark red = high regions, light area = depressions) with pronounced roughness highly on both size and height of grains on top of the surface. Improper grain boundaries arguing deposition via coalescence. The image also shows size of grain

heterogeneities; considerably big clusters (⩾0.5 µm) and smaller grains (<0.2 µm). Quantitative properties: the Gwyddion software shows ($R_a = 39.19\,nm$ average roughness), root mean square roughness $R_q = 55.59\,nm$ and valley to peak height $R_t = 503.09\,nm$, which indicates very roughness. Sharp, spiky features (positive skewness $R_{sk} = 154.67\,nm$; ultra-high kurtosis $R_{ku} = 6063.71\,nm$) Positive Overall uniformity of kurtosis Homogeneity in spatial metrics (mean spacing of defects, $S_m = 20.82nm$) proves close-packed grains, and the hybrid topographic parameters (e.g., RMS slope $\Delta_q = 13.37\,\mu m^{-1}$) that peak flattening is pronounced.

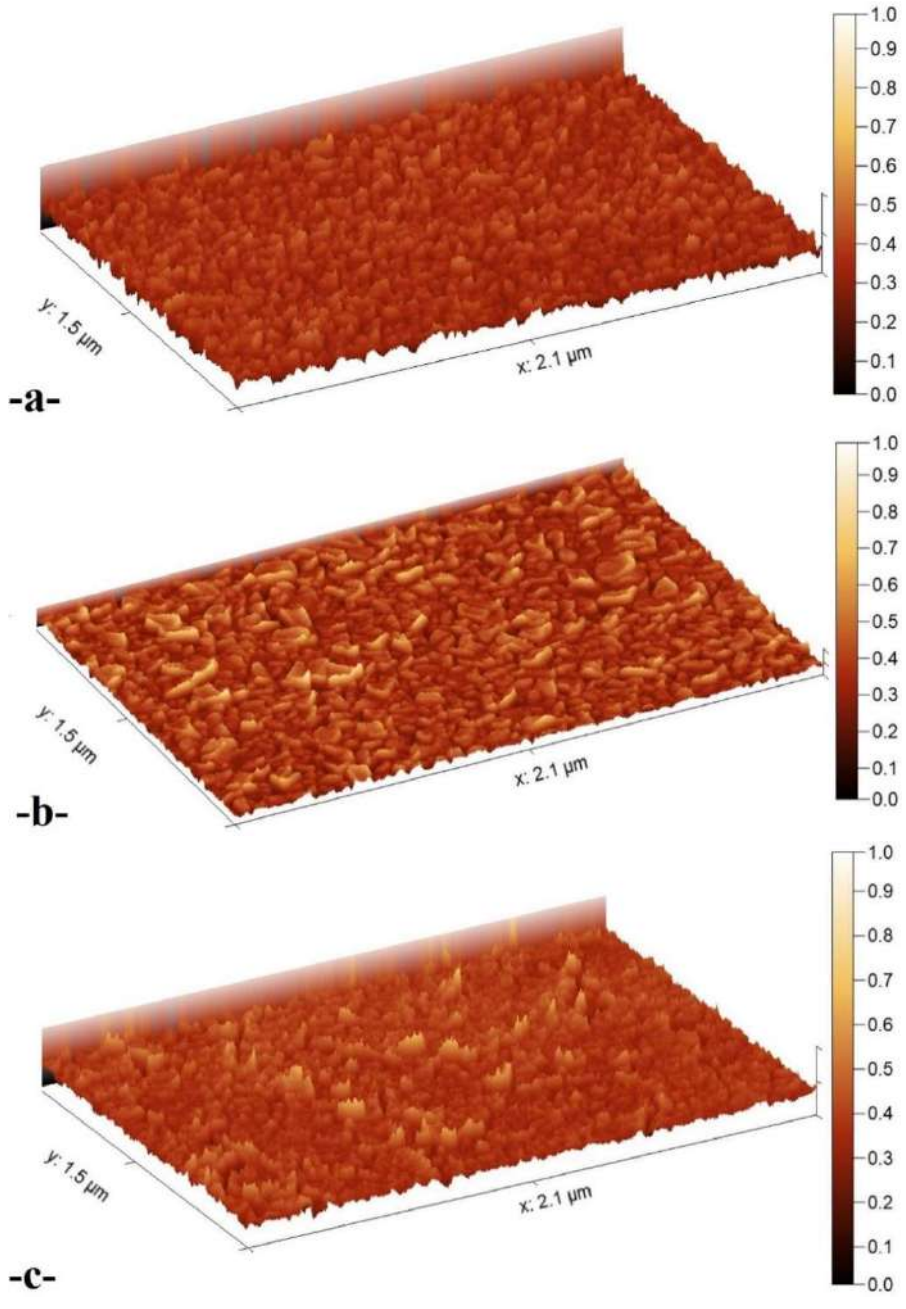

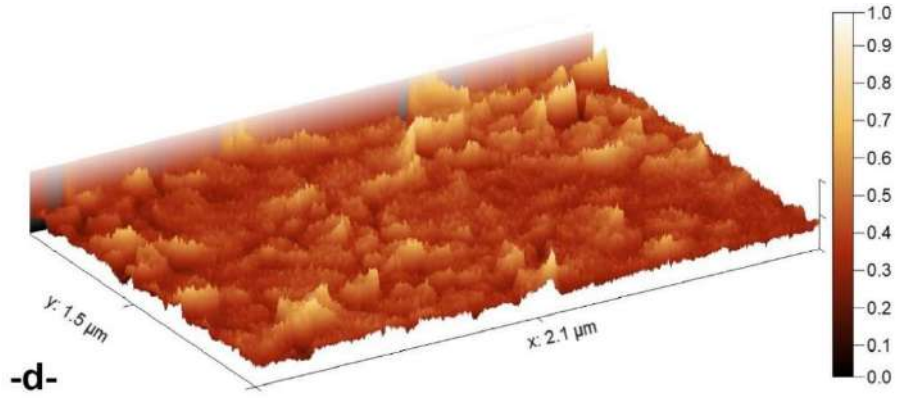

Figure 4.19: Three-dimensional scanning electron microscopy image of the topographical representation of Ba-doped ZnO thin films prepared using SPT at 450°C.

4.3.1. c- Surface state analysis of deposited Ba-doped ZnO thin films

In the following subsection, the surface state deposited Ba-doped ZnO thin film will be analyzed in details.

Fig. 4.20(a) — SEM tree-cracks on the measured line section of deposited Ba 2% Ba-doped ZnO thin film prepared via spray pyrolysis at the substrate temperature =450°C SEM analysis of Ba-2% doped ZnO thin films (Annex-G-) incorporates into a wholly distinct surface as compared with ZnO without dopant (**Figure 4**). Average roughness value ($R_a = 35.08\,nm$) and root mean square roughness ($R_q = 43.54\,nm$) are markedly larger, thus with even enhanced surface roughness in comparison to typical undoped ZnO (R_a~$27\,nm$). This is consistent with recent research, demonstrating that dopants such as Ba can impact grain growth and lattice surface phenomenon. Localization of sharp features will be indicated by the $R_{(max)} = 262.57\,nm$d, are highly peaked $R_{3z_{ISO}} of\ 161.12\,nm$, peak-to-valley heights. The skewness ($R_{sk} = -225.93\,nm$) is less negative than in undoped films; meaning the peaks and valleys are better balanced. Relative to nucleation in undoped substrates, Kurtosis ($R_{ku} = 2954.25\,nm$) is large but less that in undoped values to suggest fewer extreme height variations. Waviness parameters ($W_a = 25.89\,nm, W_q = 32.42\,nm$) exceed those of undoped ZnO, again implicating large-scale waviness induced by the incorporation of Ba.

Surface features as revealed by spatial metrics: mean spacing (35.67 nm) with dopant-modified crystallinity, and RMS wavelength ($\lambda_q = 28.38\,nm$) of the surfaces, lower spatial resolution predict Spatial metrics (e.g. hybrid parameters $\Delta a = 7.52\ \mu m^{-1}$; $\Delta q = 9.64\ \mu m^{-1}$) indicate steeper slopes relative to undoped films and thus possibly charge carrier mobility. These fit the dopant induced changes of orientation and grain size within doped ZnO systems observed in crystallographic studies. Collectively, the data points to a rougher, more heterogeneous surface

which is anticipated to increase photocatalytic activity through increased active site availability (such as are noted in [8, 202, 208, 212] challenges smooth interfaces though.

Figure 4.20(b): profiles in z along the lines with arrows marked in SEM morphology plot of Ba doped ZnO (4%-doped films) prepared by spray pyrolysis at temperature of 450 ℃. The Area analysis of Ba-doped ZnO thin films by SEM i.e.,(Annex-H) shows drastic morphological changes comparing with small dopage levels. Highly characterize as visible in Fig. 7 and are arguably the biggest changes: surface roughness averages ($R_a = 58.08\,nm$) and [root mean sq in relation deal caliaretta-root mean square riprows] ($R_q = 77.27nm$)both are markedly higher than either while comparing undoped or 2% Ba doped counterparts suggesting enhanced surface roughness. The maximum peak-to-valley height ($R_{max} = 446.99\,nm$hows intense protrusions and also extremely high roughness peak height ($R_p = 270.67\,nm$ vs. a valley depth ($R_v = 217.36\,nm$) indicates deeper valleys. Because positive skewness ($R_{SK} = 393.11\,nm$) higher peaks than valleys. The profile, a leptokurtic one with sharp peaks and long tails portends the $R_{ku} = 3816.11\,nm$ high kurtosis indicating clustered surface features. Large-scale undulations, as evidenced by waviness parameter ($W_a = 40.73\,nm;\ W_q = 49.07\,nm$) and maximum waviness ($W_{max} = 188.80\,nm$ven further.

Spatial metrics ($S_\lambda = 36.08\,nm, \lambda_a \approx 37.91\,nm$) imply localized features that are too close yet with longer wavelengths while hybrid parameters ($\Delta_a = 9.62\ \mu m^{-1}, \Delta_q = 12.65\ \mu m$) suggest steep slopes. These trends were found correlating with increased atomic doping-induced structural disorder that could in turn affect optical scattering and electronic. In various applications requiring tunable surface modification, these results are consistent with agent induced agglomeration or growth morphology non-uniformity [8, 202, 208, 212].

Fig. 4.20(c) shows SEM profile curves measured along the lines described on the SEM Image of Ba 6%doped ZnO thin films from spray pyrolysis at 450°C.

SEM characterization of the surface morphology of undoped (**Fig. 1**) and Ba-6% doped ZnO thin films (Inserts in Annex-I) Roughness ($R_a = 34.29\,nm, R_q = 45.19\,nm$) are less than Ba-4% doped films $R_a = 58.08\,nm, R_q = 77.27\,nm$ undoped (ZnO)), but higher than undoped ZnO ($R_a = 27\,nm$). As a consequence, this shows a non-linear dependence of the Ba doping concentration on surface roughness, which could be attributed to a dopant-induced structural reorganization. Interestingly, very high R_t exit peak-to-valley height ($R_t = 383\,nm$) and R_v: valley depth of 216.3 nm suggest large surface irregularities although both are lower than Ba-

4% films. The skewness ($R_{sk} = -246.69\ nm$) gives an indication of negatively skewed profile with valleys having larger values than peaks and the kurtosis ($R_{ku} = 4272.75\ nm$) means leptokurtic, has sharp peak with deep valleys. They may have an effect on the charge transport and/or adsorption properties as well in device applications Surface features are mentioned with these spatial parameters like mean spacing ($S_m = 23.2$) and mean wavelength $\lambda_a = 25.94\ nm$ indicating dense surface structures that might be associated with a denser grain structures for increased doping. The wave number parameters ($W_a = 20.64\ nm,, W_q = 24.86\ nm$) smaller than those of Ba-4 % films, which indicate less long-range undulations. Hybrid metrics, e.g., RMS slope ($\Delta_q = 10.48\ \mu m^{-1}$) are moderate surface steepness which could theoretically change optical scattering in thin-film Overall, the data seem to tell us that more than ~4% Ba doping may stabilize surface morphology, which is either less rough or very localized. This behavior may be related to the dopant influence on how fast crystallization proceeds or stress relaxes [1]. Nevertheless, an investigation concerning the interplay between surface morphology and functionality (e.g. optoelectronic devices) should be pursued [2, 8, 178, 279-281, 285-287].

4.20(d) is the profile curves measured along the lines indicated in SEM photograph of Ba 8% doped ZnO Thin film prepared by spray pyrolysis at 450 °C. Roughness characteristics: Surface analysis of Ba-8% doped ZnO thin films (Appendix –J-) Roughness average ($R_a = 39.19\ nm$) and root mean square ($R_q = 55.59nm$): Moderately rough surface due to higher doping concentrations that modify grain growth dynamics. Indicates a moderately disordered surface; However the maximum peak to valley height [$R_t = 503.09\ nm$] and deepest valley [$R_v = 231.20\ nm$] of exceed pronounced surface modifications (most probably due to structural changes that are brought in as a result of doping)

Extreme skewness ($R_{sk} = 154.67\ nm$) points towards occurrence of high number of peaks and absence of valleys while large kurtosis ($R_{ku} = 6063.71$)|| indicate high climaxis in height, implying tight clustered surfaces Features The waviness ($W_a = 65.26\ nm, W_q = 77.92\ nm$) higher than for less-doped samples, showing giant-scale undulations that may act in optical scattering. Measurement Averaging metrics, $S_m = 20.82nm\ and\ \lambda_a = 23.34nm$ are indicative of finer and likely film adhesion/ properties, due to related distortions in surface-structure. The increased RMS slope ($\Delta_q = 13.36\ \mu m^{-1}$) reveals steeper local gradients which in turn may modify the performance of these devices by increasing surface reactivity, light

trapping. These trends parallel the effects of doping on the crystalline and morphology due to higher Ba [2, 8, 178, 279-281, 285-287].

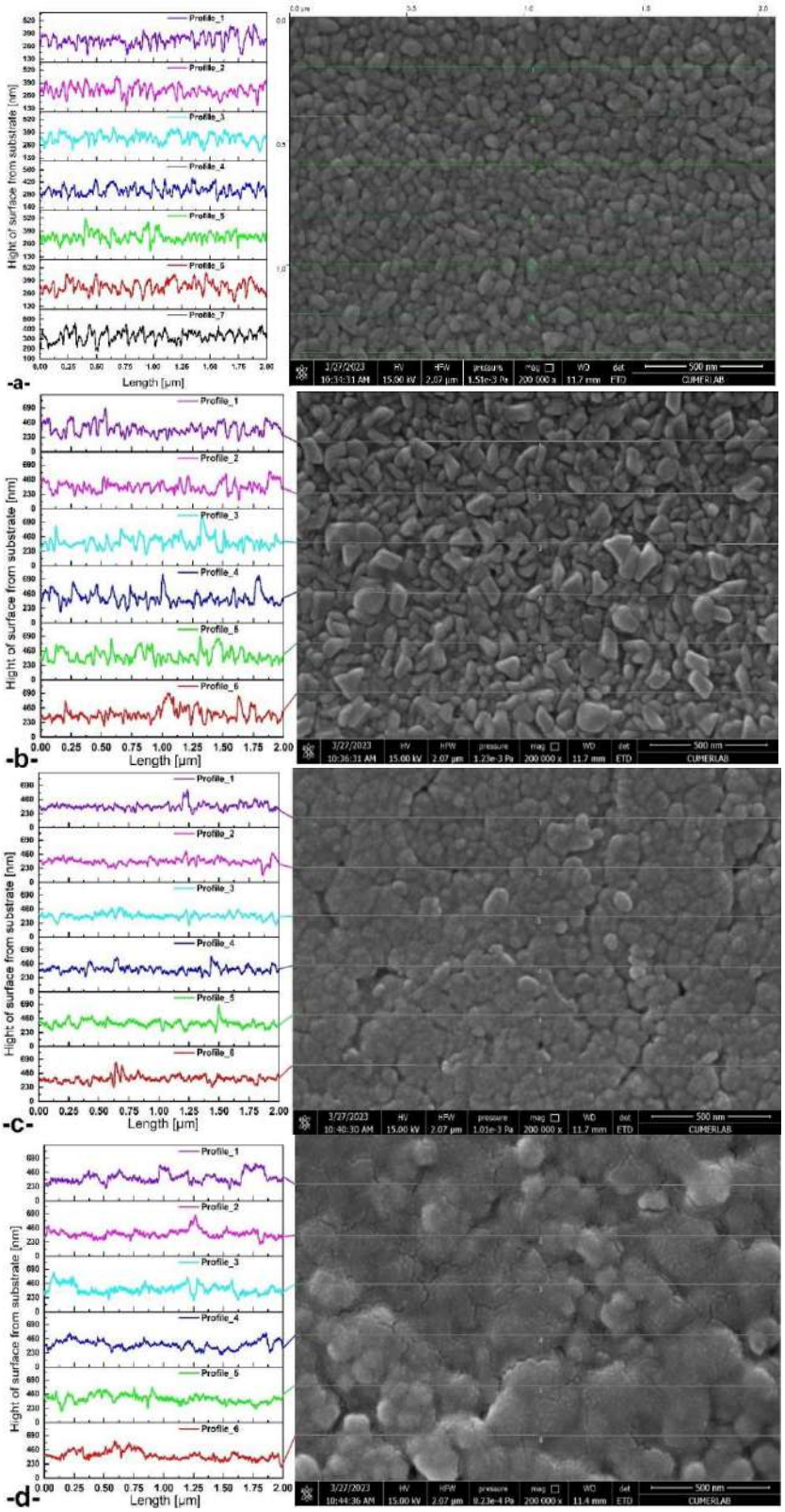

Figure 4.20: Profile curves measured along the lines shown on the SEM image of Ba-doped ZnO thin films prepared by the spray pyrolysis technique at 450°C.

4.4. Optical properties of Ba-doped ZnO thin films

The transmittance spectrum (optical) shown in Figure 4.21 reveals that the Ba-doped ZnO thin films (2%–8% Ba) transmittance is above 85% which is considered high transparency in the visible range (400-700 nm) with peaks of ~92% at 8% percent Ba doping. ZnO demonstrates a sharp UV (~350 nm) cutoff blue shifting with 2% Ba doping (cutoff around 370 nm) to shifting around 375 nm with 4-6% Ba. Corresponds to an absorption edge, which aligns with ZnO's band edge. The observed initial blue-shift matching the Burstein-Moss effect [142] indicating the steep rise in carrier concentration increases effective bandgap required. At 8% doping the edge shifts to suggest narrow bandgap (3.279-3.268 eV, Table 4.9) and defect states from 370nm. You could see that the differences in transmittance less than 5% between samples indicates the homogeneity of the films, paired with the absence of interference fringes demonstrating low refractive index suggests optimized thickness from minimized deposition related effects. These findings show Ba doping conclusively alters the optical properties of ZnO and maintains steady transparency along with UV absorption changes which supports transparent conductive uses.

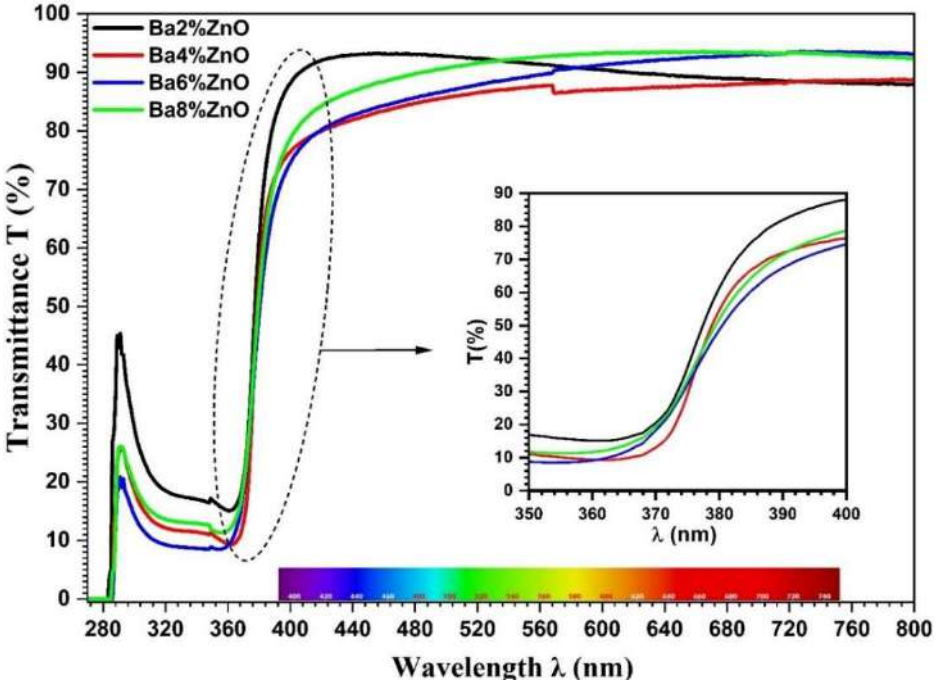

Figure 4.21: Transmission spectra of Ba-doped ZnO thin film samples for different precursor molarities.

Tauc plots as shown in Fig. 4.22 verify the direct band gap of Ba-doped ZnO thin films with $(\alpha h\nu)^2$ linear versus photon energy ($h\nu$) regions only. Table 4.9 Extrapolated bandgap values drop systematically from 3.279 eV (2% Ba) to 3.268 eV at 8% Ba (Table 4.9), pointing to doping-induced compressed bandgap. In general, this is in concert with the structural changes

or the defect states that Ba introduces and so make electronic transitions more favorable in energy. In linear line, shape (small Urbach tail) is indicative of low disorder and retained film quality. The precise E_g tuning (negligible Urbach tail) in a doped ZnO material confirms that Ba-doped ZnO is very promising for UV optoelectronic applications relying on the tuning of absorption edge.

Table 4.9: Optical bandgap and Urbach disorder energies of Ba-doped ZnO thin film for varying precursor molarities.

Sample	Optical energy bandgap	Urbach energy disorder
	E_g [eV]	E_u [meV]
Ba2%ZnO	3.279	69.35
Ba4%ZnO	3.277	77.53
Ba6%ZnO	3.274	101.69
Ba8%ZnO	3.268	103.70

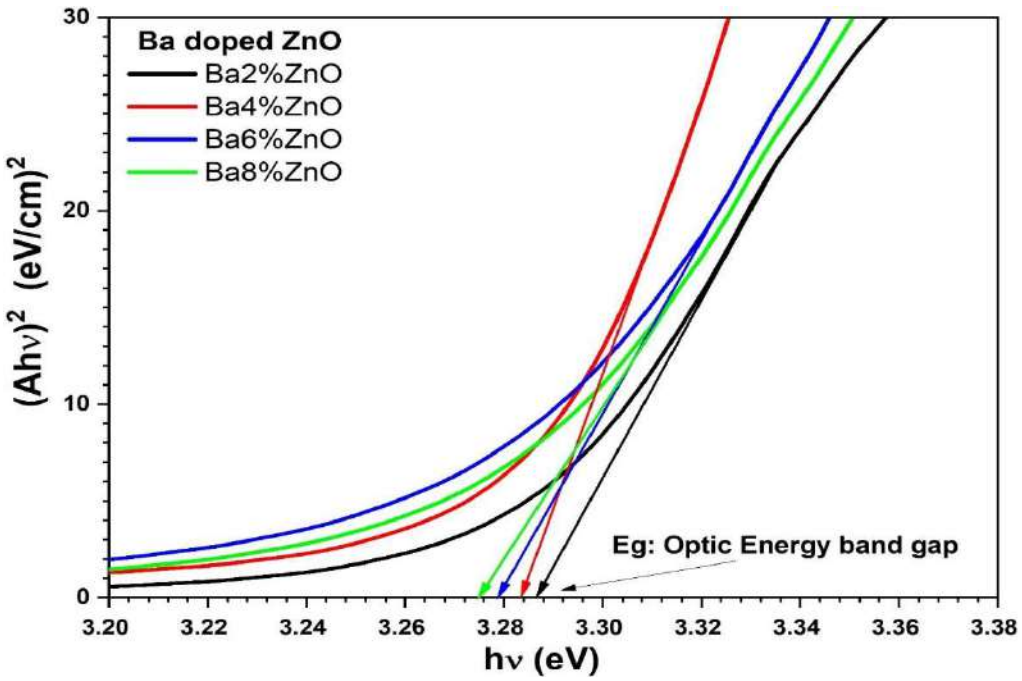

Figure 4.22: Plot of $(\alpha h\nu)^2$ versus incident photon energy $(h\nu)$ of Ba-doped ZnO thin films at different precursor doping levels.

Figure 4.23 shows the Urbach plots (ln(A) against photon energy hν) for the thin films of ZnO doped with Ba at 2%, 4%, 6%, and 8% .

We have noticed that the Urbach energy (E_u) increases from 69.35 meV (2% Ba) to 103.70 meV (8% Ba), which indicates greater structural disorder and higher defect density with an

increase in doping. On the other side, for lower values of the Urbach energy E_u, greater slopes of the curves were observed, while for the higher levels of doping, shallower slopes of the curves were observed, which reflects an increased disorder and supports the Urbach tail model. In addition, it ca be remarked that the increase in absorption in the sub-bandgap region at lower photon energy for the higher-doped thin films drives to defect-induced diffusion. This phenomenon leads to a broadening of the absorption edge and reduces the effective optical bandgap (E_g). The greatest increase of E_u occurred between 6% and 8% Ba, showing that after a certain threshold of doping the crystallinity starts to degrade due to distortions of the lattice or oxygen vacancies, but allows for bandgap tuning. The inset in the figure illustrates the use of the derivative technique in calculating E_u and demonstrates that the slope (θ) of the Urbach tail is a significant parameter. The data presented here remarkably deepens understanding of how Ba-doping in ZnO alters its optical properties, highlighting approaches aimed at making the materials more effective for use in optoelectronics and light harvesting devices. All arguments remain consistent with accepted theories, which correlate the structural disorder in the material to the response of the doped semiconductor.

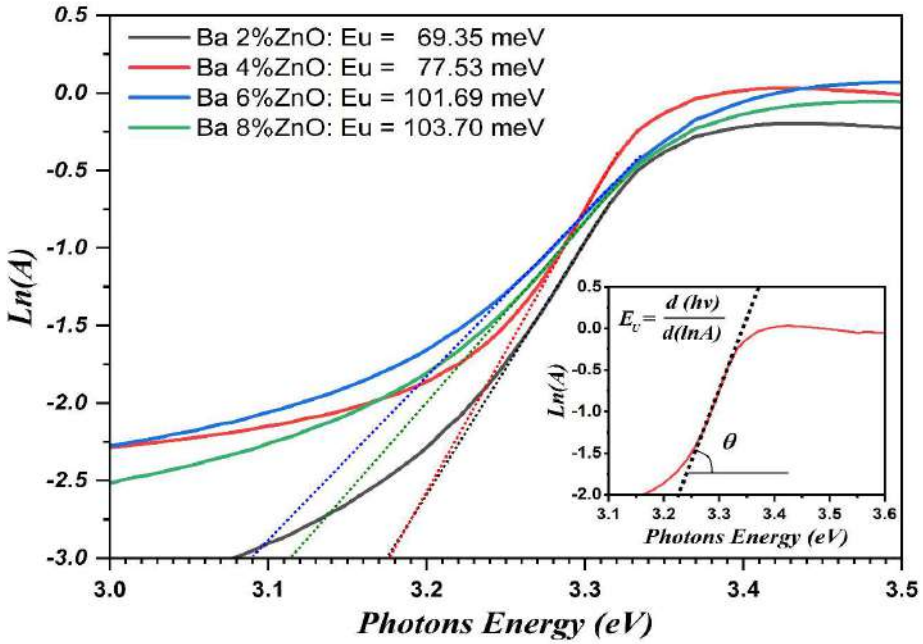

Figure 4.23: Plot of $Ln(A)$ versus incident photon energy $(h\nu)$ of Ba-doped ZnO thin films at different precursor doping levels.

Figure 4.24 shows the relationship of optoelectronics bandgap (E_g) and Urbach depth (E_u) in Ba doped ZnO thin films inversely. E_g decreases upon (2%) Ba doping to (8%), is E_g- from 3.279 eV to 3.268 eV and E_u rapidly increases from 69.35 meV to103.70 meV (Table. 4.9)

such an effect demonstrates the doping disorder as more defect states and lattice distortions broaden effective bandgap resulting in band-tail enhancement. This contradicts the Burstein-Moss effect in which deviation from the direct band gap state to indirect happens induced by disorder order of magnitude more than carrier filling, causing a narrowing of E_g and absorption edge broadening. E_u is lower, degradation of material quality these trade-off allow to control optical properties suitable for applications like photovoltaics i.e. defect engineering can be used to enhance the absorption at a specific wavelength.

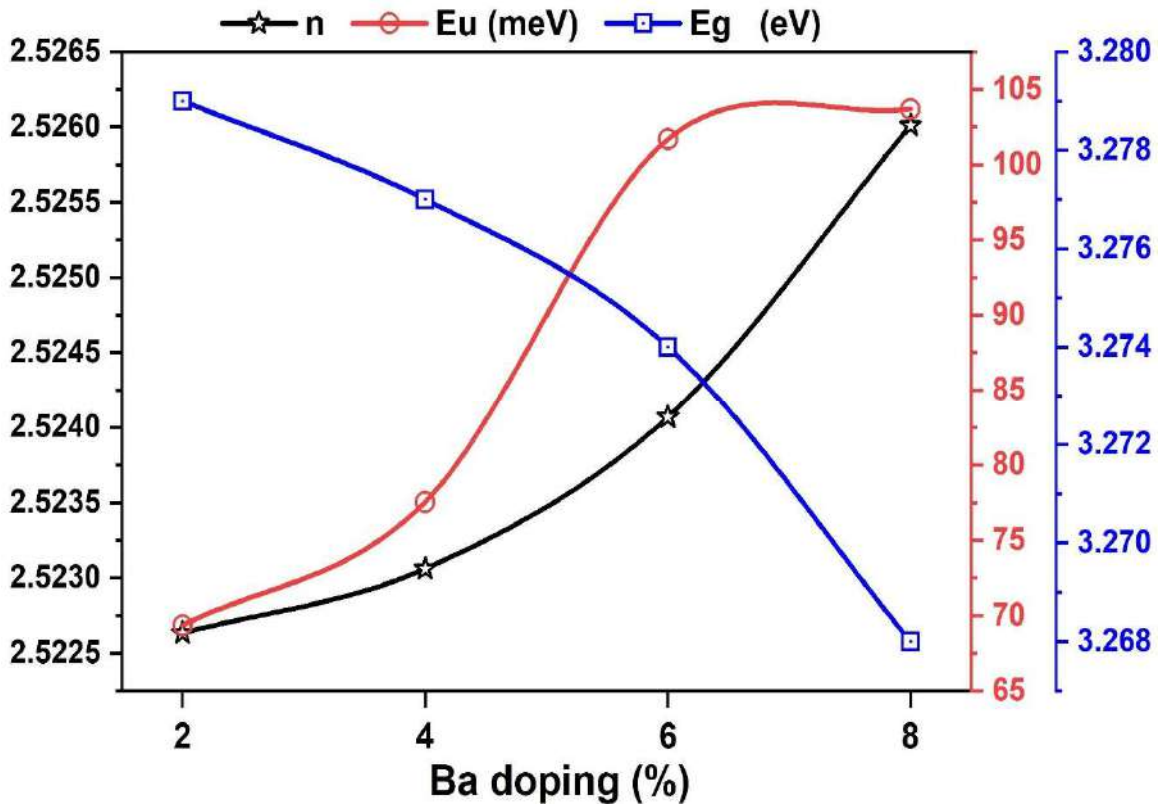

Figure 4.24: Variation of refraction index (n), Urbach disorder and optical bandgap energies of Ba-doped ZnO thin films as a function of doping level.

From Table 4.10, the optical band gap (E_g) of Ba-doped ZnO thin film decrease slightly from 3.279 eV to 3.268 eV while Ba doping increased from 2% and 8% (doping-induced the bandgap narrowing due to structural changes or electronic interactions are typically observed by increasing the amount of impurity) [318]. With increasing Ba concentration, the experimental refractive index (n) has slight (2.5226–2.5260) increase (as sown in Figure 4.25), which indicate inverse relationship between E_g and (n) as is shown for reference. These theoretical models do not agree well: Reddy-Nazeer [139] [33] mis-predicts n (2.6963–2.6988), and both Kumar-Singh [141], to which our results belong (2.2960–2.2986) or Moss' model [142] (2.3201–2.3220), undershot. Model by Ravindra [3] gives the least values (2.0511–2.0580), probably

because of some other empirical assumptions. The results from Herve-Vandamme [144] (2.2496–2.2526) were the most close indicating a better modelling of the dopant effect. The variations between experimental and theoretical values could be due to other factors such as film morphology, dopant placement or some limitations of either the model-parameters. The context-dependency of model choice for optical properties of doped semiconductors needs to be considered again these results.

Table 4.10: Refractive index variation as function of the dopant percentage of Ba doped ZnO calculated different relations.

Samples	Optical energy bandgap E_g(eV)	Refractive index (n)					
		Exp.	Reddy-Nazeer[139] Eq. (1)	Kumar-Singh[141] Eq. (2)	Moss[142] Eq. (3)	Ravindra[3] Eq. (4)	Herve-Vandamme[144] Eq. (4)
Ba2%ZnO	3.279	2.5226	2.6963	2.2960	2.3201	2.0511	2.2496
Ba4%ZnO	3.277	2.5231	2.6966	2.2964	2.3203	2.0520	2.2500
Ba6%ZnO	3.274	2.5241	2.6974	2.2971	2.3209	2.0541	2.2509
Ba8%ZnO	3.268	2.5260	2.6988	2.2986	2.3220	2.0580	2.2526

4.5. Electrical properties

Figure 4.25 presents the dependency of electrical conductivity of pure ZnO thin films on precursor's concentration. Graph 3.5: Conductivity vs precursor concentration ranges from 0.05M $[0.1077(\Omega.m)^{-1}]$ up to its highest ($1.0856\,(\Omega\cdot m)^{-1}$) at 0.25M then quickly decreasing to $0.0987(\Omega\cdot m)^{-1}$ at 0.40M.

This non-linear behavior indicates the presence of an optimal precursor concentration (0.25M) for the enhancement of conductivity. The initial increases may be attributed to improved crystallinity and diminished grain boundary scattering at intermediate concentrations, which collectively enhance the mobility of charge carriers. The observed reduction at elevated concentrations is likely a consequence of the emergence of structural defects, such as oxygen vacancies or interstitial zinc atoms, which function as charge traps and consequently diminish conductivity. A comparable phenomenon has been documented in ZnO systems, wherein excessive precursor concentrations compromise film uniformity and instigate the formation of defects. These observations are consistent with investigations that correlate ZnO conductivity with processing parameters and defect density. In their study, F. Zahedi et al. [300] examined the electrical conductivity of $undoped\ ZnO$ thin films deposited at 450°C. They found that the conductivity values increased with increasing precursor concentration, ranging from 0.01 to 0.4

M, specifically, the conductivity values were 0.0201, 0.1453, 0.4785, and 0.2933 $(\Omega.cm)^{-1}$, respectively. On the other hand, P. Nunes et al [319] had measured electrical conductivity values of $0.0114\ and\ 0.1031\ (\Omega.\mathrm{cm})^{-1}$ for undoped zinc oxide thin films prepared from a 0.2 M solution and then annealed at 200°C for 2 hours.

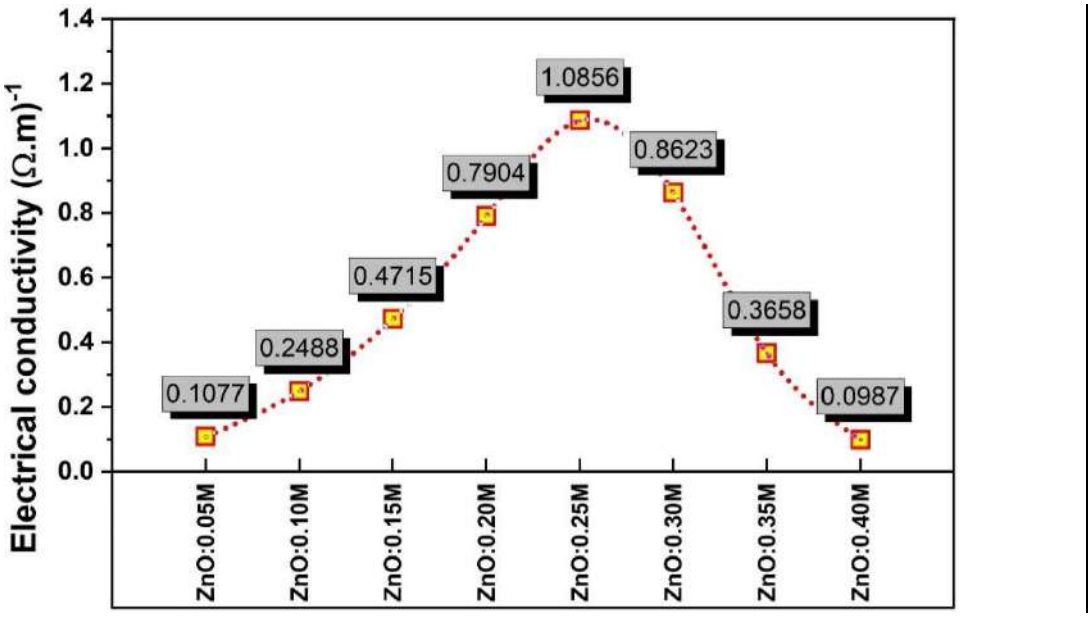

Figure 4.25. Plot of electrical conductivity of doped ZnO thin films with various molar concentrations of precursor.

Chapter-5 Discussion and interpretation of results for Ba-doped $ZnNiO$ thin films

Chapter-5
Discussion and interpretation of results for Ba-doped $ZnNiO$ thin films

5.1. Introduction

In this chapter we deal with the detailed account of preparation and its characterization for undoped ZnNiO as well as barium -doped ZnNiO (~0; 1-8 at%) thin films-- material systems with evident applications as gas sensors or photocatalytic surfaces are under research.

The samples were thoroughly manufactured by spray pyrolysis on high vacuum cleaned glass substrates to ensure reproducible and homogeneous film deposition. This work investigate the influence of different Ba contents in the range from 0 to 8 atomic percent on the structural, morphological and optical properties of these thin films. We perform complementary studies X-ray diffraction (XRD), scanning electron microscopy (SEM) and UV-visible spectroscopy leading to remarkable new insights into the microstructural evolution, surface properties and optical fingerprints of these films. Not only the fundamental science of Ba and 0 doped ZnNiO systems is gaining attention from this structured study but also helps in reaching the desired technological applications by tuning properties.

5.2 Analysis and interpretation of results for Ba-doped $ZnNiO$ thin films

Fig. 5.2 Displays a series of XRD diffractograms for Ba- doped ZnNiO thin films prepared in 450 °C varying Ba concentrations (0%, 2%, 4%, 6%, and 8% at.%)

The figures 5.2 (a and b) show the XRD patterns of 0 and 2 at.% Ba containing films, respectively; as shown for the 0 at.% Ba sample, the dominant peaks mainly originate from the hexagonal wurtzite structure of ZnNiO, suggesting the intrinsic structure of as-fabricated undoped film.

With 2 at.% Ba, i.e. Ba starting to be introduced, its effects on initial are witnessed by the 0 Ba sample. Throughout the whole series, we expect to observe this trend for the intensity of the (002) peak with larger Ba doping. This is believed to be higher crystallinity and the c-axis orientation of the film prefers with increasing Ba content as previously reported in similar studies of metallic oxide thin films with Ba doping [320, 321]. The lack of any apparent secondary phases in these lower-doping patterns indicates that Ba ions are incorporated stoichiometrically into the ZnNiO lattice without the formation of separate oxide phases, demonstrating this at least at these low levels.

Figure 5.2(c) shows XRD diffractogram of the 4 at.% Ba-in-film. In the pattern, we see a crystalline film with clear peaks that are linked to both ZnNiO and Ba containing phases [1]. The appearance of such phases means that the material is composite or mixed-phase. The markedly strong peak at ~36 degrees 2θ, [ZnO (101): 36.279° and NiO (111): 37.026°] which appears to be indexed as the sum of peaks associated with ZnNiO and a phase containing Ba hence suggesting a preferred orientation. Inset: Schematics of the ZnNiO and Ba structures [110, 322, 323]

Figure 5.2 d) XRD diffractogram of 6 at. % Ba-doped film [14] reveals a significant shift in the diffraction pattern to the right in respect to Figure 4 [here the 4 at. %]. The peak at according to ZnO (101): 36.851° ≈ 37°; 2θ holds the largest characteristic (strong preferred orientation and a phase perhaps corresponding to Ba-containing [ZnNiO = BaNiO], 43°: ZnNiO-edge-|II|, 42.704°). At 25.405°, the peak shows confirms that Ba is present: a peak (110) reflection of index provides.

Figure 5.2(e) shows the XRD pattern of the Ba-doped film at 8 atomic percent, which demonstrates a further distinct change in the diffraction pattern. We have observed a big peak at approximately 25.488degrees 2θ, corresponding to the (110) reflection of Ba, that indicates a significant presence of the Barium phase. Peaks corresponding to the mixture ZnNiO are also observed at 34.202° [ZnO (002)], 35.999° s [ZnO (101)], 47.302° [ZnO (002)], and at 62.523° there are two superimposed peaks[ZnO (103) and NiO (220)]. The increased intensity of the Ba (110) peak suggests a higher degree of crystallinity or a larger proportion of the Ba phase at 8 at.% Ba doping. The presence of both ZnO, NiO and Ba peaks confirms the multiphase nature of the film. The well-defined structure of the crystal is indicated by the sharpness and the intensity of the peaks [320-322].

The structural modifications induced by the incorporation of the barium atoms into the (ZnO and NiO) mixture thin films, which are revealed by the XRD analysis, are expected to affect the optical and electrical properties of these thin films.

Figure 5.3 shows the relative location of measured diffraction peaks to those taken from the ICDD reference cards. We have observed some shifts relative to the peak positions in the undoped (NiO, ZnO) thin films.

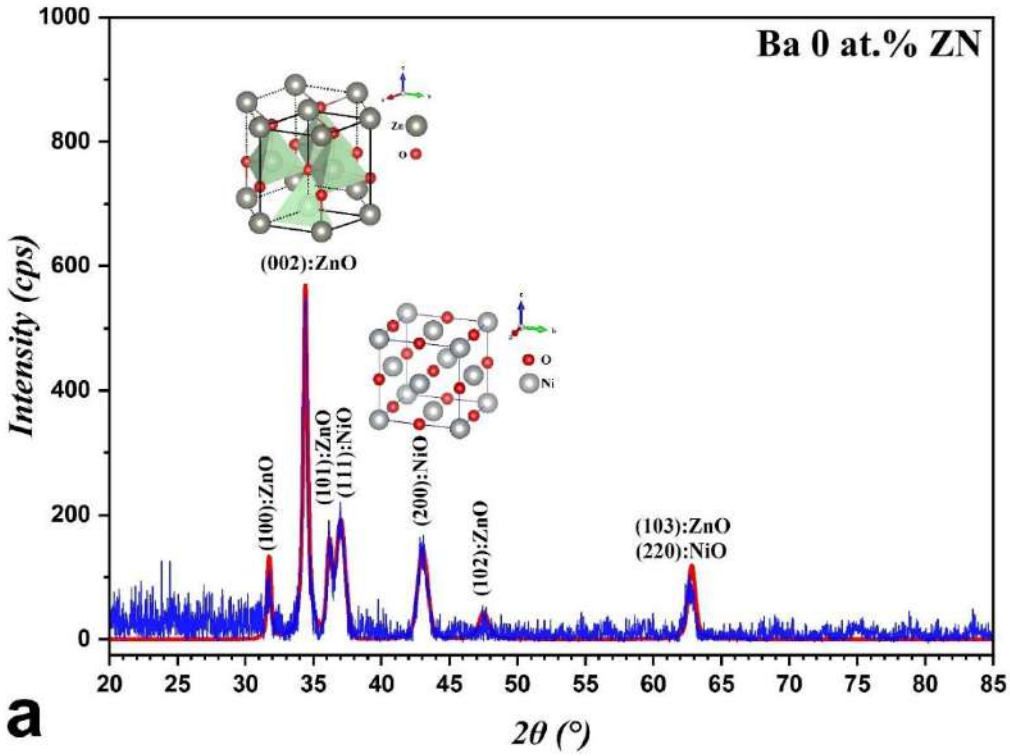

Figure 5.1 (a): X-ray diffraction diffractograms of undoped ZnNiO.

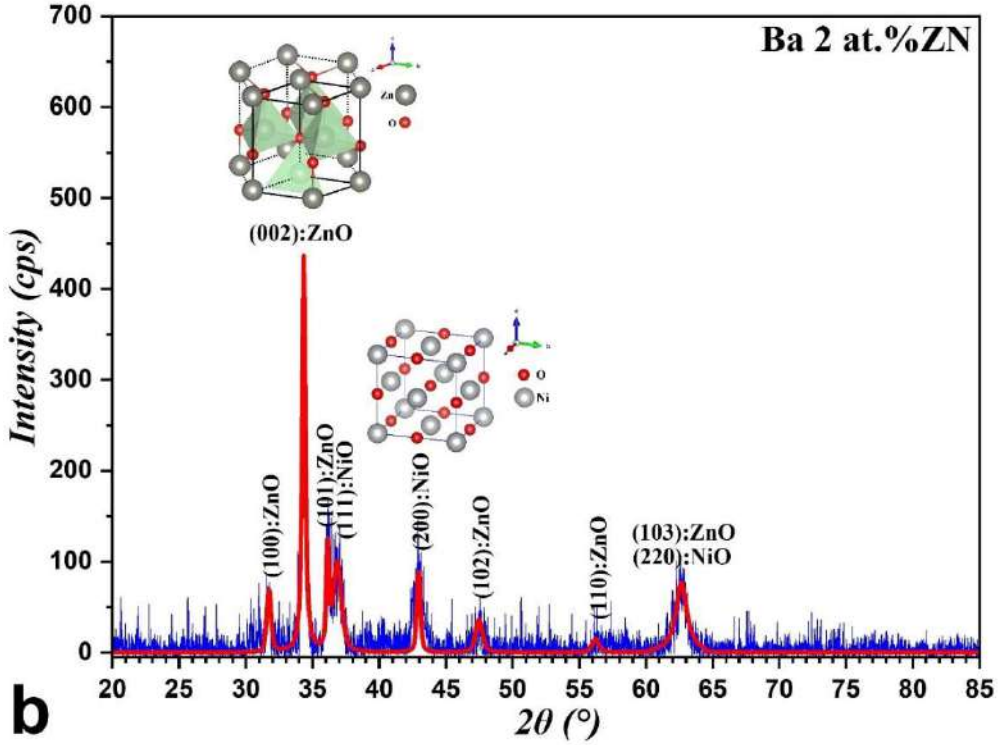

Figure 5.1 (b): X-ray diffraction diffractograms of undoped ZnNiO and Ba 24 at-% doped ZnNiO thin films prepared at 450 °C.

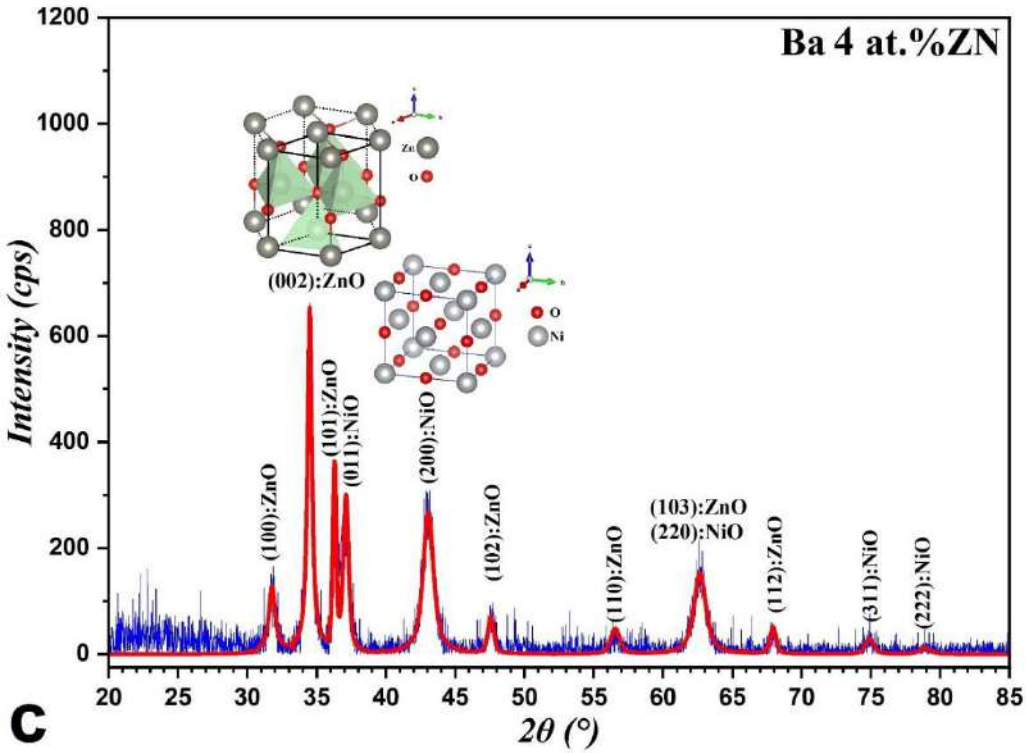

Figure 5.1 (c): X-ray diffraction diffractograms of undoped ZnNiO and Ba 4 at-% doped ZnNiO thin films prepared at 450 °C.

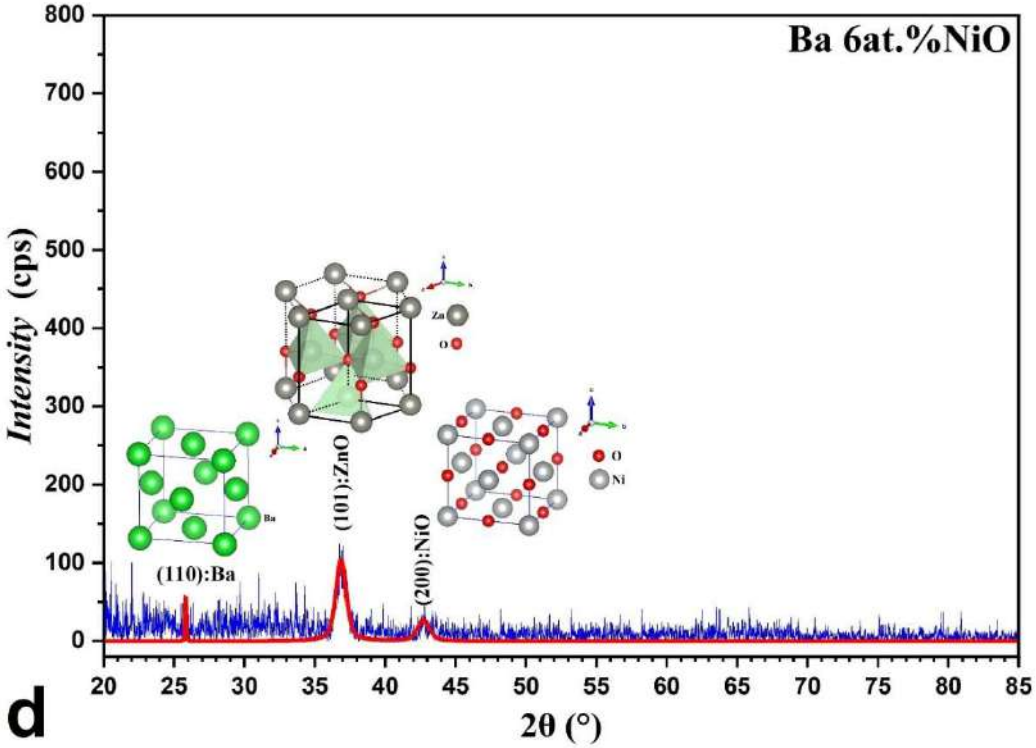

Figure 5.1 (d): X-ray diffraction diffractograms of undoped ZnNiO and Ba 6 at-% doped ZnNiO thin films prepared at 450 °C.

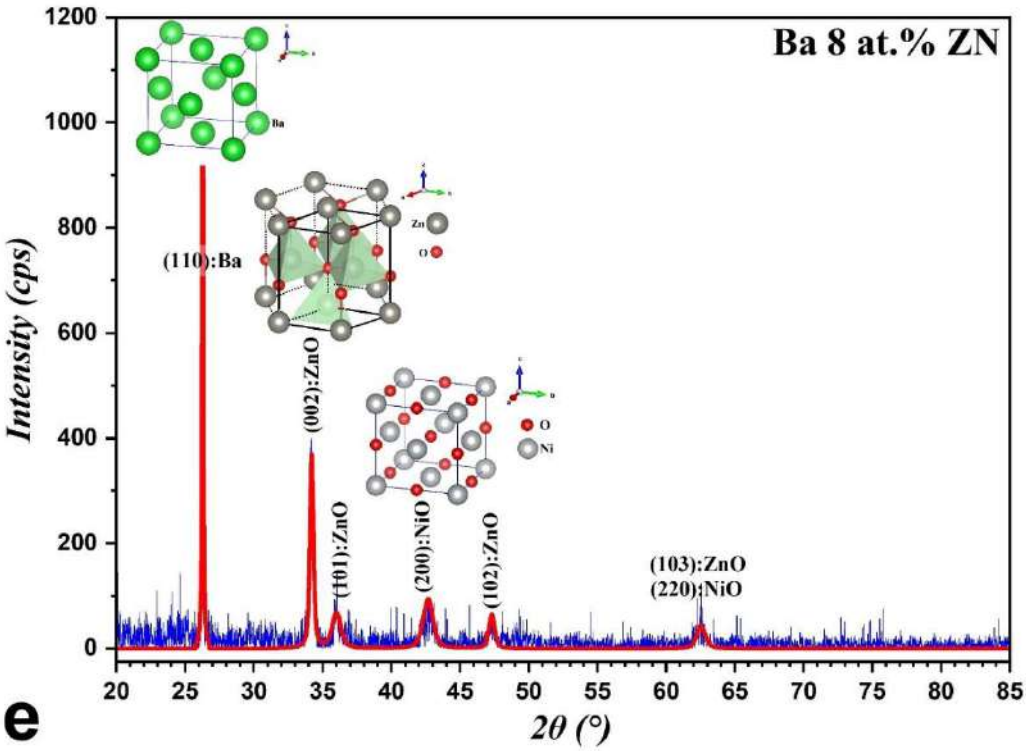

Figure 5.1 (e): X-ray diffraction diffractograms of undoped ZnNiO and Ba 8 at-% doped ZnNiO thin films prepared at 450 °C.

As indicated in various previous studies, we can attribute these peaks' shifts to various factors, which includes the impurities incorporation [324], the elevated temperature of substrate, the lattice distortions [325], the formation of defects (such as dislocations) [326], and the coalescence of grains during the crystallization process [327].

Each sub-image shows the variation in peak location as a function of increasing Ba content (at. %), which facilitates the evaluation of structural modifications induced by doping process.

As indication, the dashed horizontal lines represent the reference peak positions from the ICDD database for ZnO (#00-036-1451, blue), NiO (#00-047-1049, green)[328], and Ba (#00-047-1431, black)[329].

The experimental data (red lines) for ZnO diffraction peaks (i. e. (100), (002), (101), (102), (110), (103) and (112)) display peak shifts with increasing Ba concentration. In particular, ZnO (002) and ZnO (101) shows very small deviations from standard peak positions, which could indicate minimal, lattice distortions of the type. The invariable behavior for various ZnO peaks suggests changes in crystallographic parameters, probably resulting from substitutional content of Ba in ZnO or secondary phases [325-327].

Table 5.1: Structural parameters of undoped NiZnO: (0% Ba).

Parameter		NiZnO:0%Ba				
hkl		ZnO(100)	ZnO(002)	ZnO(101)	NiO(111)	NiO(200)
2θ	(°)	31.692	34.407	36.174	36.993	43.025
d	(Å)	2.82105	2.60446	2.48114	1.89548	1.48098
β	(°)	-	0.43505	0.43265	0.73971	0.74525
D	(nm)	-	19.12	19.32	11.32	11.46
$\delta\, x10^{15}$	(lines/m^{-2})	-	2.737	2.68	7.797	7.617
ε	(%)	-	0.316	0.313	0.306	0.303

Table 5.2: Structural parameters of NiZnO: 2% Ba thin films.

Parameter		NiZnO:2%Ba				
hkl		ZnO(100)	ZnO(002)	ZnO(101)	NiO(111)	ZnO(102)
2θ	(°)	31.673	34.355	36.138	36.869	47.514
d	(Å)	2.82276	2.60825	2.48357	2.43596	1.9121
β	(°)	-	0.3247	0.34367	0.85167	-
D	(nm)	-	25.61	24.37	9.83	-
$\delta\, x10^{15}$	$(lines/m^{-2})$	-	1.525	1.684	1.034	-
ε	(%)	-	0.236	0.248	0.353	-

hkl		NiO(200)	ZnO(103)
2θ	(°)	42.924	62.641
d	(Å)	2.10533	1.48184
β	(°)	0.89966	-
D	(nm)	9.49	-
$\delta\, x10^{15}$	$(lines/m^{-2})$	1.111	-
ε	(%)	0.365	-

While for NiO, diffraction peaks (111) ((200) and (311) are considerably better aligned in terms of their ICDD reference (green dashed line)). This indicates that NiO lattice is not perturbed by Ba doping or it has a low enough concentration to measureable strain. However, still slight tuning in intensities of peak may happen due to minor structural perturbations.

Although the position of the Ba (110) peak is shifted, it stays very close to the reference location (black dashed line) suggesting that separate Ba-containing phases may nucleate rather than extensive incorporation in ZnO or NiO lattices. This is consistent with existing studies on Ba doping into ZnO and NiO systems where phase segregation is dominant over lattice incorporation, and in general a limited solubility [328-330].

In general, there is not significant changes in the ZnO and NiO peaks were revealed by Ba doping and, although the existence of localized distorted lattices or the formation of a secondary phase could be assumed, it was not possible to obtain significant results [324-327].

Table 5.3: Structural parameters of NiZnO: 4% Ba thin films.

Parameter		NiZnO:4%Ba				
hkl		ZnO(100)	ZnO(002)	ZnO(101)	NiO(111)	NiO(200)
2θ	*(°)*	31.777	34.492	36.279	37.026	43.049
d	*(Å)*	2.81369	2.59819	2.47421	2.42598	2.09949
β	*(°)*	-	0.45123	0.47218	0.78402	0.93552
D	*(nm)*	-	18.43	17.63	10.69	9.13
$\delta\, x1015$	$(lines/m^{-2})$	-	2.943	3.218	8.758	1.2
ε	*(%)*	-	0.328	0.343	0.324	0.38

	ZnO(102)	ZnO(110)	NiO(220)	ZnO(103)	ZnO(112)	NiO(311)
	47.586	56.522	62.651	62.651	67.928	74.9
	1.90934	1.62687	1.48164	1.48164	1.37881	1.2668
	-	-	-	-	-	-
	-	-	-	-	-	-
	-	-	-	-	-	-

Table 5.4: Structural parameters of NiZnO: 6% Ba thin films.

Parameter		NiZnO:6%Ba			
hkl		ZnO(100)	ZnO(002)	ZnO(101)	NiO(200)
2θ	(°)	31.675	34.323	36.851	42.704
d	(Å)	2.82253	2.61057	2.43713	2.11567
β	(°)	-	-	0.50941	0.81667
D	(nm)	-	-	16.44	10.44
$\delta\, x10^{15}$	$lines/m^{-2}$	-	-	3.701	9.167
ε	(%)	-	-	0.368	0.332

Table 5.5: Structural parameters of NiZnO: 8% Ba thin films.

Parameter		NiZnO:8%Ba				
hkl		Ba(110)	ZnO(002)	ZnO(101)	ZnO(102)	NiO(200)
2θ	*(°)*	25.488	34.202	35.999	47.302	42.669
d	*(Å)*	3.4918	2.61956	2.49282	1.92017	2.11732
β	*(°)*	-	0.32424	-	-	0.65144
D	*(nm)*	-	25.63	-	-	13.09
$\delta\, x1015$	$(lines/m^{-2})$	-	1.522	-	-	5.834
ε	*(%)*	-	0.236	-	-	0.462

	NiO(220)	ZnO(103)
	62.523	62.523
	1.48437	1.48437
	0.60038	-
	15.48	-
	-	-

Figure 5.4 gives the evolution of the lattice parameters in ZnO (hexagonal) & NiO (face–centered–cubic) phases as a function of Ba content (x at. %) at NiZnO: Ba thin films deposited at 450 Celsius degrees. The cubic lattice parameter of NiO (a_{cub}) and the hexagonal lattice (a_{hex} and c_{hex}) of ZnO are plotted against Ba concentration to understand the structural changes due to doping.

As shown in Tables 5.9, the NiO parameter a_{cub} vary from 4.1985 Å to 4.2450 Å and total mean of a_{cub} is 4.2197 Å; On the other hand, a_{hex} (ZnO) varies from 3.2514 Å to 3.2619 Å resulting in mean value of 3.2595 Å, and c_{hex} ranges from 5.1903 to 5.2391 Å with an average of 5.2143 Å.

In addition, with increasing Ba content, a_{cub} is almost not changing while there is a little increase in c_{hex} for ZnO. This means that doping with Ba introduces relatively minor structural changes, probably because of ionic radius difference: Ba^{2+} (1.35 Å) and Zn^{2+} (0.74 Å). Herissi et al (2020) [331], the thin films of $(NiO)_{0.5}(ZnO)_{0.5}$ are reported to have a heterostructure in terms of composition of given matrix, separated NiO and ZnO phases with well-defined compositions.

The lattice parameters (a_{cub}~ 4.21 Å, a_{hex}~ 3.26 Å and c_{he} ~5.21 Å), as reported by Zhong et al., are in good agreement with our experimental results which provides a strong support for Ba does not change the ZnO and thus NiO lattice parameter substantiating our hypothesis [331]. If the lattice constants only vary in a limited range then addition of the Ba, is either non-radial straining or almost no dilution in ZnO (or minimal). In keeping with Fiévet et al. (2019) [332], lattice constants usually increase with decreasing crystallite size, which is induced by surface stress.

For Ba doped NiO, there is a mild enhancement to a_{cub}, suggesting limited expansion of the lattice-curvature parameter. Since Ni^{2+} (0.69 Å) is significantly smaller than Ba^{2+} (135 Å) radius a strong trend may be attributed to partial Ba-substitution at Ni sites or local lattice strain [332-334]. Nevertheless, the small a_{cub} shift could only mean that Ba is immiscible in the NiO matrix resulting in possible phase segregation and not lattice solubility. The same is something reported by Lacz et al (2018) and Wang et al. (2020) [335, 336] who stated that Ba: NiO often gives rise to different phase formation due to its limited solubility [332, 333, 337, 338].

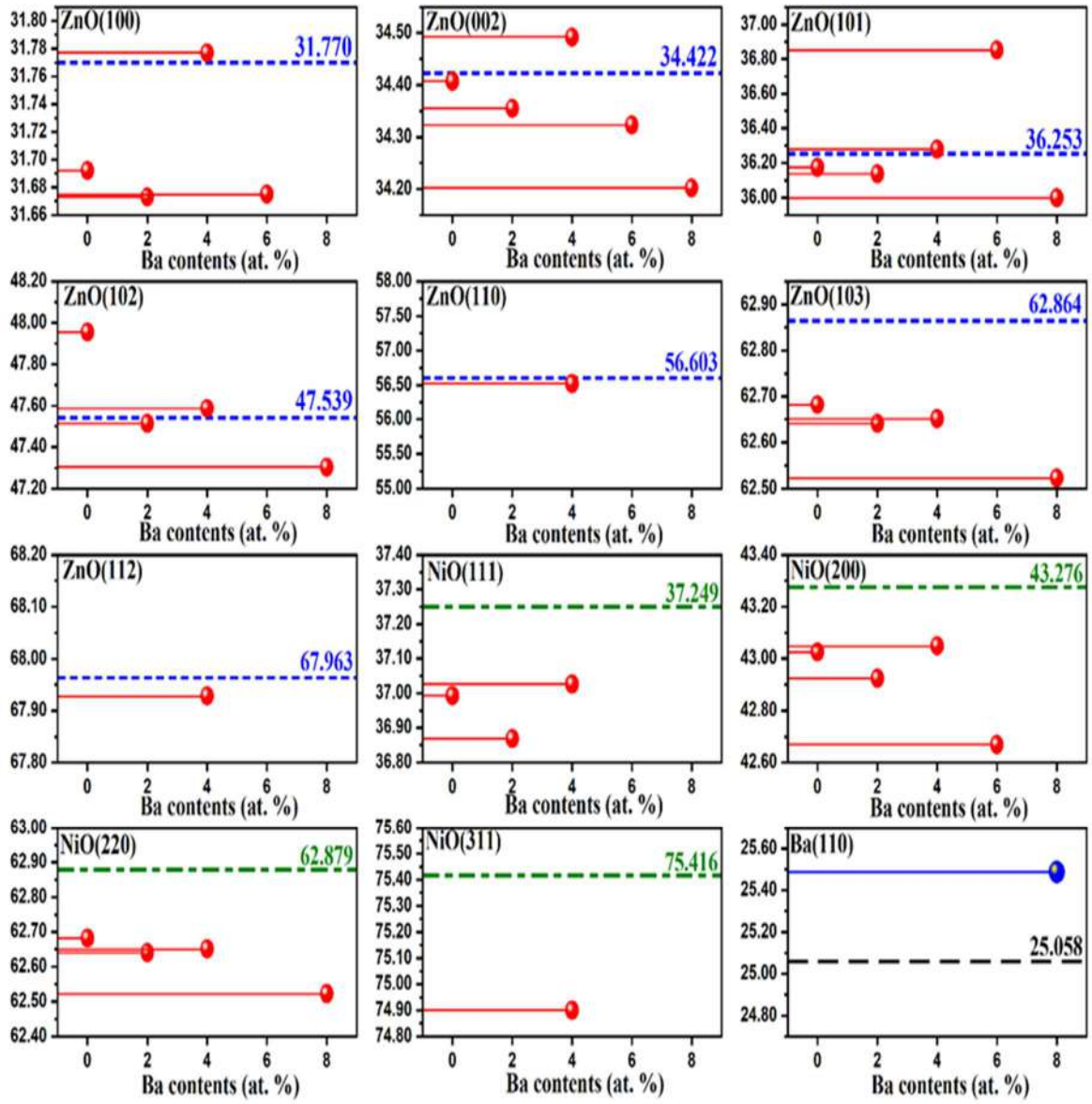

Figure. 5.2. Location of the diffraction peaks on the patterns obtained in comparison to the peaks given in the ICDD cards. The horizontal dashed lines indicate the position of the diffraction peaks as given on the ICDD cards: (blue lines, ZnO, #00-036-1451), (green lines, NiO, #00-047-1049), and (black line, Ba, #00 -047-1431).

Table 5.6: Lattice parameters of $ZnNiO$: x% Ba thin films ($x = 0, 2, 4, 6\ and\ 8$).

Samp.	ZnO (hexagonal)					NiO (cubic)		Ba (cubic)	
	a_{hex}(Å)	c_{hex}(Å)	c/a	V_{hex}(Å^3)	APF	a_{cub} (Å)	V_{cub}(Å^3)	a_{Ba}(Å)	V_{Ba}(Å^3)
S1	3.2575	5.1903	1.5934	47.6964	0.7589	4.1985	74.0105	-	-
S2	3.2594	5.2159	1.6003	47.9870	0.7556	4.2070	74.4613	-	-
S3	3.2514	5.2049	1.6009	47.6514	0.7554	4.2450	76.4945	-	-
S4	3.2592	5.2211	1.6020	48.0301	0.7548	4.2313	75.7590	-	-
S5	3.2619	5.2391	1.6062	48.2756	0.7529	4.2165	74.9665	4.9382	120.4182

In conclusion, the observed changes in lattice parameters suggest that Ba incorporation primarily affects the ZnO lattice along the c-axis, while it not significantly affects the NiO, except for little distortions. We have observed that these results are consistent with previous studies on Ba-doped ZnO and NiO, where doping-induced strain and secondary phase formation were reported as the dominant structural effects [329, 339]

Further analysis using Rietveld refinement or Raman spectroscopy could provide deeper insight into the extent of Ba incorporation and its influence on lattice strain and defect formation.

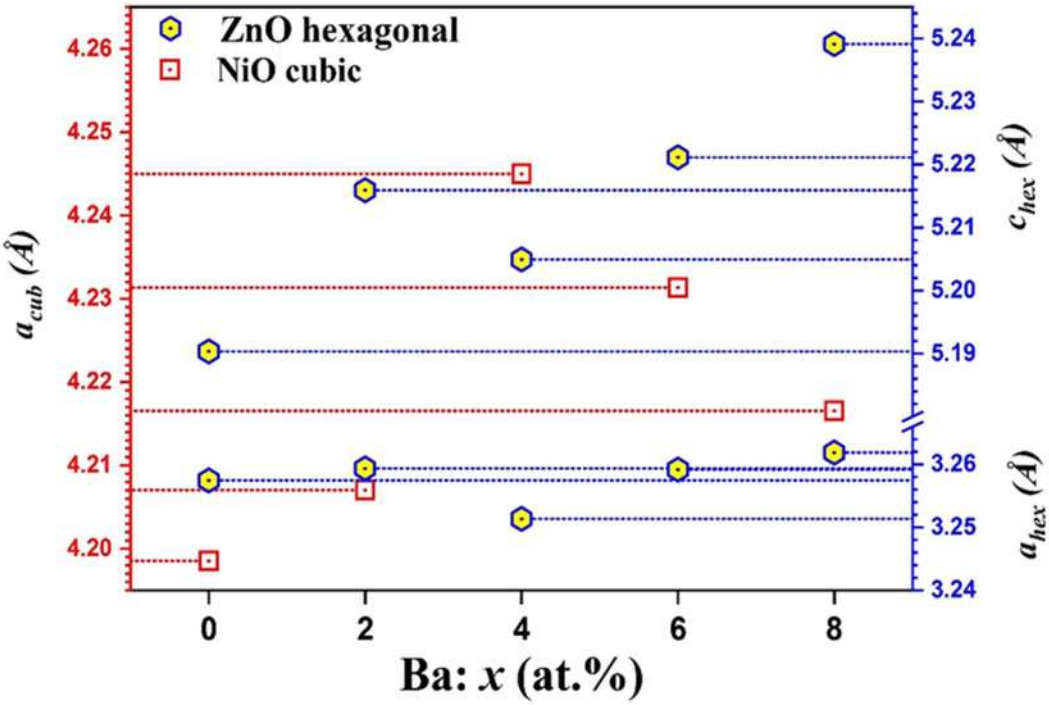

Figure 5.3. Evolution of lattice parameters of ZnO and NiO phases as a function of the ratio x in NiZnO: x at. % Ba thin films deposited at 450 °C.

5.3. Morphological properties of $Ba - doped\ ZnNiO$ thin films

5.3.1 General Scanning Electronic Microscopy Study

Figure 5.4(a) refers to the Scanning Electron Microscope (SEM) image of 2-atom % Ba doped $ZnNiO$ thin film, showing upper layer surface morphology. The image shows that through-and-around granular structures have an average distribution on the surface, which suggests polycrystalline structure.

Inset histogram- particle size distribution revealing a near-Gaussian distribution with a mean particle size = 23.89 nm. This implies that barium doping has little effect on the overall granular morphology, although it does impact particle size. The existence of such grains is characteristic, in thin films fabricated by solution processing [325] the nucleation and growth processes result in isolated crystallites. Thus, the standard deviation of 6.14 nm calculated implies moderate

particle size dispersion [334]. Such a morphology and size distribution are key for the optical and electrical properties of thin cells, as grain boundaries can be scattering centers and carrier recombination center [8, 110, 340].

Figure 5.4(b) shows a SEM image of 4 atomic per cent barium-doped zinc-nickel oxide (ZnNiO) thin film showing upper film surface morphology; similar granular structure to the 2 at% doped film, Figure 5.4 (a); however, differences in particle size and distribution are quite significant from this sample compared with the other. The figure inset shows an histogram, near-Gaussian in nature with a mean particle size of 20.10 nm, which is significantly less than 23.89 nm from that of our previously mentioned 2 at% doped film. This tells us that incorporation of barium from 2 at.% to 4 at.% leads the average particle size down. A standard deviation of 4.76 nm calculates a narrow size distribution, which means that the grain growth process is more consistent at this doping level. Original SEM image shows a uniform distribution of these tiny grains over the surface. Due to the effect of barium ions in barium doping, increased dopant concentration will change naturally nucleation and growth kinetics of deposited films leading to a variation on density of particles size with increased particle size without significant change in particle size, apart from as detailed below. Decreased grain size and decrease distribution can change the films optical as well electrical properties (surface area, grain boundary density, carrier transport etc.) [8, 110, 340].

Figure 5.4(c) SEM image of ZnNiO (6 atomic percent barium-doped) thin Film surface morphology. In this image, which contrasts with the microstructure changes shown in the previous figures (5.4(a) as barium doping increase from 0 % ZnNiO thin film. Figure also depicts a particle size distribution histogram inset with a distinctive near-Gaussian digital image, mean particle size of 16.82 nm; a smaller mean size than the mean sizes observed at 2 and 4 at.% levels of $ZnNiO$ doping. This remarks a possible reduction in particle size with increasing barium concentration, trend as indicated in the figures above. A standard deviation of 4.01 nm implies that it possesses a discrete size distribution, comparable to that in the case of a 4 at.%, suggesting the same grain growth mechanism for the grains. SEM image (right) indicates that these smaller grains are well distributed on the surface The decrease in grain size to 6 at.% doping on one hand may be consequence of the more barium ions where the formation growing could be inhibited by generating more nucleation sites and reducing the atoms diffusion during film creation. Such improved microstructure -with smaller size and narrower size distribution of grains can have profound impact on film levels physical properties, transmittance, electrical here and surface reactivity [8, 110, 340].

Table 5.7: The grain size, roughness, and thickness parameters of undoped and doped NiO nanostructured films.

Samples	D: Particle size				Ra	t
	Mean (nm)	Min. (nm)	Max. (nm)	SD (nm)	(nm)	(nm)
Undoped NiO	12.50	7.30	19.60	2.78	23.57	560.3
Ba2%NiO	22.30	17.10	29.40	2.75	27.89	213.2
Ba4%NiO	23.29	11.70	35.10	4.56	30.35	240.5
Ba6%NiO	20.75	7.70	38.10	6.65	36.46	375.6
Ba8%NiO	27.11	10.40	60.00	9.75	39.06	236.5

Figure 5.4(d) Scanning Electron Microscope (SEM) image to show surface morphology of as-deposited 8 atomic% barium doped zinc-nickel oxide (ZnNiO) thin film SEM

The SEM image of 8 atomic percentage barium-doped zinc-nickel oxide (ZnNiO) thin film (d), (Figure compared to the figures 5.4(a, b, c), reveal local variations in its microstructure under the highest barium doping level from aforementioned figures (5.4). On subplot d inset Histogram, distances of near-Gaussian particle size distribution with 18.42 nm average size slightly larger than the16.82 nm at 6 at.% doping suggest that at higher doping levels are not relatively all decreasing as lower doping levels.

The 4.45 nm standard deviation implies that the size is not as monodisperse like the previous samples: a small grain growth process can be seen, as all of these appear to originate from somewhat similar to each other. In the SEM image, grains are uniformly distributed over the surface, but all have grain boundaries looking a little more separable in some places and minor agglomeration. It could be that at higher doping concentration barium ions are affected in an incomers complex way also do that they influence the grain growth. There is the possibility that with that more doping concentration the film forming process is getting less uniform. Grain growth inhibition and agglomeration at higher doping levels can have propensity in physical properties of film (optical transmittance, electric conductivity etc.) that are direct contributions to surface reactivity.

Finally, the observed changes in particle size and morphology with the increase of doping are consistent with some previous studies on doped metal oxide thin films, where dopant concentration plays a crucial role in controlling the microstructure [8, 110, 340].

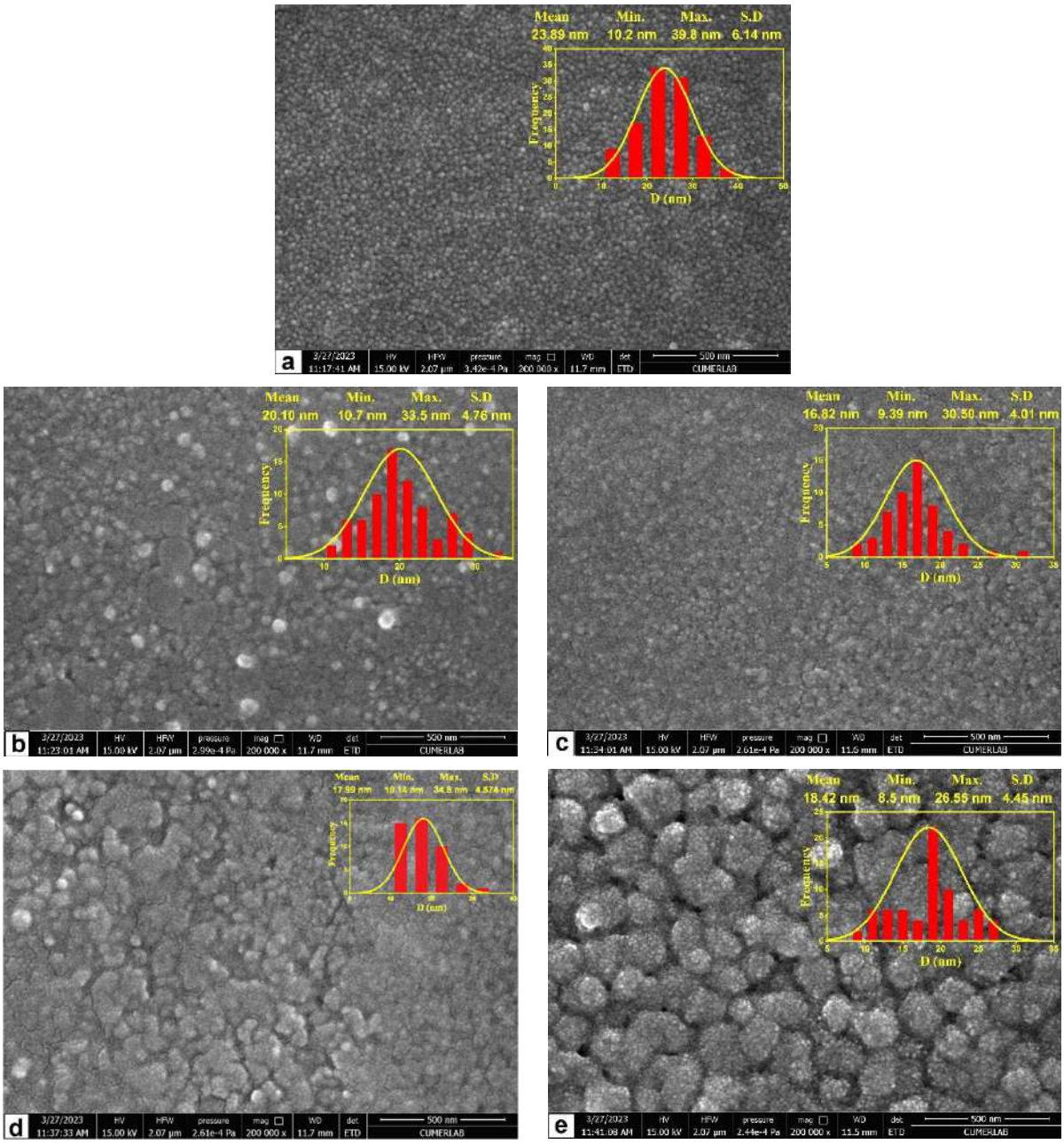

Figure 5.4: Various morphologies of SEM images of as-deposited ZnNiO thin films: (a) Ba 2 at. % ZnNiO, (b) Ba 4 at. % ZnNiO, (c) Ba 6 at. % ZnNiO and (d) Ba 8 at. % ZnNiO.

5.3.2 Surface state analysis of deposited Ba-doped *ZnNiO* thin films

5.3.2.a Surface morphology description

Figure 5.5 shows the three-dimensional scanning electron microscopy images of the surface topography of barium-Ba doped zinc-nickel oxide ($ZnNiO$) thin films by the spray pyrolysis technique (SPT) at 450°C; with varying Ba doping atomic percentage concentrations: 2 at% (a), 4 at% (b), 6 at% (c), and 8 at% (d)

In Figure 5.5(a), the granular structure is irregular on a rather sparse surface with discernible gaps suggesting the grain structure is not fully filled or uniform film formation (i.e. porous structure). In Fig. 5.5(b), there are more effects on the surface coverage which also accompanied by a finer grain size in a more uniform distribution. This observation implies that an increased concentration of Ba does improve nucleation and growth, and then results in a denser film.

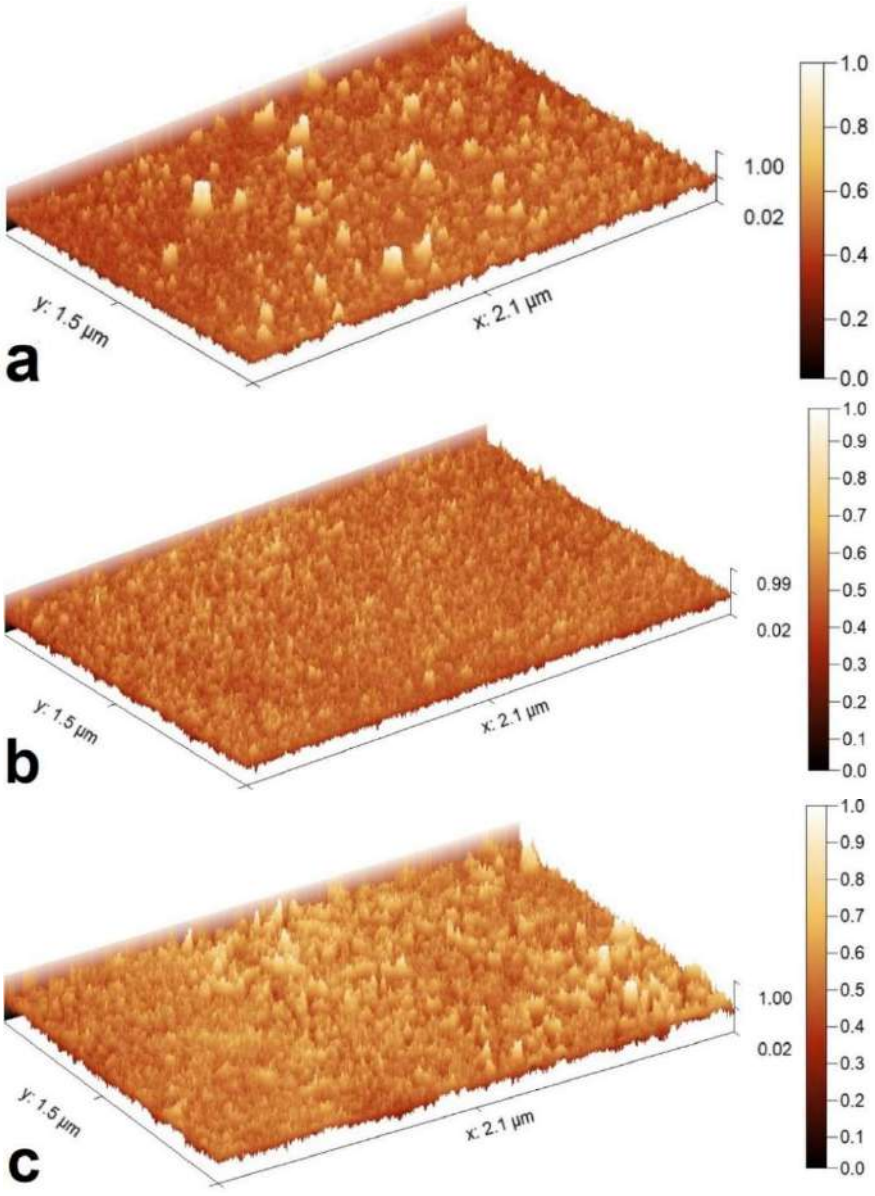

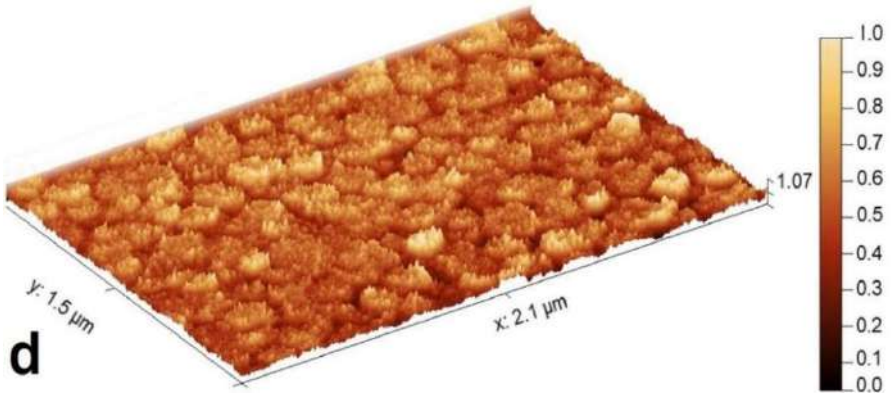

Figure 5.5: Three-dimensional scanning electron microscopy image of the topographical representation of Ba-doped ZnNiO thin films prepared using SPT at 450°C.

Fig. 5.5 (c) Further refinement of the grain structure appears to be attained with an even denser and uniform surface over a film consisting of well-aligned fine granular morphology. Fig.5.5 (d) The surface/wall area of the as-received sample reveals presence of larger, more well defined grains and beginning agglomeration. This observation suggests that for high Ba concentration, the mechanism of growth undergoes transformations that would turn out in grain coalescence.

The differences in the surface morphology observed at increasing Ba doping concentration could be related to the effect of barium ions on nucleation and growth kinetics during SPT. Initially as low level of doping allows Ba ions to act as primary nucleation sites, this will result in enhancement of grains creation and dense film. However, for higher Ba concentration, it might cause the surface energy and the diffusion rates to change, leading to fewer grains, thus uniform distribution. However, at higher doping levels (8 at.%), the excess Ba ions may restrict the mobility of other species leading to agglomeration and contamination causing a non-uniform film.

Such a behavior matches previous results on doped thin metal oxide films where the nature of dopant has already been suggested to have a massive impact on microstructure [341]. Changes in grain size and distribution can significantly influence the physical properties of the film; optical transmittance, electrical conductivity or surface reactivity are some production features. On the other hand, a higher surface area of smaller grains and denser film is convenient for catalytic applications. On the other hand, the formation of defects has been demonstrated to result in grain agglomeration, which decreases the performance of the film as a component.

ZnNiO thin films surface morphology can be adjusted by Ba doping, opening a route for tuning the properties of ZnNiO thin films towards desired applications. For example, for gas sensing or photocatalysis desirous with a high surface area (4-6at.-% Ba doping), and for controlled

grain size and distribution is requisite to tailor the electrical / optical properties of the films for various electronic / optoelectronic devices.

5.3.2.b Surface roughness analysis

Figure 5.6 presents SEM images and profile curves for Ba-doped ZnNiO thin films. We analyzed four doping concentrations: 2, 4, 6, and 8 at.%. The surface morphology changes significantly with Ba content.

At 2 at.% Ba, the film shows moderate roughness. The average roughness (Ra) is 0.054 µm. Positive skewness (Rsk=0.72) indicates a surface dominated by peaks. High kurtosis (Rku=5.06) suggests nanoscale clustering. These features create steep slopes. Such irregularities may scatter charge carriers in electronic devices [342].

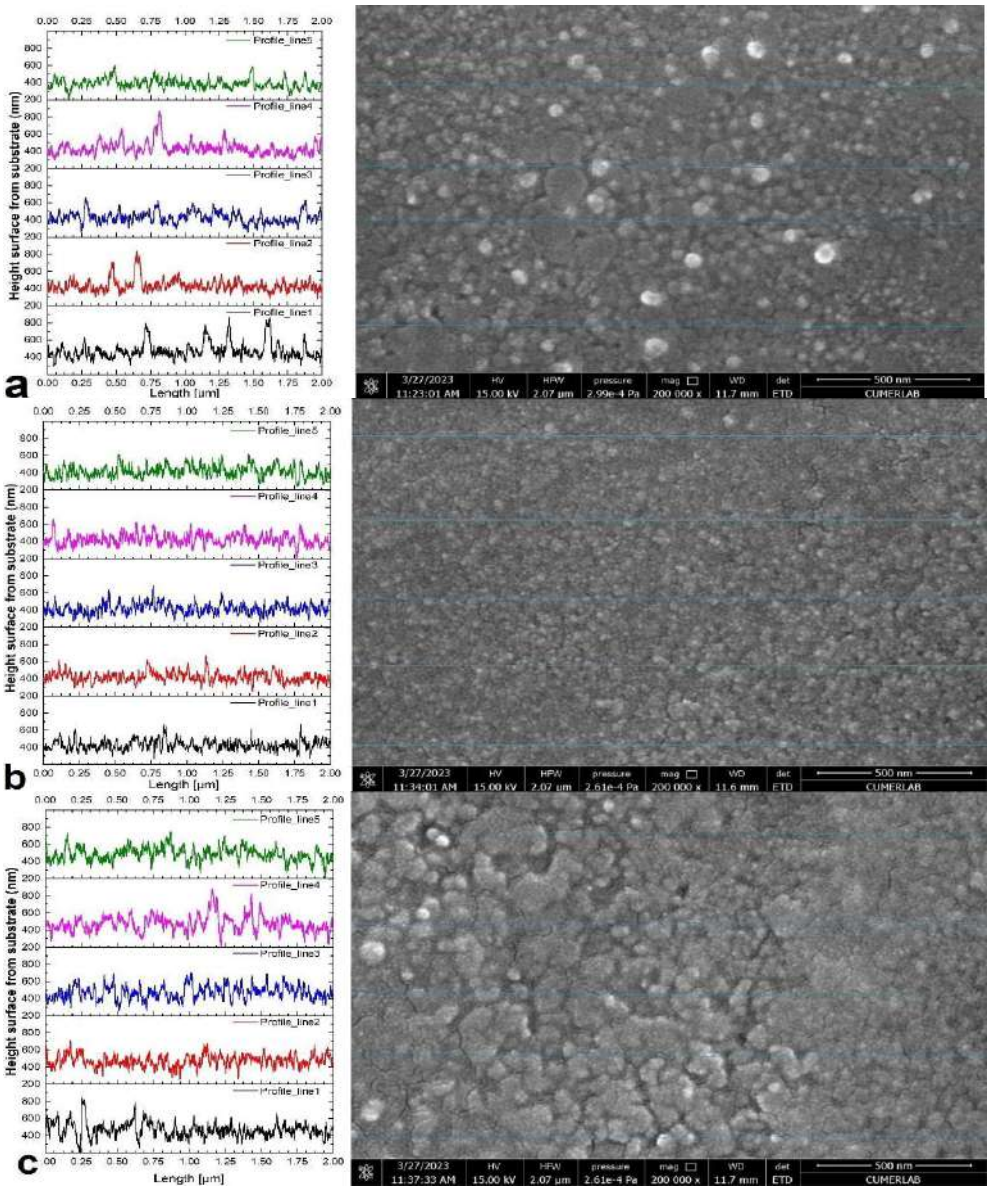

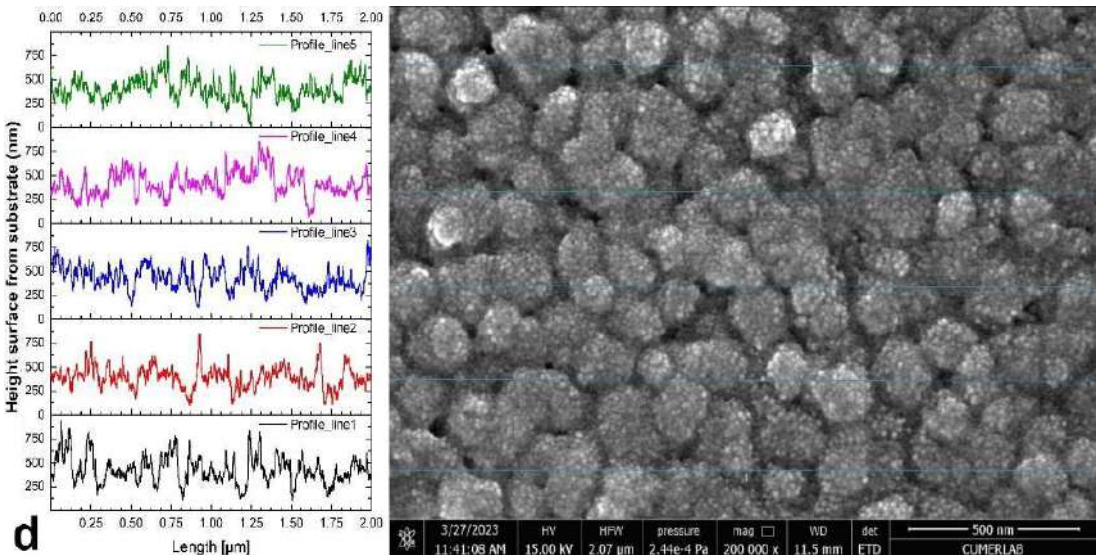

Figure 5.6: Profile curves measured along the lines shown on the SEM image of as-deposited ZnNiO thin films: (a) Ba 2 at. % ZnNiO, (b) Ba 4 at. % ZnNiO, (c) Ba 6 at. % ZnNiO and (d) Ba 8 at. % ZnNiO.

The 4 at.% sample displays the smoothest surface. The Ra value drops to 0.046 µm. Both skewness and kurtosis decrease. This implies better dopant incorporation and reduced clustering [343]. Surface features are uniform. Spatial parameters indicate consistent nucleation dynamics. This concentration optimizes structural homogeneity. It balances dopant integration with lattice stability.

At 6 at.%, roughness increases slightly. The Ra rises to 0.052 µm. This suggests strain saturation begins at this level. However, the surface remains smoother than the 2 at.% film. Spatial parameters show sparser surface features. Gentle slopes indicate smoother transitions between peaks and valleys. This morphology may reduce carrier scattering compared to lower doping levels [343].

The 8 at.% sample shows significant disorder. The Ra reaches 0.077 µm. Large defects and agglomerates appear. The ionic radius of Ba^{2+} exceeds that of Zn^{2+} and Ni^{2+}. This mismatch causes excessive lattice strain [344]. Steep slopes return, indicating abrupt surface transitions. Elevated waviness confirms large-scale undulations. This trend aligns with studies showing that excessive doping degrades morphological stability [341].

Overall, the results highlight a critical doping threshold. Moderate Ba content (4 at.%) optimizes surface quality. Higher levels reintroduce defects and disrupt growth kinetics. This balance is essential for maintaining optical and electronic performance.

5.4. Optical properties of Ba-doped $ZnNiO$ thin films

5.4.1 Study of the transmission of $ZnNiO$ thin films

Figure 5.7 displays the optical transmittance of barium-doped zinc-nickel oxide ($ZnNiO$) thin films, with barium concentrations ranging from 0 to 8 atomic percent, across wavelengths from 300 to 800 nanometers. The undoped film exhibits a high transmittance, approximately 70 to 80 percent, within the visible light spectrum (400–700 nm), a typical characteristic of wide-bandgap semiconductors that possess few defects within their bandgap. As the barium doping level increases, the absorption edge shifts towards shorter wavelengths (a blue shift), which corresponds to an observed increase in the bandgaps (E_{g1} and E_{g2}), as discussed in the following section. This shift can be explained by the Burstein-Moss effect, whereby the introduction of barium ions (Ba^{2+}) leads to a higher concentration of charge carriers. Consequently, the lower energy states within the conduction band become filled, requiring higher photon energies for optical absorption [295]. Simultaneously, the transmittance within the visible range experiences a slight reduction, for instance, a 5 to 10 percent decrease at 8 atomic percent barium.

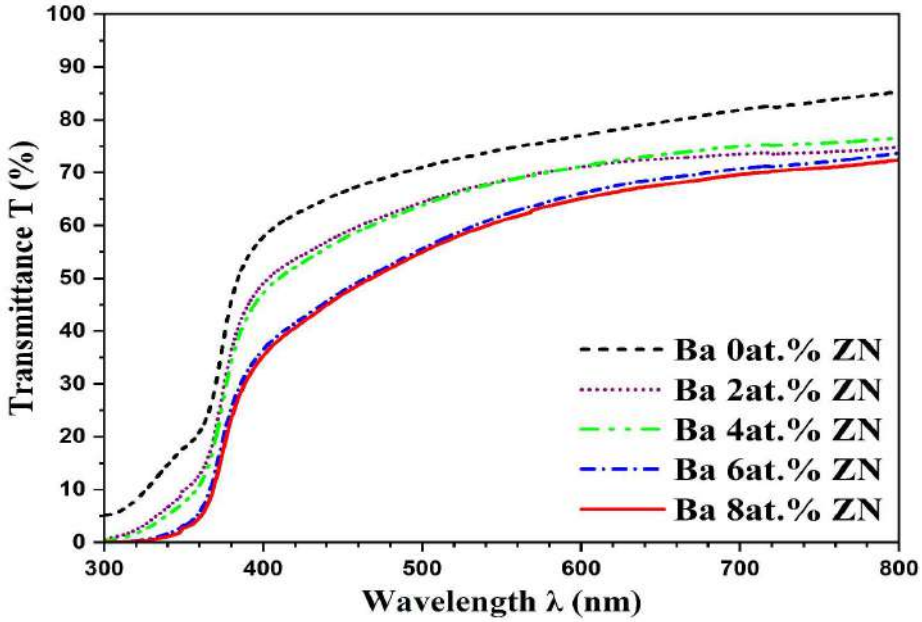

Figure 5.7: Transmission spectra of undoped and Ba-doped ZnNiO thin films: (a) undoped NiO, and (b) Ba 2 at. % NiO, (c) Ba 4 at. % NiO, and (d) Ba 6 at. % NiO, and (e) Ba 8 at. % NiO-doped.

This decrease is attributed to increased light scattering caused by structural distortions and defect formation, such as oxygen vacancies, resulting from the incorporation of barium. These

defects contribute to an elevated Urbach energy (E_u), leading to the formation of localized electronic states at the conduction band's tail. This phenomenon broadens the absorption edge and diminishes transparency, a behavior commonly observed in disordered oxide systems [313]. The spectra also reveal minor interference patterns, suggesting a relatively consistent film thickness. However, the intensity of these patterns decreases with higher doping levels, potentially due to increased surface irregularities or compositional variations. The balance between bandgap modification and defect-induced optical losses is crucial for optimizing barium-doped ZnNiO films for applications in transparent electronic devices or photovoltaic cells [247].

5.4.2 Study of the bandgap energy and Urbach disorder energy

As illustrated in Figure 5.8, the plots of $(\alpha h\nu)^2$ as a function of photon energy $(h\nu)$ are presented for the following: (a) undoped NiO, and (b) Ba 2 at. % NiO, (c) Ba 4 at. % NiO, and (d) Ba 6 at. % NiO, and (e) Ba 8 at. % NiO-doped thin films.

The UV-visible spectroscopy analysis of barium-doped zinc nickel oxide thin films (0–8 atomic percent) elucidates systematic variations in optical characteristics (see Table 5.11). The primary bandgap E_{g1} exhibits a slight increase from 3.239 eV (0% Ba) to 3.271 eV (8% Ba), whereas the secondary bandgap E_{g2} demonstrates a more significant escalation from 3.493 eV to 3.680 eV. This dual-bandgap phenomenon aligns with the Burstein-Moss effect [345], wherein an augmented carrier concentration resulting from Ba^{2+} substitution at zinc and nickel sites populates conduction band states, thereby inducing a blue shift in absorption thresholds. The comparatively larger ionic radius of Ba^{2+} (1.35 Å) in relation to Zn^{2+} (0.74 Å) and Ni^{2+} (0.69 Å) is likely to introduce compressive lattice strain, contributing to the bandgap widening by altering the density of states in proximity to the conduction band, as evidenced in similar doped zinc oxide systems (Özgür et al., 2005) [295]. Simultaneously, the Urbach energy E_u is observed to increase from 198.96 meV (0% Ba) to 230.46 meV (8% Ba), signifying an escalation in structural disorder and the presence of localized tail states within the bandgap. This disorder is attributable to lattice distortions and defect generation (e.g., oxygen vacancies) resulting from barium incorporation, which is consistent with investigations that correlate Urbach energy E_u with dopant-induced microstructural alterations in oxides (Cody, 1984)[313]. The amalgamated trends imply that optimal doping levels near 6–8% Ba may be favorable for applications necessitating adjustable bandgaps, albeit with concomitant compromises in crystallographic uniformity.

Figure 5.9 presents plots of $ln(\alpha)$ versus incident photon energy ($h\nu$) for Ba-doped ZnNiO thin films with varying Ba concentrations (0, 2, 4, 6, and 8 atomic percentages, represented by Figures 5.9 (a-e) respectively). Instead of Tauc plots, these are plots used to determine the Urbach energy (E_u), which represents the disorder or tailing of the band edges in the material. The red dashed lines represent linear fits to the exponential absorption edge region. The inverse slope of these lines gives the Urbach energy, as indicated by $E_u = \frac{1}{slope}$ in each figure.

As presented in Table 5.8, the calculated Urbach energies are reported in each panel, ranging from 198.96 meV for 0 at.% Ba to 230.46 meV for 8 at.% Ba. The trend observed is an increase in the Urbach energy with increasing Ba concentration. This indicates that the disorder in the ZnNiO thin films increases as the Ba doping level is raised. This could be due to several factors:

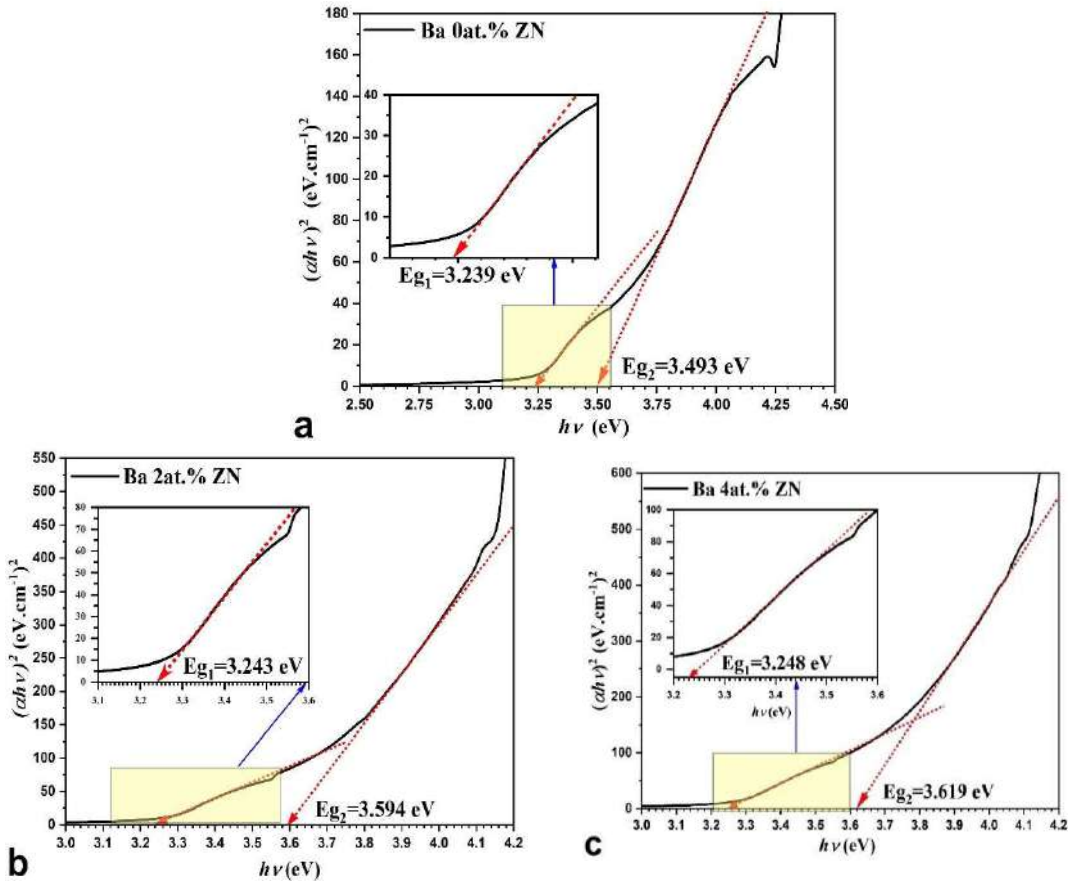

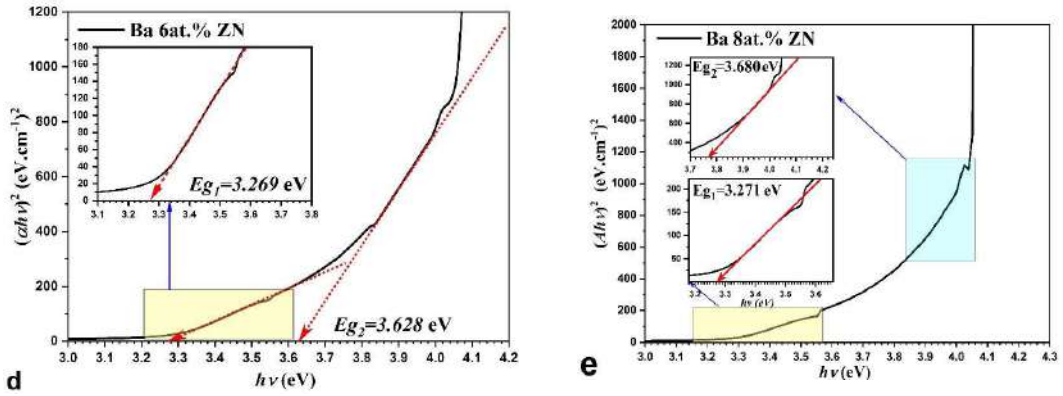

Figure 5.8: Plots of $(\alpha h\nu)^2$ vs $h\nu$ for: (a) undoped ZnNiO, (b) Ba 2 at. % ZnNiO, (c) Ba 4 at. % ZnNiO, (d) Ba 6 at. % ZnNiO, (e) Ba 8 at. % ZnNiO doped thin films.

Table 5.8: Optical bandgap energy and Urbach disorder energy of undoped and Ba-doped ZnNiO nanostructured films.

Percentage of Ba dopant	E_{g1}	E_{g2}	E_u
	$[eV]$	$[eV]$	$[meV]$
$x = 0\%$	3.239	3.493	198.96
$x = 2\%$	3.243	3.594	210.63
$x = 4\%$	3.248	3.619	211.51
$x = 6\%$	3.269	3.628	228.05
$x = 8\%$	3.271	3.680	230.46

Increased structural disorder: Ba doping might introduce more defects, dislocations, or variations in the local atomic arrangement, leading to increased structural disorder. Compositional fluctuations: The incorporation of Ba could result in compositional inhomogeneities within the ZnNiO matrix, contributing to the disorder. Strain effects: The difference in ionic radii between Ba and Zn/Ni might induce strain in the lattice, affecting the band edge tailing. Increased point defects: Ba doping can increase the concentration of oxygen vacancies or other point defects. The Urbach energy is a measure of the disorder-induced broadening of the band edges, which can significantly affect the optical and electronic properties of the material. A higher Urbach energy signifies a larger degree of disorder and a broader tail in the density of states near the band edges.

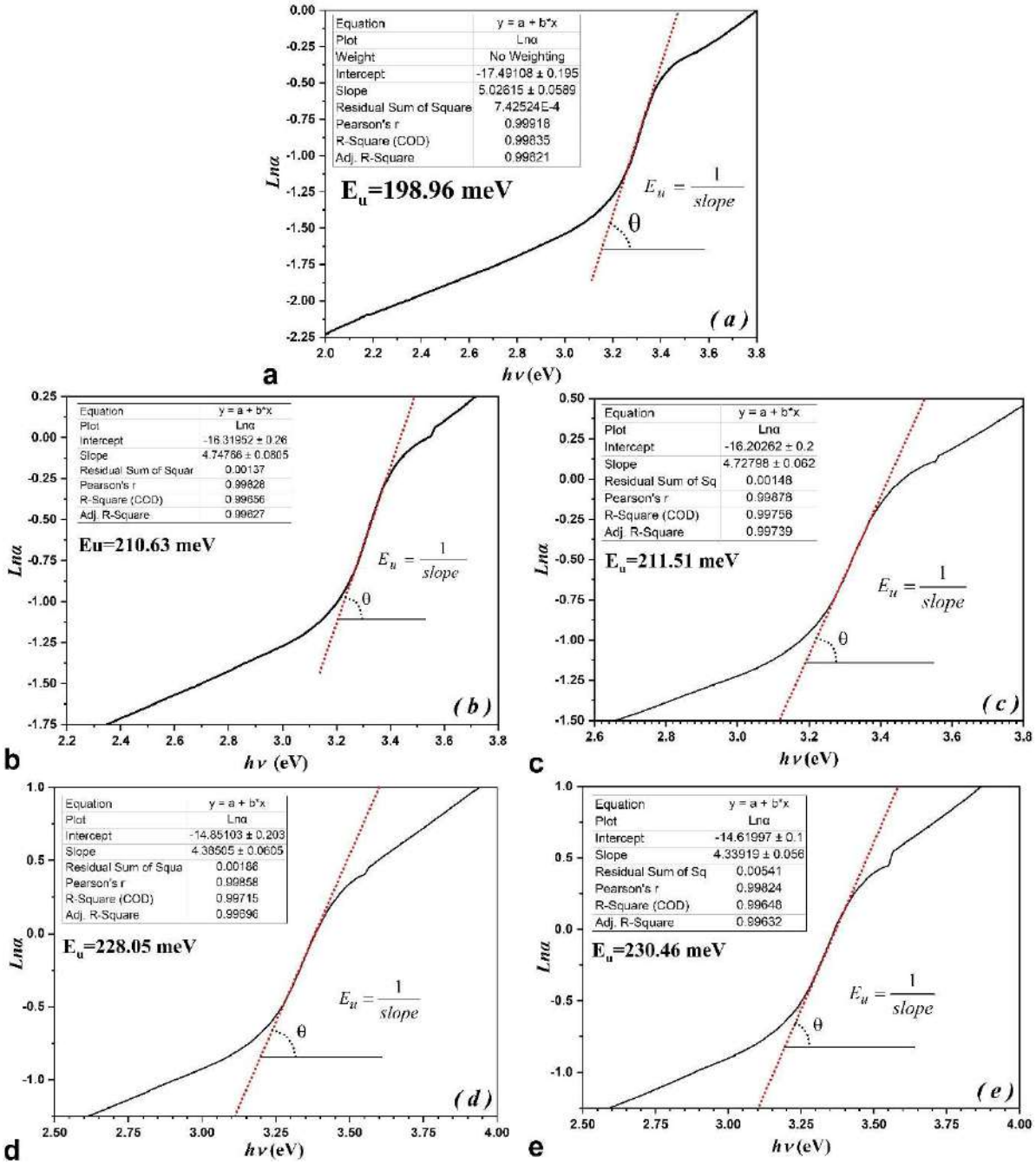

Figure 5.9: Plot of $Ln(\alpha)$ versus incident photon energy ($h\nu$) of Ba-doped NiO thin films at different precursor molarities.

Figure 5.10 illustrates the evolution of optical bandgap energies (E_{g1}, E_{g2}) and Urbach energy (E_u) in Ba-doped ZnNiO thin films as a function of Ba concentration (0–8 at.%). The correlation between bandgap energy (E_g) and Urbach energy (E_u) in Ba-doped ZnNiO thin films reflects the interplay between electronic structure modifications and structural disorder induced by doping. As Ba concentration increases (0–8 at.%), both E_{g1} *and* E_{g2} exhibit a widening trend ($\Delta E_{g1} \approx 0.032\ eV$, $\Delta E_{g2} \approx 0.187\ eV$), while E_u rises significantly from ~199 meV to ~230 meV. This positive correlation arises from two interconnected mechanisms:

1. **Bandgap Widening**: The increase in E_g is primarily attributed to the Burstein-Moss effect, where Ba^{2+} doping elevates carrier concentration, filling conduction band states and shifting the absorption edge to higher energies (blue shift). Concurrently, the larger ionic radius of Ba^{2+} (1.35 Å vs. Zn^{2+}/Ni^{2+} <0.74 Å) introduces compressive lattice strain, perturbing the density of states near the conduction band and amplifying the bandgap (Özgür et al., 2005)[295].
2. **Urbach Energy Increase**: The rise in E_u signifies enhanced structural disorder, including lattice distortions, localized tail states, and defect formation (e.g., oxygen vacancies). These defects disrupt the periodicity of the crystal lattice, creating energy states within the bandgap that broaden the Urbach tail. The strong correlation between E_g *and* E_u highlights that dopant-induced strain and defect generation are concurrent processes: while strain modifies the band structure, defects degrade crystallographic order (Cody, 1984)[313].

This duality underscores a trade-off in doped systems: higher doping enhances bandgap tunability (desirable for optoelectronic applications) but compromises material homogeneity. The trend aligns with studies showing that dopants introducing lattice mismatch (e.g., Ba in ZnO-based systems) simultaneously alter electronic and structural properties (Janotti & Van de Walle, 2007)[247].

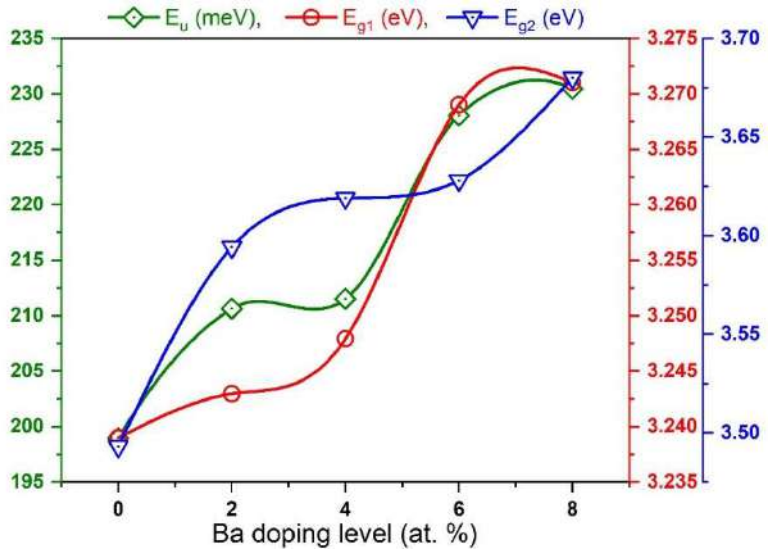

Figure 5.10: Evolution of the optical bandgap energy and Urbach energy as a function of the atomic concentration of the precursor solution for undoped and Ba-doped ZnNiO thin films.

In certain instances, the Tauc curve displays linear segments that extend to the zero ordinate, suggesting the presence of two bandgaps of direct transition. This phenomenon has been documented by numerous researchers. Mann et al. [346] have identified two direct transition band gaps of 1.87 eV for pure single-layer MoS_2 and 1.55 eV for pure single-layer $MoSe_2$,

suggesting that the bandgap can be continuously tuned through the SSe composition ratio. Luo et al. [347] have identified two direct band gaps: the monolayer arsenene has a direct band gap of approximately 0.903 eV, while the bilayer arsenic exhibits a direct band gap of about 0.489 eV, transitioning as layers increase. Zhu et al. [348] have studied the alloy $Si_xGe_{1-x-y}Sn_y$, and found that the indirect-direct bandgap transition occurs in the range of $0 < x \leq 0.20$, with the conduction band-edge broadening indicating the presence of two direct transition band gaps as Si concentration increases.

5.4.3 Study of the refractive index of $ZnNiO$ thin films

Table 5.19 summarizes the refractive index values (n) calculated according to different theoretical models.

The refractive index (n) of Ba-doped $ZnNiO$ thin films (0–8 at.%) exhibits a gradual decrease in experimental values from 2.6148 (undoped) to 2.6050 (8% Ba), reflecting subtle structural and electronic modifications induced by doping. This trend aligns with the progressive bandgap widening (E_{g1} and E_{g2}) observed in prior optical analyses, as increased carrier concentration and compressive lattice strain from Ba^{2+} incorporation (ionic radius mismatch) reduce the material's electronic polarizability, a key factor influencing n. Theoretical models diverge in their predictions:

Reddy-Nazeer (Eq. 1)[139] overestimates n (~2.7056–2.6981) but tracks the experimental trend closely, likely due to its reliance on bandgap-energy relationships that may insufficiently account for defect-mediated polarization losses.

Kumar-Singh (Eq. 2)[141] underpredicts n (~2.3051–2.2978), possibly due to its emphasis on polarizability terms sensitive to dopant-induced lattice distortions.

Moss (Eq. 3)[142] and Ravindra (Eq. 4)[3] models, which directly link n to bandgap energy, show systematic deviations (Moss: ~2.3272–2.3215; Ravindra: ~2.0758–2.0560). Ravindra's lower values suggest stronger sensitivity to E_g widening, while Moss's relation partially captures the inverse correlation between n and E_g.

Herve-Vandamme (Eq. 5)[144], which incorporates electronegativity and bandgap, yields intermediate values (~2.2604–2.2517), balancing electronic and structural contributions.

The discrepancies between experimental and theoretical values highlight the limitations of universal models in capturing dopant-specific effects, such as oxygen vacancy formation or localized strain fields, which alter polarizability and dielectric response. For instance, Ravindra's model, optimized for covalent semiconductors, underestimates n in ionic oxides like ZnNiO, while Herve-Vandamme's semi-empirical approach offers better agreement due to its

flexibility in parameterization. These results emphasize the need for doping-adjusted models to predict optical constants in complex oxide systems accurately.

A thorough examination of the experimental and theoretical values of the refractive index (n), as calculated according to various models, reveals a partial correlation between them, but significant discrepancies arise due to the assumptions and limitations inherent to each model. Therefore, we can give a detailed analysis:

- **Trend Consistency:**

- Experimental values decrease slightly from 2.6148 (0% Ba) to 2.6050 (8% Ba), reflecting a minor reduction in refractive index with doping.
- All theoretical models (Reddy-Nazeer, Kumar-Singh, Moss, Ravindra, and Herve-Vandamme) also predict a downward trend with increasing Ba concentration, aligning qualitatively with the experimental trend. This suggests that the models capture the general inverse relationship between doping-induced bandgap widening (as seen in prior UV-vis data) and refractive index, consistent with the Moss rule and similar semi-empirical relationships.

- **Magnitude Discrepancies:**

- Reddy-Nazeer (Eq. 1)[139] overestimates n by ~3.5% (e.g., 2.7056 vs. 2.6148 for 0% Ba), but its trend slope matches experiments closely. This model likely relies on oversimplified bandgap-polarizability relationships, ignoring defect-mediated dielectric losses.
- Kumar-Singh (Eq. 2)[141] underestimates n by ~12% (e.g., 2.3051 vs. 2.6148 for 0% Ba), possibly due to its sensitivity to lattice distortions not fully quantified in its parameterization.
- Moss (Eq. 3)[142] and Herve-Vandamme (Eq. 5)[144] show intermediate deviations (~11% and ~13.5% lower than experiments, respectively), but their trends mirror the experimental slope more faithfully.
- Ravindra (Eq. 4)[3] deviates most severely (~20% lower), as its linear dependence on $1/E_g$ oversimplifies the complex interplay between bandgap, electronegativity, and ionic polarizability in oxides.

- **Model-Specific Limitations:**

- Moss and Ravindra models assume a direct correlation between $and\ E_g$, which holds broadly but fails to account for dopant-induced defects (e.g., oxygen vacancies) that alter local polarizability.

- Herve-Vandamme [144] incorporates electronegativity, improving its alignment with trends, but still neglects strain effects from Ba^{2+} substitution.
- Reddy-Nazeer [139] and Kumar-Singh [141] may lack universality, as they are tailored for specific material systems (e.g., covalent semiconductors) and poorly capture ionic contributions in ZnNiO.

▪ **Interpretation**

The partial correlation underscores that while semi-empirical models broadly reflect the inverse relationship between n *and* E_g, they struggle to quantify dopant-specific effects such as:

- Lattice strain (from ionic radius mismatch: Ba^{2+} = 1.35 Å vs. Zn^{2+} = 0.74 Å), which modifies dielectric response.
- Defect states (e.g., oxygen vacancies), which reduce electronic polarizability and amplify scattering losses.
- Localized tail states (linked to rising Urbach energy), which broaden optical transitions and perturb n.

Table 5.9: Refractive index variation as function of the dopant percentage of Ba doped NiZnO calculated different relations.

Samples of Ba-x%-doped ZnNiO thin films	**Refractive index (n)**					
	Our work	Reddy-Nazeer [139]	Kumar-Singh [141]	Moss[142]	Ravindra [3]	Herve-Vandamme [144]
$x\ (at.\%)$	Exp.	Eq. (2.21)	Eq. (2.22)	Eq. (2.23)	Eq. (2.24)	Eq. (2.25)
$x = 0$	2,6148	2,7056	2,3051	2,3272	2,0758	2,2604
$x = 2$	2,6136	2,7046	2,3042	2,3265	2,0734	2,2593
$x = 4$	2,6121	2,7035	2,3031	2,3256	2,0703	2,2580
$x = 6$	2,6056	2,6986	2,2983	2,3218	2,0572	2,2523
$x = 8$	2,6050	2,6981	2,2978	2,3215	2,0560	2,2517

5.4. Electrical properties of Ba-doped *ZnNiO* thin films

The previous Table 5.10 shows the resistivity (ρ) of $Ba - x\ at.\%\ ZnNiO$ thin films as vary by atomic percentage doping (x = 0 - 8%). There is a clear trend visible, in which resistivity increases as doping increases and peaks at x = 6% value of $\rho = 0.9015\ (\Omega \cdot m)^{-1}$ then drops dramatically at x = 8% with a value of $\rho = 0.6124\ (\Omega \cdot m)^{-1}$. The trend is non-linear suggesting a changing aspects of a materials electrical properties due to competing effects; an increase in the concentration of charge carriers at lower doping levels and a loss of carriers to

defect based scattering or stress induced lattice distortions at higher concentrations (x = 8%). Observational tables of this nature are important to consider when documenting and organizing complex datasets with the intention of making identifying groups, trends and unexpected variations rapid at a glance (as already indicated). For example, the peak at x = 6% may represent an ideal equilibrium point for maximizing resistivity, while the decrease at x = 8% may suggest some type of phase separation or lattice structural instability, two phenomena that are often the focus of analysis in physical science based studies aimed at identifying doping efficiency. Such interpretations are along the lines of criteria outlined numerous times in scientific analysis of data, particularly using tables to assign an orderly approach to analyzing the results of experimental work.

Table 5.10. Electrical conductivity of Ba-doped $ZnNiO$ thin films with various atomic concentrations of precursor.

$x\ (at.\%)$	$x = 0$	$x = 2$	$x = 4$	$x = 6$	$x = 8$
$\rho(\Omega \cdot m)^{-1}$	0.3267	0.4378	0.7843	0.9015	0.6124

5.5. Conclusions

In conclusion, this chapter has systematically explored the structural, morphological, and optical properties of undoped and $Ba - doped\ ZnNiO$ thin films, revealing key insights into their behavior under varying Ba concentrations. The XRD analysis demonstrated that moderate Ba doping enhances crystallinity and induces preferential c-axis orientation, while higher doping levels lead to phase segregation and the formation of distinct Ba-containing phases. Morphological investigations via SEM highlighted a non-linear trend in surface roughness and grain size, where optimal homogeneity was achieved at 4 at.% Ba, but excessive doping beyond 6 at.% resulted in increased surface disorder, agglomeration, and defect formation. These structural and morphological changes were closely tied to the optical properties, as evidenced by the blue shift in the absorption edge and the widening of bandgaps ($E_{g1}\ and\ E_{g2}$) due to the Burstein-Moss effect, alongside a rise in Urbach energy indicating heightened structural disorder. The refractive index exhibited a subtle decrease with doping, reflecting the interplay between bandgap widening and dopant-induced lattice distortions, though theoretical models struggled to fully capture these effects due to oversimplified assumptions. Collectively, these findings underscore the delicate balance between enhancing optoelectronic performance through doping and maintaining structural integrity, suggesting that moderate Ba doping (4–6 at.%) offers the best compromise for tailoring ZnNiO thin films for specific applications.

General Conclusion

General conclusion and Prospective future works.

I-General conclusion

This doctoral research meticulously investigated the elaboration, characterization of undoped, and barium (Ba)-doped metal oxide thin films, specifically nickel oxide (NiO), zinc oxide (ZnO), and zinc-nickel oxide ($ZnNiO$) composites, with a view towards their application in gas detection.

Employing the cost-effective and scalable spray pyrolysis technique, the study systematically explored the intricate relationships between deposition parameters, doping concentrations, and the resulting structural, morphological, optical, and electrical properties of these advanced materials. The overarching aim was to address critical challenges in optimizing metal oxide thin films, particularly the elusive goal of achieving stable p-type conductivity in NiO and enhancing the overall performance for gas sensing applications.

The experimental findings demonstrate that the chosen synthesis approach yielded crystalline thin films for all studied systems, with their properties significantly influenced by precursor molarity and Ba doping. For NiO films, a face-centered cubic structure was confirmed, where increasing precursor concentration notably affected crystallite size, microstrain, and dislocation density. Ba doping in NiO led to observable modifications in structural parameters, surface morphology-including grain size distribution-and optical characteristics, highlighting its role in tuning bandgap energy and defect states.

Similarly, ZnO films exhibited a hexagonal wurtzite structure with preferential orientation, and Ba incorporation systematically influenced their crystallinity, grain morphology, and optical properties, affecting transmission and bandgap.

The most significant contribution lies in the comprehensive analysis of the novel Ba-doped $ZnNiO$ composite films, where the coexistence of both ZnO and NiO phases was confirmed. Ba doping in these composites induced notable structural shifts and modulated their granular morphology and particle size, directly affecting their optical and electrical responses, indicating a promising avenue for tailoring their functionality.

Despite these advancements, the research also underscored inherent limitations and challenges. The persistent difficulty in achieving robust and stable p-type conductivity in NiO due, in part, to intrinsic self-compensation effects and potential dopant migration under operational stress, remains a critical hurdle. While spray pyrolysis proved scalable and cost-effective, maintaining perfect film quality-such as homogeneous dopant distribution and ideal crystallinity-across varying doping levels presented challenges, as evidenced by observed morphological irregularities and localized defects.

Furthermore, the long-term operational stability of these doped systems in fluctuating thermal and humid environments requires continuous investigation to prevent device deterioration.

II- Prospective future works

Looking forward, this work opens several compelling avenues for future research. The integration of advanced computational modeling, such as density functional theory (DFT), with experimental efforts could significantly accelerate the rational design of new dopant-host combinations and predict optimal defect chemistries, thereby minimizing trial-and-error in material development.

Further studies should focus on innovative interface engineering and co-doping strategies to overcome persistent challenges in p-type doping and to create stable heterojunctions for enhanced charge transport.

Exploring post-deposition treatments and effective encapsulation methods could also bolster long-term operational stability. Ultimately, continued refinement of synthesis techniques to precisely control nanoscale morphology and grain boundaries will be vital for translating these laboratory-scale breakthroughs into high-performance, commercially viable gas sensors and other optoelectronic devices, cementing the role of metal oxide semiconductors in sustainable technological advancements.

Annexes

Roughness Parameters of undoped NiO thin films		
Cut-off	53.9562	nm
Amplitude		
Roughness average (Ra)	23.2613	
Root mean square roughness (Rq)	29.8583	
Maximum height of the roughness (Rt)	0.226038	
Maximum roughness valley depth (Rv)	0.11386	
Maximum roughness peak height (Rp)	0.112178	
Average maximum height of the roughness (Rtm)	0.186595	
Average maximum roughness valley depth (Rvm)	0.100861	
Average maximum roughness peak height (Rpm)	0.0857338	
Average third highest peak to third lowest valley height (R3z)	0.185279	
Average third highest peak to third lowest valley height (R3z ISO)	0.138963	
Average maximum height of the profile (Rz)	0.198497	
Average maximum height of the roughness (Rz ISO)	0.186595	
Maximum peak to valley roughness (Ry = Rmax)	0.224076	
Skewness (Rsk)	-0.143465	
Kurtosis (Rku)	3.54545	
Waviness average (Wa)	24.455	
Root mean square waviness (Wq)	30.7431	
Waviness maximum height (Wy = Wmax)	0.166794	
Maximum height of the profile (Pt)	0.309459	
Spatial		
Mean spacing of profile irregularities (Sm)	10.3104	nm
Average wavelength of the profile (λa)	10.296	nm
Root mean square (RMS) wavelength of the profile (Δq)	10.1535	nm
Hybrid		
Average absolute slope Δa)	14.1953	μm^{-1}
Root mean square (RMS) slope (Δq)	18.4769	μm^{-1}
Length (L)	2.08271	µm

Roughness Parameters of Ba-doped NiO thin films (2at.%Ba)		
Cut-off	53.9591	nm
Amplitude		
Roughness average (Ra)	27.888	
Root mean square roughness (Rq)	37.244	
Maximum height of the roughness (Rt)	0.357937	
Maximum roughness valley depth (Rv)	0.181524	
Maximum roughness peak height (Rp)	0.176413	
Average maximum height of the roughness (Rtm)	0.232816	
Average maximum roughness valley depth (Rvm)	0.109174	
Average maximum roughness peak height (Rpm)	0.123643	
Average third highest peak to third lowest valley height (R3z)	0.247557	
Average third highest peak to third lowest valley height (R3z ISO)	0.160639	
Average maximum height of the profile (Rz)	0.263713	
Average maximum height of the roughness (Rz ISO)	0.232816	
Maximum peak to valley roughness (Ry = Rmax)	0.357937	
Skewness (Rsk)	0.0676107	
Kurtosis (Rku)	4.95219	
Waviness average (Wa)	0.0355797	
Root mean square waviness (Wq)	0.0518251	
Waviness maximum height (Wy = Wmax)	0.308212	
Maximum height of the profile (Pt)	0.490629	
Spatial		
Mean spacing of profile irregularities (Sm)	10.8047	nm
Average wavelength of the profile (λa)	11.5612	nm
Root mean square (RMS) wavelength of the profile (λq)	12.0116	nm
Hybrid		
Average absolute slope (Δa)	15.1563	μm^{-1}
Root mean square (RMS) slope (Δq)	19.4819	μm^{-1}
Length (L)	2.26898	µm

Roughness Parameters of Ba-doped NiO thin films (4at.%Ba)		
Cut-off	53.96	nm
Amplitude		
Roughness average (Ra)	0.030347	
Root mean square roughness (Rq)	0.038142	
Maximum height of the roughness (Rt)	0.251758	
Maximum roughness valley depth (Rv)	0.112061	
Maximum roughness peak height (Rp)	0.139697	
Average maximum height of the roughness (Rtm)	0.215542	
Average maximum roughness valley depth (Rvm)	0.097798	
Average maximum roughness peak height (Rpm)	0.117744	
Average third highest peak to third lowest valley height (R3z)	0.206988	
Average third highest peak to third lowest valley height (R3z ISO)	0.184385	
Average maximum height of the profile (Rz)	0.217130	
Average maximum height of the roughness (Rz ISO)	0.215542	
Maximum peak to valley roughness (Ry = Rmax)	0.230986	
Skewness (Rsk)	0.241712	
Kurtosis (Rku)	2.984130	
Waviness average (Wa)	0.019093	
Root mean square waviness (Wq)	0.025341	
Waviness maximum height (Wy = Wmax)	0.146815	
Maximum height of the profile (Pt)	0.288285	
Spatial		nm
Mean spacing of profile irregularities (Sm)	6.95	nm
Average wavelength of the profile (λa)	7.37	nm
Root mean square (RMS) wavelength of the profile (λq)	7.29	
Hybrid		μm^{-1}
Average absolute slope (Δa)	25.88	μm^{-1}
Root mean square (RMS) slope (Δq)	32.87	µm

Roughness Parameters of Ba-doped NiO thin films (6at.%Ba)		
Cut-off	53.963	nm
Amplitude		
Roughness average (Ra)	0.0364553	
Root mean square roughness (Rq)	0.0466679	
Maximum height of the roughness (Rt)	0.356823	
Maximum roughness valley depth (Rv)	0.155758	
Maximum roughness peak height (Rp)	0.201065	
Average maximum height of the roughness (Rtm)	0.264977	
Average maximum roughness valley depth (Rvm)	0.124649	
Average maximum roughness peak height (Rpm)	0.140328	
Average third highest peak to third lowest valley height (R3z)	0.262971	
Average third highest peak to third lowest valley height (R3z ISO)	0.2081	
Average maximum height of the profile (Rz)	0.28207	
Average maximum height of the roughness (Rz ISO)	0.264977	
Maximum peak to valley roughness (Ry = Rmax)	0.356823	
Skewness (Rsk)	0.174564	
Kurtosis (Rku)	3.42279	
Waviness average (Wa)	0.0368749	
Root mean square waviness (Wq)	0.0488402	
Waviness maximum height (Wy = Wmax)	0.269691	
Maximum height of the profile (Pt)	0.511852	
Spatial		
Mean spacing of profile irregularities (Sm)	10.3633	nm
Average wavelength of the profile (λa)	10.7941	nm
Root mean square (RMS) wavelength of the profile (λq)	10.8979	nm
Hybrid		
Average absolute slope (Δa)	21.2204	μm^{-1}
Root mean square (RMS) slope (Δq)	26.9064	μm^{-1}
Length (L)	2.05194	µm

Roughness Parameters of Ba-doped NiO thin films (8at.%Ba)		
Cut-off	53.9591	nm
Amplitude		
Roughness average (Ra)	39.0632	
Root mean square roughness (Rq)	48.9644	
Maximum height of the roughness (Rt)	350.895	
Maximum roughness valley depth (Rv)	159.909	
Maximum roughness peak height (Rp)	190.986	
Average maximum height of the roughness (Rtm)	276.64	
Average maximum roughness valley depth (Rvm)	133.195	
Average maximum roughness peak height (Rpm)	143.445	
Average third highest peak to third lowest valley height (R3z)	284.548	
Average third highest peak to third lowest valley height (R3z ISO)	223.911	
Average maximum height of the profile (Rz)	296.929	
Average maximum height of the roughness (Rz ISO)	276.64	
Maximum peak to valley roughness (Ry = Rmax)	350.895	
Skewness (Rsk)	46.9661	
Kurtosis (Rku)	3.14267	
Maximum height of the profile (Pt) 370.3505	0.511852	
Spatial		
Mean spacing of profile irregularities (Sm)	7.28638	nm
Average wavelength of the profile (λa)	7.84559	nm
Root mean square (RMS) wavelength of the profile (λq)	7.7838	nm
Hybrid		
Average absolute slope (Δa)	31.284	μm^{-1}
Root mean square (RMS) slope (Δq)	39.5247	μm^{-1}
Length (L)	2.06933	µm

Annex –F –

Roughness Parameters of undoped ZnO thin films		
Cut-off	0.1741	nm
Amplitude		
Roughness average (R_a)	0.0327	
Root mean square roughness ($R_{q)}$	0.0416	
Maximum height of the roughness (R_t)	0.2910	
Maximum roughness valley depth (R_v)	0.1120	
Maximum roughness peak height (R_p)	0.1789	
Average maximum height of the roughness (R_{tm})	0.2162	
Average maximum roughness valley depth (R_{vm})	0.1032	
Average maximum roughness peak height (R_{pm})	0.1130	
Average third highest peak to third lowest valley height (R_{3z})	0.1976	
Average third highest peak to third lowest valley height ($R_{3z\ ISO}$)	0.1727	
Average maximum height of the profile (R_z)	0.2180	
Average maximum height of the roughness ($R_{z\ ISO}$)	0.2162	
Maximum peak to valley roughness ($R_y = R_{max}$)	0.2903	
Skewness (R_{sk})	0.0332	
Kurtosis (R_{ku})	3.3874	
Waviness average (W_a)	0.0247	
Root mean square waviness (W_q)	0.0316	
Waviness maximum height ($W_y = W_{max}$)	0.1565	
Maximum height of the profile (P_t)	0.4098	
Spatial		
Mean spacing of profile irregularities (S_m)	29.2679	nm
Average wavelength of the profile (λ_a)	25.8005	nm
Root mean square (RMS) wavelength of the profile (Δ_q)	26.0380	nm
Hybrid		
Average absolute slope Δ_a)	7.9747	μm^{-1}
Root mean square (RMS) slope (Δ_q)	10.0271	μm^{-1}
Length (L)	2.3122	µm

Annex –G –

Name and formula

Reference code:	00-047-1049
Mineral name:	Bunsenite, syn
Compound name:	Nickel Oxide
PDF index name:	Nickel Oxide
Empirical formula:	NiO
Chemical formula:	NiO

Crystallographic parameters

Crystal system:	Cubic
Space group:	Fm-3m
Space group number:	225
a (Å):	4.1771
b (Å):	4.1771
c (Å):	4.1771
Alpha (°):	90.0000
Beta (°):	90.0000
Gamma (°):	90.0000
Calculated density (g/cm^3):	6.81
Volume of cell (10^6 pm^3):	72.88
Z:	4.00
RIR:	6.15

Subfiles and quality

Subfiles:	Alloy, metal or intermetalic Common Phase Corrosion Forensic Inorganic Mineral
Quality:	Star (S)

Comments

Color:	Green
Creation Date:	01/01/1970
Modification Date:	01/01/1970
Color:	Green
Sample Source or Locality:	Sample obtained from J.T. Baker Chemical Corporation
Sample Preparation:	Sample annealed for 72 hours at 1100 C. Average relative standard deviation in intensity of the 5 strongest reflections for 3 specimen mounts = 1.1%. Validated by calculated pattern
Additional Patterns:	To replace 00-004-0835
Optical Data:	B=2.27.

References

Primary rference:	Martin, K., McCarthy, G., North Dakota State Univ., Fargo, ND, USA., *ICDD Grant-in-Aid*, (1991)
Optical data:	Winchell, Winchell., *Elements of Optical Mineralogy*, 58, (1964)

Peak list

No.	h	k	l	d [A]	2Theta[deg]	I [%]
1	1	1	1	2.41200	37.249	61.0
2	2	0	0	2.08900	43.276	100.0
3	2	2	0	1.47680	62.879	35.0
4	3	1	1	1.25940	75.416	13.0
5	2	2	2	1.20580	79.409	8.0
6	4	0	0	1.04430	95.059	4.0
7	3	3	1	0.95830	106.993	3.0
8	4	2	0	0.93400	111.123	7.0

Stick Pattern

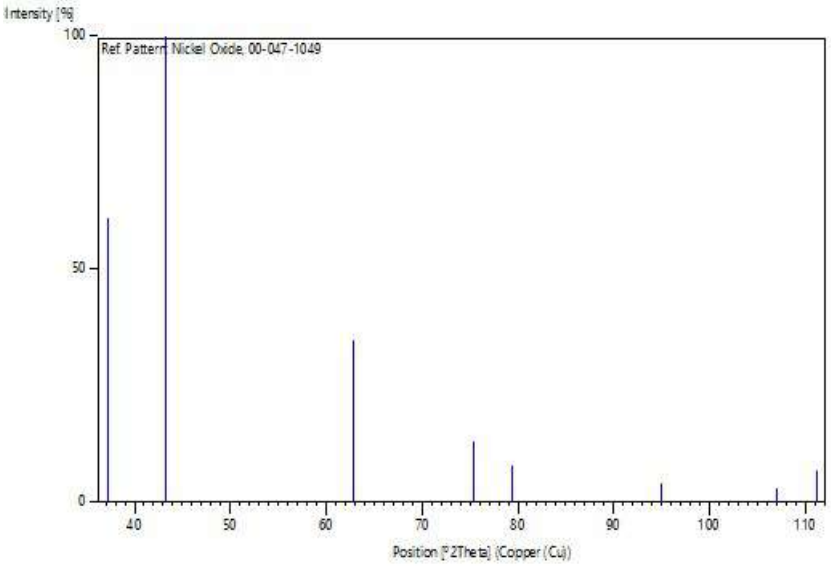

Annex –H –

Name and formula

Reference code:	00-036-1451
Mineral name:	Zincite, syn
Compound name:	Zinc Oxide
Common name:	zinc white
PDF index name:	Zinc Oxide
Empirical formula:	OZn
Chemical formula:	ZnO

Crystallographic parameters

Crystal system:	Hexagonal
Space group:	P63mc
Space group number:	186
a (Å):	3.2498
b (Å):	3.2498
c (Å):	5.2066
Alpha (°):	90.0000
Beta (°):	90.0000
Gamma (°):	120.0000
Volume of cell (10^6 pm^3):	47.62
Z:	2.00
RIR:	-

Subfiles and quality

Subfiles:	Alloy, metal or intermetalic Common Phase Corrosion Educational pattern Forensic Inorganic Mineral NBS pattern Pharmaceutical Pigment/Dye
Quality:	Star (S)

Comments

Color:	Colorless
Creation Date:	01/01/1970
Modification Date:	01/01/1970
Sample Source or Locality:	The sample was obtained from the New Jersey Zinc Co., Bethlehem, Pennsylvania, USA
Powder Data:	References to other early patterns may be found in reference (5)
Optical Data:	B=2.013, Q=2.029, Sign=+
Color:	Colorless. The structure was determined by Bragg (1) and refined by Abrahams, Bernstein (2). A high pressure cubic NaCl-type of ZnO is reported by Bates et al. (3) and a cubic, sphalerite type is reported by Radczewski, Schicht (4)
Temperature of Data Collection:	The approximate temperature of data collection was 26 C
Additional Patterns:	To replace 00-005-0664 (5)
Additional Patterns:	See ICSD 31052 (PDF 01-075-1526).

References

Primary reference: McMurdie, H., Morris, M., Evans, E., Paretzkin, B., Wong-Ng, W., Ettlinger, L., Hubbard, C., *Powder Diffraction*, **1**, 76, (1986)

Structure: 2. Abrahams, S., Bernstein, J., *Acta Crystallogr., Sec. B*, **25**, 1233, (1969)

Optical data: *Dana's System of Mineralogy, 7th Ed.*, **I**, 504

Other: 5. Swanson, H., Fuyat, R., *Natl. Bur. Stand. (U.S.), Circ. 539*, **2**, 25, (1953)

Peak list

No.	h	k	l	d [A]	2Theta[deg]	I [%]
1	1	0	0	2.81430	31.770	57.0
2	0	0	2	2.60332	34.422	44.0
3	1	0	1	2.47592	36.253	100.0
4	1	0	2	1.91114	47.539	23.0
5	1	1	0	1.62472	56.603	32.0
6	1	0	3	1.47712	62.864	29.0
7	2	0	0	1.40715	66.380	4.0
8	1	1	2	1.37818	67.963	23.0
9	2	0	1	1.35825	69.100	11.0
10	0	0	4	1.30174	72.562	2.0
11	2	0	2	1.23801	76.955	4.0
12	1	0	4	1.18162	81.370	1.0
13	2	0	3	1.09312	89.607	7.0
14	2	1	0	1.06384	92.784	3.0
15	2	1	1	1.04226	95.304	6.0
16	1	1	4	1.01595	98.613	4.0
17	2	1	2	0.98464	102.946	2.0
18	1	0	5	0.97663	104.134	5.0
19	2	0	4	0.95561	107.430	1.0
20	3	0	0	0.93812	110.392	3.0
21	2	1	3	0.90694	116.279	8.0
22	3	0	2	0.88256	121.572	4.0
23	0	0	6	0.86768	125.188	1.0
24	2	0	5	0.83703	133.932	3.0
25	1	0	6	0.82928	136.521	1.0
26	2	1	4	0.82370	138.513	2.0
27	2	2	0	0.81247	142.918	3.0

Stick Pattern

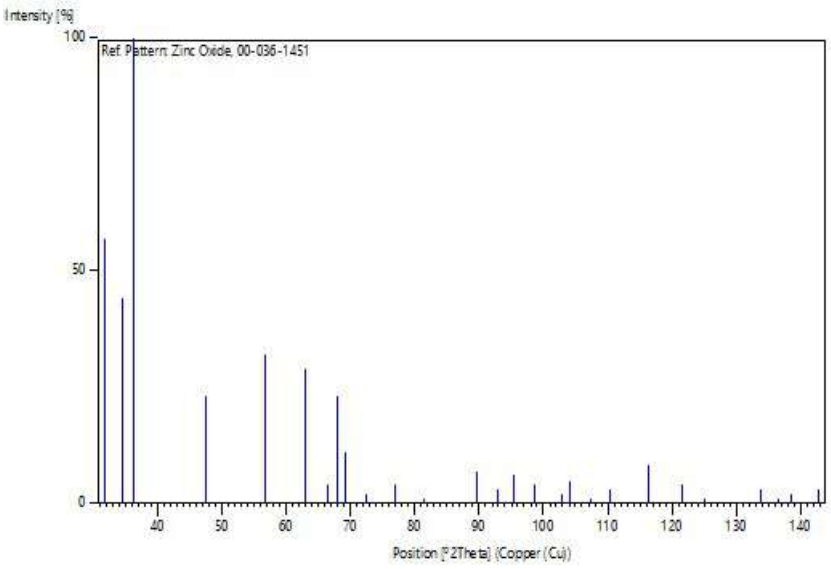

Annex –I –

Name and formula

Reference code:	00-047-1431
Compound name:	Barium
PDF index name:	Barium
Empirical formula:	Ba
Chemical formula:	Ba

Crystallographic parameters

Crystal system:	Cubic
Space group:	Im-3m
Space group number:	229
a (Å):	5.0280
b (Å):	5.0280
c (Å):	5.0280
Alpha (°):	90.0000
Beta (°):	90.0000
Gamma (°):	90.0000
Volume of cell (10^6 pm^3):	127.11
Z:	2.00
RIR:	-

Subfiles and quality

Subfiles:	Alloy, metal or intermetalic Common Phase Inorganic
Quality:	Star (S)

Comments

Creation Date:	01/01/1970
Modification Date:	01/01/1970
Sample Preparation:	High purity barium was prepared by distilling commercially available metal in ultrahigh vacuum
Additional Patterns:	To replace 00-006-0235.

References

Primary reference:	Evers, J., Oehlinger, G., Sendlinger, B., Weiss, A., Schmidt, M., Schramel, P., *J. Alloys Compds.*, **182**, 175, (1992)

Peak list

No.	h	k	l	d [A]	2Theta[deg]	I [%]
1	1	1	0	3.55092	25.058	100.0
2	2	0	0	2.51670	35.646	16.0
3	2	1	1	2.05312	44.072	54.0
4	2	2	0	1.77765	51.358	28.0
5	3	1	0	1.59015	57.949	21.0
6	2	2	2	1.45215	64.072	8.0
7	3	2	1	1.34367	69.959	29.0
8	4	0	0	1.25662	75.613	4.0
9	4	1	1	1.18477	81.109	13.0
10	4	2	0	1.12385	86.536	7.0
11	3	3	2	1.07222	91.848	6.0
12	4	2	2	1.02630	97.278	5.0
13	5	1	0	0.98622	102.716	8.0
14	5	2	1	0.91805	114.082	5.0
15	4	4	0	0.88876	120.157	3.0
16	5	3	0	0.86205	126.650	4.0
17	6	0	0	0.83798	133.628	2.0
18	6	1	1	0.81597	141.478	3.0
19	6	2	0	0.79499	151.364	2.0

Stick Pattern

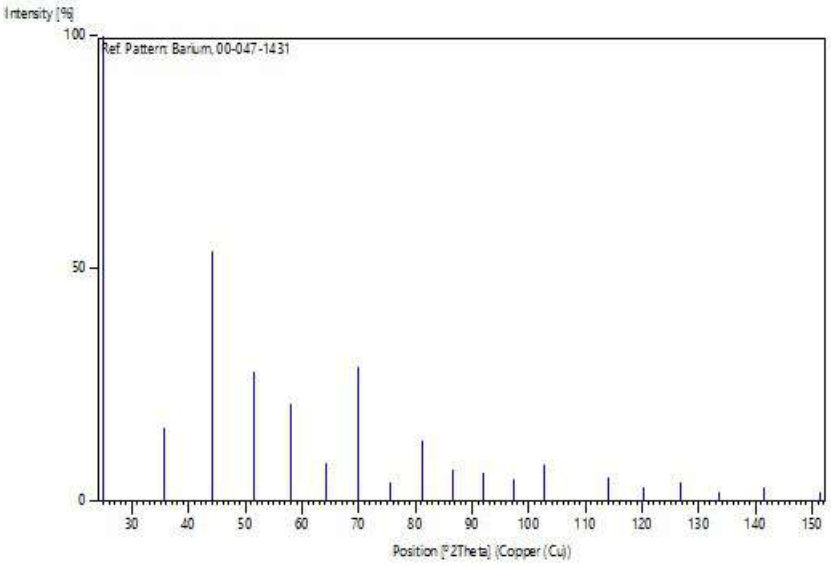

Bibliographical References

[1] S. Sanctis: 'Multinary metal oxide semiconductors - A study of different material systems and their application in thin-film transistors', Doctoral Thesis thesis, Technische Universität Darmstadt, Darmstadt, Germany, 2020

[2] M. A. Haque, A. D. Sheikh, X. Guan, and T. Wu: *Advanced Energy Materials*,Vol. 7, 2017, No 20, p. 1602803, DOI: https://doi.org/10.1002/aenm.201602803

[3] A. Lamichhane and N. M. Ravindra: *Materials*,Vol. 13, 2020, No 8, p. 1917, https://www.mdpi.com/1996-1944/13/8/1917

[4] E. A. R. Assirey: *Saudi Pharmaceutical Journal*,Vol. 27, 2019, No 6, p. 817-829, DOI: https://doi.org/10.1016/j.jsps.2019.05.003

[5] A. Landström: 'Nanostructured Metal Oxide Semiconductors for Functional Applications', Doctoral thesis thesis, Luleå University of Technology, 2021

[6] G. Korotcenkov: Metal Oxides. In: *Handbook of Gas Sensor Materials: Properties, Advantages and Shortcomings for Applications Volume 1: Conventional Approaches*, edited by, Springer New York, New York, NY, 2013, p. 49-116, DOI: 10.1007/978-1-4614-7165-3_2

[7] G. Korotcenkov: Thin Metal Films. In: *Handbook of Gas Sensor Materials: Properties, Advantages and Shortcomings for Applications Volume 1: Conventional Approaches*, edited by, Springer, New York, 2013, p. 153-166, DOI: 10.1007/978-1-4614-7165-3_4

[8] M. Ohring: *Materials Science of Thin Films: Depositon and Structure*, 2nd, Academic Press, San Diego, California, USA, 2001, DOI,

[9] H. He: 2 - Metal oxide semiconductors and conductors. In: *Solution Processed Metal Oxide Thin Films for Electronic Applications*, edited by eds. Z. Cui, et al., Elsevier, 2020, p. 7-30, DOI: https://doi.org/10.1016/B978-0-12-814930-0.00002-5

[10] N. Srinatha, P. Raghu, H. Mahesh, and B. Angadi: *Journal of Alloys and Compounds*,Vol. 722, 2017, p. 888-895,

[11] S. Itapu: 'Microstructuring of Nickel Thin Films and Property Modification of Nickel Oxide Films by Pulsed Laser Irradiation', PhD thesis, University of Toledo, Toledo and OhioLINK., Spain, 2017

[12] Romana Cerc Korošec and P. Bukovec: *Acta Chimica Slovaka*,Vol. 53, 2006, p. 136-147,

[13] M. Tyagi, M. Tomar, and V. Gupta: *Advanced Materials Research*,Vol. 488-489, 2012, p. 103-108, DOI: 10.4028/www.scientific.net/AMR.488-489.103

[14] L. Cattin, B. A. Reguig, A. Khelil, M. Morsli, K. Benchouk, and J. C. Bernède: *Applied Surface Science*,Vol. 254, 2008, No 18, p. 5814-5821, DOI: https://doi.org/10.1016/j.apsusc.2008.03.071

[15] U. Patil, R. Salunkhe, K. Gurav, and C. Lokhande: *Applied Surface Science*,Vol. 255, 2008, No 5, p. 2603-2607,

[16] B. A. Reguig, A. Khelil, L. Cattin, M. Morsli, and J. C. Bernède: *Applied Surface Science*,Vol. 253, 2007, No 9, p. 4330-4334, DOI: https://doi.org/10.1016/j.apsusc.2006.09.046

[17] L. Soriano, M. Abbate, J. Vogel, J. C. Fuggle, A. Fernández, A. R. González-Elipe, M. Sacchi, and J. M. Sanz: *Chemical Physics Letters*,Vol. 208, 1993, No 5, p. 460-464, DOI: https://doi.org/10.1016/0009-2614(93)87173-Z

[18] A. Baptista, F. J. G. Silva, J. Porteiro, J. L. Míguez, G. Pinto, and L. Fernandes: *Procedia Manufacturing*,Vol. 17, 2018, p. 746-757, DOI: https://doi.org/10.1016/j.promfg.2018.10.125

[19] J. A. Luceño-Sánchez, A. M. Díez-Pascual, and R. Peña Capilla: *International Journal of Molecular Sciences*,Vol. 20, 2019, No 4, p. 976, https://www.mdpi.com/1422-0067/20/4/976

[20] J. E. Greene: *Applied Physics Reviews*,Vol. 1, 2014, No 4, DOI: 10.1063/1.4902760

[21] R. W. Cahn, F. E. Fujita, H. Fujita, U. Gonser, J. Kanamori, K. Motizuki, R. Siegel, N. Sumida, K. Suzuki, and N. Suzuki: *Physics of new materials*, Springer Science & Business Media, Berlin/Heidelberg, 2013, DOI,

[22] W. R. Grove: *Philosophical Transactions of the Royal Society of London*,Vol., 1852, No 142, p. 87-101,

[23] W. R. Grove: *The London, Edinburgh, and Dublin Philosophical Magazine and Journal of Science*,Vol. 15, 1839, No 96, p. 287-293, DOI: 10.1080/14786443908649881

[24] S. O. Mbam, S. E. Nwonu, O. A. Orelaja, U. S. Nwigwe, and X.-F. Gou: *Materials Research Express*,Vol. 6, 2019, No 12, p. 122001, DOI: 10.1088/2053-1591/ab52cd

[25] Akhlesh Lakhtakia and R. Messier: *Sculptured Thin Films: Nanoengineered Morphology and Optics*, SPIE Press, Bellingham, WA 98227-0100, 2005, DOI,

[26] A. Kundt: *Annalen der Physik*,Vol. 270, 1888, No 7, p. 469-489, DOI: 10.1002/andp.18882700705

[27] L. S. Swenson Jr.: *Physics Today*,Vol. 40, 1987, No 5, p. 24-30, DOI: https://doi.org/10.1063/1.881107

[28] K. Bädeker: *Annalen der Physik*,Vol. 327, 1907, No 4, p. 749-766, DOI: https://doi.org/10.1002/andp.19073270409

[29] G. Rupprecht: *Zeitschrift für Physik*,Vol. 139, 1954, No 5, p. 504-517, DOI: 10.1007/BF01374559

[30] K. L. Chopra: *Thin Film Phenomena*, McGraw-Hill, 1969, DOI,

[31] A. Adhikari: 'Bandgap tunability and properties of (Cd, Mg) O random alloys and quasi-ternary alloys-[CdO/MgO] superlattices–obtained by MBE', Doctoral Dissertation thesis, Poland, 2024
[32] K. W. Böer and U. W. Pohl: Bands and Bandgaps in Solids. In: *Semiconductor Physics*, edited by, Springer International Publishing, Cham, 2023, p. 257-317, DOI: 10.1007/978-3-031-18286-0_8
[33] E. S. Araújo, M. F. G. Pereira, G. M. G. da Silva, G. F. Tavares, C. Y. B. Oliveira, and P. M. Faia: *Toxics*,Vol. 11, 2023, No 8, p. 658, DOI: 10.3390/toxics11080658
[34] B. Xu, J. Park, D. Zhang, H. A. De Santiago, W. Li, X. Liu, J. Luo, S. Lany, and Y. Qi: *Chemistry of Materials*,Vol. 36, 2024, No 10, p. 4990-5001, DOI: 10.1021/acs.chemmater.3c03038
[35] S. Förster and W. Widdra: Ternary Oxide Layers: Novel Crystal Structure Concepts. In: *Encyclopedia of Interfacial Chemistry*, edited by K. Wandelt, Elsevier, Oxford, 2018, p. 344-350, DOI: https://doi.org/10.1016/B978-0-12-409547-2.12884-7
[36] Y. Elbaz, A. Rosenfeld, N. Anati, and M. Caspary Toroker: *Journal of The Electrochemical Society*,Vol. 169, 2022, No 4, p. 040542, DOI: 10.1149/1945-7111/ac644a
[37] E. Fazio, S. Spadaro, C. Corsaro, G. Neri, S. G. Leonardi, F. Neri, N. Lavanya, C. Sekar, N. Donato, and G. Neri: *Sensors*,Vol. 21, 2021, No 7, p. 2494, DOI: https://doi.org/10.3390/s21072494
[38] H. Zheng, S. Ling, B. Kong, T.-X. Zeng, S. Jiang, and W. Wang: *Inorganic Chemistry*,Vol. 64, 2025, No 5, p. 2443-2457, DOI: 10.1021/acs.inorgchem.4c04888
[39] W. Fu, M. Li, J. Li, G. Fang, P. Ye, W. E, X. Xiao, H. Wei, B. Liu, Y. Lu, and Y. He: *Applied Physics Letters*,Vol. 118, 2021, No 11, DOI: 10.1063/5.0045663
[40] S. Ramanathan: *Thin Film Metal-Oxides: Fundamentals and Applications in Electronics and Energy*, 1st, Springer New York, NY, 2010, DOI: https://doi.org/10.1007/978-1-4419-0664-9
[41] G. A. Sawatzky: The Character of Band Gaps in Transition Metal Compounds. In: *Narrow-Band Phenomena—Influence of Electrons with Both Band and Localized Character*, edited by eds. J. C. Fuggle, et al., Springer US, Boston, MA, 1988, p. 117-122, DOI: 10.1007/978-1-4684-5559-5_18
[42] H. Meng, S. Huang, and Y. Jiang: *AIMS Materials Science*,Vol. 7, 2020, No 5, p. 665-683, DOI: 10.3934/matersci.2020.5.665
[43] K. Nomura, H. Ohta, A. Takagi, T. Kamiya, M. Hirano, and H. Hosono: *Nature*,Vol. 432, 2004, No 7016, p. 488-492, DOI: 10.1038/nature03090
[44] S. Pandey, S. Marasini, and R. R. Ghimire: *Revista de Ciencias Tecnológicas*,Vol. 7, 2024, No 4, p. 1-16, DOI: 10.37636/recit.v7n4e375
[45] H. Chen, Q. Sun, T. Tian, L. Zheng, M. Barré, I. Monot-Laffez, M. Makowska-Janusik, G. Li, and A. H. Kassiba: *Journal of the European Ceramic Society*,Vol. 40, 2020, No 15, p. 5529-5534, DOI: https://doi.org/10.1016/j.jeurceramsoc.2020.06.030
[46] S.-G. Lee, S.-B. Han, W.-J. Lee, and K.-W. Park: *Catalysts*,Vol. 10, 2020, No 8, p. 866, https://www.mdpi.com/2073-4344/10/8/866
[47] A. Kumar: *Advanced Ceramics for Energy and Environmental Applications*, CRC Press, Boca Raton, 2021, DOI: https://doi.org/10.1201/9781003005155
[48] T. Çayir TaşdemİRcİ: *Chemical Physics Letters*,Vol. 738, 2020, p. 136884, DOI: https://doi.org/10.1016/j.cplett.2019.136884
[49] A. L. Chown: 'Synthetic Optimization and Electrochemical Studies of Delafossite CuCrO2 for Solar Energy Conversion and Storage Applications', Doctoral Dissertation thesis, 2022
[50] A. Mingorance Ferrer: 'Solution processable oxides for inverted and carbon-based perovskite solar cells', Doctoral Dissertation thesis, Universitat Autònoma de Barcelona, 2019
[51] R. Woods-Robinson: 'Bridging the Computational-Experimental Divide to Design Transparent Contact Materials for Solar Energy', Doctoral Dissertation thesis, 2021
[52] F. Qin: 'A Metal Percolation Path in Metal/Semiconductor Composites and its Effect on Electric Conductivity in Different Ambiances', Doctoral Dissertation thesis, University of Pittsburgh, 2020
[53] M. Aftab, M. Z. Butt, D. Ali, F. Bashir, and T. M. Khan: *Optical Materials*,Vol. 119, 2021, p. 111369, DOI: https://doi.org/10.1016/j.optmat.2021.111369
[54] Y. Akaltun and T. Çayır: *Journal of Alloys and Compounds*,Vol. 625, 2015, p. 144-148, DOI: https://doi.org/10.1016/j.jallcom.2014.10.194
[55] R. Barir, B. Benhaoua, S. Benhamida, A. Rahal, T. Sahraoui, and R. Gheriani: *Journal of Nanomaterials*,Vol. 2017, 2017, No 1, p. 5204639, DOI: https://doi.org/10.1155/2017/5204639
[56] A. H. Hammad, M. S. Abdel-wahab, S. Vattamkandathil, and A. R. Ansari: *Coatings*,Vol. 9, 2019, No 10, p. 615, https://www.mdpi.com/2079-6412/9/10/615
[57] C.-C. Diao, C.-Y. Huang, C.-F. Yang, and C.-C. Wu: *Nanomaterials*,Vol. 10, 2020, No 4, p. 636, https://www.mdpi.com/2079-4991/10/4/636
[58] V. Ganesh, B. R. Kumar, Y. Bitla, I. S. Yahia, and S. AlFaify: *Journal of Inorganic and Organometallic Polymers and Materials*,Vol. 31, 2021, No 6, p. 2691-2699, DOI: 10.1007/s10904-021-01889-3
[59] Y. E. Firat and A. Peksoz: *Electrochimica Acta*,Vol. 295, 2019, p. 645-654, DOI: https://doi.org/10.1016/j.electacta.2018.10.166

[60] M. M. Gomaa, G. R. Yazdi, S. Schmidt, M. Boshta, V. Khranovskyy, F. Eriksson, B. S. Farag, M. B. S. Osman, and R. Yakimova: *Materials Science in Semiconductor Processing*,Vol. 64, 2017, p. 32-38, DOI: https://doi.org/10.1016/j.mssp.2017.03.009
[61] R. S. Kate, S. C. Bulakhe, and R. J. Deokate: *Optical and Quantum Electronics*,Vol. 51, 2019, No 10, p. 319, DOI: 10.1007/s11082-019-2026-2
[62] C. Mrabet, M. Ben Amor, A. Boukhachem, M. Amlouk, and T. Manoubi: *Ceramics International*,Vol. 42, 2016, No 5, p. 5963-5978, DOI: https://doi.org/10.1016/j.ceramint.2015.12.144
[63] C.-H. Chao, P.-W. Chi, and D.-H. Wei: *The Journal of Physical Chemistry C*,Vol. 120, 2016, No 15, p. 8210-8219, DOI: 10.1021/acs.jpcc.6b01573
[64] F. K. Konan, B. Hartiti, H. J. Tchognia Nkuissi, and A. Boko: *Journal of Materials and Environmental(Sciences*,Vol. 10, 2019, No 10, p. 1003-1010,
[65] R. Kumar, G. Kumar, O. Al-Dossary, and A. Umar: *Materials Express*,Vol. 5, 2015, No 1, p. 3-23, DOI: 10.1166/mex.2015.1204
[66] A. Mallick and D. Basak: *Progress in Materials Science*,Vol. 96, 2018, p. 86-110, DOI: https://doi.org/10.1016/j.pmatsci.2018.03.004
[67] K. Ellmer and A. Bikowski: *Journal of Physics D: Applied Physics*,Vol. 49, 2016, No 41, p. 413002, DOI: 10.1088/0022-3727/49/41/413002
[68] H. Ennaceri, A. Taleb, M. Boujnah, A. Khaldoun, J. Ebothé, A. Ennaoui, and A. Benyoussef: *Journal of Computational Electronics*,Vol. 20, 2021, No 5, p. 1948-1958, DOI: 10.1007/s10825-021-01744-1
[69] M. Rouchdi, E. Salmani, B. Fares, N. Hassanain, and A. Mzerd: *Results in Physics*,Vol. 7, 2017, p. 620-627, DOI: https://doi.org/10.1016/j.rinp.2017.01.023
[70] B. Adisak and R. L. L. Walter: *physica status solidi (b)*,Vol. 250, 2013, DOI: 10.1002/pssb.201370567
[71] G. Williams and G. S. V. Coles: *MRS Bulletin*,Vol. 24, 2013, No 6, p. 25-29, DOI: 10.1557/S0883769400052477
[72] David C. Look, D. C. Reynolds, C. W. Litton, R. L. Jones, D. B. Eason, and G. Cantwell: *Applied Physics Letter*,Vol. 81, 2002, No 10, p. 1830-1832,
[73] A. M. Reddy, A. S. Reddy, and P. S. Reddy: *Physics Procedia*,Vol. 49, 2013, p. 9-14, DOI: https://doi.org/10.1016/j.phpro.2013.10.005
[74] P. J. Kelly and R. D. Arnell: *Vacuum*,Vol. 56, 2000, No 3, p. 159-172, DOI: https://doi.org/10.1016/S0042-207X(99)00189-X
[75] M. Leskelä and M. Ritala: *Thin Solid Films*,Vol. 409, 2002, No 1, p. 138-146, DOI: https://doi.org/10.1016/S0040-6090(02)00117-7
[76] D. Perednis and L. J. Gauckler: *Journal of Electroceramics*,Vol. 14, 2005, No 2, p. 103-111, DOI: 10.1007/s10832-005-0870-x
[77] A. S. Safwat A. Mahmoud, Mou'ad A. Tarawnh: *Journal of Modern Physics*,Vol. 2, 2011, No 10, p. 1178-1186, DOI: 10.4236/jmp.2011.210147
[78] F. Y. Yang, Kai Liu, Kimin Hong, D. H. Reich, P. C. Searson, and C. L. Chien: *Science*,Vol. 284, 1999, No 5418, p. 1335-1337, DOI: 10.1126/science.284.5418.1335
[79] J. C. Osuwa and G. I. Onyejiuwa: *Journal of Ovonic Research* Vol. 9, 2013, No 1, p. 9-15,
[80] Y. Z. Liu, C. C. Wang, and M. Chu: *Journal of Applied Physics*,Vol. 63, 1988, No 6, p. 2151-2153, DOI: 10.1063/1.341177
[81] D. J. Estes and M. Mayer: *Colloids and Surfaces B: Biointerfaces*,Vol. 42, 2005, No 2, p. 115-123, DOI: https://doi.org/10.1016/j.colsurfb.2005.01.016
[82] P. Baudry, A. C. M. Rodrigues, M. A. Aegerter, and L. O. Bulhões: *Journal of Non-Crystalline Solids*,Vol. 121, 1990, No 1, p. 319-322, DOI: https://doi.org/10.1016/0022-3093(90)90151-B
[83] M. M. Khan: 4 - Hydrothermal synthesis method. In: *Photocatalysts: Synthesis and Characterization Methods*, edited by M. Mansoob Khan, Elsevier, 2025, p. 37-45, DOI: https://doi.org/10.1016/B978-0-443-28913-2.00005-8
[84] J. C. Rendón-Angeles and G. Seong: *Nanomaterials (Basel, Switzerland)*,Vol. 13, 2023, No 9, DOI: 10.3390/nano13091463
[85] T. Q. Tazim, M. Kawsar, M. Sahadat Hossain, N. M. Bahadur, and S. Ahmed: *Next Nanotechnology*,Vol. 7, 2025, p. 100167, DOI: https://doi.org/10.1016/j.nxnano.2025.100167
[86] L. Ndlwana, N. Raleie, K. M. Dimpe, H. F. Ogutu, E. O. Oseghe, M. M. Motsa, T. A. M. Msagati, and B. B. Mamba: *Materials (Basel, Switzerland)*,Vol. 14, 2021, No 17, DOI: 10.3390/ma14175094
[87] S. Avola, M. Guillot, D. d. Silva-Perez, S. Pellet-Rostaing, W. Kunz, and F. Goettmann: *Pure and Applied Chemistry*,Vol. 85, 2012, No 1, p. 89-103, DOI: doi:10.1351/PAC-CON-12-04-01
[88] K. E. v. Schafhäutl: *Gelehrte Anzeigen (published by: die königliche Bayerische Akademie der Wissenschaften (the Royal Bavarian Academy of Sciences)), 20 :* ,Vol. 20, 1845, p. 557, 561-567, 569-576, 577-596. On page 578,
[89] R. Bunsen: *Annalen der Chemie und Pharmacie,*,Vol. 65, 1848, p. 70-85, on page 83,
[90] H. d. Sénarmont: *Comptes rendus*,Vol. 28, 1849, p. 693-696,

[91] G. Demazeau and A. Largeteau: *Zeitschrift für anorganische und allgemeine Chemie*,Vol. 641, 2015, No 2, p. 159-163, DOI: https://doi.org/10.1002/zaac.201400515
[92] K. Byrappa and M. Yoshimura: 4 - Physical Chemistry of Hydrothermal Growth of Crystals. In: *Handbook of Hydrothermal Technology (Second Edition)*, edited by eds. K. Byrappa, et al., William Andrew Publishing, Oxford, 2013, p. 139-175, DOI: https://doi.org/10.1016/B978-0-12-375090-7.00004-9
[93] D. Hooper, P. Barnes, J. K. Cockcroft, A. C. Jupe, S. D. M. Jacques, S. P. Bailey, F. Lupo, M. Vickers, and M. Hanfland: *Physical Chemistry Chemical Physics*,Vol. 5, 2003, No 21, p. 4946-4950, DOI: 10.1039/B309144A
[94] Y. Mori, M. Imade, S. Komatsu, and M. Yoshino: Crystal growth apparatus and crystal production method, 2018, Google Patents.
[95] S. Yazdani Darki, M. Eslami-Kalantari, H. Zare, and Z. Shahedi: *Materials Chemistry and Physics*,Vol. 262, 2021, p. 124305, DOI: https://doi.org/10.1016/j.matchemphys.2021.124305
[96] F. U. Kosasih, E. Erdenebileg, N. Mathews, S. G. Mhaisalkar, and A. Bruno: *Joule*,Vol. 6, 2022, No 12, p. 2692-2734, DOI: https://doi.org/10.1016/j.joule.2022.11.004
[97] W. L. Ang, P. J. McHugh, and M. D. Symes: *Chemical Engineering Journal*,Vol. 444, 2022, p. 136573, DOI: https://doi.org/10.1016/j.cej.2022.136573
[98] S. S. Sutar, S. M. Patil, S. J. Kadam, R. K. Kamat, D.-k. Kim, and T. D. Dongale: *ACS Omega*,Vol. 6, 2021, No 44, p. 29982-29992, DOI: 10.1021/acsomega.1c04521
[99] D. E. Navarro-López, Y. Perfecto-Avalos, A. Zavala, M. A. de Luna, A. Sanchez-Martinez, O. Ceballos-Sanchez, N. Tiwari, E. R. López-Mena, and G. Sanchez-Ante: *Antibiotics*,Vol. 13, 2024, No 3, p. 220, https://www.mdpi.com/2079-6382/13/3/220
[100] R. M. Almeida and M. C. Gonçalves: Sol–Gel Process and Products. In: *Encyclopedia of Glass Science, Technology, History, and Culture*, edited by, 2021, p. 969-979, DOI: https://doi.org/10.1002/9781118801017.ch8.2
[101] M. Murthi and J. F. Destino: *Journal of Sol-Gel Science and Technology*,Vol., 2025, DOI: 10.1007/s10971-025-06664-1
[102] H. Kamal, E. K. Elmaghraby, S. A. Ali, and K. Abdel-Hady: *Journal of Crystal Growth*,Vol. 262, 2004, No 1, p. 424-434, DOI: https://doi.org/10.1016/j.jcrysgro.2003.10.090
[103] V. Kumar, K. N. R. Sinha, and R. Raj: *Soft Matter*,Vol. 16, 2020, No 26, p. 6145-6154, DOI: 10.1039/D0SM00622J
[104] B. Correa-Lozano, C. Comninellis, and A. De Battisti: *Journal of Applied Electrochemistry*,Vol. 26, 1996, No 7, p. 683-688, DOI: 10.1007/BF00241508
[105] T. Maruyama and J. Shionoya: *Journal of Materials Science Letters*,Vol. 11, 1992, No 3, p. 170-172, DOI: 10.1007/BF00724682
[106] R. Hayami, N. Endo, Y. Miyase, K. Yamamoto, and T. Gunji: *Journal of Sol-Gel Science and Technology*,Vol. 91, 2019, No 2, p. 255-260, DOI: 10.1007/s10971-019-05043-x
[107] G. L. Mar, P. Y. Timbrell, and R. N. Lamb: Formation of Zinc Oxide Thin Films by the Thermal Decomposition of Zinc Acetate. In: *Surface Science: Principles and Applications*, edited by eds. R. F. Howe, et al., Springer Berlin Heidelberg, Berlin, Heidelberg, 1993, p. 177-192, DOI: 10.1007/978-3-642-84933-6_15
[108] A. Tiburcio-Silver, J. C. Joubert, and M. Labeau: *Thin Solid Films*,Vol. 197, 1991, No 1, p. 195-214, DOI: https://doi.org/10.1016/0040-6090(91)90232-M
[109] H. G. McAdie: *Journal of Inorganic and Nuclear Chemistry*,Vol. 28, 1966, No 12, p. 2801-2809, DOI: https://doi.org/10.1016/0022-1902(66)80005-2
[110] B. D. Cullity and S. R. Stock: *Elements of X-ray Diffraction*, 3rd edition, Prentice-Hall, New York, 2001, DOI,
[111] J. Müller, J. Nowoczin, and H. Schmitt: *Thin Solid Films*,Vol. 496, 2006, No 2, p. 364-370, DOI: https://doi.org/10.1016/j.tsf.2005.09.077
[112] Y. Benkhetta: 'L'effet du débit de la solution sur les propriétés des couches minces d'oxyde de zinc (ZnO) déposées par spray ultrasonique.', Mémoire de master thesis, Université de Mohamed Kheider, Biskra, 2013
[113] B. D. Cullity and S. R. Stock: *Elements of X-ray Diffraction*, 3rd Prentice Hall, Upper Saddle River, NJ, New York, 2001, DOI,
[114] S. D. Lokhande, M. B. Awale, G. Umadevi, and V. D. Mote: *Materials Chemistry and Physics*,Vol. 301, 2023, p. 127667, DOI: https://doi.org/10.1016/j.matchemphys.2023.127667
[115] U. Holzwarth and N. Gibson: *Nature nanotechnology*,Vol. 6, 2011, No 9, p. 534-534,
[116] S. Mustapha, M. Ndamitso, A. Abdulkareem, J. Tijani, D. Shuaib, A. Mohammed, and A. Sumaila: *Advances in Natural Sciences: Nanoscience and Nanotechnology*,Vol. 10, 2019, No 4, p. 045013,
[117] J. Epp: Chap. 4, X-ray diffraction (XRD) techniques for materials characterization. In: *Materials Characterization Using Nondestructive Evaluation (NDE) Methods*, edited by eds. G. Hübschen, et al., Woodhead Publishing, 2016, p. 81-124, DOI: https://doi.org/10.1016/B978-0-08-100040-3.00004-3
[118] A. N. Hadri, C.; Chafi, F. Z.; Loghmarti, M.; Mzerd, A.: *Energy and Environment Focus*,Vol. 4, 2015, No 1, p. 12-17, DOI: https://doi.org/10.1166/eef.2015.1129

[119] P. Singh, A. Kumar, A. Kaushal, D. Kaur, A. Pandey, and R. N. Goyal: *Bulletin of Materials Science*,Vol. 31, 2008, No 3, p. 573-577, DOI: 10.1007/s12034-008-0089-y
[120] K. S. Usha, R. Sivakumar, C. Sanjeeviraja, and J. Vivekanandan: *Materials Chemistry and Physics*,Vol. 294, 2023, p. 127007, DOI: https://doi.org/10.1016/j.matchemphys.2022.127007
[121] S. Muthukumaran and R. Gopalakrishnan: *Optical Materials*,Vol. 34, 2012, No 11, p. 1946-1953, DOI: https://doi.org/10.1016/j.optmat.2012.06.004
[122] P. kumar, V. Chauhan, R. Singh, and P. C. Pandey: *Materials Chemistry and Physics*,Vol. 291, 2022, p. 126661, DOI: https://doi.org/10.1016/j.matchemphys.2022.126661
[123] M. Von Ardenne: *Zeitschrift für technische Physik*,Vol. 19, 1938, No 11, p. 407-416,
[124] V. Zworykin: *Philadelphia USA*,Vol., 1942,
[125] C. W. Oatley, D. McMullan, K. C. A. Smith, and P. Hawkes: Chapter Nine - The development of the scanning electron microscope. In: *Advances in Imaging and Electron Physics*, edited by eds. P. W. Hawkes, et al., Elsevier, 2022, p. 255-287, DOI: https://doi.org/10.1016/bs.aiep.2022.03.009
[126] R. F. W. Pease and W. C. Nixon: *Journal of Scientific Instruments*,Vol. 42, 1965, No 2, p. 81, DOI: 10.1088/0950-7671/42/2/305
[127] G. Haggis and B. Phipps-Todd: *Freeze-fracture for scanning electron microscopy*. In:Proceedings of the Fifth European Congress on Electron Microscopy". Institute of Physics, London and Bristol,Vol. 250, 1972,
[128] H. Ris: *EMSA Bull*,Vol. 21, 1991, No 1, p. 54-56,
[129] M. J. Dykstra and L. E. Reuss: Scanning Electron Microscopy. In: *Biological Electron Microscopy: Theory, Techniques, and Troubleshooting*, edited by, Springer US, Boston, MA, 2003, p. 357-383, DOI: 10.1007/978-1-4419-9244-4_21
[130] Y. Liao: *online Book: Practical Electron Microscopy and Database*, 2nd, 2006, DOI,
[131] Micro-Optics: A Scanning Electron Microscope (SEM) basis, https://micro-optics.com.sg/sem-theory/, 2025.
[132] G. P. Eppeldauer and R. J. Martin: *Journal of research of the National Institute of Standards and Technology*,Vol. 106, 2001, No 3, p. 577-587, DOI: 10.6028/jres.106.024
[133] M. Fox: *Optical Properties of Solids*, 2nd, Oxford University Press, Oxford, UK, 2010, DOI,
[134] B. A. Sperling, B. Kalanyan, and J. E. Maslar: *The Journal of Physical Chemistry C*,Vol. 124, 2020, No 5, p. 3410-3420, DOI: 10.1021/acs.jpcc.9b11291
[135] Douglas A. Skoog, F. James Holle, and S. R. Crouch: *Principles of Instrumental Analysis*, 6th, Cengage Learning, 2006, DOI,
[136] S. A. Panda, S. Choudhary, S. Barala, A. Hazra, S. K. Jena, and S. Gangopadhyay: *RSC Advances*,Vol. 14, 2024, No 38, p. 28086-28097, DOI: 10.1039/D4RA03128H
[137] N. P. Chadwick, S. Sathasivam, S. M. Bawaked, M. Mokhtar, S. A. Althabaiti, S. N. Basahel, I. P. Parkin, and C. J. Carmalt: *Journal of Materials Chemistry A*,Vol. 3, 2015, No 9, p. 4811-4819, DOI: 10.1039/C4TA05922K
[138] H. Benamra: 'L'effet de la température du substrat et de la molarité sur les propriétés des couches minces de sulfure de zinc déposées par spray ultrasonique', Thesis thesis, Mohamed Kheider University of Biskra, Biskra, Algeria, 2013
[139] R. R. Reddy and Y. Nazeer Ahammed: *Infrared Physics & Technology*,Vol. 36, 1995, No 5, p. 825-830, DOI: https://doi.org/10.1016/1350-4495(95)00008-M
[140] A. Diha, S. Benramache, and B. Benhaoua: *Optik*,Vol. 172, 2018, p. 832-839, DOI: https://doi.org/10.1016/j.ijleo.2018.07.062
[141] V. Kumar and J. K. Singh: *Indian Journal of Pure & Applied Physics*,Vol. 48, 2010, No 08, p. 571-574, DOI: http://nopr.niscpr.res.in/handle/123456789/9962
[142] T. S. Moss: *physica status solidi (b)*,Vol. 131, 1985, No 2, p. 415-427, DOI: https://doi.org/10.1002/pssb.2221310202
[143] M. Mekhnache, A. Drici, L. Saad Hamideche, H. Benzarouk, A. Amara, L. Cattin, J. C. Bernède, and M. Guerioune: *Superlattices and Microstructures*,Vol. 49, 2011, No 5, p. 510-518, DOI: 10.1016/j.spmi.2011.02.002
[144] P. Hervé and L. K. J. Vandamme: *Infrared Physics & Technology*,Vol. 35, 1994, No 4, p. 609-615, DOI: https://doi.org/10.1016/1350-4495(94)90026-4
[145] A. A. Ramadan, R. D. Gould, and A. Ashour: *Thin Solid Films*,Vol. 239, 1994, No 2, p. 272-275, DOI: https://doi.org/10.1016/0040-6090(94)90863-X
[146] D. K. Schroder: Resistivity. In: *Semiconductor Material and Device Characterization*, edited by, John Wiley & Sons, Inc., 2005, p. 1-59, DOI: https://doi.org/10.1002/0471749095.ch1
[147] S. Benramache, Y. Aoun, S. Lakel, B. Benhaoua, and C. Torchi: *Sādhanā*,Vol. 44, 2019, No 1, p. 26, DOI: 10.1007/s12046-018-1003-y
[148] S. Yilmaz: *Journal of Semiconductors*,Vol. 36, 2015, No 8, p. 082001, DOI: 10.1088/1674-4926/36/8/082001
[149] D. E. Vaughan: *British Journal of Applied Physics*,Vol. 12, 1961, No 8, p. 414, DOI: 10.1088/0508-3443/12/8/312

[150] R. Sharma, A. D. Acharya, S. B. Shrivastava, T. Shripathi, and V. Ganesan: *Optik*,Vol. 125, 2014, No 22, p. 6751-6756, DOI: https://doi.org/10.1016/j.ijleo.2014.07.104
[151] S. Joishy and B. V. Rajendra: *Journal of Electronic Materials*,Vol. 47, 2018, No 11, p. 6681-6690, DOI: 10.1007/s11664-018-6575-0
[152] N. M. Al-Hada, R. Md. Kasmani, H. Kasim, A. M. Al-Ghaili, M. A. Saleh, E. M. Banoqitah, A. M. Alhawsawi, A. A. Baqer, J. Liu, S. Xu, Q. Li, A. M. Noorazlan, A. A. A. Ahmed, M. H. Flaifel, S. Paiman, N. Nazrin, B. Ali Al-Asbahi, and J. Wang: *Nanomaterials*,Vol. 11, 2021, No 8, p. 2143, https://www.mdpi.com/2079-4991/11/8/2143
[153] F. T. Z. Toma, M. S. Rahman, and K. H. Maria: *Discover Materials*,Vol. 5, 2025, No 1, p. 60, DOI: 10.1007/s43939-025-00201-1
[154] J. Wang, Li, Y., and S. Chen: *Journal of Materials Science: Materials in Electronics*,Vol. 51, 2017, No 1, p. 100-108,
[155] M. M. Selim, N. M. Deraz, and M. Ramadan: *Adsorption Science & Technology*,Vol. 27, 2009, No 9, p. 883-891, DOI: 10.1260/0263-6174.27.9.883
[156] H. Kim, T. Park, and J. Lee: *Catalysis Today*,Vol. 302, 2018, p. 31-38,
[157] Z. Zhang, A. Ghasemi, N. Koutná, Z. Xu, T. Grünstäudl, K. Song, D. Holec, Y. He, P. H. Mayrhofer, and M. Bartosik: *Materials & Design*,Vol. 207, 2021, p. 109844, DOI: https://doi.org/10.1016/j.matdes.2021.109844
[158] B. Zhang and Y. Zhang: *Materials Science and Engineering: A*,Vol. 741, 2019, p. 184-190,
[159] V. K. Pecharsky and P. Y. Zavalij: *Fundamentals of powder diffraction and structural characterization of materials*, Springer, 2009, DOI,
[160] E. M. Yoshio Waseda, Kozo Shinoda: *X-Ray Diffraction Crystallography, book subtitle: Introduction, Examples and Solved Problems*, Springer Berlin, Heidelberg, 2011, DOI: https://doi.org/10.1007/978-3-642-16635-8
[161] M. A. Islam, M. S. Hossain, M. M. Aliyu, P. Chelvanathan, Q. Huda, M. R. Karim, K. Sopian, and N. Amin: *Energy Procedia*,Vol. 33, 2013, p. 203-213, DOI: https://doi.org/10.1016/j.egypro.2013.05.059
[162] N. Khedmi, M. Ben Rabeh, and M. Kanzari: *Journal of Materials Science & Technology*,Vol. 30, 2014, No 10, p. 1006-1011, DOI: https://doi.org/10.1016/j.jmst.2014.03.019
[163] M. S. Al-Alwani, A. A. Al-Amiery, and A. H. Kadhum: *Journal of Materials Science: Materials in Electronics*,Vol. 27, 2016, p. 11843-11851,
[164] T. Amakali, L. S. Daniel, V. Uahengo, N. Y. Dzade, and N. H. de Leeuw: *Crystals*,Vol. 10, 2020, No 2, p. 132, https://www.mdpi.com/2073-4352/10/2/132
[165] M. Bououdina, M. Benhaliliba, and A. Bouzid: *Journal of Alloys and Compounds*,Vol. 488, 2009, p. 575-579,
[166] J. Liu, X. Zhao, L. Duan, M. Cao, M. Guan, and W. Guo: *Journal of Materials Science: Materials in Electronics*,Vol. 24, 2013, p. 4932-4937,
[167] Sariya D. Al-Algawi, Rashed T. Rasheed, Hadeel S. Mansor, and E. A. Jassem: *Asian Journal of Materials Chemistry*,Vol. 2, 2017, No 1, p. 30-34, DOI: https://doi.org/10.14233/ajmc.2017.AJMC-P33
[168] W. D. Nix and B. M. Clemens: *Journal of Materials Research*,Vol. 14, 1999, No 8, p. 3467-3473, DOI: 10.1557/JMR.1999.0468
[169] S. Yu, L. Ma, L. He, and Y. Ni: *Physical Review E*,Vol. 100, 2019, No 5, p. 052804, DOI: 10.1103/PhysRevE.100.052804
[170] O. Shorinov: *Tensile Stress as a Factor of Deformation and Failure of Thin Films and Coatings*. Cham, Springer International Publishing2022, p. 26-35
[171] K. Bera, D. Chugh, H. H. Tan, A. Roy, and C. Jagadish: *Journal of Applied Physics*,Vol. 132, 2022, No 10, DOI: 10.1063/5.0102617
[172] L. Guo, Y. Hongjun, and W. Linzhi: Thermal Fracture of Nonhomogeneous Materials with Complex Interfaces. In: *Fracture Mechanics of Nonhomogeneous Materials*, edited by, Springer Nature Singapore, Singapore, 2023, p. 235-274, DOI: 10.1007/978-981-19-4063-7_7
[173] A. Zeilinger, J. Todt, C. Krywka, M. Müller, W. Ecker, B. Sartory, M. Meindlhumer, M. Stefenelli, R. Daniel, C. Mitterer, and J. Keckes: *Sci Rep*,Vol. 6, 2016, No 1, p. 22670, DOI: 10.1038/srep22670
[174] Y. Zhang, L. Guo, F. Guo, and S. Zhong: *Acta Mechanica*,Vol. 225, 2014, No 9, p. 2485-2500, DOI: 10.1007/s00707-014-1087-3
[175] D. Rajkumar and H. Umamahesvari: *In ECS Sensors Plus, Published on behalf of The Electrochemical Society by IOP Publishing Limited*,Vol. 24, 2024, No 1, DOI: DOI 10.1149/2754-2726/ad4045
[176] U.-J. Choi, H. Kim, Y.-S. Park, and J. S. Lee: *Bulletin of the Korean Chemical Society*,Vol. 39, 2018, No 1, p. 119-122, DOI: https://doi.org/10.1002/bkcs.11344
[177] J. Li, Q. An, and H. Fang: *Applied Surface Science*,Vol. 646, 2024, p. 158914, DOI: https://doi.org/10.1016/j.apsusc.2023.158914
[178] I. Ohlídal, M. Čermák, and J. Vohánka: Optical Characterization of Thin Films Exhibiting Defects. In: *Optical Characterization of Thin Solid Films*, edited by eds. O. Stenzel, et al., Springer International Publishing, Cham, 2018, p. 271-313, DOI: 10.1007/978-3-319-75325-6_10
[179] H. Kim, M. T. Tofail, and C. John: *JOM*,Vol. 70, 2018, No 4, p. 473-478, DOI: 10.1007/s11837-018-2739-x

[180] R. A. Babatunde and R. K. Odunaike: *Journal of Engineering Technology and Applied Physics*,Vol. 4, 2022, No 2, p. 4, DOI: https://doi.org/10.33093/jetap.2022.4.2.1
[181] M. Vujisic, P. Osmokrovic, A. Vasic, and K. Stankovic: Characterization of Thin Films for Solar Cells and Photodetectors and Possibilities for Improvement of Solar Cells Characteristics. In: *Solar Cells - Silicon Wafer-Based Technologies*, edited by L. A. Kosyachenko, IntechOpen, Rijeka, 2011, DOI: 10.5772/23157
[182] A. G. Evans, M. D. Drory, and M. S. Hu: *MRS Online Proceedings Library*,Vol. 108, 1987, No 1, p. 213-217, DOI: 10.1557/PROC-108-213
[183] P. Mallick, R. Biswal, C. Rath, D. C. Agarwal, A. Tripathi, D. K. Avasthi, D. Kanjilal, P. V. Satyam, and N. C. Mishra: *Nuclear Instruments and Methods in Physics Research Section B: Beam Interactions with Materials and Atoms*,Vol. 268, 2010, No 5, p. 470-475, DOI: https://doi.org/10.1016/j.nimb.2009.11.004
[184] F. Saadati, A.-R. Grayeli, and H. Savaloni: *Journal of theoretical and applied physics (iranian physical journal*,Vol. 4, 2010, No 1, p. 22–26, DOI: https://www.sid.ir/En/Journal/ViewPaper.aspx?ID=191567
[185] A. A. Leòn Baldelli: 'On fracture of thin films : a variational approach', 2013
[186] Fatema Tuz Zohora Toma, Md. Sharifur Rahman, Kazi Md. Amjad Hussain, and Syed Ahmed: *Journal of Modern Nanotechnology*,Vol. 4, 2024, No 6, p. 1-16, DOI: 10.53964/jmn.2024006
[187] A. Kumar, N. Bhattacharjee, B. Patel, J. B. Laloë, O. O. Famodu, and I. Ferain: *IEEE Transactions on Semiconductor Manufacturing*,Vol. 32, 2019, No 1, p. 48-53, DOI: 10.1109/TSM.2018.2876463
[188] T. Venkatesan: *IN-SITU Diagnostics For Deposition And Processing Of High Tc Superconducting Thin Films*, SPIE, 1990, DOI, https://doi.org/10.1117/12.963918
[189] S. Xu and Y. Miao: *Bulletin of the Korean Mathematical Society*,Vol. 51, 2014, No 5, p. 1399–1409, DOI: https://doi.org/10.4134/BKMS.2014.51.5.1399
[190] Yanhao Dong, Hongbing Yang, Jiangong Li, Ju Li, and I.-W. Chen: *Condensed Matter; Materials Science; Cornell University docs*,Vol., 2020, DOI: https://arxiv.org/abs/2002.12286v1
[191] B. Moralejo, A. Tejero, V. Hortelano, O. Martínez, J. Jiménez, and V. Parra: *physica status solidi c*,Vol. 9, 2012, No 10-11, p. 2158-2163, DOI: https://doi.org/10.1002/pssc.201200248
[192] N. Rosenblatt, J. Hack, C. Lee, Y. H. Zhang, and W. K. Metzger: *Performance Impacts of Band Tails on Cd(Se)Te Solar Cells*. In:2024 IEEE 52nd Photovoltaic Specialist Conference (PVSC), 2024, p. 0542-0542
[193] J. Moseley, S. Grover, D. Lu, G. Xiong, H. L. Guthrey, M. M. Al-Jassim, and W. K. Metzger: *Journal of Applied Physics*,Vol. 128, 2020, No 10, DOI: 10.1063/5.0018955
[194] Chris Yang, Hao Wu, and Ian Cooper: *Materials Sciences and Applications*,Vol. 4, 2013, No 2, p. 103-108, DOI: 10.4236/msa.2013.42011
[195] Shweta and S. Jadav: *Modelling the Impact of Grain Size on Carrier Concentration & Sensitivity for Gas Sensing Applications*. In:2024 International Conference on Computer, Electronics, Electrical Engineering & their Applications (IC2E3), 2024, p. 1-6
[196] X. Zhang, R. Gu, J. Zhao, G. Jin, M. Zhao, and Y. Xue: *Journal of Materials Engineering and Performance*,Vol. 24, 2015, No 10, p. 3815-3819, DOI: 10.1007/s11665-015-1698-4
[197] A. Katoch, Z. U. Abideen, H. W. Kim, and S. S. Kim: *ACS Applied Materials & Interfaces*,Vol. 8, 2016, No 4, p. 2486-2494, DOI: 10.1021/acsami.5b08416
[198] J. Kacher, K. Hattar, and I. M. Robertson: *Materials Science and Engineering: A*,Vol. 675, 2016, p. 110-119, DOI: https://doi.org/10.1016/j.msea.2016.08.045
[199] Norfarariyanti Parimon, M. H. Mamat, Ahmad Sabirin Zoolfakar, M. F. Malek, S. B. I. B., V. N., and R. M.: *Journal of electrical and electronic systems research*,Vol. 16, 2020, p. 28-34, DOI: https://doi.org/10.24191/JEESR.V16I1.004
[200] N. R. Aswathy, J. Varghese, and R. Vinodkumar: *Journal of Materials Science: Materials in Electronics*,Vol. 31, 2020, No 19, p. 16634-16648, DOI: 10.1007/s10854-020-04218-5
[201] M. Vopsaroiu, G. Vallejo Fernandez, M. J. Thwaites, J. Anguita, P. J. Grundy, and K. O'Grady: *Journal of Physics D: Applied Physics*,Vol. 38, 2005, No 3, p. 490, DOI: 10.1088/0022-3727/38/3/022
[202] E. Nayman, M. F. Gozukizil, B. Armutci, S. Temel, and F. O. Gokmen: *Journal of Sol-Gel Science and Technology*,Vol., 2025, DOI: 10.1007/s10971-025-06678-9
[203] N. V. Srinivasa, K. Haunsbhavi, N. Srinatha, H. M. Mahesh, S. Valanarasu, and B. Angadi: *Materials Science and Engineering: B*,Vol. 301, 2024, p. 117178, DOI: https://doi.org/10.1016/j.mseb.2024.117178
[204] M. Aftab, M. Z. Butt, D. Ali, M. U. Tanveer, and A. Hussnain: *Proceedings of the Pakistan Academy of Sciences: A. Physical and Computational Sciences*,Vol. 57, 2020, No 2, p. 51-74,
[205] M. M. Gomaa, M. H. Sayed, V. L. Patil, M. Boshta, and P. S. Patil: *Journal of Alloys and Compounds*,Vol. 885, 2021, p. 160908, DOI: https://doi.org/10.1016/j.jallcom.2021.160908
[206] E. Rahmani: Preparation and Characterization of Thin Films by Sol-Gel Method. In: *Thin Films - Growth, Characterization and Electrochemical Applications*, edited by eds. F. Sarf, et al., IntechOpen, Rijeka, 2023, DOI: 10.5772/intechopen.113722
[207] Fabian I. Ezema, Chandrakant D. Lokhande, and R. Jose: *Chemically Deposited Nanocrystalline Metal Oxide Thin Films Synthesis, Characterizations, and Applications*, 1st, Springer Cham, 2022, DOI: https://doi.org/10.1007/978-3-030-68462-4

[208] Joseph I. Goldstein, Dale E. Newbury, Joseph R. Michael, Nicholas W.M. Ritchie, John Henry J. Scott, and D. C. Joy: *Scanning Electron Microscopy and X-Ray Microanalysis*, 4th, Springer New York, NY, 2017, DOI: https://doi.org/10.1007/978-1-4939-6676-9
[209] M.-W. Xu, S.-J. Bao, and H.-L. Li: *Journal of Solid State Electrochemistry*,Vol. 11, 2007, No 3, p. 372-377, DOI: 10.1007/s10008-006-0155-6
[210] X. Yan, X. Tong, J. Wang, C. Gong, M. Zhang, and L. Liang: *Journal of Alloys and Compounds*,Vol. 593, 2014, p. 184-189, DOI: https://doi.org/10.1016/j.jallcom.2014.01.036
[211] Y. Q. Zhang, X. H. Xia, J. P. Tu, Y. J. Mai, S. J. Shi, X. L. Wang, and C. D. Gu: *Journal of Power Sources*,Vol. 199, 2012, p. 413-417, DOI: https://doi.org/10.1016/j.jpowsour.2011.10.065
[212] B. Bhushan: *Modern Tribology Handbook*, 1st CRC Press, Boca Raton, 2000, DOI: https://doi.org/10.1201/9780849377877
[213] N. Yamazoe and K. Shimanoe: *Sensors and Actuators, B: Chemical*,Vol. 128, 2008, No 2, p. 566-573, DOI: 10.1016/j.snb.2007.07.036
[214] S. Chatterjee and A. K. Kar: *Journal of Materials Science: Materials in Electronics*,Vol. 33, 2022, No 11, p. 8970-8986, DOI: 10.1007/s10854-021-07010-1
[215] R. Irani, S. M. Rozati, and S. Beke: *Applied Physics A*,Vol. 124, 2018, No 4, p. 321, DOI: 10.1007/s00339-018-1744-9
[216] S. Ebrahimi, B. Yarmand, and N. Naderi: *Advanced Ceramics Progress*,Vol. 3, 2017, No 4, p. 6-12, DOI: 10.30501/acp.2017.90759
[217] A. S. AlShammari, M. M. Halim, F. K. Yam, and N. H. M. Kaus: *Results in Physics*,Vol. 19, 2020, p. 103630, DOI: https://doi.org/10.1016/j.rinp.2020.103630
[218] M. P. Sarma and G. Wary: *International Letters of Chemistry, Physics and Astronomy*,Vol. 74, 2017, p. 22-35, DOI: 10.56431/p-845mhd
[219] X.-H. Li, M. Zhang, J. Yang, S. Xing, Y. Gao, Y.-Z. Li, S.-Y. Li, and C.-J. Wang: *Acta Physica Sinica*,Vol. 71, 2022, No 4, p. 048501-048501-048501-048512, DOI: 10.7498/aps.71.20211744
[220] N. Habubi, Z. M. Abood, and A. N. Algamel: *International Letters of Chemistry, Physics and Astronomy*,Vol. 65, 2016, p. 80-90, DOI: 10.56431/p-ov20s7
[221] A. Poruba, A. Fejfar, Z. Remeš, J. Špringer, M. Vaněček, J. Kočka, J. Meier, P. Torres, and A. Shah: *Journal of Applied Physics*,Vol. 88, 2000, No 1, p. 148-160, DOI: 10.1063/1.373635
[222] J. Morris, R. R. Arya, J. G. O'Dowd, and S. Wiedeman: *Journal of Applied Physics*,Vol. 67, 1990, No 2, p. 1079-1087, DOI: 10.1063/1.345793
[223] H. Ghasemi, M. H. Mozaffari, and R. Moradian: *Physica Scripta*,Vol. 99, 2024, No 12, p. 125938, DOI: 10.1088/1402-4896/ad8d43
[224] M. G. Althobaiti, M. A. Alosaimi, S. S. Alharthi, A. A. Alotaibi, and A. Badawi: *Optical Materials*,Vol. 151, 2024, p. 115341, DOI: https://doi.org/10.1016/j.optmat.2024.115341
[225] S. Kaur, Smriti Bhatia, T. Pooja, Kshitij Sharma, V. K. Malik, J.P. Singh, and K. Sen: *Condensed Matter: Materials Science, Cornell University*,Vol., 2024, DOI: https://doi.org/10.48550/arXiv.2412.03047
[226] S. Timoshnev, A. Kazakin, K. Shubina, V. Andreeva, E. Fedorenko, A. Koroleva, E. Zhizhin, O. Koval, A. Kurinnaya, A. Shalin, V. Bobrovs, and Y. Enns: *Advanced Materials Interfaces*,Vol. 11, 2024, No 9, p. 2300815, DOI: https://doi.org/10.1002/admi.202300815
[227] F. A. F. Lahiji, S. Bairagi, R. Magnusson, M. A. Sortica, D. Primetzhofer, E. Ekström, B. Paul, A. le Febvrier, and P. Eklund: *Journal of Vacuum Science & Technology A*,Vol. 41, 2023, No 6, DOI: 10.1116/6.0002914
[228] K. O. Ukoba, A. C. Eloka-Eboka, and F. L. Inambao: *Renewable and Sustainable Energy Reviews*,Vol. 82, 2018, p. 2900-2915, DOI: https://doi.org/10.1016/j.rser.2017.10.041
[229] O. K. Ukoba, A. C. Eloka-Eboka, and F. L. Inambao: *Energy Procedia*,Vol. 142, 2017, p. 236-243, DOI: https://doi.org/10.1016/j.egypro.2017.12.038
[230] B. P. Sahu, P. Sharma, S. K. Yadav, A. Shukla, and S. Dhar: *Journal of Physics D: Applied Physics*,Vol. 58, 2025, No 8, p. 085302, DOI: 10.1088/1361-6463/ad98a4
[231] M. R. da Silva, L. V. A. Scalvi, L. H. Dall'Antonia, and D. I. dos Santos: *Journal of Materials Science: Materials in Electronics*,Vol. 24, 2013, No 6, p. 1823-1831, DOI: 10.1007/s10854-012-1019-8
[232] M. Shkir, V. Ganesh, S. AlFaify, I. S. Yahia, and H. Y. Zahran: *Journal of Materials Science: Materials in Electronics*,Vol. 29, 2018, No 8, p. 6446-6457, DOI: 10.1007/s10854-018-8626-y
[233] M. A. Mayer, K. M. Yu, D. T. Speaks, J. D. Denlinger, L. A. Reichertz, J. W. Beeman, E. E. Haller, and W. Walukiewicz: *The Journal of Physical Chemistry C*,Vol. 116, 2012, No 29, p. 15281-15289, DOI: 10.1021/jp304481c
[234] T. Wang, P. Sun, F. Liu, and G. Lu: *Sensors and Actuators B: Chemical*,Vol. 352, 2022, p. 131039, DOI: https://doi.org/10.1016/j.snb.2021.131039
[235] R. Sasaki and J. Lemos: *Sensors and Actuators B-Chemical*,Vol. 352, 2022, p. 131039, DOI: https://doi.org/10.1016/j.snb.2021.131039
[236] A. S. Ahmed, M. Shafeeq M, M. L. Singla, S. Tabassum, A. H. Naqvi, and A. Azam: *Journal of Luminescence*,Vol. 131, 2011, No 1, p. 1-6, DOI: https://doi.org/10.1016/j.jlumin.2010.07.017

[237] S. Nandy, U. N. Maiti, C. K. Ghosh, and K. K. Chattopadhyay: *Journal of Physics: Condensed Matter*,Vol. 21, 2009, No 11, p. 115804, DOI: 10.1088/0953-8984/21/11/115804
[238] D. Kaya, H. Hopoğlu, A. Çelik, M. Akyol, F. Karadag, E. Şenadım Tüzemen, and A. Ekicibil: *Materials Science and Engineering: B*,Vol. 307, 2024, p. 117507, DOI: https://doi.org/10.1016/j.mseb.2024.117507
[239] F. Anyaegbunam and C. Augustine: *Digest Journal of Nanomaterials and Biostructures*,Vol. 13, 2018, No 3, p. 847-856,
[240] A. A. Akl and S. A. Mahmoud: *Optik*,Vol. 172, 2018, p. 783-793,
[241] M. T. Greiner, M. G. Helander, Z.-B. Wang, W.-M. Tang, and Z.-H. Lu: *The Journal of Physical Chemistry C*,Vol. 114, 2010, No 46, p. 19777-19781, DOI: https://doi.org/10.1021/jp108281m
[242] A. Echresh, M. A. Abbasi, M. Z. Shoushtari, M. Farbod, O. Nur, and M. Willander: *Semiconductor Science and Technology*,Vol. 29, 2014, No 11, p. 115009,
[243] F. Saadati, A. Grayeli, and H. Savaloni, 2010,
[244] M. Gomaa, G. R. Yazdi, S. Schmidt, M. Boshta, V. Khranovskyy, F. Eriksson, B. Farag, M. Osman, and R. Yakimova: *Materials Science in Semiconductor Processing*,Vol. 64, 2017, p. 32-38,
[245] A. Loukil, A. Boukhachem, M. Ben Amor, M. Ghamnia, and K. Raouadi: *Ceramics International*,Vol. 42, 2016, No 7, p. 8274-8289, DOI: https://doi.org/10.1016/j.ceramint.2016.02.040
[246] D. Yeboah, E. G. Asenso, and P. B. Fosuah: *International Journal of Ambient Energy*,Vol. 45, 2024, No 1, p. 2367110,
[247] A. Janotti and C. G. Van de Walle: *Physical Review B*,Vol. 76, 2007, No 16, p. 165202, DOI: 10.1103/PhysRevB.76.165202
[248] D. Steiauf, J. L. Lyons, A. Janotti, and C. G. Van de Walle: *APL Materials*,Vol. 2, 2014, No 9, DOI: 10.1063/1.4894195
[249] F. A. Al-Agel: *Materials Letters*,Vol. 100, 2013, p. 115-118, DOI: https://doi.org/10.1016/j.matlet.2013.03.032
[250] S. Lany and A. Zunger: *Applied Physics Letters*,Vol. 96, 2010, No 14, DOI: 10.1063/1.3383236
[251] A. Almalki: 'Investigation of structural, electrical and optical properties of advanced wide bandgap semiconductor materials and devices', PhD thesis, thesis, University of Nottingham., 2023
[252] B. Choudhury, M. Dey, and A. Choudhury: *International Nano Letters*,Vol. 3, 2013, No 1, p. 25, DOI: 10.1186/2228-5326-3-25
[253] N. Khatun, E. G. Rini, P. Shirage, P. Rajput, S. N. Jha, and S. Sen: *Materials Science in Semiconductor Processing*,Vol. 50, 2016, p. 7-13, DOI: https://doi.org/10.1016/j.mssp.2016.04.002
[254] A. Shah: Chapter IC-1 - Thin-Film Silicon Solar Cells1. In: *Solar Cells (Second Edition)*, edited by eds. A. McEvoy, et al., Elsevier, 2013, p. 159-223, DOI: https://doi.org/10.1016/B978-0-12-386964-7.00007-X
[255] S. Bai, N. Zhang, C. Gao, and Y. Xiong: *Nano Energy*,Vol. 53, 2018, p. 296-336, DOI: https://doi.org/10.1016/j.nanoen.2018.08.058
[256] J. E. Dominguez, L. Fu, and X. Q. Pan: *Applied Physics Letters*,Vol. 81, 2002, No 27, p. 5168-5170, DOI: 10.1063/1.1530745
[257] S. Boulila, M. Ghamnia, A. Boukhachem, A. Ouhaibi, M. A. Chakhoum, C. Fauquet, V. Heresanu, and D. Tonneau: *Philosophical Magazine Letters*,Vol. 100, 2020, No 6, p. 283-293, DOI: 10.1080/09500839.2020.1760389
[258] L. Vegard: *Zeitschrift für Physik*,Vol. 5, 1921, No 1, p. 17-26, DOI: 10.1007/BF01349680
[259] R. Sharma and K. Yadav: *Applied Physics A*,Vol. 124, 2018, No 2, p. 88, DOI: 10.1007/s00339-017-1531-z
[260] N. Sharma and S. P. Choudhury: *Materials Science and Engineering: B*,Vol. 307, 2024, p. 117505, DOI: https://doi.org/10.1016/j.mseb.2024.117505
[261] M. Sharma, D. Sajwan, A. Gouda, A. Sharma, and V. Krishnan: *Photochemistry and Photobiology*,Vol. 100, 2024, No 4, p. 830-896, DOI: https://doi.org/10.1111/php.13959
[262] A. Akdağ, D. İskenderoğlu, M. E. Güldüren, S. M. Karadeniz, and H. Güney: *Ceramics International*,Vol. 50, 2024, No 18, Part A, p. 32430-32438, DOI: https://doi.org/10.1016/j.ceramint.2024.06.051
[263] S. A. Ul Islam, F. A. Andrabi, F. Mohmed, K. Sultan, M. Ikram, and K. Asokan: *Journal of Solid State Chemistry*,Vol. 290, 2020, p. 121597, DOI: https://doi.org/10.1016/j.jssc.2020.121597
[264] V. Ganesh: *Optics & Laser Technology*,Vol. 146, 2022, p. 107579, DOI: https://doi.org/10.1016/j.optlastec.2021.107579
[265] M. I. Ahmad and S. S. Bhattacharya: *Applied Physics Letters*,Vol. 95, 2009, No 19, p. 191906, DOI: 10.1063/1.3261754
[266] G. K. Williamson and W. H. Hall: *Acta Metallurgica*,Vol. 1, 1953, No 1, p. 22-31, DOI: https://doi.org/10.1016/0001-6160(53)90006-6
[267] K. Anandan and V. Rajendran: *Materials Science in Semiconductor Processing*,Vol. 14, 2011, No 1, p. 43-47, DOI: https://doi.org/10.1016/j.mssp.2011.01.001
[268] S. Benramache and B. Benhaoua: *Superlattices and Microstructures*,Vol. 52, 2012, No 4, p. 807-815, DOI: https://doi.org/10.1016/j.spmi.2012.06.005

[269] S. Benramache and B. Benhaoua: *Superlattices and Microstructures*,Vol. 52, 2012, No 6, p. 1062-1070, DOI: https://doi.org/10.1016/j.spmi.2012.08.006
[270] Hamed Sharifi Dehsari, Wolfgang Tremel, Anielen Halda Ribeiro, Gerhard Jakob, BoraErsöz, and K. Asadi: *CrystEngComm*,Vol. 19, 2017, p. 6694-6702, DOI: 10.1039/C7CE01406F
[271] T. Fazal, S. Iqbal, M. Shah, B. Ismail, N. Shaheen, A. I. Alharthi, N. S. Awwad, and H. A. Ibrahium: *Results in Physics*,Vol. 40, 2022, p. 105817, DOI: https://doi.org/10.1016/j.rinp.2022.105817
[272] K. K. Kwon YJ, Lim CS, Shim KB. : *Journal of Ceramic Processing Research*,Vol. 3, 2002, No 3, p. 146-149,
[273] N. Naveed: Fundamentals of Thin Films. In: *Thin Films and Coatings: Engineering Applications*, edited by eds. A. D. Chandio, et al., Springer Nature Singapore, Singapore, 2025, p. 25-47, DOI: 10.1007/978-981-96-0005-2_2
[274] W.-J. Liu, Y.-H. Chang, S.-T. Hsu, C.-L. Fern, Y.-T. Chen, S.-Y. Tsao, and S.-H. Lin: *Journal of Electronic Materials*,Vol. 53, 2024, No 8, p. 4498-4511, DOI: 10.1007/s11664-024-11237-z
[275] E. S. Babu, S. Kim, J.-H. Song, and S.-K. Hong: *Chemical Physics Letters*,Vol. 658, 2016, p. 182-187, DOI: https://doi.org/10.1016/j.cplett.2016.06.050
[276] F. I. Dar, K. R. Moonoosawmy, and M. Es-Souni: *Nanoscale Research Letters*,Vol. 8, 2013, No 1, p. 363, DOI: 10.1186/1556-276X-8-363
[277] S. Panwar, V. Kumar, and L. P. Purohit: 6 - Oxide thin films grown using spin-coating methods. In: *Defect-Induced Magnetism in Oxide Semiconductors*, edited by eds. P. Kumar, et al., Woodhead Publishing, 2023, p. 109-134, DOI: https://doi.org/10.1016/B978-0-323-90907-5.00012-9
[278] B. Lima: 2. Defects on sputtered ZnO. edited by, 2021, DOI: https://doi.org/10.6084/m9.figshare.14357246
[279] A. N. Ech-Chergui: 'Functional doped metal oxide: Zinc oxide (ZnO) as transparent conducting oxide (TCO) ; Titanium dioxide (TiO_2) as thermographic phosphor and protective coating', 2011
[280] T. Niu, F. Zhen, Y.-M. Xie, T. Yang, Q. Yao, J. Lu, K. Zhao, and H.-L. Yip: *ACS Applied Materials & Interfaces*,Vol. 14, 2022, No 47, p. 52838-52848, DOI: 10.1021/acsami.2c14494
[281] Y. Zhang, Y. Peng, F. Liu, K. Li, N. Zhong, Y. Liu, Y. Hao, and G. Han: *IEEE Transactions on Electron Devices*,Vol. 70, 2023, No 7, p. 3788-3793, DOI: 10.1109/TED.2023.3279064
[282] K. G. Krishna, S. Parne, N. Pothukanuri, V. Kathirvelu, S. Gandi, and D. Joshi: *Sensors and Actuators A: Physical*,Vol. 341, 2022, p. 113578, DOI: https://doi.org/10.1016/j.sna.2022.113578
[283] G. W. Ho: *Science of Advanced Materials*,Vol. 3, 2011, No 2, p. 150-168 (119), DOI: https://doi.org/10.1166/sam.2011.1145
[284] I. Lungu, S. Busuioc, E. I. Monaico, and T. Potlog: *Effect of Particle Size and Roughness on Contact Angle of ZnTe Thin Films*. Cham, Springer Nature Switzerland2024, p. 268-277
[285] G. Eranna: *Metal Oxide Nanostructures as Gas Sensing Devices*, Taylor & Francis, 2011, DOI, https://books.google.dz/books?id=lbrOOxdzursC
[286] Y. Deng: Sensing Mechanism and Evaluation Criteria of Semiconducting Metal Oxides Gas Sensors. In: *Semiconducting Metal Oxides for Gas Sensing*, edited by, Springer Singapore, Singapore, 2019, p. 23-51, DOI: 10.1007/978-981-13-5853-1_2
[287] J.-H. Lee: 4 - Technological realization of semiconducting metal oxide–based gas sensors. In: *Gas Sensors Based on Conducting Metal Oxides*, edited by eds. N. Barsan, et al., Elsevier, 2019, p. 167-216, DOI: https://doi.org/10.1016/B978-0-12-811224-3.00004-4
[288] J. Tauc: *Materials Research Bulletin*,Vol. 3, 1968, No 1, p. 37-46, DOI: https://doi.org/10.1016/0025-5408(68)90023-8
[289] H.-L. Chen, Y.-M. Lu, and W.-S. Hwang: *Surface and Coatings Technology*,Vol. 198, 2005, No 1, p. 138-142, DOI: https://doi.org/10.1016/j.surfcoat.2004.10.032
[290] T. M. Schuler, D. L. Ederer, S. Itza-Ortiz, G. T. Woods, T. A. Callcott, and J. C. Woicik: *Physical Review B*,Vol. 71, 2005, No 11, p. 115113, DOI: 10.1103/PhysRevB.71.115113
[291] J. Zhou, G. Luo, Y. Wei, J. Zheng, and C. Xu: *Electrochimica Acta*,Vol. 186, 2015, p. 182-191, DOI: https://doi.org/10.1016/j.electacta.2015.10.154
[292] A. Šurca, B. Orel, B. Pihlar, and P. Bukovec: *Journal of Electroanalytical Chemistry*,Vol. 408, 1996, No 1, p. 83-100, DOI: https://doi.org/10.1016/0022-0728(96)04509-3
[293] C. M. Santos, M. T. G. Souza, M. N. G. Santos, N. B. Lima, H. C. B. Nascimento, J. C. O. Freitas, A. C. V. Nóbrega, and E. P. Marinho: *Next Materials*,Vol. 6, 2025, p. 100502, DOI: https://doi.org/10.1016/j.nxmate.2025.100502
[294] A. F. Wells: *Structural Inorganic Chemistry," 5th ed., Clarendon Press, Oxford,1984, p. 1288 (metallic radii for 12-coordination); Huheey, pp. 292 (covalent radii for nonmetals); R.D. Shannon, Acta Crystallogr., Sect. A: Found. Crystallogr., 32, 751 (1976) (ionic radii for 6-coordination)*, 1984, DOI,
[295] Ü. Özgür, Y. I. Alivov, C. Liu, A. Teke, M. A. Reshchikov, S. Doğan, V. Avrutin, S.-J. Cho, and H. Morkoç: *Journal of Applied Physics*,Vol. 98, 2005, No 4, DOI: 10.1063/1.1992666
[296] X. d. l. Cruz Romero: *Treball de Fi de Grau*,Vol., 2020,
[297] S. Ozaki, T. Tsuchiya, Y. Inokuchi, and S. Adachi: *physica status solidi (a)*,Vol. 202, 2005, No 7, p. 1325-1335, DOI: https://doi.org/10.1002/pssa.200460905

[298] R. Chen, B. Ling, X. W. Sun, and H. D. Sun: *Advanced Materials*,Vol. 23, 2011, No 19, p. 2199-2204, DOI: https://doi.org/10.1002/adma.201100423
[299] S. T. Tan, B. J. Chen, X. W. Sun, X. Hu, X. H. Zhang, and S. J. Chua: *Journal of Crystal Growth*,Vol. 281, 2005, No 2, p. 571-576, DOI: https://doi.org/10.1016/j.jcrysgro.2005.04.093
[300] F. Zahedi, R. S. Dariani, and S. M. Rozati: *Bulletin of Materials Science*,Vol. 37, 2014, No 3, p. 433-439, DOI: 10.1007/s12034-014-0696-8
[301] V. A. F. E.S. Rajalekshmi , R. Shabu , A. Moses Ezhil Raj: *Neuroquantology*,Vol. 20, 2022, No 10, p. 8463-8478, DOI: DOI: 10.14704/nq.2022.20.10.NQ55831
[302] C. Klingshirn: *ChemPhysChem*,Vol. 8, 2007, No 6, p. 782-803, DOI: https://doi.org/10.1002/cphc.200700002
[303] O. Ako, M. Baneto, M. Senthilkumar, M. Haris, A. D. Gboglo, K. S. Gadedjisso-Tossou, A. C. Ahyi, K. Beltako, and K. A. Amou: *2025*,Vol. 14, 2025, No 3, p. 10, DOI: 10.61435/ijred.2025.61069
[304] Yus Rama Denny, Teguh Firmansyah, Adhitya Trenggono, Danu Wijaya, Ganesha Antarnusa, and A. Suherman: *The Journal of Pure and Applied Chemistry Research*,Vol. 9, 2020, No 1, p. 57-65, DOI: 10.21776/ub.jpacr.2020.009.01.514
[305] M. F. Malek, M. H. Mamat, M. Z. Musa, M. Z. Sahdan, and M. R. Mahmood: *Advanced Materials Research*,Vol. 667, 2013, p. 193-199, DOI: 10.4028/www.scientific.net/AMR.667.193
[306] C. Guillén: *Electronic Materials*,Vol. 6, 2025, No 1, p. 3, https://www.mdpi.com/2673-3978/6/1/3
[307] G. Tang, H. Liu, and W. Zhang: *Advances in Materials Science and Engineering*,Vol. 2013, 2013, No 1, p. 348601, DOI: https://doi.org/10.1155/2013/348601
[308] W. Amananti, R. Ardiyanto, H. Sutanto, I. Nurhasanah, and I. Tivani: *Journal of Natural Sciences and Mathematics Research*,Vol. 8, 2022, No 1, p. 52-58, DOI: https://doi.org/10.21580/jnsmr.2022.8.1.9623
[309] H. Zhong, F. Pan, S. Yue, C. Qin, V. Hadjiev, F. Tian, X. Liu, F. Lin, Z. Wang, and J. Bao: *The Journal of Physical Chemistry Letters*,Vol. 14, 2023, No 29, p. 6702-6708, DOI: 10.1021/acs.jpclett.3c01416
[310] H. N. Shaheen and H. M. J. Al-Taii: *Journal of Theoretical and Applied Physics*,Vol. 18, 2024, DOI: 10.57647/j.jtap.2024.si-AICIS23.16
[311] M. N. H. Mia, M. F. Pervez, M. K. Hossain, M. Reefaz Rahman, M. J. Uddin, M. A. Al Mashud, H. K. Ghosh, and M. Hoq: *Results in Physics*,Vol. 7, 2017, p. 2683-2691, DOI: https://doi.org/10.1016/j.rinp.2017.07.047
[312] J. Tauc: *Optical Properties of Amorphous Semiconductors, In: Amorphous and Liquid Semiconductors*, 1st, Springer New York, NY, 1972, DOI: https://doi.org/10.1007/978-1-4615-8705-7
[313] G. D. Cody: Hydrogenated Amorphous Silicon. In: *Semiconductors And Semimetals:hydrogenated Amorphous Silicon/part B-optical Properties*, edited by Pankove, Academic Press Inc., Orlando., 1984, p. 439, DOI,
[314] M.A. Sangamesha, K. Pushapalatha, and G. L. Shekar: *International Journal of Research in Engineering and Technology*,Vol. 2, 2013, No 11, p. 227-234, DOI: 10.15623/ijret.2013.0211035
[315] A. Lestari, S. Iwan, D. Djuhana, C. Imawan, A. Harmoko, and V. Fauzia: *AIP Conference Proceedings*,Vol. 1729, 2016, No 1, DOI: 10.1063/1.4946930
[316] L. N. Lau, N. B. Ibrahim, and H. Baqiah: *Applied Surface Science*,Vol. 345, 2015, p. 355-359, DOI: https://doi.org/10.1016/j.apsusc.2015.03.129
[317] O. D. Jumaah and Y. Jaluria: *Journal of Manufacturing Science and Engineering*,Vol. 143, 2021, No 11, DOI: 10.1115/1.4050825
[318] Y. Wang, H. Xu, C. Shao, and J. Cao: *Applied Surface Science*,Vol. 392, 2017, p. 649-657, DOI: https://doi.org/10.1016/j.apsusc.2016.09.097
[319] P. Nunes, E. Fortunato, A. Lopes, and R. Martins: *International Journal of Inorganic Materials*,Vol. 3, 2001, No 8, p. 1129-1131, DOI: https://doi.org/10.1016/S1466-6049(01)00136-2
[320] R. Zamiri, H. Mahmoudi Chenari, H. F. Moafi, M. Shabani, S. A. Salehizadeh, A. Rebelo, J. S. Kumar, M. P. F. Graça, M. J. Soares, and J. M. F. Ferreira: *Ceramics International*,Vol. 42, 2016, No 11, p. 12860-12867, DOI: https://doi.org/10.1016/j.ceramint.2016.05.051
[321] K. Adaikalam, V. S., A. A. Mossad, S. M. A., Y. Woochul, and H.-S. and Kim: *Journal of Asian Ceramic Societies*,Vol. 10, 2022, No 1, p. 108-119, DOI: 10.1080/21870764.2021.2015847
[322] Harold P. Klug and L. E. Alexander: *X-Ray Diffraction Procedures: For Polycrystalline and Amorphous Materials,* , 2nd Wiley publishing, 1974, DOI,
[323] B. E. Warren: *X-ray Diffraction*, Courier Corporation, 1990, DOI,
[324] N. Karar, F. Singh, and B. R. Mehta: *Journal of Applied Physics*,Vol. 95, 2003, No 2, p. 656-660, DOI: https://doi.org/10.1063/1.1633347
[325] M. Komaki, T. Mimura, R. Kurahasi, H. Odahara, K. Amiya, Y. Saotome, and T. Yamasaki: *Materials Transactions*,Vol. 53, 2012, No 4, p. 681-689, DOI: https://doi.org/10.2320/matertrans.M2011261
[326] V. M. Kaganer, R. Köhler, M. Schmidbauer, R. Opitz, and B. Jenichen: *Physical Review B*,Vol. 55, 1997, No 3, p. 1793-1810, DOI: https://doi.org/10.1103/PhysRevB.55.1793
[327] M. H. Frey and D. A. Payne: *Physical Review B*,Vol. 54, 1996, No 5, p. 3158-3168, DOI: https://doi.org/10.1103/PhysRevB.54.3158
[328] J. M. Polfus, M.-L. Fontaine, A. Thøgersen, M. Riktor, T. Norby, and R. Bredesen: *Journal of Materials Chemistry A*,Vol. 4, 2016, No 21, p. 8105-8112, DOI: 10.1039/C6TA02377K

[329] A. Modwi, K. K. Taha, L. Khezami, A. S. Al-Ayed, O. K. Al-Duaij, M. Khairy, and M. Bououdina: *Journal of Inorganic and Organometallic Polymers and Materials*,Vol. 30, 2020, No 7, p. 2633-2644, DOI: 10.1007/s10904-019-01425-4
[330] L. H. S. Lacerda, S. R. de Lazaro, and R. A. P. Ribeiro: *IOP Conference Series: Materials Science and Engineering*,Vol. 97, 2015, No 1, p. 012005, DOI: 10.1088/1757-899X/97/1/012005
[331] L. Herissi, L. Hadjeris, M. S. Aida, and J. Bougdira: *Thin Solid Films*,Vol. 605, 2016, p. 116-120, DOI: https://doi.org/10.1016/j.tsf.2015.09.034
[332] F. Fievet, P. Germi, F. de Bergevin, and M. Figlarz: *Journal of Applied Crystallography*,Vol. 12, 1979, No 4, p. 387-394, DOI: https://doi.org/10.1107/S0021889879012747
[333] M. Ben Amor, A. Boukhachem, K. Boubaker, and M. Amlouk: *Materials Science in Semiconductor Processing*,Vol. 27, 2014, p. 994-1006, DOI: https://doi.org/10.1016/j.mssp.2014.08.008
[334] S. K. Jesudoss, J. J. Vijaya, N. C. S. Selvam, K. Kombaiah, M. Sivachidambaram, T. Adinaveen, and L. J. Kennedy: *Clean Technologies and Environmental Policy*,Vol. 18, 2016, No 3, p. 729-741, DOI: 10.1007/s10098-015-1047-1
[335] L. Wang, R. Dou, Y. Li, H. Lu, M. Bai, D. Hall, and Y. Chen: *Materials Science and Engineering: A*,Vol. 658, 2016, p. 280-288, DOI: https://doi.org/10.1016/j.msea.2016.02.008
[336] A. Lacz, B. Bak, and R. Lach: *Journal of Thermal Analysis and Calorimetry*,Vol. 133, 2018, No 1, p. 107-114, DOI: 10.1007/s10973-018-6968-6
[337] I. Massoudi: *Physica Scripta*,Vol. 100, 2025, No 3, p. 035911, DOI: 10.1088/1402-4896/adafe6
[338] C. C. Okorieimoh, U. Chime, A. C. Nkele, A. C. Nwanya, I. G. Madiba, A. K. H. Bashir, S. Botha, P. U. Asogwa, M. Maaza, and F. I. Ezema: *Superlattices and Microstructures*,Vol. 130, 2019, p. 321-331, DOI: https://doi.org/10.1016/j.spmi.2019.05.010
[339] M. K. Gurjar, T. Harsh, R. Dash, and A. S. Bhattacharyya: *MRS Advances*,Vol. 8, 2023, No 16, p. 925-930, DOI: 10.1557/s43580-023-00588-0
[340] Joseph I. Goldstein, Dale E. Newbury, Joseph R. Michael, Nicholas W.M. Ritchie, J. H. J., and D. C. J. Scott: *Scanning Electron Microscopy and X-Ray Microanalysis*, 4th, Springer New York, NY, 2018, DOI: https://doi.org/10.1007/978-1-4939-6676-9
[341] S. Li, P. Liu, and Q. Wang: *Applied Surface Science*,Vol. 263, 2012, p. 613-618, DOI: https://doi.org/10.1016/j.apsusc.2012.09.117
[342] D. K. Schroder: *Roughness and Electronic Performance, In: Semiconductor Material and Device Characterization*, John Wiley & Sons, Inc., Hoboken, New Jersey, 2006, DOI,
[343] S. M. Rozati and E. Shadmani: *Surface and Interface Analysis*,Vol. 42, 2010, No 6-7, p. 1160-1162, DOI: https://doi.org/10.1002/sia.3273
[344] B. W. Shivaraj, H. N. N. Murthy, M. Krishna, and B. S. Satyanarayana: *Procedia Materials Science*,Vol. 10, 2015, p. 292-300, DOI: https://doi.org/10.1016/j.mspro.2015.06.053
[345] E. Burstein: *Physical Review*,Vol. 93, 1954, No 3, p. 632-633, DOI: 10.1103/PhysRev.93.632
[346] J. Mann, Q. Ma, P. M. Odenthal, M. Isarraraz, D. Le, E. Preciado, D. Barroso, K. Yamaguchi, G. von Son Palacio, A. Nguyen, T. Tran, M. Wurch, A. Nguyen, V. Klee, S. Bobek, D. Sun, T. F. Heinz, T. S. Rahman, R. Kawakami, and L. Bartels: *Advanced Materials*,Vol. 26, 2014, No 9, p. 1399-1404, DOI: https://doi.org/10.1002/adma.201304389
[347] K. Luo, S. Chen, and C. Duan: *Science China Physics, Mechanics & Astronomy*,Vol. 58, 2015, No 8, p. 87301, DOI: 10.1007/s11433-015-5665-8
[348] Z. Zhu, J. Xiao, H. Sun, Y. Hu, R. Cao, Y. Wang, L. Zhao, and J. Zhuang: *Physical Chemistry Chemical Physics*,Vol. 17, 2015, No 33, p. 21605-21610, DOI: 10.1039/C5CP02558C

الملخص:
ركز بحث الدكتوراه هذا على تطوير وتوصيف الأغشية الرقيقة من أكسيد الفلزات غير المخدرة والمخدرة بالباريوم - (Ba) بما في ذلك مركبات والزنك و أكسيد الزنك- النيكل المخصصة لاستشعار الغازات. باستخدام تقنية الانحلال الحراري بالرش، فحصت الدراسة تأثير معلمات الترسيب وتطعيم الباريوم على الخواص الهيكلية و المورفولوجيا والبصرية والكهربائية لهذه المواد. كان الهدف الرئيسي هو تحسين هذه الأفلام لتحقيق توصيل مستقر من النوع p في NiO وتحسين أداء مستشعر الغاز. أظهرت النتائج أن طريقة التوليف أنتجت أغشية بلورية تم تعديل خصائصها من خلال تركيز السلائف وتطعيمها بمنشطات Ba. ولوحظت تغيرات كبيرة في المعلمات الهيكلية ومورفولوجيا السطح والخصائص البصرية لكل من أغشية NiO وZnO. و تكمن المساهمة الأكثر أهمية في تحليل مركبات أكاسيد الزنك والنيكل المنشطة بالباريوم، حيث تم تأكيد التعايش بين طوري أكسيد الزنك و أكسيد النيكل و أثر التشويب مباشرة على استجاباتها البصرية والكهربائية. على الرغم من هذه التطورات، لا تزال هناك تحديات، ليس أقلها صعوبة تحقيق توصيلية مستقرة من النوع p في أكسيد النيكل، والحفاظ على جودة الغشاء المتجانس. يتطلب الاستقرار طويل الأمد في البيئات المتغيرة بحثًا مستمرًا. وتشمل السبل المستقبلية النمذجة الحاسوبية، وهندسة الواجهة، واستراتيجيات المنشطات المشتركة (التنشيط المختلط)، وتحسين المعالجة بعد الترسيب لتحسين الأداء والجدوى التجارية لمستشعرات الغاز هذه.
الكلمات المفتاحي: الأغشية الرقيقة؛ أكاسيد المعادن؛ كشف الغازات؛ التحلل الحراري بالرش؛ منشطات الباريوم؛ أجهزة الاستشعار

Abstract :
This doctoral research focused on the development, characterization of undoped, and barium (Ba)-doped metal oxide thin films - including NiO, ZnO and ZnNiO composites - intended for gas sensing. Using the spray pyrolysis technique, the study examined the influence of deposition parameters and Ba doping on the structural, morphological, optical and electrical properties of these materials. The main objective was to optimize these films to achieve stable p-type conductivity in NiO and improve gas sensor performance. The results showed that the synthesis method produced crystalline films whose properties were modulated by precursor concentration and Ba doping. Significant changes in structural parameters, surface morphology and optical characteristics were observed for both NiO and ZnO films. The most important contribution lies in the analysis of Ba-doped ZnNiO composites, where the coexistence of ZnO and NiO phases was confirmed, and doping directly affected their optical and electrical responses. Despite these advances, challenges remain, not least the difficulty of achieving stable p-type conductivity in NiO and maintaining homogeneous film quality. Long-term stability in variable environments requires ongoing research. Future avenues include computational modeling, interface engineering, co-doping strategies, and optimization of post-deposition processing to improve the performance and commercial viability of these gas sensors.
Keywords: Thin films; Metal oxides; Gas detection; Spray pyrolysis; Barium doping; Sensors

Résumé:
Cette recherche doctorale s'est concentrée sur l'élaboration et la caractérisation de films minces d'oxydes métalliques non dopés et dopés au baryum (Ba)- notamment NiO, ZnO et composites ZnNiO- destinés à la détection de gaz. En utilisant la technique de pyrolyse par pulvérisation, l'étude a examiné l'influence des paramètres de dépôt et du dopage Ba sur les propriétés structurales, morphologiques, optiques et électriques de ces matériaux. L'objectif principal était d'optimiser ces films pour atteindre une conductivité p-type stable dans le NiO et d'améliorer les performances des capteurs de gaz. Les résultats ont montré que la méthode de synthèse produisait des films cristallins dont les propriétés étaient modulées par la concentration des précurseurs et le dopage au Ba. Des modifications significatives des paramètres structuraux, de la morphologie de surface et des caractéristiques optiques ont été observées pour les films de NiO et ZnO. La contribution la plus importante réside dans l'analyse des composites ZnNiO dopés au Ba, où la coexistence des phases ZnO et NiO a été confirmée, et où le dopage a impacté directement leurs réponses optiques et électriques. Malgré ces avancées, des défis persistent, notamment la difficulté à obtenir une conductivité p-type stable dans le NiO et à maintenir une qualité de film homogène. La stabilité à long terme dans des environnements variables nécessite des recherches continues. Des pistes futures incluent la modélisation computationnelle, l'ingénierie des interfaces, les stratégies de co-dopage, et l'optimisation des traitements post-dépôt pour améliorer les performances et la viabilité commerciale de ces capteurs de gaz.
Mots-clés: Couches minces ; Oxydes métalliques ; Détection de gaz ; Pyrolyse par pulvérisation ; Dopage au baryum ; Capteurs